UNIVERSITÀ DEGLI STUDI DI NAPOLI FEDERICO II

Ph.D. School in Earth Sciences, Environment and Resources

XXIX Cycle

Ph.D. Thesis

Geophysical modeling for groundwater and soil contamination risk assessment

Payal Rani

Supervisor

Prof. Rosa Di Maio

Co-supervisor

Dr. Ester Piegari
Prof. Pantelis Soupios

2017

Contents

Introduction

In last few decades, contamination of soil and groundwater has become a progressively important problem at global scale. The improper deposition of various anthropogenic sources (wastes, chemicals, oil spills, etc.) and their infiltration in the subsurface has largely affected the quality of the soil and groundwater. Many studies have been carried out for the identification and solution of this problem around the world.

However, in recent years, environmental geophysics has emerged as a field of fertile research, developed for exploring the potential of the geophysical methods to monitor the environment and characterize the subsurface properties and processes relevant to the hydrological studies, such as those associated with water resources and contaminant transport. In this PhD thesis, attention is focused on identification of possible phenomenon of contaminant transport in soil and groundwater, through a multidisciplinary approach that integrates geophysical data with hydrogeological and geochemical studies, and modelling of groundwater flow and contaminant transport.

After a brief introduction on the theoretical background of the considered geophysical methods and simulation models presented in Chapter 1, the original contributions of the present work are discussed in Chapter 2. They mainly concern: *i)* development of new inversion methods of self-potential (SP) data for the full characterization of the contaminant source parameters; *ii)* identification of possible phenomenon of contaminant transport in soil and groundwater and simulation of contaminant propagation in unsaturated zone by cellular automata modeling.

Even though self-potential data are easy to acquire and often provide good qualitative information about subsurface flows and other processes, a quantitative interpretation of SP data is often complicated as it is linked to both multiplicity and complexity of the sources that cause the observed surface SP anomalies. Therefore, to solve this task, new inversion methods have been proposed that allow a full characterization of the SP anomaly source parameters. The first

part of Chapter 2 is devoted to these methods, specifically based on spectral, tomographical and global optimization approaches. The efficiency of these methods is checked on several synthetic examples and for different anomalous structures (most often expected geological structures), such as sphere, horizontal and vertical cylinder and inclined sheet. Then, to test the applicability and effectiveness of the proposed methods, various real field data sets taken from the literature were used and their results were compared with those coming from other numerical approaches.

In the second part of Chapter 2, two different cellular automaton models are also presented. They have been developed to simulate diffusion-dispersion phenomena of pollutant in saturated and unsaturated conditions and to delineate the most dangerous scenarios in terms of maximum distances travelled by the contaminant. At the end of the Chapter 2, the results of simulations obtained for simple homogeneous soil layers are discussed.

Then, two applications of the developed models to different study areas are discussed in Chapter 3 and 4, respectively.

The first discussed investigated area is located in the western part of Crete Island (Greece) and it is characterized by contamination due to Olive Oil Mills' waste in a pond located close to the Keritis river (the main riverine of Chania valley). In particular, previously collected electrical resistivity and self-potential data have been analyzed to detect and monitor the organic contaminant. The numerical methods proposed in Chapter 2 for SP data inversion have been applied to study the time-evolution of SP data and characterize the source parameters of the anomalous sources. Then, by using information on the area coming from geological, geochemical and geophysical surveys, the cellular automaton developed in Chapter 2 for modeling contaminant propagation in unsaturated zones has been applied to simulate contaminant transport and to outline the most dangerous scenarios. Finally, by using the commercial software FEFLOW, a numerical model based on finite element analysis has been developed for simulating groundwater flow in the investigated area.

The second test area has been selected in the western basin of Solofrana river valley in southern Italy. This area is affected by heavy floods and has high chances of contamination due to agricultural and industrial activities in the surroundings. Therefore, a multi-methodological geophysical survey, including electrical resistivity and induced polarization tomography and self-potential measurements, has been carried out to obtain a hydrogeophysical characterization of the area by integration with hydrogeological and geochemical data coming from stratigraphical logs and water samples, respectively. In particular, the SP electrokinetic component of the observed SP signals has been correlated with the water fluxes and a possible mechanism to explain the unusual sign of the charge carriers in the groundwater flow direction is proposed. Finally, the cellular automaton proposed in the Chapter 2 for modeling infiltration of contaminant has been applied to simulate propagation of contaminant related to flood water retention.

Chapter 1

Geophysics applied to environmental problems

1.1 Introduction

Environmental geophysics is a relatively new branch of the applied geophysics, primarily used to identify, map or predict the presence and potential movement of surface water and groundwater and to identify contaminants in the soil within the upper part (about 50 m) of the Earth's surface. It was born in 80's, but its use for both groundwater resource mapping and for water quality evaluation and monitoring has increased significantly over the last 20 years in large part due to the rapid advancement in data acquisition and inversion techniques as well as to the development of numerical modelling methods (e.g., Cassiani and Binley, 2005 and references therein).

Many geophysical techniques are commonly applied to groundwater investigations: potential field methods, such as gravity and magnetics, are generally used to map regional aquifers and large scale basin features, while seismic methods are substantially employed to delineate bedrock aquifers and fractured rock systems. However, it is with the electrical and electromagnetic methods that the greatest success has been achieved in groundwater studies as many of the geological formation properties that are critical to hydrogeology, such as porosity and permeability of rocks, can be correlated with electrical conductivity signatures. During the last years, indeed, many studies have shown that the integration of geoelectrical and hydrogeological methods allows to obtain more accurate hydrostratigraphical models and useful hints for modeling hydraulic processes (groundwater flow, solute transport) over a wide range of spatial scales, thus reducing both risk and cost of drilling holes (e.g., Nwankwoala and Udom, 2008; Breede et al., 2011; Falgas et al., 2011; Ramalho et al., 2012; Di Maio et al., 2013a).

Nevertheless, established standard procedures for the assessment of groundwater conditions and contaminant transport and monitoring are not yet available.

In such a context, the present study aims at providing a multimethodological and multidisciplinary approach that integrates geoelectrical, stratigraphic, hydrogeological and hydrochemical data for charactering possible polluted areas and for modeling space and time contaminant transport. Specifically, the procedure is based on *i)* the integration of geological, hydrogeological and geochemical data with geophysical data coming from three electrical methods (i.e. direct current electrical resistivity, induced polarization and self-potential) for mapping depth and thickness of aquifers, locating preferential fluid migration paths, such as fractures and fault zones, and identifying possible soil and groundwater contamination; *ii)* numerical modelling for identifying possible phenomena of pollutant migration in soils and groundwater and for simulation of contaminant propagation in the unsaturated zone.

The innovative aspects of the current study substantially rely on the development of: new approaches for SP data inversion, for an accurate estimation of self-potential anomaly sources, currently considered as a useful tool for assessing groundwater flow characteristics; cellular automata models, for simulating the groundwater flow and contaminant transport.

In this Chapter, a brief description of the basic principles of the three mentioned geoelectrical methods and the used numerical models for simulating flow and transport processes is presented.

1.2 Geoelectrical prospecting

Among the geophysical exploration methods, in this research project direct current geoelectrical methods, such as electrical resistivity, time-domain induced polarization and self-potential, have been used to identify and characterize groundwater and soil contaminations from organic and/or

inorganic pollutants. In this section, a brief detail on the main physical and methodological aspects of these three methods along with their applications in environmental problems is given.

1.2.1 Electrical resistivity method

Direct current (DC) electrical resistivity technique is one of the oldest and most commonly used geophysical exploration methods aimed at estimating the electrical resistivity of the subsurface (see standard textbooks on the subject, for example: Parasnis, 1986; Telford et al., 1990; Reynolds, 2011).

Electrical resistivity, ρ, (or its inverse, electrical conductivity, σ) is an intrinsic electrical property of a material that measures its ability to resist an electrical current flow. The latter is governed by the well-known Ohm's law, which can be expressed in scalar form as:

$$J = \frac{1}{\rho} E , \tag{1.1}$$

where ρ is the electrical resistivity of the medium, J is the current density and E is the electric field intensity. In practice, the electric potential V is measured, which is linked to the electric field intensity by the following equation:

$$E = -\nabla V, \tag{1.2}$$

Combining equations (1.1) and (1.2), the resistivity ρ can be obtained.

Such a parameter is a function of three different conduction mechanisms: electronic, electrolytic and dielectric. Since most of the earth materials are insulators, the main conduction is of electrolytic type, i.e. current flows by ions in the fluids permeating porous and/or fractured soils and rocks. This means that the resistivity parameter is strongly affected by porosity, ground water content and percentage of dissolved salts (e.g., Sumner, 1976; Sharma, 1997).

In practice, for a semi-infinite homogeneous and isotropic medium, which is the simplest Earth model, the DC resistivity measurements are performed by injecting a DC flow, I, through

two electrodes (current electrodes) placed on the land surface and measuring the resulting electrical voltage, ΔV, from another two electrodes (potential electrodes), also placed on the surface. The electrical resistivity, ρ, is then calculated based on the mutual distance between the four electrodes, the electrical current injected into the ground, and the measured electrical potential difference, i.e.

$$\rho = K \frac{\Delta V}{I}, \tag{1.3}$$

where K is the so-called geometric coefficient depending on the four electrode configuration (e.g., Reynolds, 2011). For non-homogeneous soils, the eq. (1.3) defines an apparent resistivity value that is a function of the geometry of the electrode array and the true resistivities and other characteristics of the subsurface materials, such as layer thicknesses, angles of dip, anisotropic properties, traversed by the electric current flow.

In the last few decades, due to significant progresses in instrumentation and data acquisition, processing and interpretation procedures, the electrical resistivity tomography (ERT), in 2D or 3D configuration, is among the most widely used techniques for DC resistivity measurements in the field of the geophysical prospecting as it allows very high resolution imaging of the electrical properties of the subsurface (e.g., Revil et al., 2012; Loke et al., 2013). The 2D (or 3D) ERT prospecting (Fig. 1.1) is usually realized by using an array of electrodes disposed along a profile (or an area) that allows the estimation of a large number of resistivity values at varying depths along the investigated profile (or area) to produce a very detailed image of the subsoil in terms of an apparent resistivity pseudosection (or pseudovolume). The latter enables a qualitative estimation of the electrical parameters of the medium but does not give the true resistivity and shapes of the anomalies. Each data acquisition, indeed, corresponds to a volumetric measurement and constitutes qualitative information that is plotted against a pseudo-depth. Thus, the apparent resistivity values in a pseudo-section (or pseudo-volume) distort the

real subsurface model picture and are closely dependent on the type of electrode array configuration. Subsequent inversion processing of the observed apparent data permits to retrieve the true resistivity distribution of the underground (e.g., Fig. 1.1c and d), which is useful to define the geometry and nature of subsurface targets, such as the soil/bedrock interface, strata thickness, or depth and width of anomalous zones (e.g., Chambers et al., 2012; Kumar, 2012; Di Maio et al., 2015c).

For the inversion of the 2D ERT data along profiles, which is the technique used for the present study, the most common and widely used inversion algorithm is Res2Dinv (Loke and Barker, 1996; Loke et al., 2003). It is based on a smoothness-constrained least-squares method which allows to obtain two-dimensional sections through finite differences or finite elements computations, taking into account also the topographic corrections. To evaluate the fit of the obtained resistivity model, the root mean square error (RMS) is considered, which provides the percentage difference between measured and calculated values. As an example, figures 1.1c and 1.1d show the inversion results of 2D and 3D ERT data acquired in an area affected by leachate infiltration by applying the Res2Dinv and Res3Dinv software, respectively. Although it is the most widely applied software, many other inversion software, such as EarthImager (Yang, 1999), DC2DPro (Kim et al., 2009), are currently available for the electrical resistivity data inversion, as reported in Perrone et al. (2014).

As it is well-known, the ERT imaging provides a static description of the geometrical and physical properties of the investigated subsoil as it refers to a specific data acquisition time (Perrone et al., 2014). This means that no information is given about dynamic phenomena that could affect the study area. Recently, thanks to the development of proper instrumental devices and computing facilities, which allow to perform resistivity tomography surveys with reasonable effort in terms of both time consumption and computation costs, a new acquisition procedure, known as time-lapse ERT, has been proposed (e.g., Supper et al., 2012; Loke et al., 2014). The latter can be set up to provide ERT measurements at specific times in order to give ERT images

at very close time intervals, thus allowing to track temporal changes in the subsurface electrical properties likely associated to variations of water content, salt concentrations, fluid infiltration and so on. It is worth to point out that, although some software for the processing of time-lapse ERT data has already been developed, further improvements are necessary as well to search proper relationships between electrical resistivity variations and hydrological parameter changes (Perrone et al., 2014).

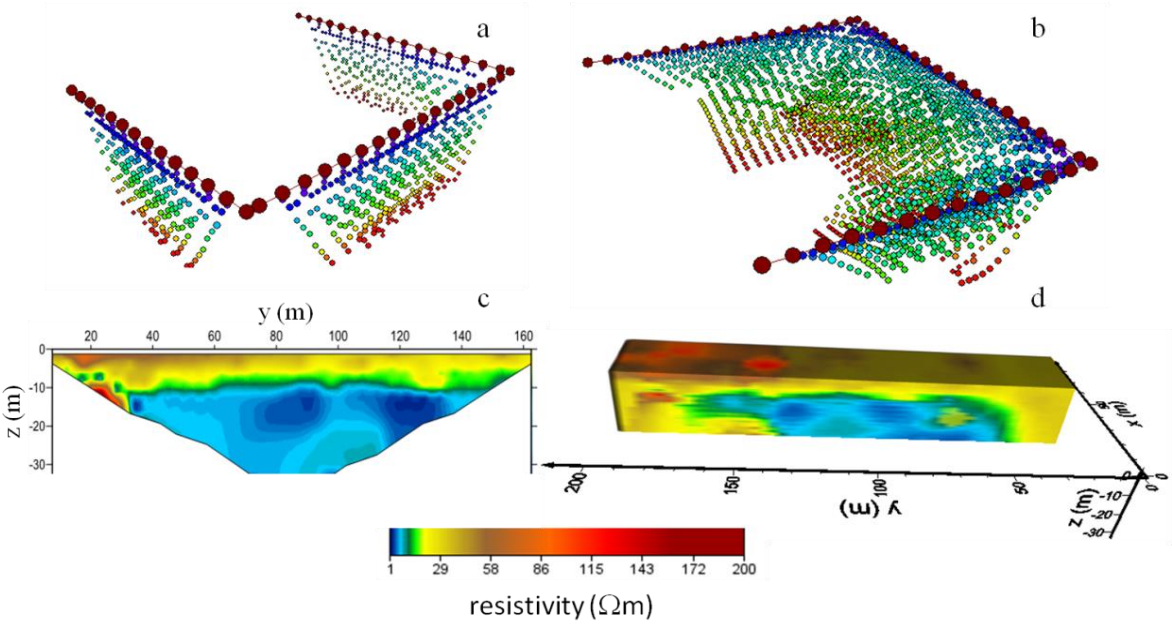

Figure 1.1 Establishment of 2D electrical resistivity pseudo-sections (a) and 3D electrical resistivity pseudo-volume (b) (after GeoStudi Astier, 2014, modified). Inversion results of 2D (c) and 3D (d) ERT prospecting performed in an area affected by leachate infiltration induced by a municipal solid waste landfill (Di Maio and Piegari, unpublished paper).

The possibility to get very detailed information, and the further development of time-lapse systems, made the ERT prospecting a very attractive method for environmental applications. Hydrogeophysical studies, indeed, are conducted to monitor flow and transport of water and contaminants in the vadose zone (e.g. Dahlin, 2001; Binley et al., 2002; Cassiani et al., 2006; Chambers et al., 2006; Slater and Binley, 2006; Koestel et al., 2009; Rucker et al., 2010), in aquifers and fractured rocks (e.g. Daily et al., 1992; Binley et al., 1996; Slater et al., 1996, 1997),

to delineate contaminant plumes and landfill leachates (e.g. Daily et al., 1995; Abu-Zeid et al., 2004; Naudet et al., 2004; Soupios et al., 2007a,b, 2008; Ntarlagiannis et al., 2016), and to follow the evolution of remediation processes in contaminated sites (e.g. Ramirez et al., 1993, LaBrecque et al., 1996; Slater and Binley, 2003; Halihan et al., 2005; Wilkinson et al., 2008).

1.2.2 Time-domain induced polarization method

The induced polarization (IP) method extends the resistivity method by making an additional measurement of the ability of the ground to reversibly store electrical charge (e.g., Sumner, 1976; Reynolds, 2011). The low frequency capacitance of rocks and soils is primarily a function of the surface chemical properties of the investigated materials. In non-metallic environments, the IP response is an indicator of surface area and charge density of the material. IP measurements are therefore sensitive to clay content as well as mineralogy and pore fluid composition (Slater and Lesmes, 2002).

The canonical IP experiment in the time domain (Fig. 1.2), which is the technique used in the present thesis, consists of energizing an earth material by a long period square pulse of current, and observing the secondary voltage following the switch-off of the primary current (e.g., Sumner, 1976; Keller and Frischknecht, 1966; Kearey et al., 2002; Binley and Kemna, 2005). The ground thus acts as a capacitor and stores electrical charge that is released at the interruption of the current for establishing the initial state of electrical balance.

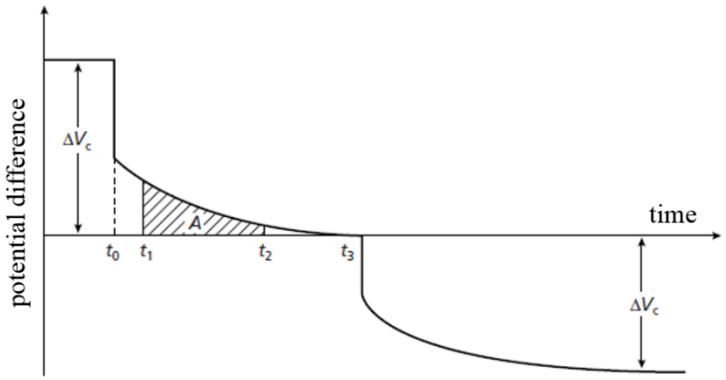

Figure 1.2 Time-domain IP measurement. At time t_0 the energizing current is switched off and the measured potential difference, after an initial instantaneous drop from the steady-state value *ΔVc*, decays gradually to zero. A similar sequence occurs when the current is switched on at time t_3. *A* represents the area under the decay curve in the time interval t_1-t_2 (after Kearey et al., 2002, modified).

The characteristics of the decay curve, in terms of initial magnitude, slope and relaxation time, are strictly related to the fluid conductivity, diffuse presence and relative abundance of highly conductive particles in the rock matrix, synthesized in the well-known chargeability parameter, *M*. The latter is quantitatively defined as the area *A* beneath the decay curve over a specific time interval (t_1-t_2 in Fig. 1.2) after the polarizing current is cut off normalized by the steady-state potential difference (*ΔV_c* in Fig. 1.3):

$$M = \frac{A}{\Delta V_c} = \frac{1}{\Delta V_c}\int_{t_1}^{t_2} V(t)dt, \tag{1.4}$$

Therefore, the chargeability gives a measure of the IP effect that is mainly due to presence of clay or metallic minerals in the rock matrix or soil, which give rise to two types of polarization phenomena, respectively, membrane and electrode polarization, induced by the passage of the current flow through the rock and accomplished mainly by the electrolytic flow in the pore fluid. The membrane polarization (Fig. 1.3a) is substantially linked to the property of most of the rock-forming minerals (such as clay) to show a net negative charge on their external surfaces in contact with the pore fluid and to attract the positive ions on these surfaces (e.g., Kearey et al., 2002). Input current flow in the subsoil alters this normal distribution of charges, causing the

accumulation of ions that, at the interruption of current, return to their original positions over a finite period of time causing a gradually decaying voltage. The membrane effect decreases with increasing salinity of the pore fluid.

The electrode polarization (Fig. 1.3b) generates when metallic minerals are present in the rock (e.g., Kearey et al., 2002). In this case, an alternative electronic path is available for the current flow applied to either sides of the pore space. Negative and positive ions then accumulate on either surfaces of the grain which are attempting either to release electrons to the grain or to accept electrons conducted through the grain. The rate at which the electrons are conducted is slower than the rate of electron exchange with the ions. Consequently, ions accumulate on either side of the grain and cause a build-up of charge. Due to interruption of current, ions slowly diffuse back to their original locations and cause a transitory decaying voltage. All minerals which are good conductors (e.g. metallic sulphides and oxides, graphite) contribute to this effect.

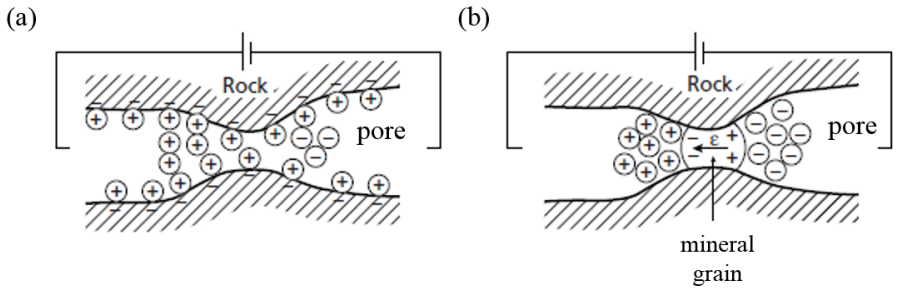

Figure 1.3 Mechanisms of induced polarization: (a) membrane polarization and (b) electrode polarization (after Kearey et al., 2002, modified).

The modern field equipments commonly used for the time-domain IP measurements are the same as used for the ERT prospecting, such as IRIS instruments (France), ABEM Geophysics (Sweden) and Advanced Geosciences (USA). As well, the chargeability data inversion methods are the same as used for the ERT prospecting, and hence the result is a 2D (or 3D) tomographic image of the chargeability values characterizing the survey area, which can improve the understanding of the subsoil electrical properties relative to resistivity imaging

alone. Usually, ERT and IPT are used jointly in order to discriminate between materials displaying comparable resistivity values, such as saline water-saturated aquifers and clay or shale layers (Slater and Glaser, 2003), but different induced polarization phenomena. The joint use of this two techniques is, in fact, nowadays widely applied in a variety of situations concerning contaminated environments (e.g. Mondal et al., 2010; Leroux et al., 2010; Auken et al., 2011; Gazoty et al., 2011; Pierwoła, 2013) for non-invasive mapping and monitoring of contaminants at industrial and waste disposal sites, where the pollution zones are usually identified as high chargeability anomalies.

As an example, Fig. 1.4 shows 3D detailed reconstructions of the same landfill site of Fig. 1.3 in terms of resistivity and chargeability distributions. As it can be seen, the comparisons between the two images allows to detect and map contaminant plumes of the waste disposal and hosting materials, as they are characterized by both low resistivity and high chargeability value distributions.

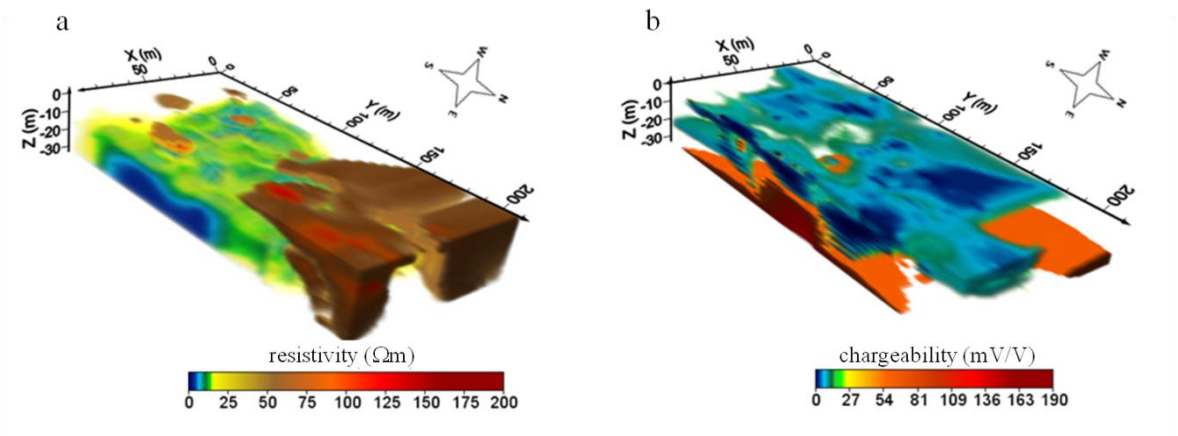

Figure 1.4 Volumetric view of the 3D inversion of the resistivity (a) and chargeability (b) tomography data acquired in a landfill site, with a clipping plane that highlights the zones most likely affected by contamination as characterized by high conductivity and chargeability trends (Di Maio and Piegari, unpublished paper).

1.2.3 Self-potential method

Self-potential (SP) is one of the oldest passive geophysical method (e.g., Parasnis, 1986; Telford et al., 1990) that consists on measurement at the ground surface of anomalous potential drops at the ends of a passive line in which impolarizable electrodes are grounded. Therefore, the equipment for SP measurements consists of a digital voltmeter and two non-polarizable electrodes made of metal-salt couples, such as copper rods immersed in copper sulphate solution or lead rods immersed in lead chloride (Petiau, 2000), which create the ionic contact with the ground through the porous base of the electrolyte reservoir. The SP prospecting thus is a very easy measurement technique and requires a non-expensive equipment.

The SP data can be acquired by using two different procedures: gradient and fixed base technique (Fig. 1.5). The gradient (or leap-frog) acquisition method consists of measuring the potential difference between two consecutive electrodes that are moved, with a constant spacing, along the whole measurement circuit (Fig. 1.5a). The fixed base method, instead, uses an electrode as reference fixed base, while the second electrode is moved along the measuring network to scan the electric potential at the ground surface (Fig. 1.5b).

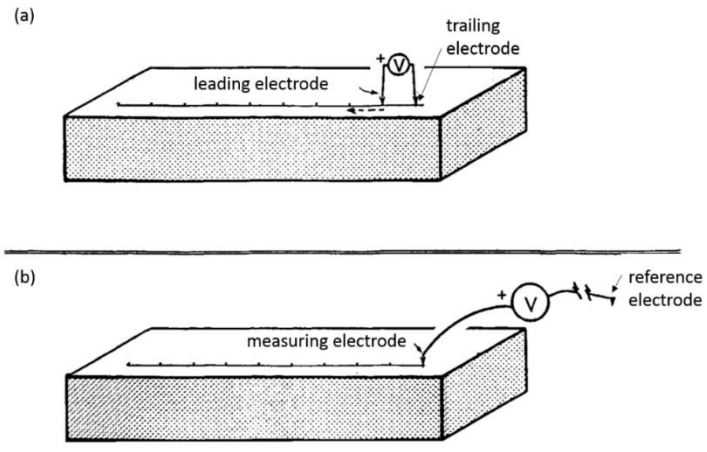

Figure 1.5 Electrode arrangement for SP survey. (a) Gradient (or leap-frog) configuration; (b) fixed base configuration (modified after Sharma, 1997).

Despite the relative simplicity of the SP measurement technique, only in recent decades its application in environmental studies, such as evaluation and monitoring of soil and groundwater pollution risk, has received an increasing interest from the worldwide geophysical community (e.g., Revil et al., 2012; Revil and Jardani, 2013). This is substantially due to the difficulty to interpret the SP signals observed in areas characterized by complex dynamic phenomena as well as to the lack of proper SP data inversion methods for the definition of the anomaly source parameters. As for the first aspect, indeed, the anomalous potentials recorded in contaminated areas are generated mainly by electrochemical and electrokinetic effects (flows) due to forcing mechanisms related to chemical and hydraulic gradients, respectively (e.g., Sill, 1983; Revil et al., 2012; Revil and Jardani, 2013). In general, these forces, and related electric and non-electric flows, may contribute to the observed SP signals, even if the electrokinetic phenomena are the main responsible of the SP anomalies observed in fluid-saturated porous and/or fractured environments. The most reliable physical model for interpreting the SP anomalous signals generated by electrokinetic phenomena is the one predicted by Onsager's theory of coupled flows (Onsager, 1931), originally introduced in geophysics by Nourbehecht (1963), then comprehensively examined by Mizutani et al. (1976), Sill (1983), Di Maio and Patella (1991), Pride (1994), Revil et al. (1999a,b), Garambois and Dietrich (2001, 2002), Garambois et al. (2002). In brief, the quoted authors derive the general equations of particle diffusion in porous media under the action of forces related to electric potential, pressure, temperature and electric charge concentration gradients, in a general framework that includes the physical parameters characterizing the investigated media (i.e., electrical conductivity, chargeability, permeability, porosity, etc). Taking into account the properties of the media where the signal propagates is crucial for modeling the self-potential anomalies associated with groundwater flow movement and contaminant mass propagation. In fact, in the last years several studies that correlates the observed SP anomalies with results of electromagnetic, resistivity and induced polarization investigations as well hydrogeological investigations have been proposed (e.g., Naudet et al.,

2004; Jardani et al., 2006; Zogala et al., 2012). As an example, figures 1.6 illustrates an example of application of the SP method for studying the contamination induced by landfill leachate infiltration (Naudet et al., 2004). In particular, Fig. 1.6a and 1.6b show, respectively, the electrokinetic component of the measured SP and its correlation with the piezometric level, while Fig. 1.6c and 1.6d represent, respectively, the residual component of the observed SP distribution, calculated by removing the electrokinetic component, and its linear correlation with the redox potential measured in the boreholes, thus, indicating that the redox potential gradient is the driving force for the observed SP signals in the landfill area.

Finally, as it concerns the SP anomaly source characterization, despite many inversion methods have been proposed for the quantitative interpretation of the SP data (e.g., Bhattacharya and Roy, 1981; Di Maio and Patella, 1994; Patella 1997a, b; Essa et al., 2008; Agarwal and Srivastava, 2009), currently a well-established procedure does not yet exist as for the resistivity and IP data inversion (see Section 1.2.1). With the main intent to contribute to this issue, part of the present thesis has been devoted to the development of new inversion approaches for defining the SP anomaly source parameters. In Chapter 2, after a brief introduction of the most commonly used forward and inverse modeling procedures, a detailed description of the proposed SP data inversion methods is provided and the results of their application to synthetic and field data are shown.

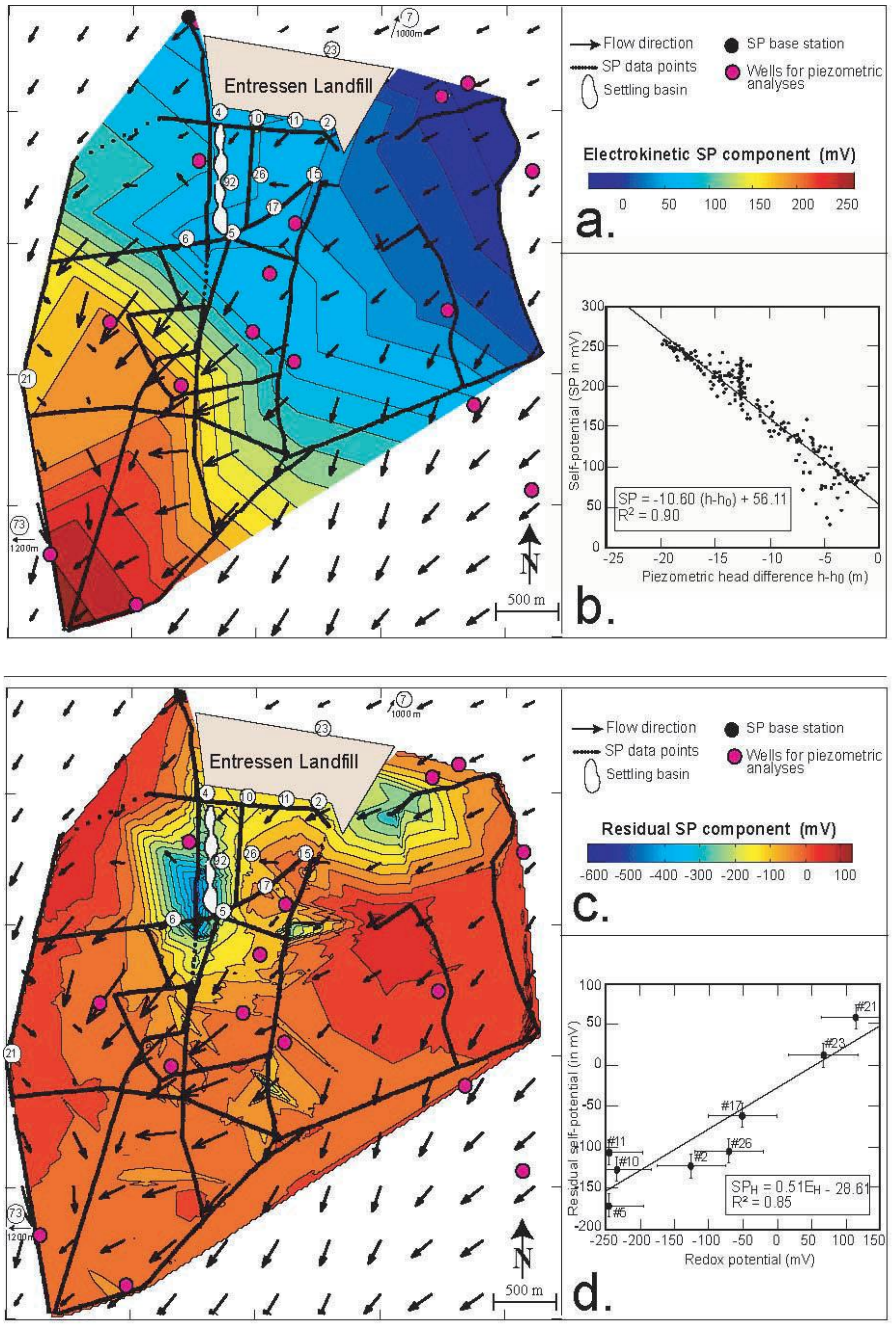

Figure 1.6 (a) SP electrokinetic component map (in mV) obtained by linear interpolation of the SP calculated from the correlation shown in (b). (b) Correlation between the piezometric head difference and the SP measured in the test site. (c) Map of the SP residual component (in mV) calculated by removing the electrokinetic component from the measured SP data. (d) Correlation between the redox potential measured on boreholes (numbered circles) and the residual SP component (after Naudet et al., 2004).

1.3 Modeling

In order to protect and manage the groundwater system effectively, it is necessary to understand the effect of the contaminant transport on the groundwater system. The latter, indeed, undergoes various changes due to complex mass transfer processes, such as advection, dispersion, abiotic

and biotic reactions (Jegathambal and Sundarambal, 2014). The subsurface dynamic processes can be mainly understand by: *i)* field experiments, *ii)* laboratory experiments, *iii)* mathematical and computational modeling. However, due to limitations in carrying out field work and laboratory experiments, the use of mathematical and computational modeling has been significantly increased (Narasimhan, 1982; Bear and Verruijt, 1987; Anderson and Woessner, 1992; Lloyd, 1999; Indraratna and Ranjith, 2001; Anderson et al., 2002; Bear and Chang, 2009 and references therein). Modeling techniques are widely used to estimate the effect of contaminant injection and transport in space and time. Once a model is validated for a particular type of hydrogeological setting, it can be used for studying different scenarios (e.g. Pinder, 2002; Rushton, 2003; Thangarajan, 2004; Meijerink et al., 2007).

Over time, different physical and analogue models, like sand tank and electric analogue, have been used for simulating groundwater systems (e.g. Bhagavantam, 1975; Canter et al., 1987; Strack, 1989; Fujinawa et al., 2009; Illman et al., 2012; Mamer and Lowry, 2013); though, with the advent of powerful and versatile computers and development of software, computer modeling has replaced other modeling techniques. These computer models or numerical models have been proposed to solve the basic modeling equations, such as the finite difference method (FDM), the finite volume method (FVM) and the finite element method (FEM) (e.g. Bear and Cheng, 2009). Currently, different numerical codes are available to solve these mathematical equations, such as modular computer software (MODFLOW) (McDonald and Harbaugh, 1988) and finite element subsurface flow simulation system (FEFLOW) (Diersch, 2002).

As these standard numerical techniques require a huge amount of geological, geochemical and hydrogeological data, in the framework of my PhD project a new modeling approach based on Cellular Automata (CA) have been proposed to model the infiltration processes of soil contaminants and simulating their propagation in unsaturated and saturated zones.

In the following sections, a brief detail of the two different simulation models used in the present thesis, i.e. FEFLOW and CA techniques, is presented.

1.3.1 Finite element subsurface flow simulation modeling

Modeling of groundwater systems with numerical methods can be subdivided in three steps: preprocessing, which consists in transformation of data into a format appropriate for the used numerical algorithm and grid generation; numerical calculation, which provides a direct modeling of the phenomenon under study; calibration, which models the phenomenon by inverse modeling. Fig. 1.7 shows a simplified flow diagram that illustrates all the steps required for groundwater flow modeling that, in this work, has been performed by using the FEFLOW simulation software.

FEFLOW (Finite element subsurface flow system) is an interactive, graphical user interface (GUI) based on finite element method. It can be used for two (2D) and three-dimensional (3D) modeling of groundwater flow, contaminant mass and heat transport in isotropic or anisotropic soil domain, under saturated, partially saturated or unsaturated conditions (Fig 1.8). The main governing equations used by FEFLOW are derived from the macroscopic-phase-related conservation principals of flow, mass, momentum and energy, which result in non-linear system of equations (Diersch, 2002). This software has been successfully applied for laboratory and field-scale environmental studies (e.g., Green et al., 2006; Peleg and Gvirtzman, 2010; Jakovovic et al., 2011; Dokou and Karatzas, 2012; Seferou et al., 2013).

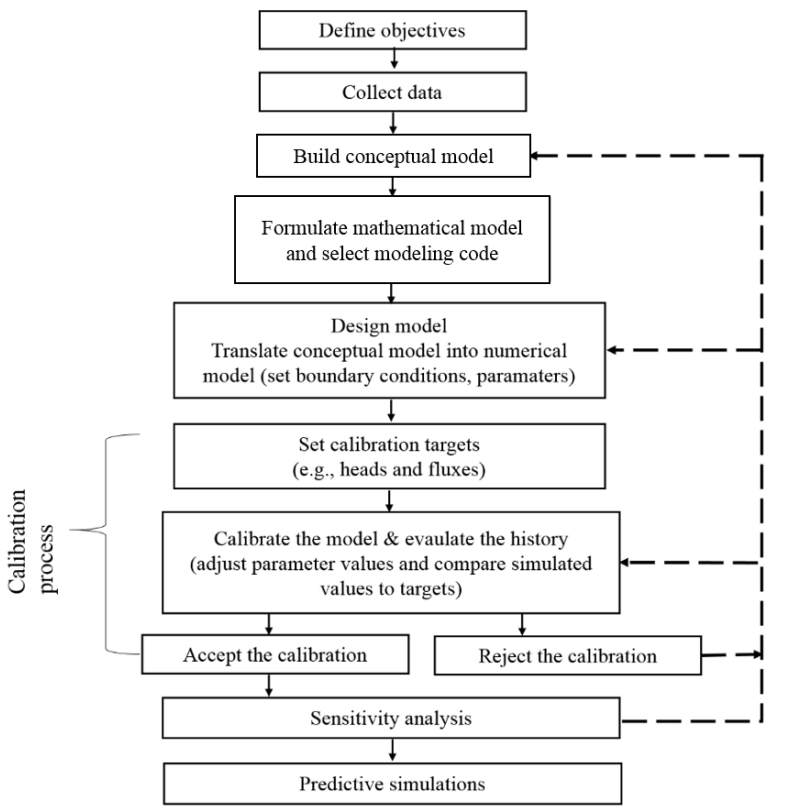

Figure 1.7 Workflow for groundwater modeling (after Anderson and Woessner, 1992, modified).

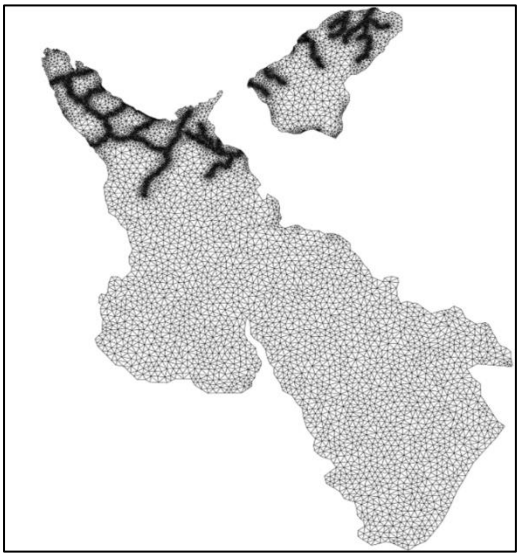

Figure 1.8 Schematic representation of finite element mesh generated by FEFLOW.

Unsaturated-saturated zone modeling

To model the groundwater flow and mass transport in unsaturated-saturated conditions, several alternatives exist for numerically solving the governing balance equations with their nonlinear

constitutive relationships (Diersch and Perrochet, 2009). The Darcy equation of fluid motion and the fluid mass conservation equation form the physical basis (Bear and Bachmat, 1991).

In the context of unsaturated flow, the basic formulation involves both the fluid pressure head and the saturation as unknown variables. For these two unknowns only one balance equation, the basic Richards equation (Hillel, 1980), is available. To close the mathematical model one constitutive relationship in form of the capillary pressure head-saturation function is additionally needed to convert one variable to the other (and vice versa). Consequently, the modeler has to decide between primary (head, mass concentration, groundwater age, temperature) and secondary variables. Depending on such a choice, different modeling approaches result which are mathematically equivalent in the continuous formulation, but their discrete analogs are different.

As a result, three forms of the unsaturated flow equation can be derived: (1) the pressure-based (ψ) form, where the primary variable is the pressure head (or the hydraulic head); (2) the saturation-based (s) form, where the saturation (or the moisture content) is chosen as the primary variable, and (3) the mixed (ψ, s) form, where both variables are employed and, in solving the discrete equation system, the pressure head is actually used as the primary variable.

All the three approaches have their significant advantages and drawbacks in groundwater modeling (Van Genuchten, 1978; Paniconi et al., 1991; Diersch and Perrochet, 2009). Recently, Forsyth et al. (1995) proposed a powerful new idea in the context of saturated-unsaturated flow simulations, which is based on a primary variable switching technique during the multiphase flow modeling. By using this technique, FEFLOW allows to switch the variables in different regions of the model depending on the prevailing saturation conditions at each node of a mesh. The basic equations of FEFLOW for unsaturated-saturated zone modeling have been summarized in Appendix A.

Once the model is simulated, the calibration of some parameters, such as hydraulic heads or fluxes, performed by assigning some known values, has to be carried out for model validation.

1.3.2 Cellular Automata

Cellular Automata (CA) represent an alternative approach to differential equations to model and simulate complex dynamical systems, whose evolution depends on the local interactions of their constituent parts. A cellular automaton is a discrete model that essentially consists on: *(i)* a grid with a finite number of cells; *(ii)* a finite (usually small) set of states that grid cells can have, i.e. the values of the variables selected to describe the state of the grid cells; *(iii)* a neighborhood, which is a definition of which nearby cells may affect the state of a given grid cell; *(iv)* a set of rules, which describe interactions among neighbouring cells and determine how the states of cells change over time. These rules, which can be either deterministic or stochastic, are generally simple and local. The automaton evolves according to them and, surprisingly, complex global behaviors can emerge from very simple local rules under different starting configurations.

CA, first introduced by Von Neumann in 1950 to study self-reproducing systems (Burks, 1970), have been used in last decades for modeling many complex dynamics and physical systems. In particular, they have been used for modeling and simulating many natural phenomena, such as seismicity (Olami et al., 1992; Helmstetter et al., 2004), snow avalanches (Bak et al., 1987; Faillettaz et al., 2004), landslides (Noever, 1993; Hergarten and Neugebauer, 1998; Piegari et al., 2006, 2009; Juanico et al., 2008), and volcanic eruptions (Lahaie and Grasso, 1998; Lemarchand and Grasso, 2007; Piegari et al., 2011). Another important field of CA application is fluid-dynamics. Frisch et al. (1986) have introduced lattice gas automata models for describing the motion and collision of particles on a grid and they have shown that their model follows the behavior of the Navier-Stokes equation of hydrodynamics in the long-time and large-scale limits, in spite of the discrete dynamic description of the model (Chen et al., 1992; Ladd, 1994). A different approach characterizes the so-called lattice Boltzmann models (Chopard and Masselot, 1999), where the state variables can take continuous values, as they are supposed to represent the density of fluid particles located in each cell (space and time are

discrete, as in lattice gas models). In both such lattice-gas approaches a fluid amount moves from a cell to another one in a CA step (which is a constant time), which implies a constant "velocity" in the CA context of discrete space/time. Nevertheless, velocities can be deduced by analyzing the global behavior of the system in time and space. In such models, the flow velocity can be deduced by averaging on the space (i.e. considering clusters of cells) or by averaging on the time (e.g. considering the average velocity of the advancing flow front in a sequence of CA steps).

Many complex macroscopic fluid dynamical phenomena seem difficult to be modelled in these CA frames, because they take place on a large space scale and need practically a macroscopic level of description that involves the management of a large amount of input data. To overcome these limits Avolio et al. (2008) have proposed an empirical method where: *(i)* the state is composed of substates; *(ii)* each substate describes a feature of the space portion related to the own cell; *(iii)* the transition function is split in several parts, each one corresponds to an "elementary" process of the macroscopic phenomenon; *(iv)* substates of type "outflow" are used in order to account for quantities moving from a cell toward another one in the neighboring. Such an approach allows to define macroscopic surface flows and then introduces the use of macroscopic cellular automata. In particular, as concerns soil contamination, which is one of the major environmental problems in industrial countries, Di Gregorio et al. (1999) have presented a macroscopic CA, which describes the major phenomena that take place in bioremediation. The model is composed of the following three layers (where each layer depending on the others): a fluid dynamical layer, which describes multiphase flow through the soil; a solute description layer, which deals with solute transport, adsorption/desorption, and chemical reactions; a biological layer, which describes biomass growth and its interaction with the different chemicals. The results of such model, which has been tested in a pilot plant in the case of contamination by phenol, have demonstrated how such a complex phenomenon can be precisely described by a simulation model, and that CA can be usefully applied to a real-world problem of very high environmental and economic importance.

In this thesis, two simple (macroscopic) cellular automata are presented in Chapter 2 and applied to specific survey areas in Chapter 3 and 4, as starting point to study contamination infiltration in saturated and unsaturated conditions.

Chapter 2

New approaches to self-potential data inversion and contamination flow modeling

2.1 Introduction

Nowadays, the quality of soil and ground waters is largely affected by the increased industrialization, urbanization and agricultural activities, which cause the release of different types of contaminants at the ground surface. The migration of these contaminants pollutes the subsurface in many areas worldwide through spills, leaks and uncontrolled releases and disposals (Pankow et al., 1996; Tait et al., 2004; Lawrence et al., 2006; Rivett and Clark, 2007; Zhao et al., 2013). The most common remediation techniques, such as containment, pump-and-treat, extraction, stabilization/solidification, soil washing, air stripping, precipitation, vitrification, thermal desorption and biological remediation (Zhang, 2009), are able to recover contaminated areas, but they do not permit their time monitoring. In this framework, the geophysical methods are useful tools not only to identify the contamination but also to validate and monitor the remediation processes (e.g., Binley et al., 1996). Therefore, during the last few decades, the use of geophysical techniques for real-time monitoring as well as of simulation methods for predicting solute transport mechanisms through the unsaturated/saturated zone has been a priority for the environmental scientists (e.g. Cassiani and Binley, 2005; Bloem et al., 2010; Müller et al., 2010; Gasperikova et al., 2012).

In this context, the present thesis has been mainly focused on the development of *(i)* new inversion methods of self-potential data for the full characterization of the contaminant source parameters; *(ii)* numerical models for identification of possible phenomena of pollutant

migration in soils and groundwater and for simulation of contaminant propagation in the unsaturated zone. Therefore, this chapter is divided into two parts: in the first part, innovative procedures for the quantitative interpretation of self-potential data are presented, while in the second part, a new technique based on cellular automata is proposed for modeling the underground contaminant propagation.

2.2 New methods for self-potential data inversion

Over the last few decades, there has been a growing interest in the self-potential (SP) method for applications in a wide range of fields, such as exploration geophysics, hydrogeophysics and environmental problems (e.g., Revil and Jardani, 2013). Compared with other geophysical methods, the SP prospecting is particularly attractive because of its versatility, ease of use and non-expensive equipment. However, the relative simplicity of the measurement technique is counterbalanced by a not easy interpretation of measured data, which represent the response to different SP sources.

Over the time, different methods have been proposed to interpret the self-potential anomaly sources, which can be roughly categorized in three main groups: graphical, tomographical and numerical procedures. The first are the oldest methods and are mainly based on use of nomograms and characteristics curves (Yüngül, 1950; Paul, 1965; Rao et al., 1970; Bhattacharya and Roy, 1981; Atchuta Rao and Ram Babu, 1983; Agarwal, 1984; Sundararajan and Srinivas, 1996). Then, tomographic approaches have been proposed to localize the underground self-potential sources in terms of electric charge occurrence probability (COP) function (Di Maio and Patella, 1994; Patella 1997a,b) or electric dipole occurrence probability (DOP) function (Iuliano et al., 2001; Revil et al., 2001; Iuliano et al., 2002). The COP and DOP functions are computed by cross-correlating the SP field data with the synthetic electric field generated by an elementary pole or dipole source, respectively, located at any arbitrary point of

the subsurface. As concerns the numerical methods, a wide range of techniques have been developed for the interpretation of SP anomalies: methods based on spectral analysis (Atchuta Rao et al., 1982; Rao and Mohan, 1984; Asfahani et al., 2001; Das and Agarwal, 2012), methods that solve the governing differential equations (Jardani et al., 2006; Agarwal and Srivastava, 2009; Li and Yin, 2012), methods that use sophisticated global optimization techniques, such as least squares inversion (Abdelrahman et al., 2006a, 2006b, 2008; Essa et al., 2008; Essa, 2011), genetic algorithms (Abdelazeem and Gobashy, 2006; Göktürkler and Balkaya, 2012), particle swarm optimization (Monteiro Santos, 2010; Pekşen et al., 2011), adaptive simulated annealing (Tlas and Asfahani, 2008), very fast simulated annealing (Biswas and Sharma, 2014) and ant colony optimization (Gupta et al., 2012; Srivastava et al., 2014).

Considering the complexity of the SP data inversion process, which is linked to both the multiplicity and the unknown position of the causative sources, in the present work new methods have been developed for the quantitative interpretation of self-potential data that allow a full characterization of the SP source parameters. In particular, three different approaches have been proposed, respectively based on spectral, tomographical and global optimization methods.

As concerns the spectral analysis, Periodogram (PM), Multi Taper (MTM) and Maximum Entropy (MEM) methods have been proposed for source depth estimation of SP anomalies generated by some simple geometrical bodies, like sphere, horizontal and vertical cylinder and inclined sheet (Rani et al., 2015; Di Maio et al., 2017).

As the spectral methods are not able to fully characterize the SP anomaly source, an integrated approach based on spectral analysis and 2D tomographic technique has been then proposed (Di Maio et al., 2016a) as an effective inversion procedure of SP data for defining all parameters that characterize the anomaly causative source. In particular, MEM is used to find the source depth and, then, the 2D tomographic technique, based on the underground charge occurrence probability (COP) function (Patella, 1997a), is used to get information about the polarization angle of the anomaly source. From the numerical study performed on synthetic SP

data generated by simple geometrical structures, mathematical relations between patterns of zero values of the COP function and polarization angles have been found and used to interpret SP field data. The good agreement between the estimated source parameters and the results obtained from different numerical approaches shows the potentiality of integrating high-resolution spectral analysis and tomographic procedure.

Finally, a more sophisticated approach based on the integration of available global optimization methods has been proposed to estimate the source parameters of SP anomalies (Di Maio et al., 2016b). In particular, a hybrid Genetic-Price algorithm is proposed as a suitable method for an accurate determination of the SP source parameters, which is also able to provide information useful to discriminate the shape of the anomalous source.

A detailed description of all three proposed approaches and their applications on synthetic and field examples are presented below.

2.2.1 Spectral methods

In recent years, various spectral methods have been successfully applied for depth estimation of potential field sources, like gravity and magnetic anomaly sources (Spector and Grant, 1970; Negi et al., 1986; Maus and Dimri, 1995; Bansal et al., 2006; Bansal and Dimri, 2010), and climatic time series (Ghil et al., 2002). In particular, the exact similitude between gravitational and electrical potential suggests and guarantees the applicability of the same analysis procedures to SP data.

Principally, the spectral approach is based on selection of an appropriate method for power spectrum estimation. The spectral methods used for power spectrum estimation can be categorized in parametric and nonparametric methods (Stoica and Moses, 2005). The nonparametric methods apply a band pass filter with a narrow bandwidth to a data sequence and use the filter output power divided by the filter bandwidth as a measure of the spectral content of

the input data. The parametric methods select a model, estimate the model parameters for the given data and, then, compute the power spectrum by using the estimated parameters. The most accurate estimates of the power spectrum can be obtained by using parametric or nonparametric methods depending on if the data indeed satisfy or not the model assumed by the parametric methods (Stoica and Moses, 2005).

In the present study, the power spectrum of SP data is computed by using the nonparametric methods PM and MTM and the parametric method MEM, which are briefly described below.

PM

PM is a conventional method to compute the power spectrum of discrete time series. It estimates the power spectrum by computing the Discrete Fourier Transform (DFT) and appropriately scaling the magnitude squared of the result. The DFT is evaluated with a Fast Fourier Transform (FFT) algorithm. In particular, the so called radix-2 FFT procedure is generally used, which is easy to encode and quite computationally efficient (Cooley and Tukey, 1965). The PM method provides reasonably high resolution for sufficiently large number of data, but it is a poor spectral estimator because its variance is high and does not decrease with increasing data length. However, PM is considered a relevant basic spectral estimator as many other nonparametric estimators derive from it (Stoica and Moses, 2005).

MTM

MTM is a nonparametric method (Thomson, 1982; Percival and Walden, 1993) that reduces the variance of spectral estimates by using a small set of tapers rather than a single taper (or spectral window), like conventional PM does. The data are multiplied by orthogonal tapers and the power spectrum is obtained by averaging over the set of independent computed power spectra. The orthogonal tapers are constructed to minimize the leakage outside of a frequency band with bandwidth equals to $2pf$, where $f = 1/(N\Delta)$ is the Rayleigh frequency, N is the number of data

points, Δ is the sampling interval and p is a suitably chosen integer related to the number of tapers J. Actually, since only the first 2p-1 tapers provide usefully small spectral leakage (Slepian, 1978; Thomson, 1982; Park et al., 1987), J should be < 2p-1. However, the optimal choice of p and J depends on length and properties of the data series under study.

MEM

MEM consists in approximating the data series under study by a linear autoregressive (AR) process of order M (Burg, 1975; Ulrych and Bishop, 1975; Kay and Marple, 1981; Dimri, 1992). Power spectrum estimation from MEM is basically a two-step process that requires the selection of the order M of the AR model and the evaluation of the AR coefficients. The latter can be estimated by using the Yule–Walker's or Burg's approach. In the following, the Burg's approach (Burg, 1975) is applied, which finds a set of AR parameters that minimizes the sum of the squares of the forward and backward prediction errors. The minimization is performed by using recursion equations and direct estimation of the reflection coefficients (Stoica and Moses, 2005). As concerns the selection of the order M of the AR process, several criteria have been proposed in the literature (Kay and Marple, 1981), such as Akaike's final prediction error (FPE), Akaike information criterion (AIC), criterion autoregressive transform (CAT), characteristic correlation time (CCT), etc. The selection of M is crucial, as if M is too small, the spectral estimation will have poor resolution, on the other hand, if M is too large, power spectrum may display spurious peaks and line splitting. In the following, the FPE criterion is used, which is suggested by Ulrych and Bishop (1975) for selection of M for geophysical data. The FPE is written as:

$$FPE = \frac{N + M + 1}{N - M - 1}\sigma^2, \tag{2.1}$$

where N is the number of data points in the profile, M is the order of AR process and σ^2 is the variance of residual noise after fitting the AR model to the series. FPE is plotted versus M and the order corresponding to the first minimum of plot is selected as the order of the AR process.

2.2.1.1 Source depth estimation

Spector and Grant (1970) first found the relation between power spectrum and wavenumber for retrieving the depth of potential fields anomaly sources. They modeled the magnetic anomaly source distribution by a statistical ensemble of rectangular prismatic bodies and found the following linear relationship between the logarithmic power spectrum of aeromagnetic data and the depth of the anomaly source:

$$log\ P(k) = log\ A - 2|k|z, \tag{2.2}$$

where *P(k)* is the power spectrum, *A* is the constant when the source distribution is uncorrelated, *k* is the wavenumber and *z* is the depth to the top of the anomalous source. From eq. (2.2), *z* is estimated as half of the slope of the straight line fitted to the log *P(k)* as a function of *k*. If more than one straight line can be fitted in the log *P*-*k* plot, the slopes of subsequent line fits will give the shallower source depths for higher wavenumbers (Spector and Grant, 1970).

Later, the direct proportionality between the logarithmic power spectrum and the source depth, eq. (2.2), was also retrieved for other different source geometries (Naidu, 1972; Hahn et al., 1976; Pedersen, 1991; Garcia-Abdeslem and Ness, 1994; Pawlowski, 1994). Then, Maus and Dimri (1995) improved the Spector and Grant approach by developing an inversion method that is able to estimate the depth of magnetic and gravity anomaly sources and to take into account the scaling behavior of the corresponding geophysical parameters, i.e. magnetic susceptibility and density, respectively. This method is based on scaling source distributions with power spectra proportional to $f^{-\beta}$, where f is the wavenumber and β is the scaling exponent of the source distribution. The best values of the source depths and the scaling exponents are then obtained by minimizing the difference between the theoretical power spectrum of the assumed scaling source distribution and the power spectrum of the measured data.

Actually, as the equations governing gravitational and electrical fields are the same, in the present work the application of the above mentioned spectral analysis methods for the SP data inversion has been proposed and validated on synthetic and field SP data generated by single anomaly sources.

2.2.1.2 Spectral analysis of SP synthetic data

The effectiveness of the spectral analysis for the inversion of self-potential anomalies has been tested on synthetic data generated by different simple source models, such as sphere, vertical cylinder, horizontal cylinder and inclined sheet (Rani et al., 2015; Di Maio et al., 2017). For each dataset, the numerical analysis has been carried out by varying the source parameters and the level of random noise on the original dataset. In this section, the results of the performed analyses are shown.

SP anomalies due to polarized spherical and cylindrical sources

The SP observed at any point *P* (x, z) along a profile line over a polarized body whose center is placed at P_0 (x_0, z_0) can be expressed as (Yüngül, 1950; Bhattacharya and Roy, 1981; Agarwal and Srivastava, 2009):

$$V(x) = K \frac{(z - z_0)\sin\alpha - (x - x_0)\cos\alpha}{\left[(x - x_0)^2 + (z - z_0)^2\right]^p}, \tag{2.3}$$

where, K is the electric dipole moment, α is the polarization angle between polarization and horizontal axes, x_0 and z_0 are the coordinates of the center axis of the body and p is the shape factor, which is 1.5, 1 or 0.5 in case of sphere, horizontal cylinder or vertical cylinder, respectively. The numerical analysis has been performed by varying the shape factor, p, in eq. (2.3) for computation of SP anomalies due to different polarized structures. For each structure, the analysis has been carried out at varying the depth of the body, the polarization angle and the sampling interval. It is worth noting that if the radius of the structure is much lower than the

depth of the center, then z_0 could be approximated by the depth of the body top. In most cases, the application of MEM has provided depth values of the causative source closer to actual values than those provided by PM and MTM. As examples, Figs. 2.1, 2.2 and 2.3 illustrate the power spectrum estimated by PM (Figs. 2.1b, 2.2b and 2.3b), MTM (Figs. 2.1c, 2.2c and 2.3c) and MEM (Figs. 2.1e, 2.2e and 2.3e) for SP anomalies generated, respectively, by polarized sphere, horizontal cylinder and vertical cylinder for a profile length of 300 m and a sampling interval of 2 m. For power spectrum estimation by MEM, the order of the AR process has been selected as the order corresponding to the first minimum in the plots *FPE* vs *M*, as presented in Figs. 2.1d, 2.2d and 2.3d. Table 2.1 indicates the source parameters for the examples shown in the figures. As it can be seen, the application of MEM is successful in determining the depth of the causative source with a percent error less than 5%.

Synthetic source model	Electric dipole moment (K)	Polarization angle (α)	Body center depth (z_0)	Estimated depth (m)		
				PM	MTM	MEM
Sphere	-100 mVm	30°	30 m	25.8 ± 3.5	28.8 ± 1.1	29.6 ± 0.7
Horizontal cylinder	-100 mVm	30°	30 m	34.1 ± 4.3	31.4 ± 1.3	30.1 ± 0.4
Vertical cylinder	-100 mVm	30°	30 m	40.5 ± 17.2	35.5 ± 3.6	31.4 ± 0.7

Table 2.1 Parameters characterizing the sources of the SP anomalies shown in Figs. 2.1a, 2.2a and 2.3a. The last three columns report the depth values estimated by applying PM, MTM and MEM, respectively, to the synthetic curves.

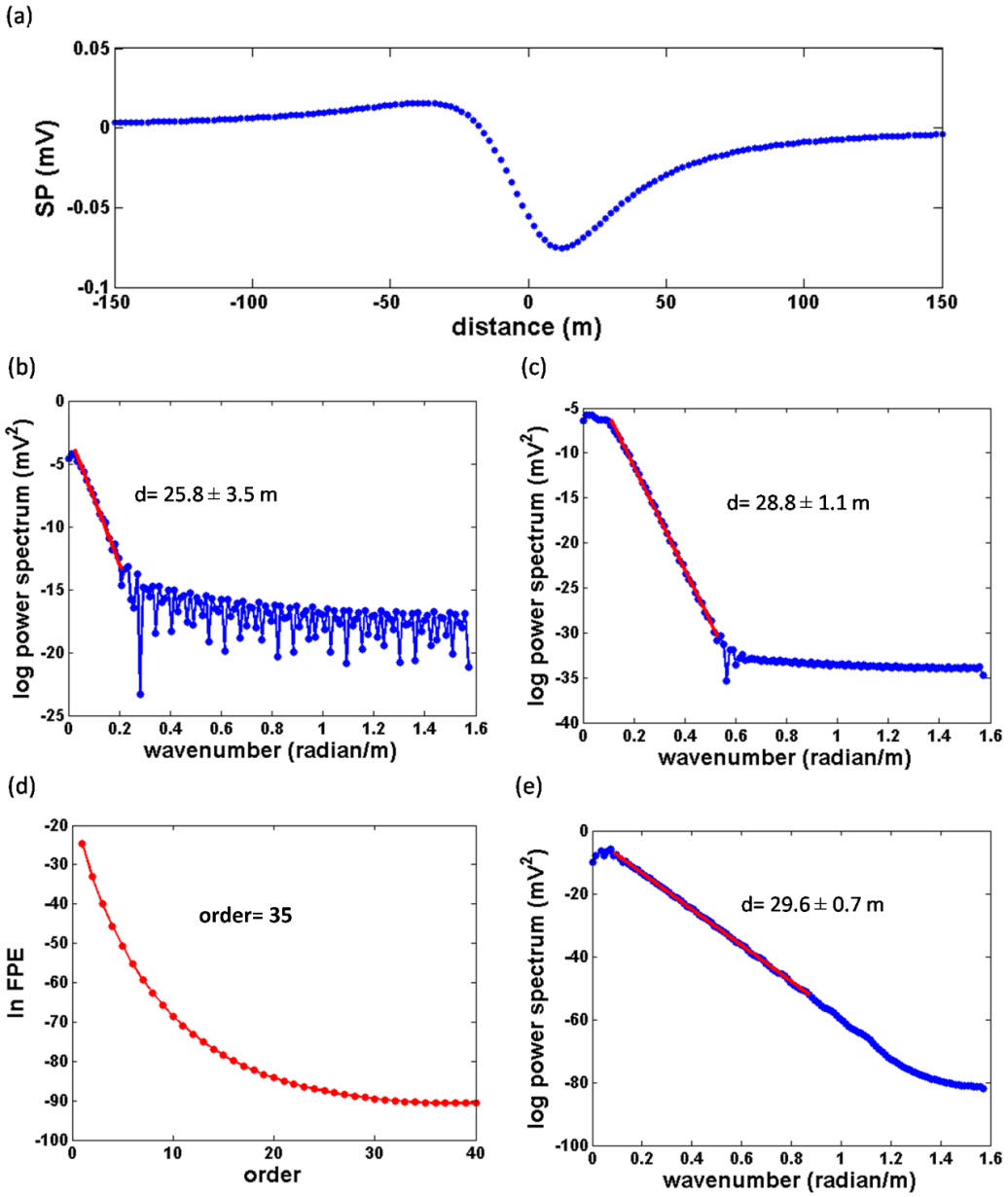

Figure 2.1 (a) SP anomaly due to a sphere characterized by the parameters indicated in Table 2.1; (b) power spectrum estimated by PM; (c) power spectrum estimated by MTM; (d) order selection for AR process and (e) power spectrum estimated by MEM.

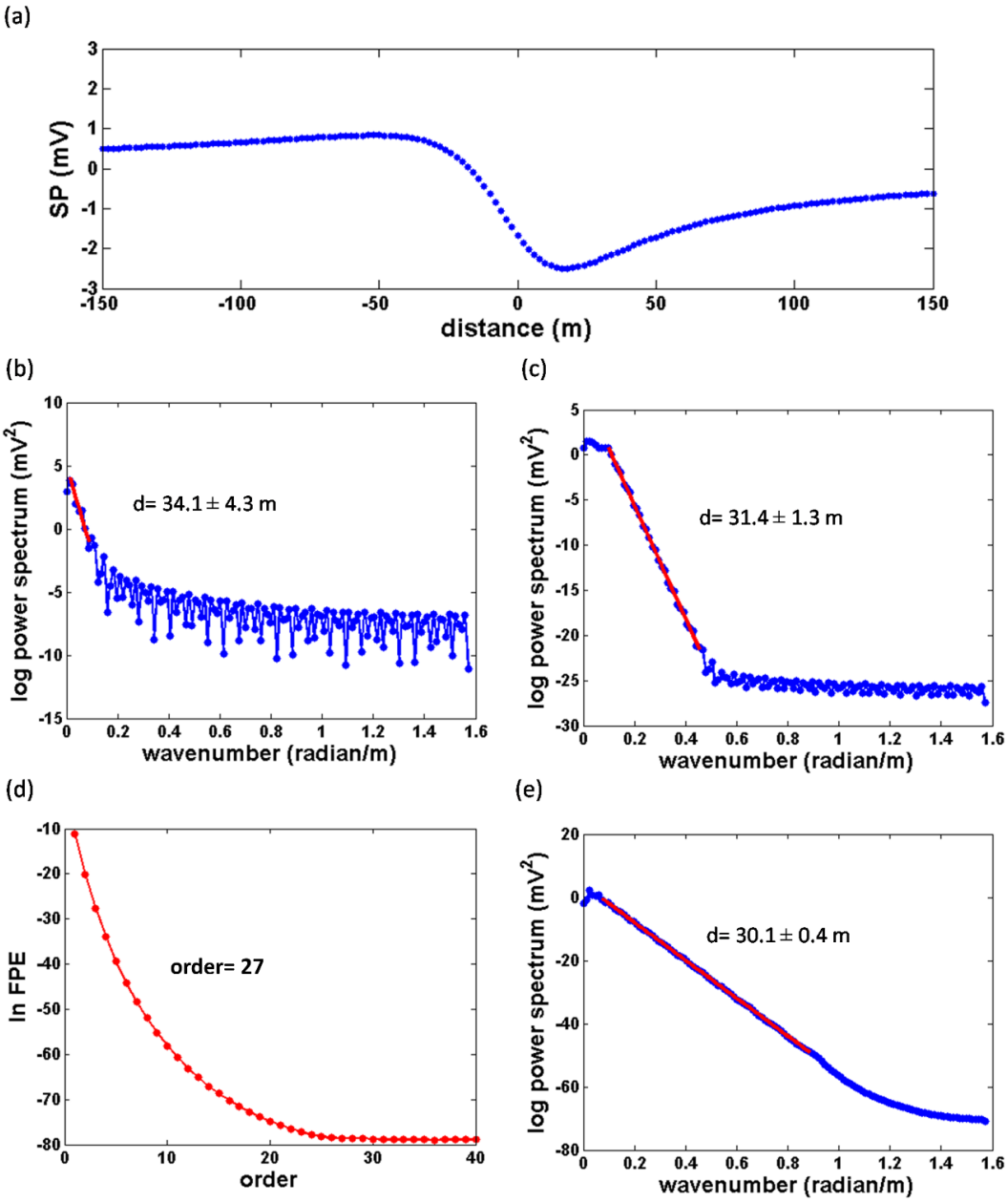

Figure 2.2 (a) SP anomaly due to a horizontal cylinder characterized by the parameters indicated in Table 1; (b) power spectrum estimated by PM; (c) power spectrum estimated by MTM; (d) order selection for AR process and (e) power spectrum estimated by MEM.

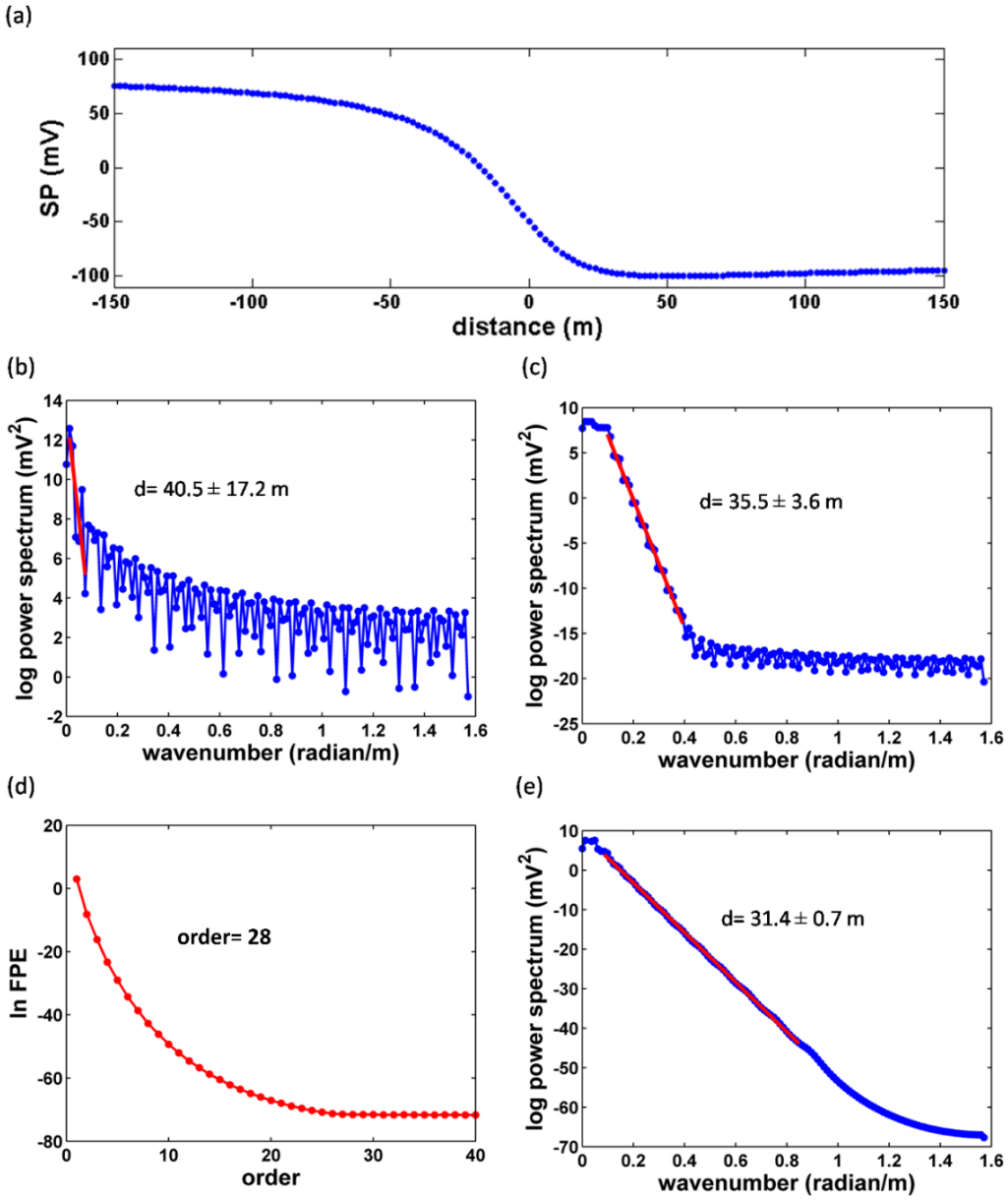

Figure 2.3 (a) SP anomaly due to a vertical cylinder characterized by the parameters indicated in Table 1; (b) power spectrum estimated by PM; (c) power spectrum estimated by MTM; (d) order selection for AR process and (e) power spectrum estimated by MEM.

To study the effect of source parameter variations on depth estimation, a detailed numerical analysis has been performed by varying the source parameters for different depth values. For instance, Table 2.2 shows the results obtained by varying the depth of the anomalous source keeping fixed polarization angle $\alpha = 50^{\circ}$, for different source models. The SP values are computed for a profile length of 300 m with a sampling interval of 2 m, and for K = -100 mVm and $x_0 = 0$. As it can be seen, the application of MEM is successful in determining the depth of

the causative source, with a percent error less than 5%. In particular, an extensive analysis, aimed at assessing the MEM resolution in retrieving the depth of the top of horizontal cylinder-type sources, has been carried out at varying the depth. It has been found that the method is able to provide correct estimates of z_0 down to depths of about 80 m, with a percent error less than 8%.

Synthetic source model	Body center depth (z_0)	Estimated depth (m)		
		PM	MTM	MEM
Sphere	20 m	16.7 ± 1.2	18.8 ± 0.5	18.7 ± 0.6
	30 m	24.9 ± 2.5	29.3 ± 1.4	28.9 ± 0.8
	40 m	35.9 ± 3.5	39.1 ± 1.6	39.0 ± 0.8
Horizontal cylinder	20 m	21.1 ± 2.6	20.3 ± 0.4	20.6 ± 0.6
	30 m	33.5 ± 5.0	31.5 ± 1.2	30.0 ± 0.4
	40 m	41.3 ± 4.8	41.6 ± 2.2	40.0 ± 0.7
Vertical cylinder	20 m	26.0 ± 13.8	22.0 ± 1.3	21.5 ± 0.8
	30 m	40.1 ± 15.6	32.4 ± 2.0	31.6 ± 0.7
	40 m	49.6 ± 22.1	42.8 ± 4.1	41.3 ± 1.4

Table 2.2 Depth values estimated for synthetic source models (sphere, horizontal and vertical cylinder) of SP anomalies by using different source depth values, for $\alpha = 50°$.

Furthermore, numerical analyses have been performed to investigate the behavior of power spectrum estimated by PM, MTM and MEM by varying the values of the polarization angle, α. Table 2.3 summarizes the results obtained for source models with center depth, z_0, of 30 m and electric dipole moment, K, equals to -100 mVm. From the analysis, it can be seen that the dependence of the power spectrum on the polarization angle can be considered negligible with good approximation for spherical and cylindrical sources, for angles in the range 0^o - 40^o.

Synthetic source model	Polarization angle (α)	Estimated depth (m)		
		PM	MTM	MEM
Sphere	10°	25.3 ± 3.8	28.7 ± 1.4	29.2 ± 0.4
	20°	25.6 ± 4.0	28.8 ± 1.2	29.3 ± 0.6
	30°	25.8 ± 3.5	28.8 ± 1.1	29.6 ± 0.7
	40°	26.0 ± 4.1	28.9 ± 1.0	29.9 ± 0.6
Horizontal cylinder	10°	33.9 ± 6.5	31.2 ± 1.7	29.9 ± 0.5
	20°	34.0 ± 6.3	31.4 ± 1.5	30.0 ± 0.5
	30°	34.1 ± 4.3	31.4 ± 1.3	30.1 ± 0.4
	40°	34.8 ± 4.8	31.5 ± 1.2	30.3 ± 0.6
Vertical cylinder	10°	39.6 ± 20.0	35.4 ± 4.6	29.9 ± 0.5
	20°	40.1 ± 18.5	35.4 ± 4.2	31.2 ± 0.7
	30°	40.5 ± 17.2	35.5 ± 3.6	31.4 ± 0.7
	40°	40.9 ± 17.5	35.6 ± 3.0	31.5 ± 0.6

Table 2.3 Depth values estimated for synthetic source models (sphere, horizontal and vertical cylinder) of SP anomalies by using different polarization angles, for $z_0 = 30$ m.

SP anomaly due to inclined sheet

The SP anomaly at any point P(x) on a profile perpendicular to the strike of a 2D inclined sheet can be written as (Murty and Haricharan, 1985; Sundararajan et al., 1998):

$$V(x) = K\, ln\left\{\frac{\left[(x - x_{0s}) - a\cos\alpha_s\right]^2 + \left(z_{0s} - a\sin\alpha_s\right)^2}{\left[(x - x_{0s}) + a\cos\alpha_s\right]^2 + \left(z_{0s} + a\sin\alpha_s\right)^2}\right\}, \tag{2.4}$$

where K is the electric dipole moment, x_{0s} and z_{0s} are, respectively, the x-coordinate and the depth of the center of the sheet, α_s is the inclination with respect to the horizontal plane, and a is the half-width of the sheet. From eq. (2.4), the SP anomaly of an inclined sheet is a function of five parameters, one more than in the case of spherical and cylindrical bodies, therefore more extended analysis is required for its numerical characterization. In Fig. 2.4, as an example, the power spectrum estimated by PM, MTM and MEM is reported for the SP anomaly computed over an inclined sheet for a profile length of 300 m and a sampling interval of 2 m. The source parameters for the example shown in the figure are reported in Table 2.4. As it can be seen, the application of MEM is successful in determining the depth of the causative source, even if with a percentage error larger than that found for the case of sphere, horizontal and vertical cylinder.

The loss of precision is due to the dependence of the power spectrum shape on the value of the half-width of the sheet, *a*. The performed numerical analysis has shown that the best agreement between predicted and actual values of the source depth are found, keeping fixed α_s, when *a* is about $z_{0s}/2$. Also in this case, an extensive study has been performed for defining the MEM resolution in identifying the causative source depth, z_{0s}. It has been found that for inclined sheet-type sources the resolution is lesser than that obtained for horizontal cylinder-type sources. Specifically, accurate z_{0s} values are found down to depths of about 60 m, with a percent error less than 9%.

A numerical analysis has been then performed to study the behavior of the power spectrum estimated by PM, MTM and MEM for different values of the polarization angle, α_s. As it can be seen from Table 2.4, for the inclined sheet the dependence of the power spectrum on the polarization angle is not negligible as for the case of sphere, horizontal and vertical cylinder. In particular, the depth of the anomaly source estimated from the slope of the log *P(k)* is less accurate as α_s grows.

Synthetic source model	Electric dipole moment (K)	Body center depth (z_0)	Half-width (a)	Polarization angle (α)	Estimated depth (m)		
					PM	MTM	MEM
Inclined sheet	-100 mVm	30 m	15 m	10°	41.3 ± 18.7	32.2 ± 4.3	30.1 ± 1.5
				20°	39.5 ± 16.8	27.6 ± 3.1	28.9 ± 1.2
				30°	35.5 ± 12.1	24.9 ± 2.5	25.8 ± 1.5
				40°	32.6 ± 9.0	23.8 ± 2.1	23.0 ± 0.9

Table 2.4 Parameters characterizing the inclined sheet source of the SP anomaly shown in Fig. 2.4a. The last three columns report the depth values estimated by applying PM, MTM and MEM, respectively, at varying the polarization angle.

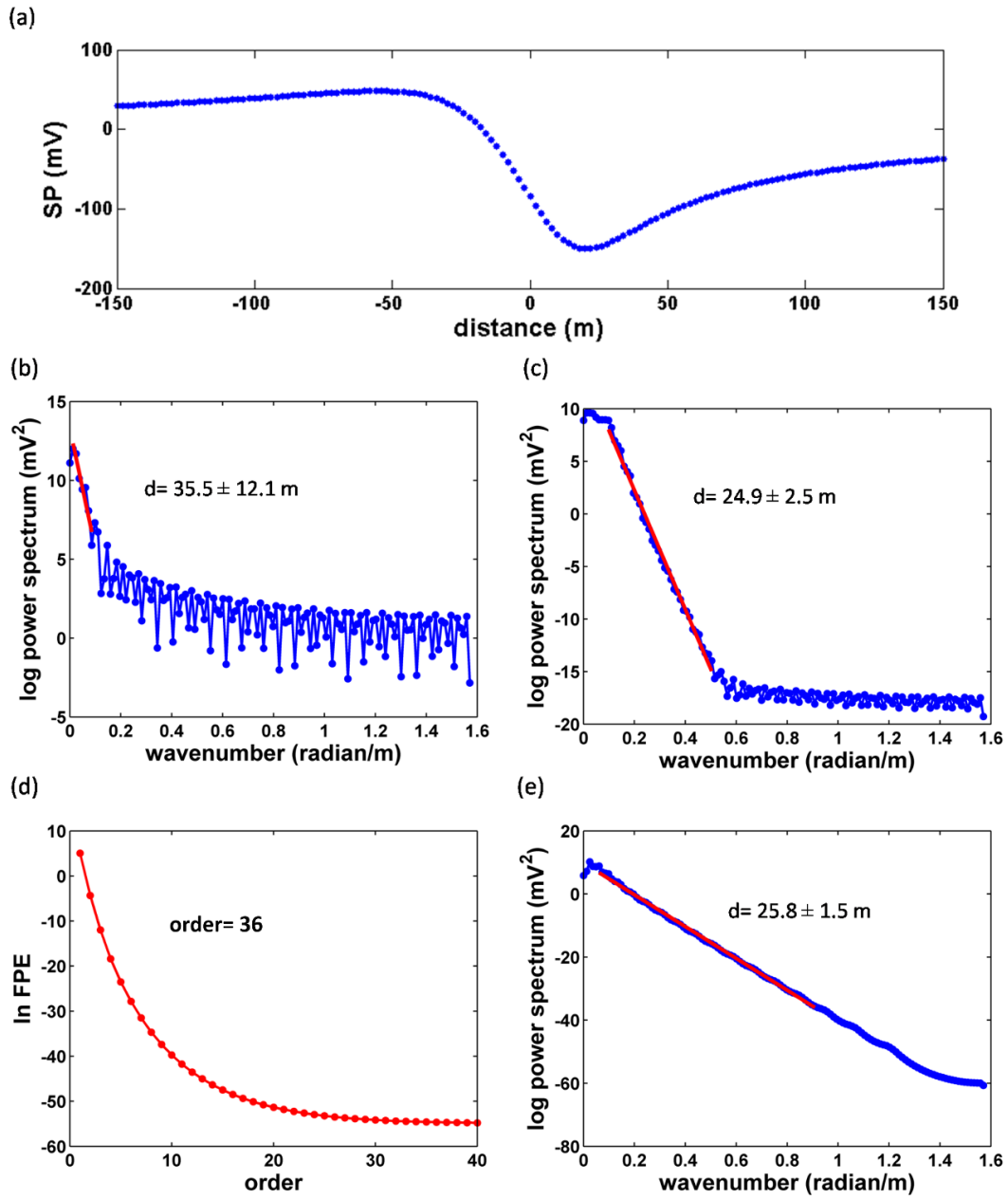

Figure 2.4 (a) SP anomaly due to an inclined sheet characterized by the parameters indicated in Table 2.4; (b) power spectrum estimated by PM; (c) power spectrum estimated by MTM; (d) order selection for AR process and (e) power spectrum estimated by MEM.

As for the previous analyzed structures, a numerical analysis has been then performed by varying the depth of the anomalous source keeping fixed the polarization angle. In Table 2.5 the results obtained for $\alpha_s = 50^\circ$ are shown. As it can be seen, MEM is the most effective method in providing the actual values of the source depth with a percent error of about 5%.

Synthetic source model	Body center depth (z_0)	Estimated depth (m)		
		PM	MTM	MEM
Inclined sheet	20 m	20.9 ± 8.1	17.5 ± 1.2	18.2 ± 1.4
	30 m	29.5 ± 5.8	25.8 ± 3.1	28.9 ± 1.2
	40 m	34.3 ± 6.7	35.2 ± 3.0	38.6 ± 2.0

Table 2.5 Depth values estimated for the inclined sheet source model by using different depth values, for $\alpha_s = 50°$.

2.2.1.3 Sensitivity analysis

As it has been mentioned in Section 2.2.1, power spectrum estimation from MTM and MEM depends on number of tapers, *J*, and suitable selection of the order of the AR process, respectively. Therefore, to investigate the effect of these parameters on the analysis results, a detailed study has been performed to check the appropriateness of the choice made.

As it concerns the number of tapers, the estimation of the power spectrum has been performed by using three different values of *J*. Specifically, we set $J = 2p - 1$ and used p = 2, 3 and 4. As it can be seen from the results summarized in Table 2.6, it has been found that p = 3 produces less variance in spectral estimation, while for p = 2 and 4, a higher error is observed between actual and estimated depth values. Thus, the value $J = 5$ has been used for all the numerical analyses discussed in the present study.

For MEM spectral estimates, the order corresponding to the first minimum in the FPE vs order plot has been selected as the order of the AR process. To check the appropriateness of such a choice, an analysis has been performed by varying the order of the AR process, for fixed values of source depth and polarization angle. As it can be seen from Table 2.6, the estimated depths of the anomaly source, obtained by considering lower and higher orders with respect to the order corresponding to the first minimum in the plot FPE vs order (indicated on the related plots and marked in bold in Table 2.7), show higher errors. Such a result validates the adopted criterion for the choice of the order of the AR process.

Synthetic source model	Body center depth (z_0)	Polarization angle (α)	Estimated depth from MTM (m)		
			p = 2	p = 3	p = 4
Sphere	30 m	10°	27.4 ± 1.5	28.7 ± 1.4	30.5 ± 1.6
		20°	27.4 ± 1.4	28.8 ± 1.2	30.6 ± 1.5
		30°	27.5 ± 1.3	28.8 ± 1.1	30.7 ± 1.4
		40°	27.6 ± 1.4	28.9 ± 1.0	30.7 ± 1.7
Horizontal cylinder	30 m	10°	30.9 ± 3.2	31.2 ± 1.7	32.0 ± 2.2
		20°	30.9 ± 2.9	31.4 ± 1.5	32.2 ± 1.8
		30°	30.9 ± 3.5	31.4 ± 1.3	32.1 ± 1.9
		40°	31.0 ± 2.2	31.5 ± 1.2	32.3 ± 1.3
Vertical cylinder	30 m	10°	33.7 ± 5.5	35.4 ± 4.6	35.2 ± 2.3
		20°	33.6 ± 5.1	35.4 ± 4.2	35.2 ± 2.2
		30°	33.4 ± 4.9	35.5 ± 3.6	35.2 ± 2.1
		40°	33.5 ± 4.3	35.6 ± 3.0	35.1 ± 2.0
Inclined sheet	30 m	10°	31.5 ± 4.6	32.2 ± 4.3	35.0 ± 2.4
		20°	27.4 ± 4.2	27.6 ± 3.1	30.8 ± 1.9
		30°	24.5 ± 3.6	24.9 ± 2.5	27.8 ± 1.7
		40°	23.2 ± 2.5	23.8 ± 2.1	25.2 ± 1.5

Table 2.6 Depth values estimated for synthetic source models (sphere, horizontal cylinder, vertical cylinder and inclined sheet) of SP anomalies due to different polarization angles by varying the number of tapers.

Synthetic source model	Body center depth (z_0)	Order	Estimated depth from MEM (m)
Sphere	30 m	25	29.2 ± 1.2
		35	29.6 ± 0.7
		45	30.1 ± 1.0
Horizontal cylinder	30 m	20	29.9 ± 1.8
		27	30.1 ± 0.4
		35	30.6 ± 0.5
Vertical cylinder	30 m	20	31.5 ± 2.0
		28	31.4 ± 0.7
		35	32.0 ± 1.1
Inclined sheet	30 m	30	24.9 ± 1.2
		36	25.8 ± 1.5
		45	27.0 ± 1.1

Table 2.7 Depth values estimated for synthetic source models (sphere, horizontal cylinder, vertical cylinder and inclined sheet) of SP anomalies by varying the order of the AR process. The numbers in bold mark the choice made for the orders of the AR process for successful applications of MEM.

Finally, in order to check the stability of the proposed inversion methods to noisy data, a numerical analysis has been performed by adding different level of Gaussian random noise to the

original synthetic datasets, at varying depth and polarization angle of the anomalous body. As an example, Table 2.8 summarizes the results obtained for the SP anomaly curves generated by a polarized horizontal cylinder and an inclined sheet with the addition of 5%, 10% and 15% of random noise. The SP values are computed for a profile length of 300 m with a sampling interval of 2 m, and for K = -100 mVm, z_0 = 30 m and $\alpha = 50°$. For all the examined cases, it has been found that MEM is able to provide the actual depths with the lowest percent error (< 12%).

Synthetic source model	Body center depth (z_0)	Random noise	Estimated depth (m)		
			PM	MTM	MEM
Horizontal cylinder	30 m	5%	28.9 ± 5.1	32.1 ± 2.7	31.2 ± 2.8
		10%	29.9 ± 5.0	32.3 ± 3.1	31.7 ± 3.0
		15%	31.3 ± 5.3	32.6 ± 4.3	32.0 ± 4.1
Inclined sheet	30 m	5%	27.3 ± 4.2	26.1 ± 2.2	30.6 ± 4.2
		10%	28.9 ± 3.7	24.4 ± 2.8	30.5 ± 5.0
		15%	29.6 ± 4.5	23.5 ± 4.7	31.3 ± 5.6

Table 2.8 Depth values estimated for synthetic SP data generated by polarized structures, like horizontal cylinder and inclined sheet, with addition of different level of random noise.

2.2.1.4 Application to field data

The spectral methods PM, MTM and MEM have been applied to different examples of SP field data taken from the published literature (Di Maio et al., 2016c; Di Maio et al., 2017). For brevity, one example of field application is provided here.

Sulleymonkoy SP anomaly, Ergani, Turkey

The above mentioned methods were applied to analyze the Sulleymonkoy SP anomaly, Ergani, Turkey (Yüngül, 1950), which has been studied by many authors with different analysis techniques (Bhattacharya and Roy, 1981; Agarwal, 1984; Sundararajan and Srinivas, 1996; Agarwal and Srivastava, 2009; Srivastava and Agarwal, 2009). For this study, the anomaly has been digitized after Bhattacharya and Roy (1981) at a sampling interval of 6 m for a profile

length of 264 m. Figure 2.5 shows the digitized SP anomaly and the power spectrum computed by PM, MTM and MEM. The obtained depth value from the spectral approach is in the range from 27 m to 30 m, which is in good agreement with the depth values provided by other authors as summarized in Table 2.9.

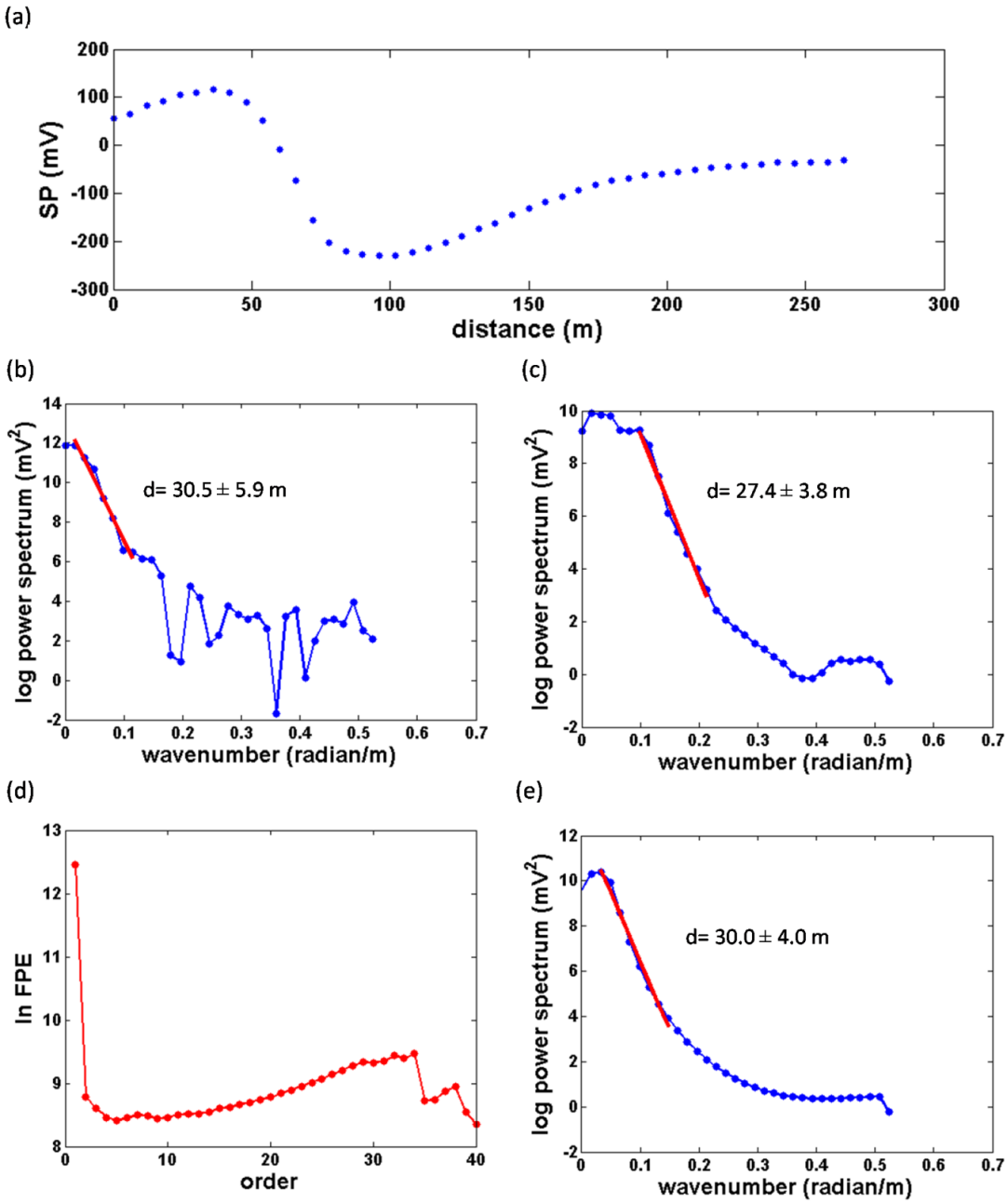

Figure 2.5 (a) Sulleymonkoy SP anomaly, Ergani, Turkey (after Bhattacharya and Roy, 1981); (b) power spectrum estimated by PM; (c) power spectrum estimated by MTM; (d) order selection for AR process and (e) power spectrum estimated by MEM.

Sulleymonkoy SP anomaly: source depth estimated by different methods	
Method	depth (m)
Characteristics curves (Yüngül, 1950)	38.8
Nomograms (Bhattacharya and Roy, 1981)	40.0
Analytic signal approach (Agarwal, 1984)	30.1
Enhanced local wavenumber (Srivastava and Agarwal, 2009)	28.9
Euler's deconvolution (Agarwal and Srivastava, 2009)	27.0
PM	30.5
MTM (Di Maio et al., 2017)	27.4
MEM	30.0

Table 2.9 Estimated depth values for the Sulleymonkoy anomaly source by different analysis methods.

2.2.2 An integrated spectral- tomographic method

As discussed earlier, from the inversion of synthetic SP data generated by geometrically simple anomalous bodies, MEM was found to be better in providing more accurate estimates of the depth of the anomalous body as compared to the nonparametric PM and MTM spectral methods. The MEM is useful to get knowledge on the depth of the causative source without a priori information, but it does not provide any information about the shape of the body. On the other hand, the tomographic approach has been demonstrated to be helpful in characterizing SP anomalies and, in particular, the 3D COP and DOP tomographic imaging has been successfully used to delineate the shape of some known ore bodies (Bhattacharya et al., 2007). To gain simplicity, we focus on 2D COP tomographic imaging and show that once depth is computed from MEM, 2D tomographic maps are able to provide information about the shape and the polarization angle of the causative source. In particular, the proposed MEM-COP integrated approach has been tested on SP synthetic data generated by a polarized horizontal cylinder and an inclined sheet. From numerical analysis, mathematical relationships among polarization

angles, positions of the causative sources along the profile and lines of zeros of the COP function have been found. These relationships turned out of great help in interpreting tomographic maps of SP field data. The results of this numerical analysis are presented in the following subsections, while details about the study of the properties of the COP functions are postponed in the appendices. It is worth noting that the performed analysis shows that the position of the zero lines does not depend on the mesh size used to obtain the analyzed synthetic SP curves.

Below a brief description of the tomographic approach is given, and then the results of the MEM-COP approach on some analyzed synthetic examples are presented.

Tomographic Imaging Method

The tomographic approach to SP data interpretation (Di Maio and Patella, 1994; Patella 1997a, 1997b) aims at defining the underground SP causative sources by using the concept of scanning function and of charge occurrence probability function to map the underground electric charge distribution (Patella 1997a). In the 2D space domain, the scanning function is the electric field component, along a selected straight-line SP profile, generated by an elementary positive charge located at any arbitrarily assigned point of the vertical section through the profile. If its direction coincides with the x-axis of a 2D rectangular coordinate system (x, z) (the tomoplane), the scanning function can be written as (Patella 1997a):

$$\Im_x\left(x-x_q, z_q\right)=\frac{x-x_q}{\left[\left(x-x_q\right)^2+z_q{}^2\right]^{3/2}}, \tag{2.5}$$

where (x_q, z_q) is the position of the elementary charge in the subsoil.

The charge occurrence probability function (COP) is defined as the cross-correlation product of the total observed electric field component, E_x, and the scanning function, normalized to the square root of the product of the respective variances. A discrete formulation of the COP for any arbitrarily assigned point of coordinates (ξ, δ) in the tomoplane is given by (Patella 1997a):

$$\eta(\xi,\delta) = -D\delta^{3/2} \sum_{\chi=\chi_{min}}^{\chi=\chi_{max}} \Delta V(\chi) \frac{(\chi-\xi)}{\left[(\chi-\xi)^2+\delta^2\right]^{3/2}}, \qquad \text{for } \delta > 0 \qquad (2.6)$$

where $\Delta V(\chi)$ is the potential drop measured along the *x*-axis at a space interval Δx and attributed to the middle point of the measurement dipole, $\chi\left(=\frac{x}{\Delta x}\right)$, $\xi\left(=\frac{x_q}{\Delta x}\right)$ and $\delta\left(=\frac{z_q}{\Delta x}\right)$ are integers and *D* is the normalizing factor that is a constant for any given profile and depends only on the electric field component $E_x(x) = \frac{-\Delta V(x)}{\Delta x}$.

The value of $\eta(x,z)$, for any assigned pair of coordinates (*x*, *z*) in the tomoplane, can be interpreted as the probability that a positive ($\eta > 0$) or negative ($\eta < 0$) electric charge there located is responsible of the SP value distribution observed along the measurement profile. The tomoplane is scanned along horizontal lines, spaced by a constant depth interval, and the value of η is calculated for each value of *x*, taking fixed *z*, and so on, until to obtain a grid distribution of η values in the tomoplane. A suitable line contour process outlines the zones where the electric charges, positive or negative, are most likely concentrated.

It is worth noting that in practice the above described 2D tomographic procedure provides a cross-sectional representation of the COP function not necessarily coinciding with a true section. In fact, while the *x*-coordinate properly denotes the horizontal offset of the charges along the profile, the tomodepth (i.e. the *z*-coordinate) may not represent the actual depth, but the composition of the true depth and a possible lateral offset *y* with respect to the SP profiling line, here coincident with the *x*-axis (Patella 1997a; Di Maio et al., 1998). Such an evident ambiguity can be eliminated by performing a SP areal investigation and applying a 3D tomographic algorithm of the COP function by using a 2D cross-correlation integral product (Patella 1997b; Di Maio et al. 2000; Di Maio et al., 2013).

2.2.2.1 MEM-COP integrated analysis of SP synthetic data

The proposed approach to the analysis of SP data, which integrates the MEM and the COP tomography methods, has been tested on SP synthetic data generated by a polarized horizontal cylinder and an inclined sheet.

Horizontal cylinder

The SP anomaly curve due to a horizontal cylinder can be obtained by using eq. (2.3) with shape factor p = 1.0. To gain simplicity and differentiate the source parameters, eq. (2.3) for horizontal cylinder-like geologic structure can be expressed as:

$$V(x) = K \frac{(x - x_{0c}) \cos \alpha_c - z_{0c} \sin \alpha_c}{\left[(x - x_{0c})^2 + z_{0c}^2\right]}, \tag{2.7}$$

where K is the electric dipole moment, x_{0c} and z_{0c} are the coordinates of the center axis of the body, and α_c is the polarization angle measured from the horizontal positive clockwise.

As shown in previous sections, MEM is able to provide depth information with error less than 5% for horizontal cylinder placed at different depths (Fig. 2.2 and Table 2.2). However, as stated earlier, MEM is not able to give any information about the polarization angle, as the power spectrum is not significantly affected by α_c changes (see Table 2.3). Thus, to gain information about α_c the tomographic approach is applied. As example, Fig. 2.6 shows 2D COP tomographic images that are computed by using eq. (2.6) for four different values of the polarization angles (α_c = 10°, 30°, 50° and 90°) and keeping fixed the depth z_{0c} (= 30 m). As it can be seen from Fig. 2.6, the 2D tomographic maps have three lines of zeros, with the central zero line well approximated by a straight line. Interestingly, it has been found that such a central zero line of the COP function changes its inclination, β_c, by varying α_c, and only for the special case α_c = 90° it disappears and two symmetrical zero lines are found. The dependence of the COP function η on the polarization angle has been investigated numerically (see Appendix B) and a relation between α_c and the inclination β_c has been identified:

$$\beta_c = 90° - 22.604\,\alpha_c\,, \tag{2.8}$$

where β_c is expressed in degrees and α_c in radians. By computing the β_c values for the investigated cases and using eq. (2.8), the estimated polarization angles from the tomographic approach are: 10.02°, 29.70°, 49.62° and 89.27°, in very good agreement, respectively, with the actual values.

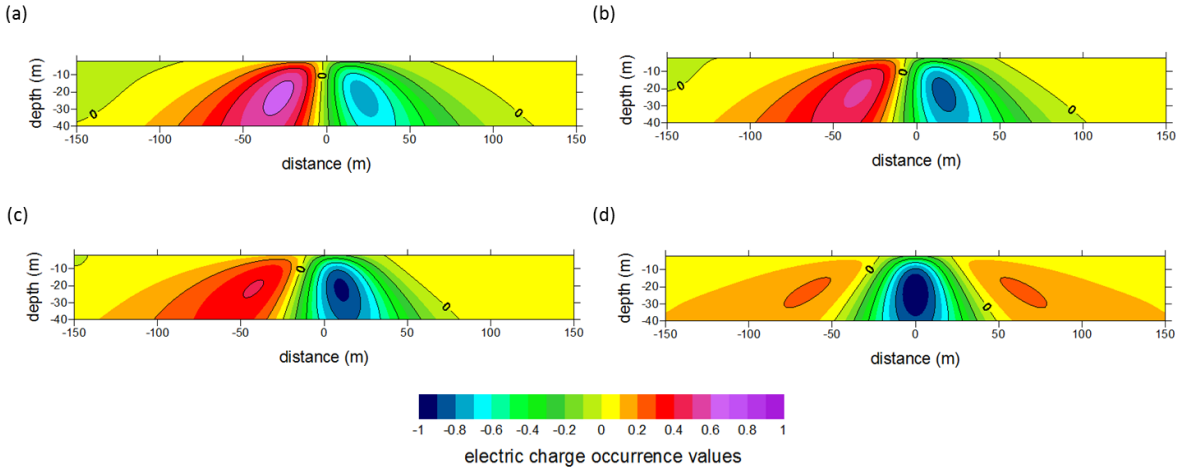

Figure 2.6 2D COP tomographies for four analyzed synthetic cases of horizontal cylinder with polarization angle α_c = 10° (a), 30° (b), 50° (c) and 90° (d).

As concerns the determination of the coordinate of the center axis of the body, x_{0c}, it has been found that x_{0c} is related to the intercept I_c of the central zero line of the COP function by a shift Δx_{0c}, which is a linear function of the source depth z_{0c} and the polarization angle α_c for $\alpha_c \leq \pi/3$. Specifically, it has been found that:

$$x_{0c} = I_c + \Delta x_{0c}\,, \tag{2.9}$$

with $\Delta x_{0c} = r\alpha|z_{0c}|$ and r = 0.38785 rad^{-1} as illustrated in the Appendix B. By using such a formula for the cases shown in Fig. 2.6, it turns out that the x_{0c} coordinates are: 0.031 m, 0.092

m and 0.154 m for polarization angles 10°, 30° and 50°, respectively, in very good agreement with the actual value (i.e. $x_{0c} = 0$).

In order to check the stability of the proposed integrated approach to noisy data, a numerical analysis has been performed by adding different level of Gaussian random noise to original synthetic datasets, at varying depth and polarization angle of the anomalous body.

Concerning the depth estimation from MEM, for all the analyzed cases the MEM method was able to provide the true depths with a percent error less than 10% (see Table 2.8). As regards the polarization angle, 2D COP tomographic distributions were computed by using eq. (2.6) for four different values of the polarization angle (α_c = 10°, 30°, 50° and 90°) and keeping fixed the depth (z_{0c} = 30 m) with addition of different level of random noise to the original dataset. As an example, Fig. 2.7 shows the results for data affected by 5% of random noise. As it can be seen, the pattern of the central zero line is slightly influenced by the occurrence of noise, especially for smaller angles. Nevertheless, by computing the β_c values for the investigated cases and by using eq. (2.8), the estimated polarization angles from the tomographic approach are: 10.38°, 30.16°, 49.72° and 89.58°, in very good agreement, respectively, with the actual values.

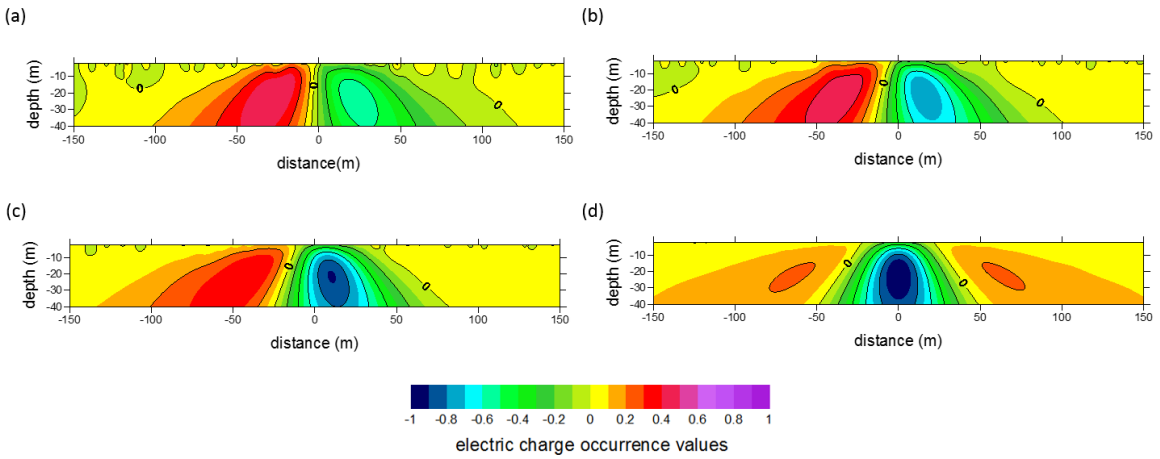

Figure 2.7 2D COP tomographies for the analyzed synthetic data affected by 5% of random noise at varying the polarization angle: α_c = 10° (a), 30° (b), 50° (c) and 90° (d).

Inclined sheet

The synthetic SP values due to an inclined sheet-like source have been calculated by using eq. (2.4). As reported in previous sections, the application of MEM is successful in determining the depth of the causative source, even if with a percentage error larger than that found for the case of the horizontal cylinder, where the best agreement between predicted and observed values of the source depths are found, keeping fixed α_s, when a is about $z_{0s}/2$ (Fig. 2.4 and Table 2.5). As concerns the dependence of the power spectrum on α_s, it is not negligible as for the case of horizontal cylinder. Indeed, the depth of the anomaly source estimated from the slope of the log $P(k)$ is less accurate as α_s grows (see Table 2.4). The 2D SP tomographic approach is then applied by varying the polarization angle α_s and the half-width a of the inclined sheet for each investigated depth of the anomalous source. As an example, Fig. 2.8 shows 2D COP tomographic images related to SP data computed by using eq. (2.6) for four different polarization angles (α_s = 10°, 30°, 50° and 90°) and keeping fixed the depth z_{0s} (= 30 m) and the half-width a (= $z_{0s}/2$). As it can be seen from the images, the 2D tomographic maps are very similar to those obtained for the case of the horizontal cylinder and have three lines of zeros, with the central zero line well approximated by a straight line. By investigating the dependence of the COP function η on the polarization angle α_s (see Appendix C), a linear relationship between α_s and the inclination of the zero line, β_s, very similar to that found for horizontal cylinder has been identified:

$$\beta_s = 90° - 23.49\,\alpha_s\,, \tag{2.10}$$

where β_s is expressed in degrees and α_s in radians. By computing the β_s values for the investigated cases, the estimated polarization angles from the tomographic approach are: 9.75°, 29.20°, 48.13° and 87.60°, in good agreement, respectively, with the actual values.

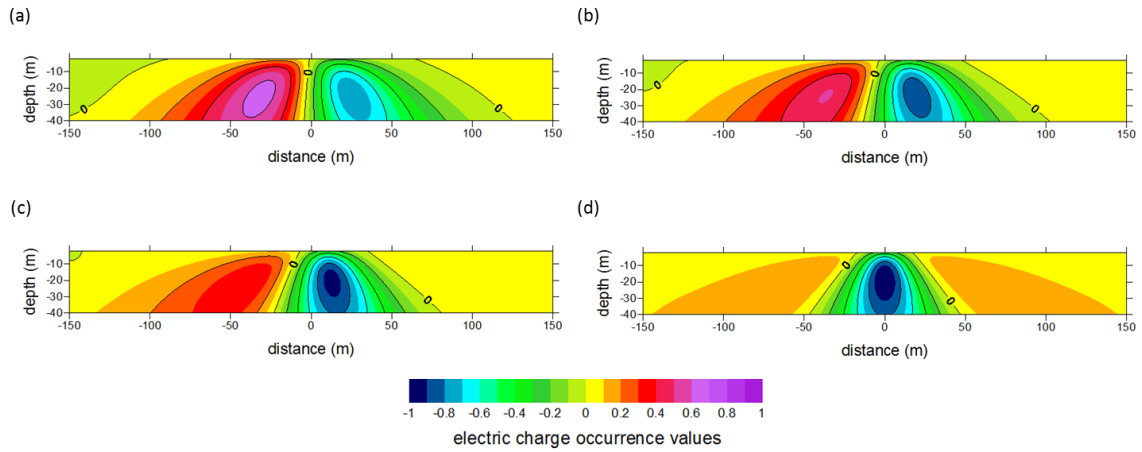

Figure 2.8 2D COP tomographies for four analyzed synthetic cases of inclined sheet with polarization angle α_s = 10° (a), α_s = 30° (b), α_s= 50° (c) and α_s = 90° (d).

As it concerns the determination of the coordinate of the center axis of the body, x_{0s}, it has been found that x_{0s} is related to the intercept I_s of the central zero line of the COP function by a shift Δx_{0s}, which is a linear function of the source depth z_{0s} and the polarization angle α_s for $\alpha_c \leq \pi/3$ and $z_{0s} \geq 20$ m. Specifically, it has been found that:

$$x_{0s} = I_s + \Delta x_{0s} \ , \tag{2.11}$$

with $\Delta x_{0s} = \alpha_s (t + r z_{0s})$, where t = -4.11 m/rad and r = 0.4169 rad^{-1} as illustrated in the Appendix C. By using such a formula for the cases shown in Fig. 2.8, it turns out that the x_{0s} coordinates are: -0.034 m, -0.397 m and 0.328 m for polarization angles 10°, 30° and 50°, respectively, in very good agreement with the actual value (i.e. x_0 = 0).

About the dependence of η on the parameter a, it has been found that the central zero line of η can be well approximated by a straight line only for a restricted range of values of a. As an example, Fig. 2.9 shows the COP function for different values of a (= 5 m, 15 m, 25 m and 50 m), keeping fixed α_s (= $\pi/4$) and z_{0s} (= 30 m). This result provides a useful constraint on the interpretation of real data as if the tomographic map shows a central straight line of zeros, reasonable values of a will be close to half the depth.

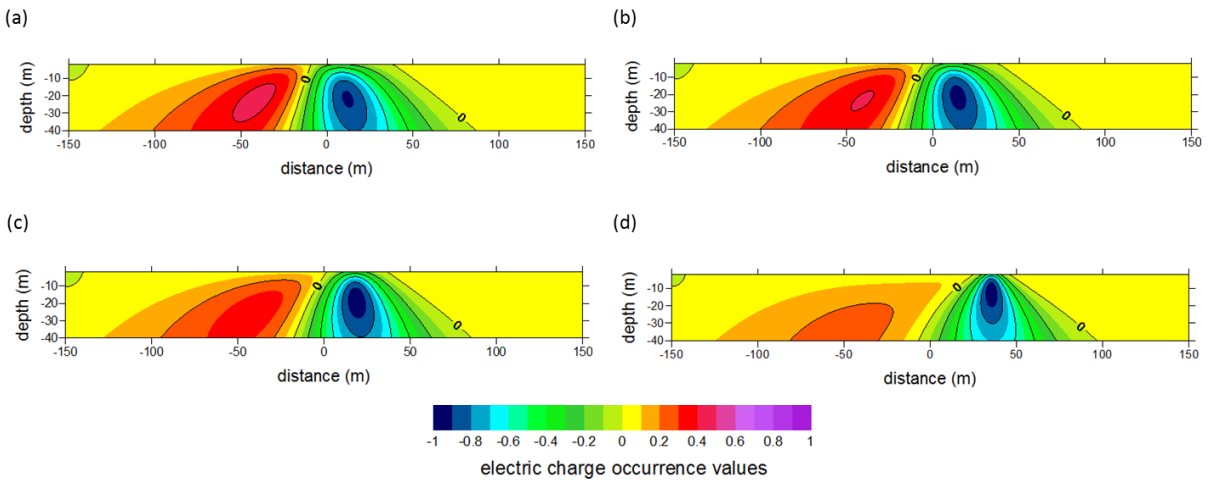

Figure 2.9 2D COP tomographies for the four analyzed synthetic cases of inclined sheet at polarization angle α_s = 45° and depth z_{0s} = 30 m, for different half-width a = 5 m (a), a = 15 m (b), a = 25 m (c), a = 50 m (d).

Finally, also in this case a numerical analysis was performed to estimate the effectiveness of the proposed approach in presence of noisy data. Different levels of random noise were added to original synthetic datasets obtained at varying the depth and the polarization angle of the body. Concerning the depth estimation from MEM, for all the analyzed cases the MEM method was able to provide the true depths with a percent error less than 13% (see last row of Table 2.8).

As regards the polarization angle, 2D COP tomographic distributions were computed by using eq. (2.6) for four different values of the polarization angle (α_s = 10°, 30°, 50° and 90°) and keeping fixed the depth (z_{0s} = 30 m) with addition of different levels of random noise to the original datasets. In particular, Fig. 2.10 shows the results for data affected by 5% of random noise. By computing the β_s values for the investigated cases and by using eq. (2.10), the estimated polarization angles from the tomographic approach are: 9.42°, 30.93°, 50.10° and 90.57°, in very good agreement, respectively, with the actual values.

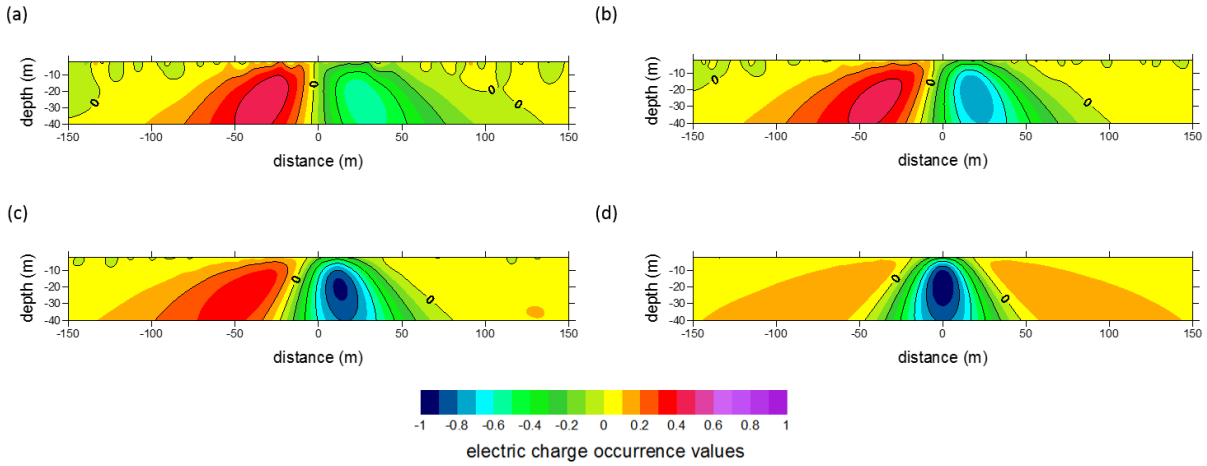

Figure 2.10 2D COP tomographies for the analyzed synthetic data affected by 5% of random noise at varying the polarization angle: α_s = 10° (a), α_s = 30° (b), α_s = 50° (c) and α_s = 90° (d).

2.2.2.2 Application to field data

The proposed integrated approach has been applied to different examples of SP field data taken from the published literature (Di Maio et al., 2016a). For the sake of brevity, one example of field application is provided here.

The Bavarian woods anomaly, Germany

The graphite deposits in Bavarian woods of Germany are situated in a hercynic gneissic complex and are conformably intercalated between paragneiss and crystalline limestone of the same age (Meiser, 1962). Generally, these deposits form seams, which are designated as bituminous sediments of presumably Precambrian age. The SP anomaly data generated by such deposits were acquired by Meiser (1962). Over time, this dataset has been studied by various authors by using different methods, whose results are summarized in Table 2.10.

For this study, the anomaly has been digitized at a space interval of 2 m for a profile length of 520 m (Fig. 2.11a). The depth of the SP anomaly source estimated from the MEM application (Figs 2.11b and c) is in the range from 35.90 m to 53.00 m, which is in good agreement with the depth obtained by other authors (see Table 2.10). The application of the tomographic approach, instead, has provided the in-depth COP distribution shown in Fig. 2.11d. Also in this case, the

tomographic image shows similarities to the COP distribution for SP anomaly curves generated by a horizontal cylinder (see Fig. 2.6) and an inclined sheet (see Fig. 2.8). To compare the results of our approach with those provided by previous studies, a horizontal cylinder source model has been chosen. Hence, eq. (2.8) has been used to find the value of the polarization angle. By estimating the slope of the central zero line from the COP distribution map in Fig. 2.11d, i.e. β_c = -66.52°, a value of the polarization angle α_c = -59.52° is obtained.

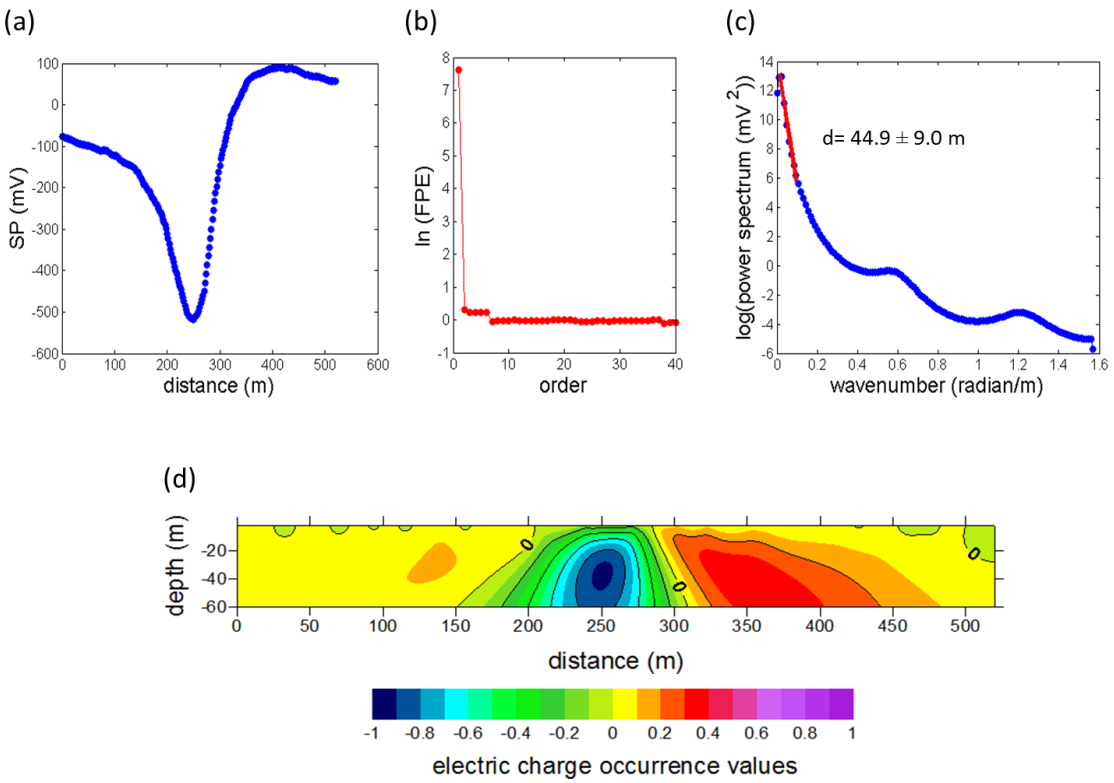

Figure 2.11 (a) Bavarian woods SP anomaly, Germany; (b) order selection for AR process; (c) power spectrum estimated by MEM; (d) COP distribution provided by tomographic approach.

Methods	p or a (m)	K (mVm)	x_0 (m)	z_0 (m)	θ (°)
Higher derivative analysis (Abdelrahman et al., 2003)	p = 0.91	2020.0	322.0	49.3	-55.7
Least square inversion (Essa et al., 2008)	p = 1.0	30608.7	-	47.7	-51.2
Least square inversion (Essa, 2011)	p = 1.0	27212.70	-	46.59	-59.04
Global optimization (Göktürkler and Balkaya, 2012)	p = 0.97 (Genetic Algorithm) p = 1.02 (Particle Swarm Opt.) p = 0.99 (Simulated Annealing)	21272.91 33343.87 26257.42	268.79 269.88 269.17	45.03 47.59 45.99	- 51.29 - 48.60 - 49.98
Integrated spectral and tomographic approach (Di Maio et al., 2016a)	p = 1.0	25000.00	265.91	44.90	- 59.52

Table 2.10 Source parameters retrieved for Bavarian woods SP anomaly (Germany) by applying different data interpretation methods.

Finally, a synthetic curve has been then computed by considering a horizontal cylinder with source depth value z_{0c} = 44.90 m (derived from the MEM application), polarization angle α_c = -59.52° and coordinate of the center axis of the body x_{0c} = 265.91 m (derived from the tomographic approach by using eqs. (2.8) and (2.9)). As it is shown in Fig. 2.12, a good correlation between synthetic and observed data has been found.

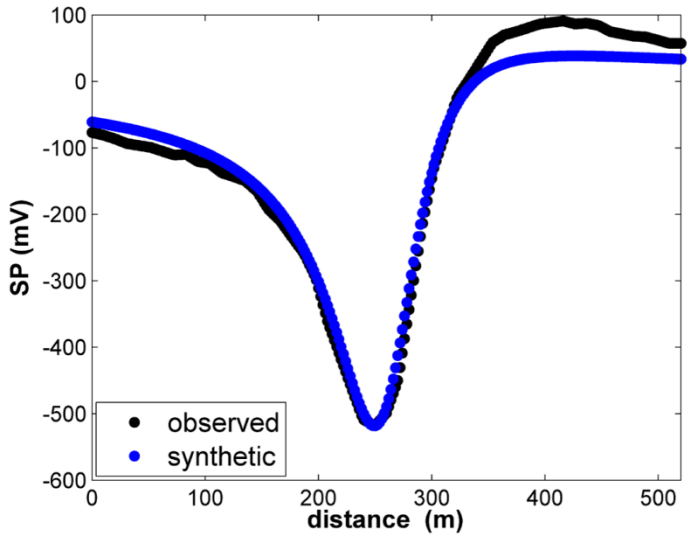

Figure 2.12 Computed SP anomaly (blue points) compared with the observed Bavarian woods SP anomaly (black points).

2.2.3 The Genetic-Price algorithm

The Genetic-Price Algorithm (GPA) is a global optimization method introduced by Bresco et al. (2005) for finding the absolute extreme point of a multimodal scalar function with many variables. This algorithm is an improvement of the first controlled random search algorithm proposed by Price (1976), and its simplified flow diagram is shown in Fig. 2.13.

Given a function *S* of *m* variables, the first step consists in assigning limits to each of the *m* variables, thus defining an initial search domain. A number *N* of trial points, with N >> m to avoid the risk of premature convergence, is chosen randomly within this domain, and the function values at each point are stored in a search array *A*. At each iteration, a trial point *P* is selected in a way that depends on the previous *N* points. If the value of *S* in *P* is less than the maximum value stored in *A*, then *P* replaces the corresponding point in *A*, otherwise a new trial point *P* is selected. Price (1976) showed that, by iterating this procedure, the set of *N* points within the array *A* tends to cluster around the minima, which are clearly better defined the higher is *N*. On the other hand, if *N* is higher, the rate of convergence is slower and the computational costs are higher. To improve the Price's algorithm, Brachetti et al. (1997) proposed a variant of the original algorithm that enhances efficiency in the local optimization phase. The main differences of the modified Price algorithm consist in selecting the trial point *P* by means of a weighted, and not simple centroid, rule and in building a quadratic approximation of the objective function based on the most promising points, which allows to perform a local minimization without further function evaluations (Bresco et al., 2005). Such an approach fails if a positive definite quadratic form cannot be defined. To avoid this problem, the employed hybrid algorithm uses the same scheme of Brachetti et al. (1997), but if the algorithm fails to find a positive definite matrix, a global minimization step based on a genetic algorithm approach is executed.

The genetic algorithms (GAs) are stochastic optimization methods inspired by the Darwin's theory of evolution, which states that the survival of an organism can be maintained through the process of reproduction, crossover and mutation (Goldberg, 1989). In GAs methods, the search for the global minimum mimics the biological evolution by taking an initial random population of individuals (or strings), *G*, which encode candidate solutions, and combining them to produce individuals that are more fit. The rules for improving individuals are based on the three mechanisms: *reproduction*, which consists in the selection of individuals chosen for mating and decides how many offsprings any individual must produce; *crossover*, which produces two new individuals interchanging some springs that represent the two individuals; *mutation*, which affects very few of offsprings and consists of altering a variable. The selection of an individual for the reproduction is performed by using a function representing the fitness of the individual. On the basis of fitness values, old population members are compared with newly generated ones, and those with the best fitness survive and constitute the new population. By iterating the processes of selection, crossover and mutation, the population evolves towards the optimal solution and the individual with the best fitness value is considered as the solution of the problem (Lee and Mohamed, 2002; Luke, 2009).

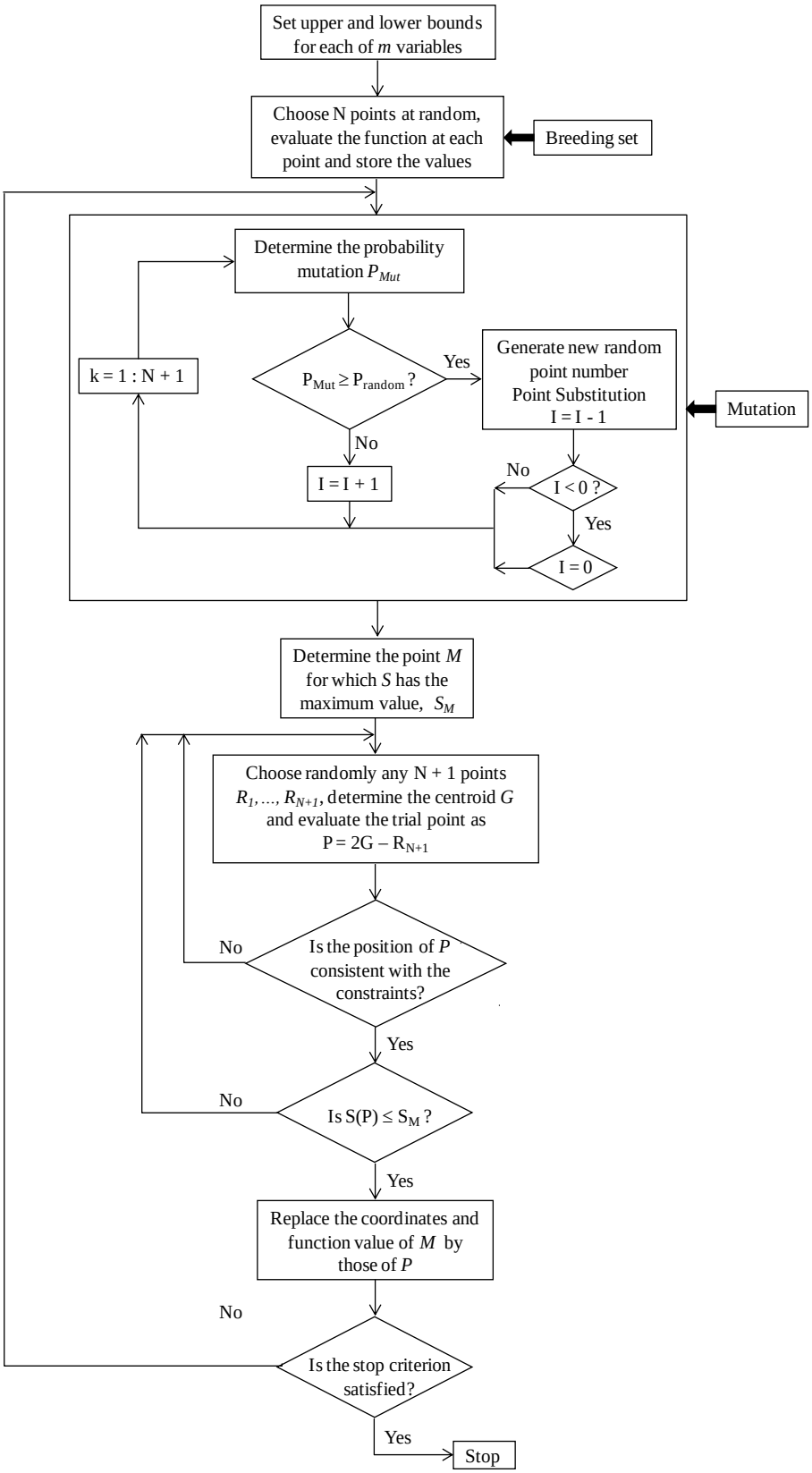

Figure 2.13 Simplified flow diagram of the Genetic-Price's algorithm.

Although the GAs are powerful approaches mainly due to their degree of randomness in the population generation mechanism, which prevent them getting stuck because of the presence of local minima, practical applications of GAs encounter many problems related to different critical points, such as difficulties in the individual coding, choice of initial population, slow evolution. To avoid the drawbacks of GAs in solving global optimization problems, various modifications of the basic evolution scheme have been developed, and hybrid approaches have been proposed. In the approach of Bresco et al. (2005), the CRS algorithm scheme has been modified to include reproduction, crossover and mutation operators in the following way. The N trial points randomly chosen within the initial search domain are considered the breeding set, as a potential new member of the population is generated from them. The recombination (crossover) process in the CRS algorithm is the reflection of the ($N+1$)'th point through the centroid of the first N points. If the newly generated point has fitness better than that of the worst population member, the former replaces the latter and the procedure is iterated with the new breeding set. Following Milano and Koumoutsakos (2002), we chose an alternative process that consists of generating $N+1$ new points instead of just one, by performing $N+1$ reflections, one for each point of the breeding set. The advantage of generating $N+1$ offsprings from the same breeding set is that, if we choose a "good" breeding set by chance, we can generate as much "good offsprings" as possible. Finally, to introduce a mutation operator in the CRS algorithm the following heuristic guidelines are taken into account: *a)* points with a fitness nearer to the threshold G_{lim} should mutate with less probability to avoid a lack of good points; for the same reason points belonging to the confidence region (i.e. with fitness better than G_{lim}) should not mutate; *b)* a mutation should be performed on the basis of an estimate of the necessity to introduce new information in the population; *c)* replacing a population member with a completely random point should rarely happen to prevent the search algorithm becoming a random search. Following these lines, a mutation probability, P_{Mut}, for each point of the breeding set, λ, is defined as:

$$P_{Mut}(\lambda) = \begin{cases} (1-\alpha^{I}) \cdot \left(1-\beta^{\frac{G(\lambda)-G_{lim}}{G_{av}}}\right) \cdot \gamma, & G(\lambda) > G_{lim} \\ 0 & otherwise, \end{cases} \tag{2.12}$$

where I is the number of consecutive iterations in which the population was not improved, $0 \leq \gamma < 1$ is the upper bound for the mutation probability, $0 \leq \alpha < 1$ and $0 \leq \beta < 1$ are tunable parameters that modulate the mutation rate, respectively, in time (measured in iterations) and in space (measured in fitness values), and G_{av} is the average fitness of the current population, used as a normalization parameter. In eq. (2.12), the first multiplicative term satisfies the condition *b)*, taking I as an estimate of the necessity of mutation at a certain stage, while the second multiplicative term satisfies the condition *a)* by assigning a lower mutation probability to points that are closer to the given threshold. Finally, the condition *c)* is satisfied by applying the mutation operator during the selection process: each breeding set element selected for mutation is substituted by a completely random one sampled in the search volume. Only when this merged selection/mutation terminates, recombination is performed. The mutated breeding set elements never directly substitute the original ones in the population. Since the mutation so defined acts on each breeding set member independently, the probability of generating a completely random point proceeds in this way:

$$P_{random} = \prod_{i=1}^{N+1} P_{Mut}(\lambda_i) \ll P_{Mut}(\lambda_i), \quad i = 1, \dots, N+1$$

as required by condition *c)*.

2.2.3.1 GPA analysis of SP synthetic data

The Genetic-Price algorithm proposed for the inversion of self-potential anomalies has been tested on synthetic SP data generated by different source models, such as sphere, vertical cylinder, horizontal cylinder and inclined sheet. For each dataset, the numerical analysis has

been carried out with no added noise and by adding Gaussian white random noise up to 30%. Moreover, for each source model different objective functions have been used. In this section, the results of the performed analyses are shown.

SP anomalies due to polarized spherical, cylindrical and inclined sheet sources

The SP observed at any point $P(x)$ on the surface along a profile line perpendicular to the strike of spherical- or cylindrical- and inclined sheet-like geologic structures can be generated by the mathematical relations given in eq. (2.3) and eq. (2.4). Starting from these equations, the following objective function is assumed for minimizing the variance of the fitting:

$$\sigma^2_{p/sheet} = \frac{1}{(N_{obs} - m)} \sum_{i=1}^{N_{obs}} \left(\hat{V}_i(\lambda)_{p/sheet} - V_{obs_i} \right)^2 , \qquad (2.13)$$

where N_{obs} is the number of measured samples, m is the number of parameters, $\hat{V}_i(\lambda)_p$ or $\hat{V}_i(\lambda)_{sheet}$ are the outputs of the model corresponding to the forward functions eq. (2.3) or eq. (2.4), respectively, for a given λ, and V_{obs_i} are the measured SP values. If the errors of the latter are known, it is possible to use the χ^2 test of the fit. By using the forward functions eq. (2.3), with different values of p, and eq. (2.4), synthetic datasets of simple geometric shaped SP models were generated and, for each synthetic curve, the GPA analysis was carried out by adding 10%, 20% and 30% of random noise to the initial data. It is worth noting that the GPA inversion method requires the selection of a forward function, but no assumption on the set of variables K, x_0, z_0, θ and p (or a) is necessary, as the global optimization process identifies the most likely SP anomaly source model without any a priori punctual starting guess on SP source parameters.

An extensive study at varying the survey parameters (i.e. length of the SP synthetic profile, L, and space sampling step, Δx) and the parameters of the selected source model (i.e. K, x_0, z_0 and θ) has been performed to demonstrate the effectiveness of the proposed approach. In the next two subsections only some examples are reported that all refer to the following parameters: K =

100 mVm, x_0 = 0 m, z_0 = 10 m, θ = 30°, L = 300 m and Δx = 1 m. The results of the simulations are summarized in Table 2.11. As it concerns the efficiency of the computation times, a study has been performed for estimating the CPU execution time necessary for solving 1000 different cases by using both the simple Price algorithm and the Genetic-Price algorithm. It has been found that GPA turns out to be slightly slower than the simple Price algorithm (about 3%). However, the main advantage of the GPA is that it can find 'minima basins' rather than single optimum points, and such a property is suitable to have a better insight into the physical system properties.

SP anomalies due to polarized spherical and cylindrical sources

The numerical analysis was performed by varying the shape factor, *p*, in eq. (2.3) for computation of SP anomalies due to different polarized structures with different level of noise on the synthetic SP data, V_{obs}. The GPA was applied to such data considering eq. (2.13) as objective function by using both forward equations given by eq. (2.3) and eq. (2.4). As expected, if eq. (2.3) is used for $\hat{V}_i(\lambda)_p$ in the objective function, the GPA provides the shape factor that characterizes the true source model, i.e. p = 1.5 (1.6 with 30% of noise added), 1.0 and 0.5 for sphere, horizontal cylinder and vertical cylindrical, respectively, thus identifying the most likely anomaly sources. Figures 2.13, 2.14 and 2.15 and Table 2.11 summarize the obtained results. In particular, the upper panels of the Figs. 2.13a-d, 2.14a-d and 2.15a-d, show the comparison between the synthetic SP curves (blue continuous lines), with different percentage of random noise, and the curves calculated by using the source parameters provided by the GPA for the two selected objective functions, σ_p^2 (red dotted lines) and σ_{sheet}^2 (green dotted lines), while the lower panels show the distribution of the residuals (i.e. the differences between synthetic and calculated data).

For any case study, as it can be seen in the upper panels of Figs. 2.13a-d and 2.14 a-d, if $\hat{V}_i(\lambda)_{sheet}$ is used in the objective function, the solution curve also overlaps the synthetic one, even if a better fit is found when a spherical and a horizontal cylindrical source is assumed, respectively. In fact, the distributions of the residuals shown in the lower panels of Figs. 2.13a-d and 2.14a-d clearly indicate that the residuals related to σ^2_{sheet} (green dotted lines) are higher than those obtained by selecting σ^2_p as objective function (red dotted lines), even if these differences decrease with increasing noise.

Concerning the vertical cylindrical source (Fig. 2.15), the upper panels of Figs. 2.15a-d show that, unlike the previous cases, a very good match between synthetic and calculated data is found only if σ^2_p is used as objective function for all the examined synthetic curves.

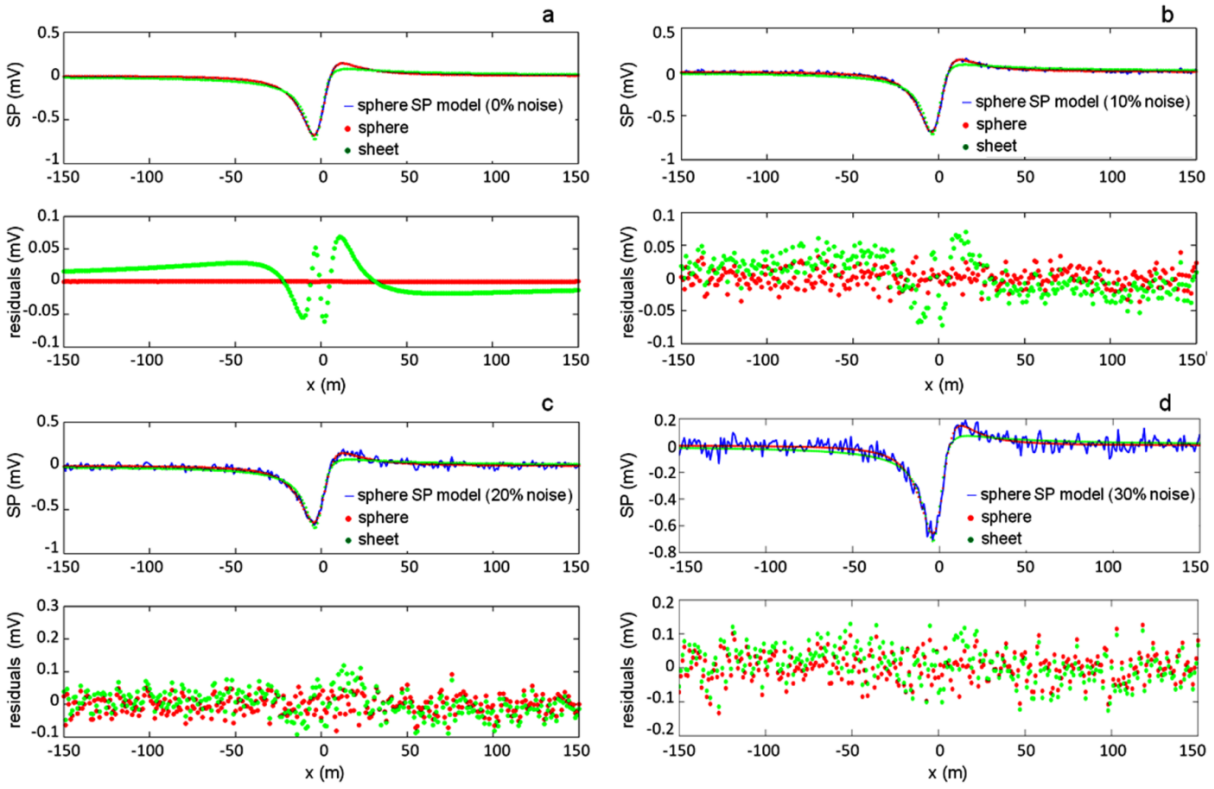

Figure 2.13 GPA inversion results of synthetic SP anomalies due to a spherical source with different level of random noise. Upper panels of a-d: comparison between synthetic SP curve (blue continuous line) and curves calculated by using eq. (2.3) (red dotted line) and eq. (2.4) (green dotted line) in the objective function eq. (2.13) with 0% (a), 10% (b), 20% (c) and 30 % (d) of random noise. Lower panels of a-d: differences between synthetic and calculated curves shown in the corresponding upper panels.

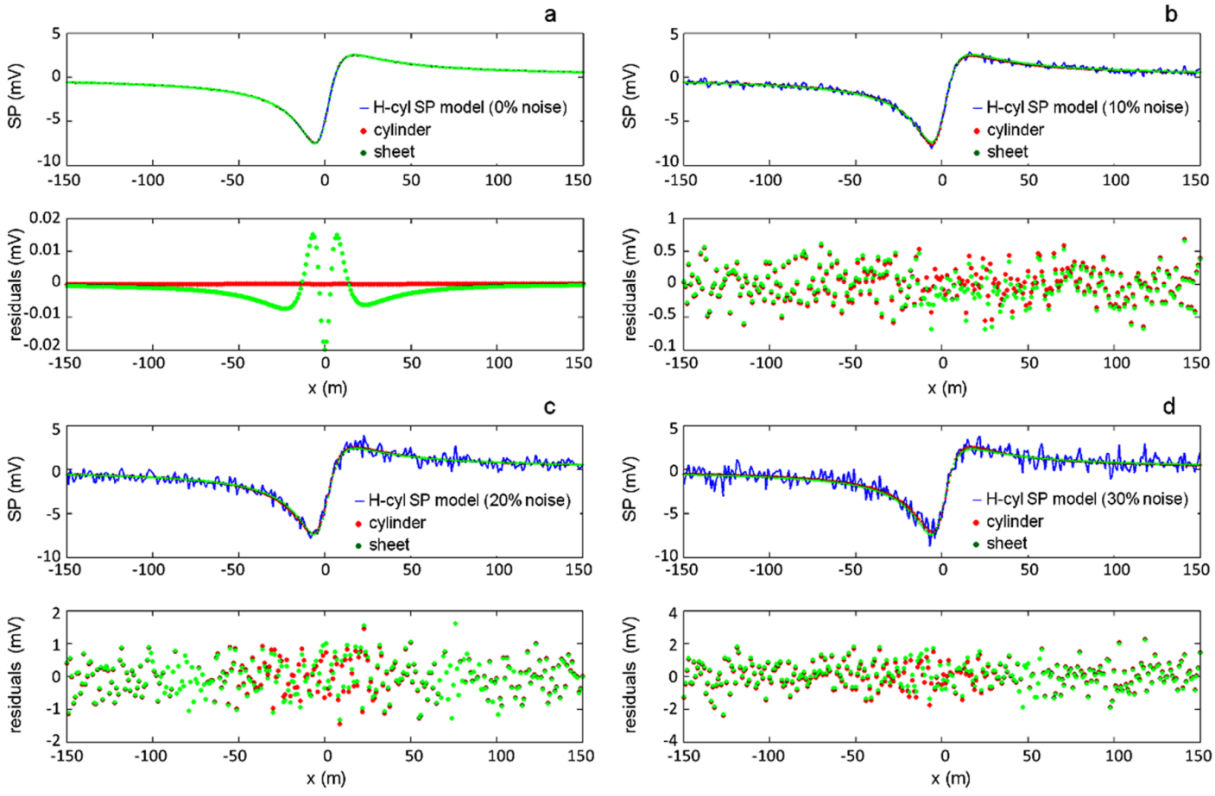

Figure 2.14 GPA inversion results of synthetic SP anomalies due to a horizontal cylinder with different level of random noise. Upper panels of a-d: comparison between synthetic SP curve (blue continuous line) and curves calculated by using eq. (2.3) (red dotted line) and eq. (2.4) (green dotted line) in the objective function eq. (2.13), with 0% (a), 10% (b), 20% (c) and 30 % (d) of random noise. Lower panels of a-d: differences between synthetic and calculated curves shown in the corresponding upper panels.

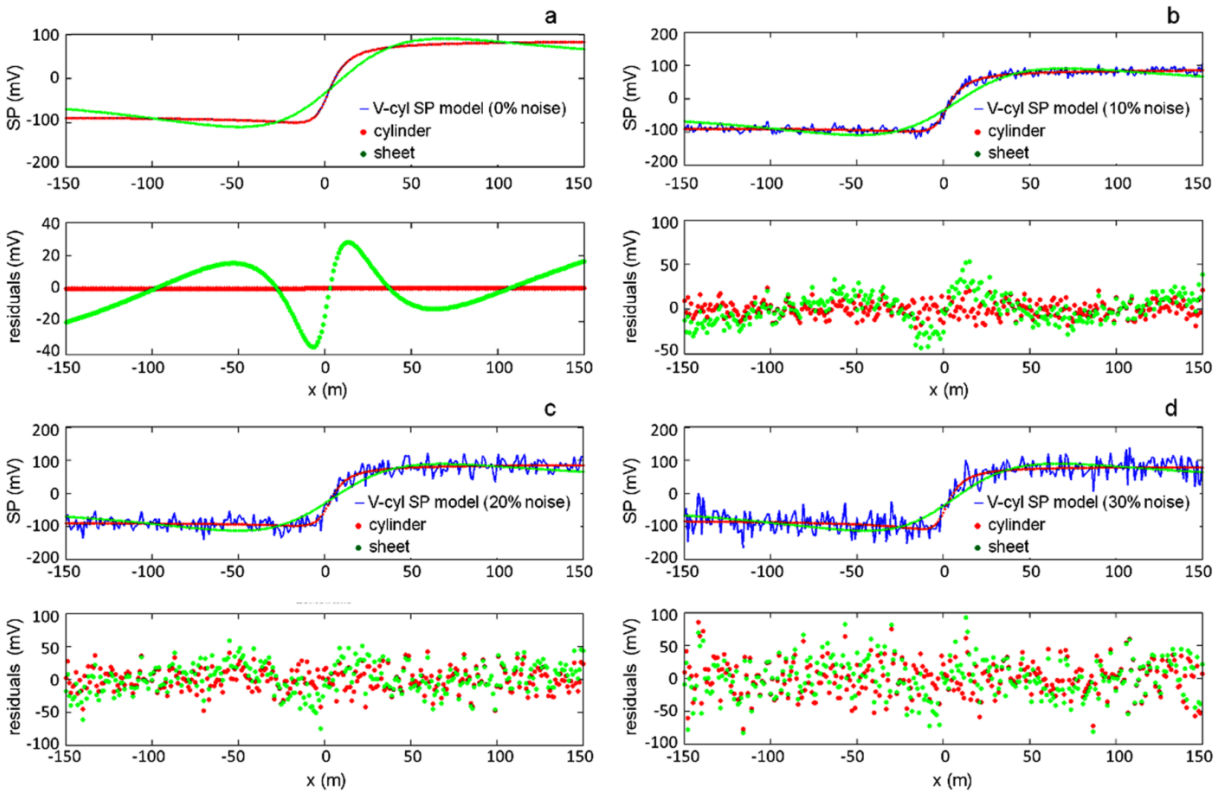

Figure 2.15 GPA inversion results of synthetic SP anomalies due to a vertical cylinder with different level of random noise. Upper panels of a-d: comparison between synthetic SP curve (blue continuous line) and curves calculated by using eq. (2.3) (red dotted line) and eq. (2.4) (green dotted line) in the objective function eq. (2.13), with 0% (a), 10% (b), 20% (c) and 30 % (d) of random noise. Lower panels of a-d: differences between synthetic and calculated curves shown in the corresponding upper panels.

SP anomalies due to inclined sheet

The synthetic SP values, V_{obs}, due to an inclined sheet-like source have been calculated by using eq. (2.4) with a = 5.0. As for the previous cases, the GPA was applied to the synthetic SP data by using the two forward functions given by eq. (2.3) and eq. (2.4) in the objective function expressed by eq. (2.13). In particular, the use of eq. (2.3) in the global optimization process has provided a shape factor value p = 1.0, which indicates that a horizontal cylinder could describe a possible anomaly source. The results of the performed analysis are shown in Fig. 2.16 and Table 2.11. As for the horizontal cylinder example (Fig. 2.14), the analysis shows that both calculated curves well overlap the synthetic ones for all the considered synthetic SP curves (upper panels of Figs. 2.16a-d), as well as the residuals distributions (lower panels of Figs. 2.16a-d) are able to

discriminate the actual source model only in the case of low-noise data. In fact, in presence of noise larger than 20%, the differences between synthetic and calculated data by using in the objective function the true source model (red dotted line) and a different source model (green dotted line) are comparable.

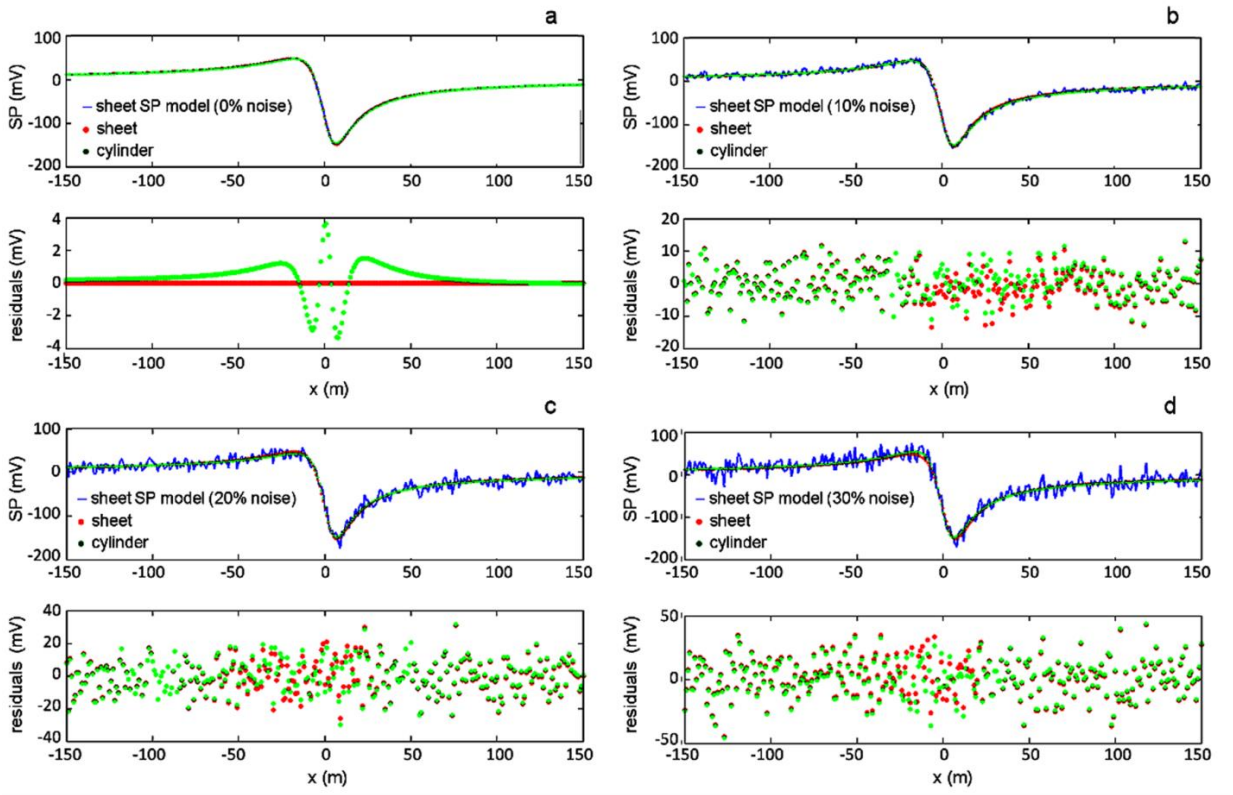

Figure 2.16 GPA inversion results of synthetic SP anomalies due to an inclined sheet with different level of random noise. Upper panels of a-d: comparison between synthetic SP curve (blue continuous line) and curves calculated by using eq. (2.4) (red dotted line) and eq. (2.3) (green dotted line) in the objective function eq. (2.13), with 0% (a), 10% (b), 20% (c) and 30 % (d) of random noise. Lower panels of a-d: differences between synthetic and calculated curves shown in the corresponding upper panels.

Source model	Forward function	Random noise (%)	K (mVm)	x_0 (m)	z_0 (m)	θ (°)	p or a (m)	RMS
Sphere	eq. (2)	0	100.0	-6.4×10^{-6}	10.0	30.0	p = 1.5	8.6×10^{-9}
		10	121.1	-0.1	10.2	30.3	1.5	0.01
		20	148.9	0.0	10.9	28.4	1.5	0.03
		30	226.7	0.4	10.8	27.2	1.6	0.04
	eq. (3)	0	2.9	-1.6	0.4	53.5	a = 5.7	0.02
		10	2.9	-1.5	0.4	52.6	5.8	0.03
		20	2.8	-1.8	0.4	54.6	5.9	0.04
		30	2.9	-1.8	0.4	54.9	5.8	0.05
Horizontal cylinder	eq. (2)	0	100.0	-6.1×10^{-7}	10.0	30.0	p = 1.0	7.0×10^{-9}
		10	97.9	-0.2	9.8	31.4	1.0	0.2
		20	127.5	-0.2	11.1	28.4	1.0	0.5
		30	118.2	0.6	10.3	27.4	1.0	0.8
	eq. (3)	0	16.4	0.1	1.5	29.9	a = 10.0	4.4×10^{-3}
		10	15.8	0.1	1.6	29.2	10.1	0.3
		20	16.1	-0.1	1.6	30.6	10.3	0.5
		30	16.7	-0.4	1.5	31.6	10.1	0.7
Vertical cylinder	eq. (2)	0	100.0	-4.8×10^{-8}	10.0	30.0	p = 0.5	9.6×10^{-9}
		10	96.5	-0.2	9.6	29.5	0.5	8.5
		20	96.9	1.1	9.2	27.4	0.5	17.3
		30	119.0	-0.4	8.9	34.8	0.5	26.4
	eq. (3)	0	1094.1	4.2	58.9	5.5	a = 2.7	13.6
		10	1153.6	4.9	59.2	5.6	2.6	16.1
		20	1067.0	2.0	58.4	7.0	2.8	22.3
		30	1342.2	4.0	55.5	6.7	2.1	26.1
Inclined sheet	eq. (3)	0	100.0	-1.3×10^{-8}	10.0	30.0	a = 5.0	6.8×10^{-7}
		10	106.3	0.2	9.9	30.3	4.6	4.9
		20	116.7	0.5	10.0	31.0	4.3	9.2
		30	93.9	0.3	10.2	30.3	5.5	13.9
	eq. (2)	0	2076.2	0.7	10.5	30.8	p = 1.0	0.9
		10	2197.1	0.6	10.8	30.8	1.0	4.8
		20	1484.9	1.7	9.5	35.0	1.0	10.0
		30	1843.9	0.4	9.9	28.3	1.0	14.6

Table 2.11 Source parameters obtained by applying the GPA with different forward functions in the objective function of eq. (2.13) to the SP synthetic data coming from: sphere, horizontal cylinder, vertical cylinder and inclined sheet. In the last column is reported the root-mean square (RMS) error provided by the Genetic-Price inversion algorithm.

2.2.3.2 Application to field data

The proposed GPA approach for the inversion of SP data has been applied to different examples of field datasets taken from the published literature (Di Maio et al., 2016b). For the sake of brevity, in the following the application to the Bavarian woods SP field data (see Section 2.2.2.2 and Fig. 2.17a) is shown.

The two forward functions given by eqs. (2.3) and (2.4) have been used in the objective function of eq. (2.13). Figure 2.17a shows the comparison between the experimental curve (blue line) and the two curves (red and green dotted lines) reconstructed with the two sets of parameters provided by the inversion procedure and reported in Table 2.12. As it can be seen in Fig. 2.17a, the inversion results indicate that both horizontal cylinder and inclined sheet source models well approximate the observed field data. Anyway, the residual distributions of Fig. 2.17b show that the residuals related to the horizontal cylinder-type source are generally lower than those observed for the inclined sheet model. In addition, as clearly emerges from Table 2.12, the set of parameters obtained for the horizontal cylinder model is in very good agreement with those provided by previous studies. It is worth noting that, as for all the analyzed synthetic SP data, a significant variation on the *K* parameter is observed.

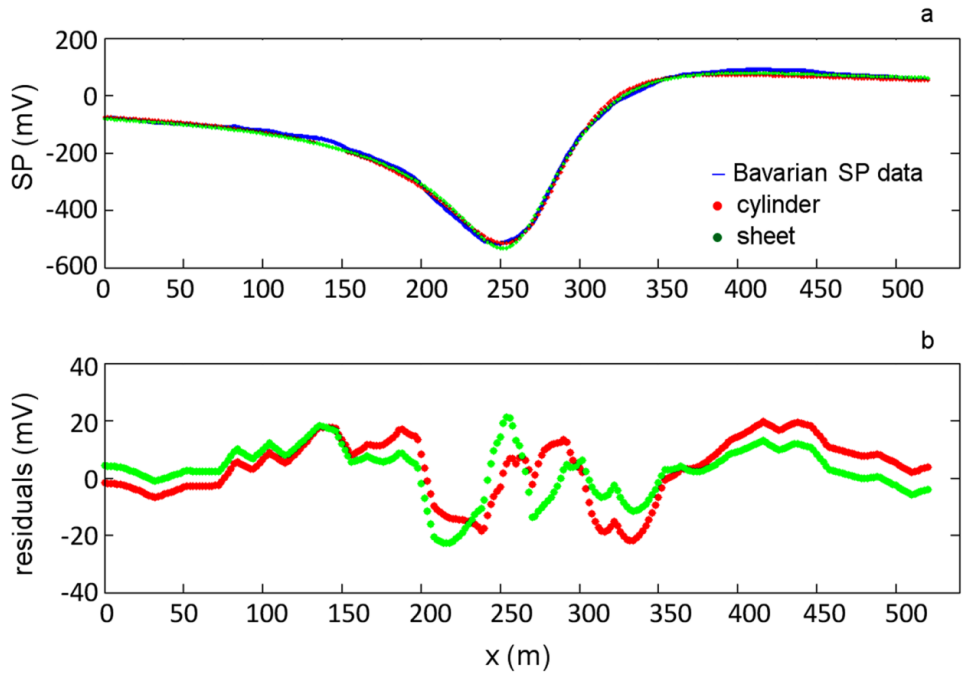

Figure 2.17 GPA inversion results of Bavarian woods SP anomaly data. (a) Comparison between observed SP curve (blue line) and curves calculated by using horizontal cylinder (red dotted line) and inclined sheet (green dotted line) as forward functions in eq. (2.13). (b) Differences between observed and calculated data shown in (a).

Methods	p or a (m)	K (mVm)	x_0 (m)	z_0 (m)	θ (°)
Higher derivative analysis (Abdelrahman et al., 2003)	p = 0.91	2020.0	322.0	49.3	-55.7
Least square inversion (Essa et al., 2008)	p = 1.0	30608.7	-	47.7	-51.2
Least square inversion (Essa, 2011)	p = 1.0	27212.70	-	46.59	-59.04
Global optimization (Göktürkler and Balkaya, 2012)	p = 0.97 (Genetic Algorithm) p = 1.02 (Particle Swarm Opt.) p = 0.99 (Simulated Annealing)	21272.91 33343.87 26257.42	268.79 269.88 269.17	45.03 47.59 45.99	- 51.29 - 48.60 - 49.98
Integrated spectral and tomographic approach (Di Maio et al., 2016a)	p = 1.0	25000.00	265.91	44.90	- 59.52
Genetic-Price algorithm (Di Maio et al., 2016b)	p = 1.0 a = 31.0	39951.67 -230.00	271.10 278.00	49.50 49.00	-47.30 -46.00

Table 2.12 Shape (*p or a*) and parameters (*K*, x_0, z_0, θ) of the source model of the Bavarian woods SP anomaly data (Germany) provided by different interpretation methods. The last two rows report the values obtained by the present study.

2.3 New modeling approaches for simulation of contaminant propagation

The transport mechanisms of a solute dissolved in water are essentially two: diffusion and advection (or convection). The first is related to the presence of solute concentration gradients and determines a movement from areas with the highest concentration to areas of lower concentration. Such a transport mechanism, which predominates in the low-permeability materials, occurs even when the groundwater is not affected by any flow. The advection occurs when the water flow transports the solutes dissolved in water. Since water moves along the direction of flow at different speeds due to differences in grain size, the solute plume spreads both parallel and transversely to the flow direction. That diffusion, linked to the different dimensions and provisions of the grains, is indicated as longitudinal dispersion (when parallel to the flow direction) or transverse dispersion (when perpendicular to the flow direction). The differential equation that describes the movement of a contaminant through a porous uniform

medium taking into account the mechanisms of diffusion, advection and dispersion is the so-called advection-dispersion equation:

$$\left[\frac{\partial}{\partial x}\left(D_x\frac{\partial C}{\partial x}\right)+\frac{\partial}{\partial y}\left(D_y\frac{\partial C}{\partial y}\right)+\frac{\partial}{\partial z}\left(D_z\frac{\partial C}{\partial z}\right)\right]-\left[\frac{\partial}{\partial x}\left(v_x C\right)+\frac{\partial}{\partial y}\left(v_y C\right)+\frac{\partial}{\partial z}\left(v_z C\right)\right]=\frac{\partial C}{\partial t},$$

where D_x, D_y and D_z are the hydrodynamic dispersion coefficients, v_x, v_y, v_z are the flow velocity components and C is the concentration of the pollutant. This partial differential equation can be solved by analytical and numerical methods. Analytical methods have been developed for many different initial conditions and boundary conditions (Ogata and Banks, 1961; Ogata, 1970; Bear 1972). These methods are limited by the simplicity of the geometry to be used and the required soil homogeneity. Conversely, the numerical methods have proven to be the most useful for practical purposes being able to find solutions to problems of increased complexity. They are essentially based on Finite Difference (or Finite Element) methods. A review of the most quoted numerical methods for the solution of the advection-dispersion equation is that of Bear and Verruijt (1987).

Since the eighties, several stochastic models for the study of solute transport were also developed (Gelhar, 1986; Neuman et al., 1987; Dagan, 1988). The stochastic models, rather than assigning single values of the input parameters are referred to a given uncertainty, considering, for example, not more individual values of hydraulic conductivity, but distributions of hydraulic conductivity values characterized by a certain mean value and a given variance, which measures the degree of heterogeneity of the aquifer under consideration. These models, always based on the advection-dispersion equation, find out the motion of the center of mass of the solute and the second moment of the distribution, which gives information on the fate of the solute plume. For the simplest cases, i.e. when all the nonlinear terms arising from the deviation of the solute particles from the average trajectory are neglected, analytical solutions for the above mentioned physical quantities are obtained, which provide asymptotic values for the longitudinal dispersion with the length of the considered flow (Dagan, 1988).

From the late eighties, in addition to the above mentioned models, fractal geometry concepts have also been introduced to describe the dispersion mechanisms (Tyler and Wheatcraft, 1988; Neuman and Zhang, 1990). The path taken by a particle of water in a porous medium is usually not straight and is, generally, longer than the distance in a straight line between the initial and final points of the path. This phenomenon is also known as tortuosity. If the tortuosity increases with the length of the flow pathway, the path taken by the water particle (or solute), called *streamtube*, can be considered a fractal way. In fractal geometry, the length of any part, x_f, of the streamtube is equal to $x_f = \eta^{1-f} x_s$, where x_s is the distance in a straight line between the two considered points, η is the unit of measure (typically the average radius of pore) and f is the fractal dimension. Since in a real aquifer the water particle (or solute) will follow one fractal streamtube, but on which, among the many possible fractal paths, there is uncertainty, it is possible to take into account many possible fractal configurations and, then, calculate the average and the variance. In particular, one has that var $(x_f) = 2D_m x_s$, where the dispersion coefficient D_m is a function of the fractal dimension, i.e. $D_m = 0.5$ var $(\eta^{1-f} x_s^{f-1})$. From the fractal analysis presented by Neuman and Zhang (1990), which has collected a number of site and laboratory data for scale lengths less than 3500 m, the longitudinal dispersion coefficient, α_m, is found to be proportional to the length x_s^f with fractal exponent f = 1.46. Subsequent studies (Xu and Eckstein, 1995) over larger flow distances have determined fractal exponent values greater than 2.

Ever since the end of the eighties, a different approach based on the use of the so-called cellular automata (CA) has been proposed for the study of diffusion phenomena (Frisch et al., 1986; Wolfram, 1986; Toffoli, 1987). In this case, the system under study is described by a discrete number of particles that move in a lattice space and interact according to specific dynamic laws that regulate the system at macroscopic scale and are obtained by averaging over a large number of particles. This description of the system can be considered "more microscopic"

of the equations in the continuous, such as the spread or the Navier-Stokes equations. In the latter case, indeed, macroscopic variables, such as the concentrations or the pressure, are themselves the result of an underlying discrete dynamics, which is, instead, directly described by the cellular automata. Two of the most cited review papers, that describe the different approaches to the study of the movement of fluids and contaminants in porous media and include cellular automata models, are Sahimi (1993) and Jennings and Manocha (1994). A significant contribution to the modeling of reaction-diffusion phenomena through cellular automata was also provided by Bandini and Simone (1996) and Bandini et al. (2001), who developed a new approach for the explicit description and simulation of the chemical reactions and movement of particles in a porous medium. According to their method, each cell is characterized by a variable identity, which defines its nature (soil, water or vacuum), and is divided into four parts to which a given number of contaminant particles is assigned. The system's evolution rules are classified in terms of reaction, balancing and diffusion (movement) rules of the contaminant and involve only certain types of cells (e.g., the contaminant particles are assigned only to cells that describe the soil and have at least one neighbouring cell empty, and the reactions occur only between the soil cells or between a soil cell and a water cell, in such a way as to ensure that the contaminant is always distributed on the surface of the grains). With this automaton model the probability of percolation of pesticides for different types of soils (i.e. grains of different sizes) and of water infiltration conditions (i.e. more or less intense rain or more or less continuous in time) was studied, thus providing indications on the most dangerous scenarios (in terms of soil types, weather conditions and so on) due to the application of a given pesticide.

Unlike the previously described approaches, at the end of the nineties Di Gregorio et al. (1999), adopting a different approach, applied the cellular automata to the study of complex environmental phenomena, such as bioremediation of contaminated land. According to their method, in fact, the cells are considered as portions of space that include multiple pores: to each cell, therefore, is assigned a space of states, which is the Cartesian product of more different

subspaces that describe the different ingredients of the problem, such as the water content, the concentration of a given chemical agent, the density of a given type of bacteria, and so on. While some of these variables, that belong to the three identified subspaces (i.e. the descriptive level of the flow dynamics, the chemistry of the solute and the biomass interaction with the environment), are usually considered to be continuous, in the model proposed by Di Gregorio et al. (1999) the range of the allowed values is limited to a discrete set. This model has proven to be able to reproduce the laboratory test results in case of phenol contamination, which, in addition to providing a significant example of application of the cellular automata to problems at a high social and economic impact, demonstrates how the research in the field of modeling can significantly improve the effectiveness of decontamination measures.

2.3.1 A cellular automaton for fluid infiltration modeling

Inspired by the modeling of Bandini et al. (2001), the first simple cellular automaton that has been developed in the present work to simulate the diffusion-dispersion processes of a contaminant consists of a grid of square cells that can be in two states: *S*, if they represent the soil, and *E*, if they represent empty spaces. Each cell has four neighbouring first cells (up, down, left and right), except the cells that are on the edge of the grid that have only three neighbouring, due to the choice of using open boundary conditions.

The initial configuration of the system, where the state values *S* or *E* are assigned to the cells, is given by using a random number generator function. A crucial parameter of the model is the filling factor *n*, which is related to the porosity of the system. The properties of the system are studied by collecting statistics at least on about one million of different initial configurations. For every initial configuration, the pollutant diffusion takes place considering all the pores filled with water (saturated condition, i.e. state of E = W state) and entering the contaminant in a W cell of the top of the grid, which is as much as possible away from both the edges. The process of

diffusion of the contaminant c_i (where i is the index of the cell) is simulated on the basis of the following rules:

if $Sc_{i,down}$ = W, the contaminant moves downward;

if $Sc_{i,down}$ = S, $Sc_{i,left}$ = S and $Sc_{i,right}$ = W, the contaminant moves to the right;

if $Sc_{i,down}$ = S, $Sc_{i,right}$ = S and $Sc_{i,left}$ = W, the contaminant moves to the left;

if $Sc_{i,down}$ = S, $Sc_{i,right}$ = W and $Sc_{i,left}$ = W, the contaminant has the same probability to move to the right or the left;

if $Sc_{i,down}$ = S, $Sc_{i,right}$ = S and $Sc_{i,left}$ = S, the contaminant stops.

Figure 2.18 shows, as an example, the configuration of a system of 128 x128 cells in which the contaminant has moved down to 37 cells, i.e. about 30% of the depth of the considered soil layer, with porosity n = 0.60. As it can be seen from the grid, the contaminant stops when it is surrounded by blue cells that describe the soil. This occurs simply because the simplest case of diffusion-dispersion process of the contaminant has been modelled, i.e. the contaminant is not absorbed by the soil, but it moves only through the filled water pores.

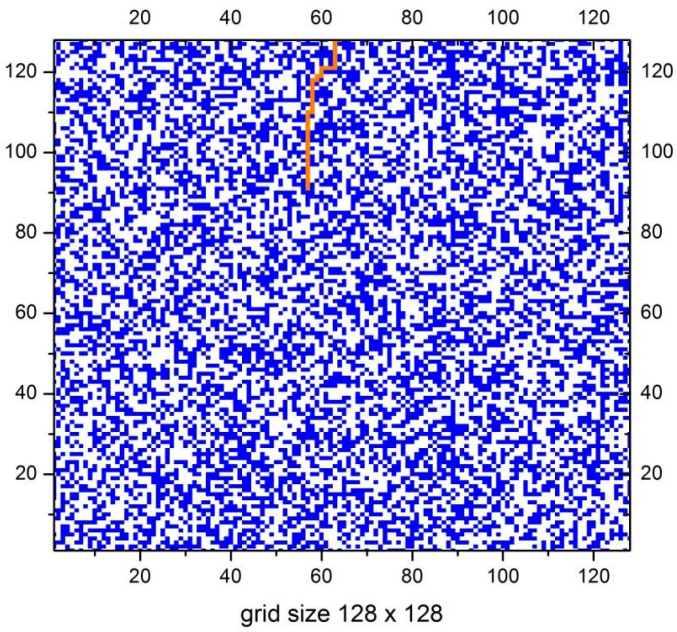

Figure 2.18 Output of the proposed CA model simulation for a grid of 128 x 128 cells. The blue cells describe the soil, the white cells describe empty (or water-filled) cells, the orange cells indicate the cells crossed by the contaminant.

In Figure 2.19, the probability, *p(L)*, that the contaminant moves along a distance *L* from the top of the grid is shown. As it can be seen, the performance of this function does not depend on the size of the system. The only effect related to the finite size of the system is the peak observed for smaller systems that corresponds to the contaminant percolation, which is simply explained by the number of configurations for which the pollutant would continue its downward path if given the chance. In the case of a 128x128 grid, with a statistic of 10^6 configurations, it is not observed contaminant percolation, therefore an analysis of a greater number of configurations is required to better define the shape of the probability distribution. However, from the analysis carried out on 32x32 and 64x64 grids, it is possible to infer that the shape of the probability distribution in the case of 128x128 grid will be similar to the previous cases, while the probability values related to percolation phenomena will be obviously smaller.

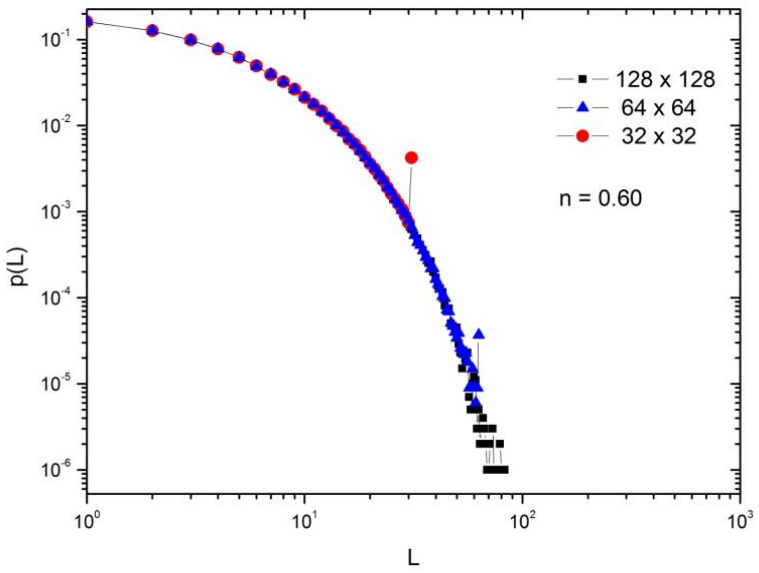

Figure 2.19 Probability distribution of the occurrence that the contaminant moves along a distance *L* as a function of *L*, by changing the system size.

To investigate the occurrence of characteristic times for given distances, the conditional probability of observing the contaminant at the time *t* and at distance *L* from the top of the grid has been calculated. As it can be seen in Figure 2.20, this probability shows a peak around a

characteristic time that can be interpreted as the average time taken by the contaminant to travel the given distance *L*. By increasing *L*, the peak decreases and moves to the right, this means that the probability that the contaminant reaches such greater distances is lower and that the travel times necessary to achieve these distances are greater.

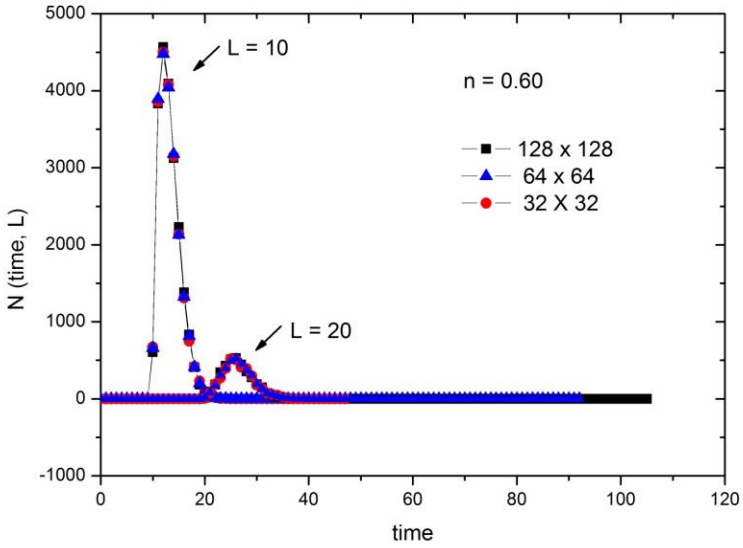

Figure 2.20 Number of configurations for which the contaminant covers the distance *L* from the top of the grid as a function of the travel time, for three different values of the grid size.

In Figure 2.21 the result of a systematic study carried out at varying the distance *L* for two different values of porosity is presented. As expected, the probabilities that the contaminant reaches a given distance *L* are greater in the case of more porous medium. In addition, the distributions are much more asymmetrical as the values of *L* decrease. This asymmetry indicates that for small values of *L* the contaminant travel time (measured as number of displacements of the contaminant from a cell to another) tends to match the distance of a straight line *L*, due to lesser chances of horizontal dispersion.

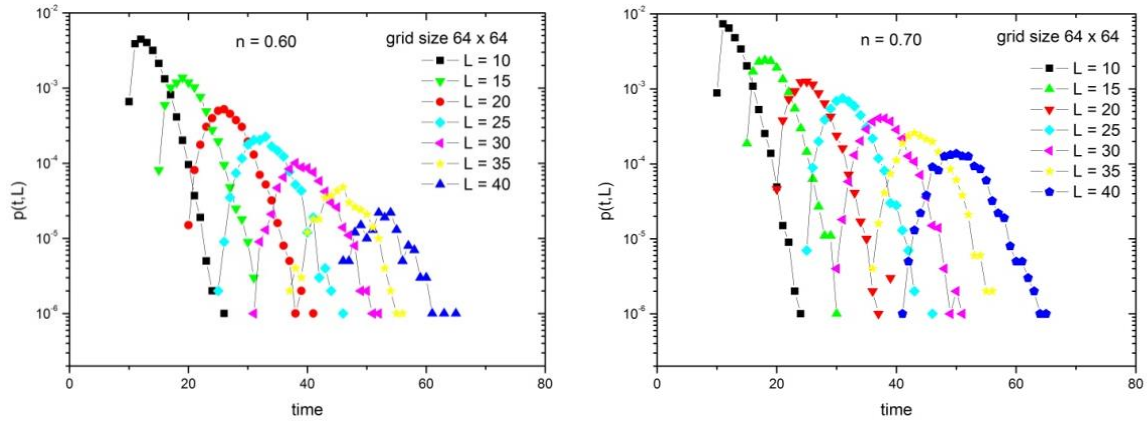

Figure 2.21 Probability that the contaminant reaches a distance *L* from the top of the grid as a function of the travel time for seven different values of *L* and two fixed values of porosity, n = 0.60 (left) and n = 0.70 (right).

If the times corresponding to the peaks of the probability distributions (Fig. 2.21) are reported as a function of the different distances *L*, the curves shown in Figure 2.22 are obtained, for three different values of porosity. As it can be seen, the relationship between the timing related to the probability of the peaks and the involved distances appears to be linear and, with good approximation, independent of the porosity value for small *L*.

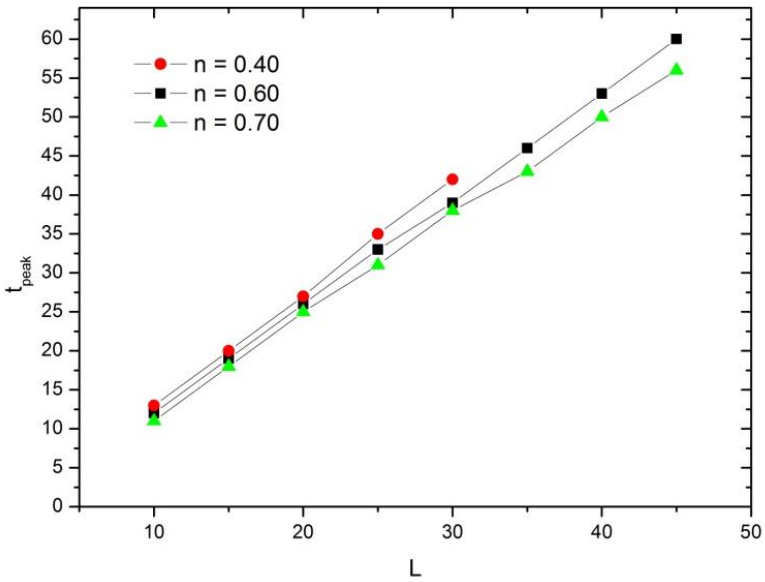

Figure 2.22 Times related to the peaks of the probability distributions shown in Fig. 2.21 according to the distance *L* traveled by the contaminant.

Moreover, if the maximum values of the probability distributions shown in Fig. 2.21 are plotted as a function of the distance *L*, the curves shown in Fig. 2.23 are obtained, for three different values of porosity. As is reasonable to expect, the probability that the contaminant travels along a given distance *L* increases with increasing porosity. It is interesting to note that the growth of such probability values with the porosity does not occur equally for small and large values of *L*. Indeed, in the inset of Fig. 2.23 the slope of the curve for the case L = 30 is greater than that corresponding to the case L = 10, which means that the effect of the porosity is higher the greater is the length of the considered distance.

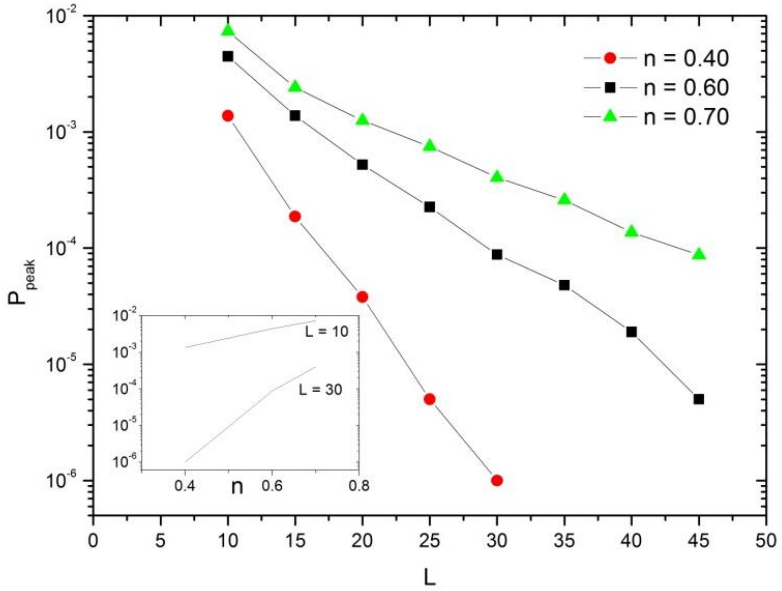

Figure 2.23 Maximum values of the probability distributions shown in Fig. 2.21 as a function of the distance *L* traveled by the contaminant. Inset: maximum values of the probability distributions shown in Fig. 2.21 as a function of porosity *n* for two different values of *L*.

Two-layer model

So far, a unique value of the fill factor of the cells has been chosen. Since such model parameter is directly related to the porosity of the soil, up to now the case of a single homogeneous layer has been considered. Therefore, the next step was to consider two layers characterized by different value of porosity and to study the effects of such discontinuity on the contaminant

propagation. Figure 2.24 shows, as an example, two models for which some of the results of the performed simulations are discussed below.

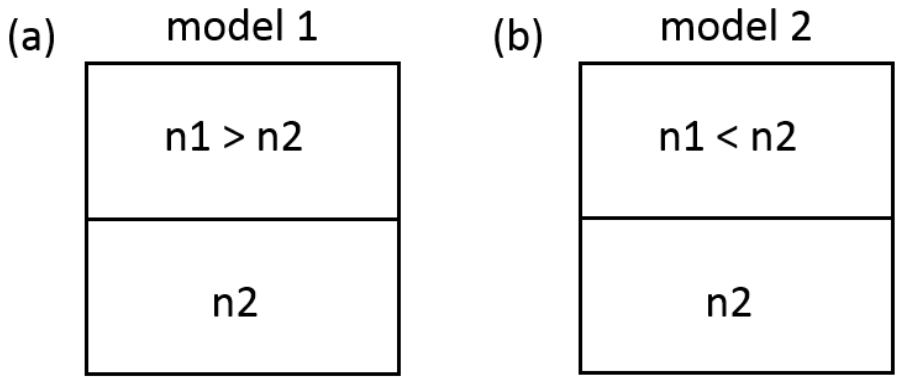

Figure 2.24 Two-layer models for the study of contaminant transport in a saturated porous medium. (a) More porous layer on the top; (b) more porous layer on the bottom.

In the first model (2.24a), the thickness, *d*, of the simulated soil is constituted by a first layer with porosity n_1 and thickness d_1 and a second less porous layer with a porosity value n_2 (= $n_1/2$) and, accordingly, a thickness $d_2 = d - d_1$. In Figure 2.25, it is reported, for this first type of model, the number of configurations for which the contaminant covers a distance equal to 34 cells of 64, for five different thicknesses of the first layer. As it can be observed in the plot of Figure 2.25, when the first layer has a thickness equal to 10% and 20% of the whole thickness *d*, the contaminant does not reach the distance *L* (on a statistical analysis of over a million of configurations). By growing the thickness of the first layer, d_1 = 30% d, a few configurations satisfying the required condition (L = 34) are observed, which appear to be characterized by a certain temporal spread and by the absence of a characteristic time. A further increase of the first layer thickness (e.g., first layer thickness equal to 40% and 50% of the entire thickness), causes, as it is reasonable to expect, an increase of the number of considered configurations and the distribution of such configurations assumes a bell-shaped curve, where the timing in

correspondence of the maximum values can be associated to average travel times of the contaminant to the considered distance *L*.

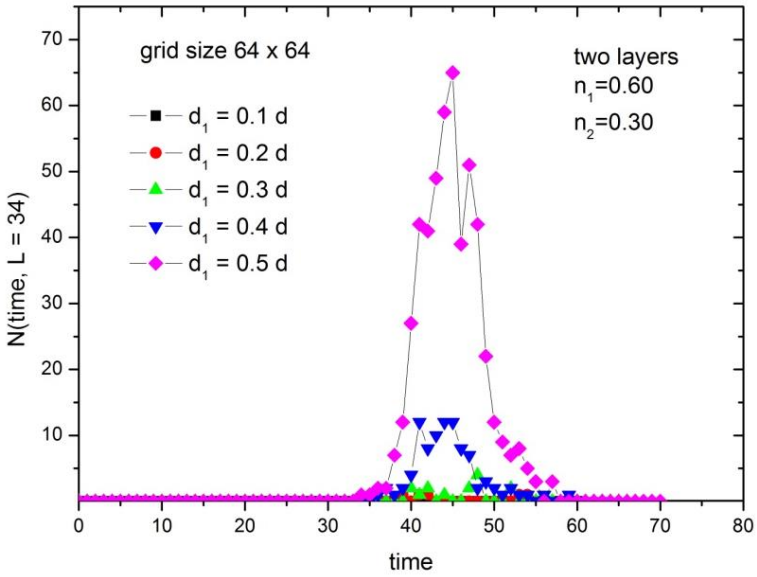

Figure 2.25 Number of configurations for which the contaminant covers a distance *L* from the top of the grid as a function of the travel time, for five different values of the thickness of the first layer, in the case $n_1 = 2n_2$.

In the second model (Fig. 2.24b), the porosity value attributed to the first layer is half of that attributed to the second layer ($n_1 = n_2/2$). As it can be observed in the plot of Figure 2.26, the scenario is reversed compared to the case of Figure 2.25. Only when the first layer thickness is smaller than that of the second layer (equal to 10%, 20% and 30% of the entire thickness *d*), the contaminant reaches the fixed distance *L* (on a statistical analysis of more than a million of configurations). In particular, the smaller is the thickness of the first layer, more peaked is the distribution of the number of considered configurations and better defined is the average travel time of the contaminant.

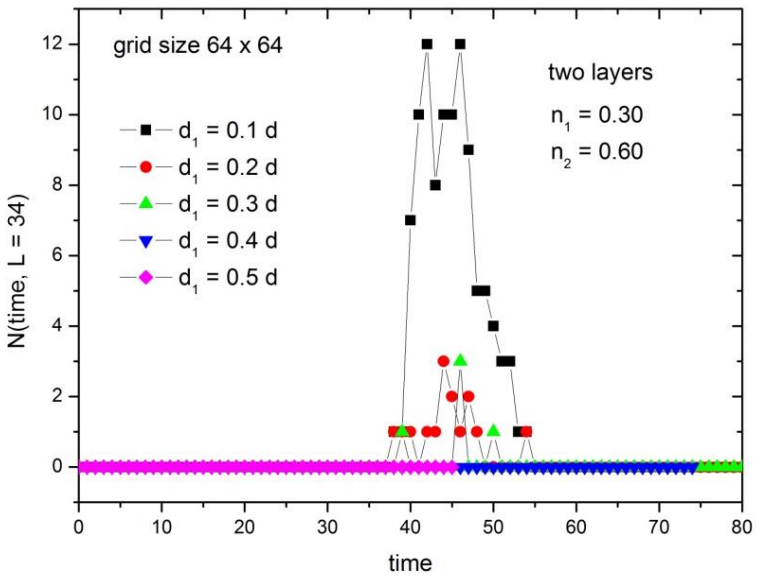

Figure 2.26 Number of configurations for which the contaminant covers a distance *L* from the top of the grid as a function of the travel time, for five different values of the thickness of the first layer, in the case $n_1 = n_2/2$.

To conclude, it is found that the probability distributions for the analyzed two-layer models are different, as expected. Indeed, there is not a complete symmetry in the two considered cases because the infiltration process is favoured when the most porous layer is the shallowest one. Finally, it is worth noting that if more than two layers are taken into account, many different distributions of porosity values are possible, which will affect the infiltration rate in different ways. Thus, a systematic study of the CA model can allow the definition of the most dangerous scenarios in terms of the highest infiltration rate for each given distribution of porosity values. An application of the three-layer model to a real scenario is analyzed at the end of Chapter 4, while the detailed study of the multiple-layer model is currently in progress.

2.3.2 A cellular automaton for fluid propagation in unsaturated zone

In addition to the previous study, a different cellular automaton model has been developed with the aim to simulate diffusion-dispersion phenomena of the pollutant in the unsaturated zone. In this case, the contaminant is supposed to be approximately in the middle of the grid and its

propagation is essentially controlled by the local porosity and the contaminant concentration gradients. To analyze the properties of the model, first a two-dimensional rectangular grid of M x L cells is used to describe a vertical section of a homogeneous soil. The state of each cell, *S*, indexed by *i*, with $1 < i <$ ML, is defined by the values of two parameters: $S(i) = \langle c; n \rangle$, where *c* is the percentage of local concentration of contaminant and *n* is the local porosity value. In the initial configuration, a rectangular contaminated area is approximately in the middle of the grid, with values of the local concentration equal to the threshold value for diffusion, $c(i) = c_{th}$. The porosity is assumed to be a uniform value $n = 0.5$. A schematic representation of the model in the initial configuration is represented in Fig. 2.27.

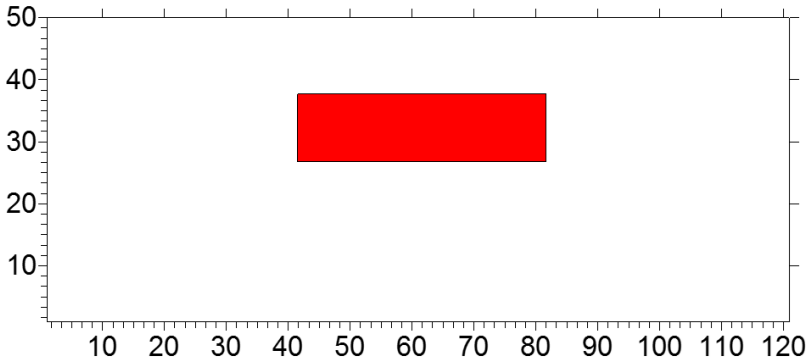

Figure 2.27 Schematic representation of the model grid that shows the initial configuration of the contaminant.

Taking inspiration from the Self-Organized-Criticality theory (Bak et al., 1989), the dynamics of the CA model is defined by the following rule:

$$c_i \geq c_{th} \rightarrow \begin{cases} c_{nn(i)}(t + \Delta t) = c_{nn(i)}(t) + f_{nn(i)} c_i(t) \\ c_i = c_{\min} \end{cases} , \qquad (2.14)$$

where *nn*(i) denotes the four neighbor sites of the over-contaminated site *i* (i.e. *nn*(*i*) = up, down, left, right). The eq. (2.14) is a relaxation rule: when the cell *i* is over-contaminated (i.e. $c(i) > c_{th} = 1$), the contaminant propagates into neighbor sites and the value of contaminant concentration

of the cell i is set to the minimum concentration value c_{min}. If the contaminant concentration of neighbor sites is larger than c_{th}, the contaminant continues to propagate by eq. (2.14), and so on. The relaxation chain process continues up to when the difference between the contaminant concentration between two adjacent cells is larger than the local concentration gradient threshold Δc_{th}. The values of the transfer coefficients f_{nn} control the diffusion in the horizontal and vertical direction and the results of a systematic study performed by varying their values is shown below. For each simulation, the threshold values of the contaminant concentration and the concentration gradient are kept fixed. As it can be seen from Fig. 2.28, the model is able to simulate the propagation of the contaminant and to reproduce the formation of areas with different contaminant concentration, which are the effect of a not-uniform diffusion in the soil. In this simple case (with uniform porosity), the anisotropic propagation can be ascribed to driving forces in the horizontal or vertical direction, while if different values of porosity are considered, it can be also related to inhomogeneity of the soil.

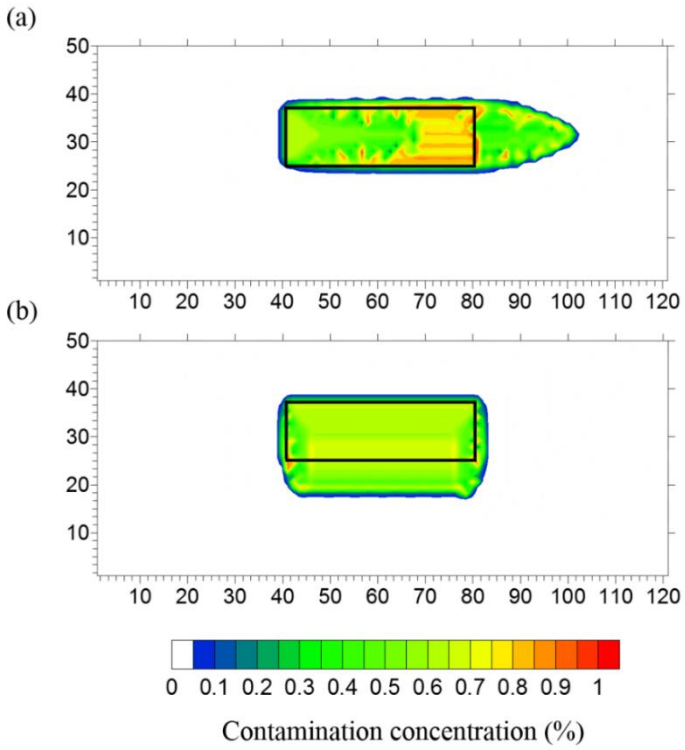

Figure 2.28 Final configuration of contaminant propagation obtained for values of ratios f_{up}/f_{down} = 1 and f_{left}/f_{right} = 0.33 (a), and f_{left}/ f_{right} = 1 and f_{up}/f_{down} = 0.33 (b), for fixed value of Δc_{th} = 0.01. Black box outlines the initial configuration of the model grid.

To delineate the most dangerous scenario, a study has been performed to analyze the maximum distance traveled by the contaminant by varying the values of the transfer coefficients f_{nn} in horizontal and vertical directions, keeping fixed the concentration gradient threshold Δc_{th} = 0.01. As it can be seen in Fig. 2.29a and b, the simulations show different results for asymmetric diffusion in the horizontal and vertical directions, respectively. As expected, the least dangerous scenario is found in the isotropic case when one has $f_{left}/f_{right} = f_{up}/f_{down} = 1$ and the contaminant travels a distance of a few cells in both directions. If anisotropy is increased, i.e. $f_{left} << f_{right}$ or $f_{up} << f_{down}$, the contaminant travels different distances, which are larger for the horizontal anisotropy case, favored by the rectangular shape of the initial configuration of the contaminant.

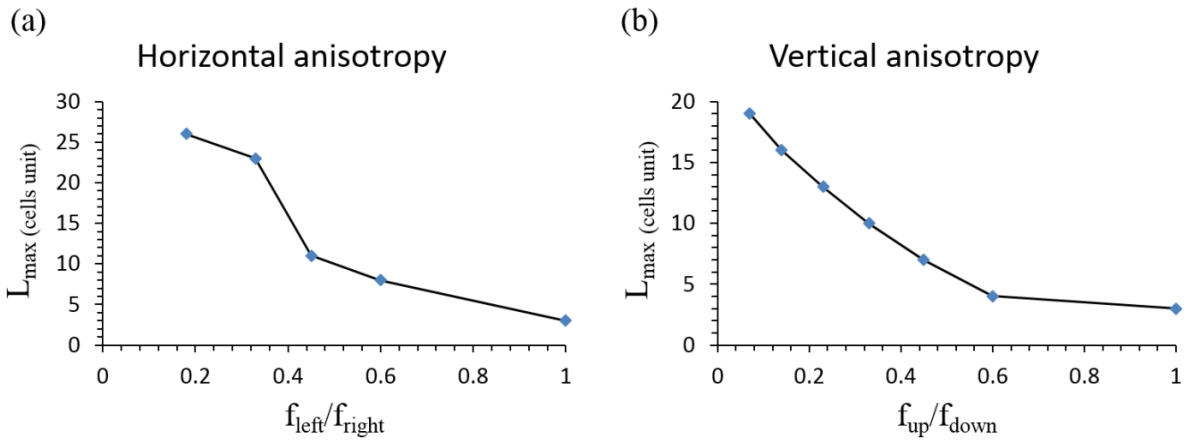

Figure 2.29 Maximum length traveled by the contaminant in the horizontal direction (a) and vertical direction (b) for different values of ratios f_{left}/f_{right} and f_{up}/f_{down}, keeping fixed Δc_{th} = 0.01.

Always with the aim to delineate the most dangerous scenario, a study has been performed by varying the values of local concentration gradient threshold Δc_{th}, which controls the ease of propagation of the contaminant in the soil. The larger the value of the threshold Δc_{th}, the more difficult the contaminant spreads. Simulations have been performed by considering different values of Δc_{th} in the range [0.001, 0.1], keeping fixed the values of the transfer coefficients. Specifically, such values have been chosen to characterize the most dangerous scenario, and,

therefore, they are those for which it has been found that the maximum distance traveled by the contaminant in both directions (see Fig. 2.29a and b). As it can be seen in Fig. 2.30, also in this case different behaviors are found for the analyzed cases of horizontal and vertical anisotropy. In particular, for the case $f_{up} << f_{down}$, the simulations show that small changes in the values of Δc_{th} around 0.05 can cause large variations in the maximum length traveled by the contaminant. However, even if Δc_{th} is set at the investigated minimum value (0.001), the contaminant does not reach the bottom of the grid, suggesting that only initial oversaturated conditions ($c(i) > c_{th}$) can achieve contaminant percolation.

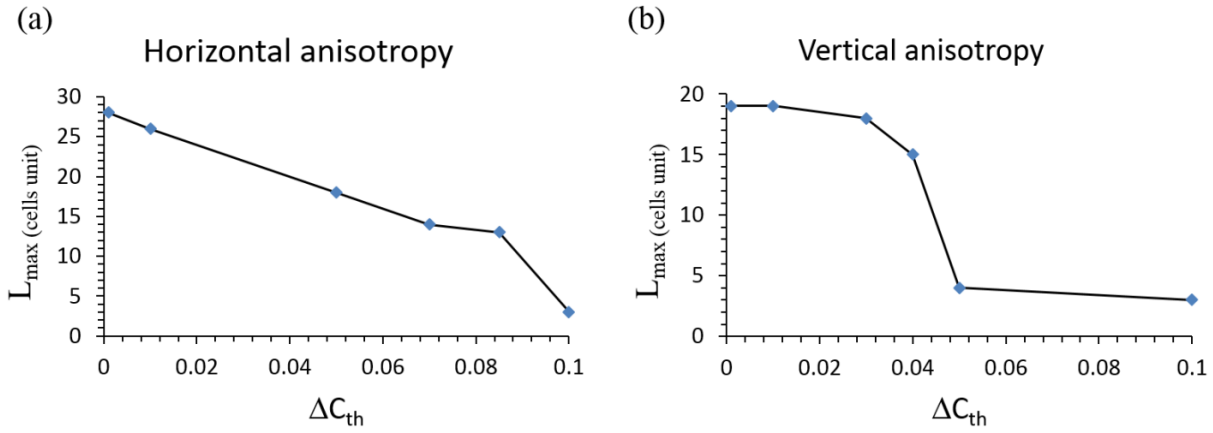

Figure 2.30 Maximum length traveled by the contaminant in the horizontal direction (a) and vertical direction (b) for different values of $\Delta c_{th} = 0.01$, keeping fixed the transfer coefficients ratios $f_{left}/f_{right} = 0.18$ and $f_{up}/f_{down} = 0.07$.

Summarizing, it is found that for the simple homogenous porous model, different behaviours characterize the contaminant propagation in horizontal and vertical directions, if an initial rectangular contaminated zone is considered. However, the model can describe also more complicated scenarios with different distributions of porosity values. As an application of such modeling, at the end of Chapter 3 a cellular automaton is developed in the attempt to simulate the contaminant propagation caused by olive oil mill wastes in soils characterized by three geo-electrical layers (see Chapter 3).

Chapter 3

Application of the proposed approaches for olive oil mill wastes contamination monitoring

3.1 Introduction

Olive oil production is one of the most important economic activity in the Mediterranean area. Greece holds the third place worldwide in production of olive oil after Spain and Italy (Beaufoy, 2001; Papadopoulos et al., 2014). Interestingly, the island of Crete contributes more than 30% of the total olive oil production in Greece. The production of olive oil generates a large volume of waste, known as olive oil mill wastes (OOMWs), which is mainly characterized by unpleasant smell, dark brown color, high organic fluid load (mainly phenols and polyphenols) and low concentration of inorganic compounds (e.g. potassium and phosphorus) (Kyriacou et al., 2005). Following the seasonal pattern of olive oil production, the waste is deposited every year from November to April and then letting it to evaporate during the summer months (May-October); once it has remained solid waste is dug out. Due to lack of proper regulation for deposition of OOMWs, these are generally disposed in poorly constructed shallow evaporation ponds, which often result into overflow or leakage of wastewater due to local geological conditions (permeable sediments and/or fractured bedrocks, shallow aquifers, etc.), hence increasing the potential for groundwater contamination and soil degradation. The high electrical conductivity is the main feature that make OOMWs detectable with geoelectrical methods (Papadopoulos and Chatziathanasiou, 2011), which, as illustrated in the Chapter 1, are increasingly used for mapping and monitoring organic plumes. Currently, the electrical resistivity tomography (ERT) has proved the most effective for delineating hydrocarbon plumes, and, in some instances, for

monitoring degradation processes (Atekwana and Slater, 2009; Atekwana et al., 2006; Heenan et al., 2015).

In the present study, time-lapse ERT and self-potential measurements repeated over time along the same profile are used to map and monitor the subsurface contamination caused by OOMWs in a test area. A first attempt has been made to model OOMWs transport by applying the inversion approaches proposed in the Chapter 2 on time varying SP data. Specifically, simple polarized source models have been employed to characterize the SP anomalous sources by using the three developed inversion methods based on high-resolution spectral analysis, tomographic approach and Genetic-Price algorithm, respectively. Moreover, two different numerical simulation models, based on finite-element modeling and cellular automata approach, respectively, have been developed to estimate the temporal and spatial distribution of the selected contaminant under unsaturated and saturated conditions.

3.2 Geological setting of the survey area

The waste site is located near the Keritis river (Fig. 3.1), the main river of Chania watershed (western Crete, Greece). The boarder area of the basin is covered by Quaternary (Pleistocene, Holocene) deposits and sediments (Miocene) that expand to NE, SE and SW of the Alikianos village situated in the south-western part of the western Crete. The study site (Fig. 3.1) is an open waste pond used for olive oil mill wastes deposition located in the Keritis river basin near Alikianos village. The area is mainly composed of alluvial deposits with variable hydraulic permeability, which mainly consist of loose sandy-clayed material, terra rossa (red clay soil), with rounded and angular pebbles in small internal basins, and alluvial mantle material (Kanta et al., 2013). As concerns the hydraulic conductivity of the alluvial formations, the in-situ geological (Nikolaidis and Karatzas, 2010) and geophysical measurements (Soupios et al., 2007c; Kanta et al., 2013) have found values of about 6.10^{-4} m/sec or 51,84 m/day.

Based on measurements acquired for more than 5 years from 97 observation points (boreholes and wells) over a broader study area, the mean depth of the groundwater table is about 11.4 m (minimum depth: 0.85 m; maximum depth: 12.2 m). According to Nikolaidis and Karatzas (2006), such a high variability of the groundwater table cannot be related to a phreatic aquifer under natural hydrostatic conditions. Indeed, the above authors hypothesize that the piezometric level dynamic describes both phreatic and confined aquifers, with the deeper karstic aquifer feeding the phreatic aquifer.

Figure 3.1 Aerial view of the study area (western Crete, Greece). The orange polygon defines the OOMW waste deposition pond located in the basin of the Keritis river (blue line). Small stream effecting the groundwater flow direction (blue dashed line). Contaminant flow direction is indicated by an arrowed white line (after Ntarlagiannis et al., 2016, modified).

3.3 Geophysical data analysis

The study site has been well characterized by different geophysical methods: time domain electromagnetics (Kanta et al., 2013); electrical resistivity tomography (Papadopoulos and Chatziathanasiou, 2011; Papadopoulos et al., 2014; Simyrdanis et al., 2016); spectral induced polarization (Kirmizakis et al., 2016; Ntarlagiannis et al., 2016); self-potential (Soupios and Karaoulis, 2015) and remote sensing imaging (Alexakis et al., 2016).

In particular, this work focuses on the analysis of time variations of electrical resistivity and self-potential data collected along a profile located close to the waste pond for detecting the organic contamination and estimating its time migration.

3.3.1 Time-lapse electrical resistivity tomography monitoring

To characterize the waste site, a 2D ERT survey along eleven profiles located around the pond (Fig. 3.2) was planned (Simyrdanis et al., 2016). Specifically, four long ERT lines were performed for large-scale characterization of the survey area, in particular three profiles cross the pond (yellow lines in Fig. 3.2b) and one profile is parallel to the river (brown line in Fig. 3.2b). Moreover, seven relatively short ERT lines were laid out horizontally and vertically around the pond (green and red lines in Fig. 3.2a) for obtaining detailed information on the geometrical and physical properties of the waste disposal. As only the Line 1 (red line in Fig. 3.2a) was used for continuous monitoring of the waste pond by electrical resistivity and self-potential measurements, the present study has been focused on the analysis and interpretation of the time variations of resistivity and self-potential data observed along the Line 1.

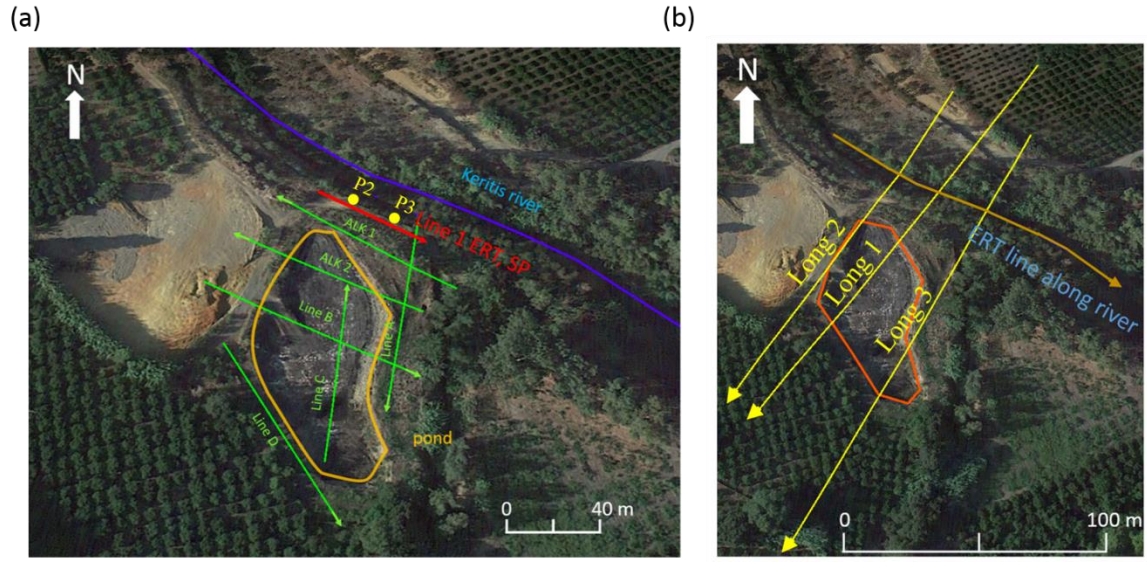

Figure 3.2 (a) Distribution of short ERT measurement lines. P2 and P3 indicate the location of sampling pits. (b) long ERT lines (yellow lines) and ERT line passing through river (brown color) (modified after Simyrdanis et al., 2016).

Time-lapse ERT measurements along the Line 1 were repeatedly collected for a period of more than one year, from June 2013 to March 2015, utilizing a single-channel resistivity meter with the Dipole-Dipole and Wenner-Schlumberger array configuration to achieve the optimum spatial and in depth resolution. The 2D and 4D inversion of the apparent resistivity (ERT) pseudosections was performed by using the DC2DPro program (Kim et al., 2009), which is based on a 2.5D finite element routine to solve the forward resistivity problem and an iterative least squares algorithm with Active Constrain Balancing (ACB) for reconstructing the subsurface resistivity models (Yi et al., 2003).

Figures 3.3 and 3.4 show, respectively, the results of the static inversion of the ERT data collected at specific dates and the resistivity ratio between sequential time phases provided by the 4D data inversion (Rani et al., 2016b). The images of both figures reflect whole olive oil production cycles, i.e. olive harvest, oil yield and OOMW deposition. For all the inverted 2D data sets, a general RMS error less than 3% was attained. The relatively higher errors obtained for the summer profiles (less than 7%) are likely due to the top dry layer.

In particular, the individual inversion models of Fig. 3.3, in addition to provide geo-structural information of the investigated subsoil, highlight the variations of its physical state likely related to the cycle of the OOMW in the deposition pond. The subsurface structure can be approximated as a three-layer earth. The upper resistive layer (more than 500 Ωm) extends down to about 3 m b.g.l. and, based on the results of the whole ERT prospecting performed in the survey area (Simyrdanis et al., 2016), can be correlated with sand and gravel materials. This layer, which appears essentially homogeneous in the winter profiles, i.e. during the deposition period, loses its homogeneity during the evaporation period in summer months. Such a hypothesis seems to be confirmed by the large variations in the resistivity value distribution observed for the second layer during the whole monitoring period (June 2013-March 2015). In fact, this layer that, according to the large-scale ERT survey, can be ascribable to sandy-clayed material, exhibits in the periods from June to September very low resistivity values (15-30 Ωm) mainly in the western portion of the profile (see Fig. 3.3), which is closer to the waste pond than the eastern part. Thus, the low conductive anomalies cyclically observed within the studied section might indicate that the contaminant is following a horizontal pathway in the north direction, i.e. towards the Keritis river. This pattern is likely induced by the dynamic conditions of the small stream indicated in Fig. 3.1. In addition, the in-depth development of such conductive anomalies, which sometimes reach the maximum exploration depth, suggests a possible infiltration of the contaminant within the third layer (i.e. the bedrock). The latter is generally visible at depths of about 8 m from the ground level and is characterized by resistivity values greater than 200 Ωm (see Fig. 3.3) attributable to alluvial sediments composed of sand, gravels, pebbles and clays. Depth and resistivity values observed for the bedrock are in very good agreement with those provided by the long ERT profiles shown in Fig. 3.2 (Simyrdanis et al., 2016). Finally, it is worth to note that the rather complex morphology of the bedrock, as well as the large variations of its physical conditions observed during the whole monitoring period

and attributed to contaminant infiltration, would confirm the presence of fault/fracture zones highlighted by the above mentioned large-scale ERT prospecting.

Figure 3.4 shows the resistivity ratio between sequential time phases (T2/T1, T3/T2, etc.) resulted by the 4D inversion of the ERT profiles acquired along the Line 1 of Fig. 3.2a during the whole monitoring period. The white colour indicates areas where no resistivity changes are observed, whilst the blue and red colours indicate areas subjected to decrease and increase of resistivity values, respectively. The resistivity decrease observed for the top layer (about 3 m thick) during the winter periods, i.e. in the time phase T4/T3 and T12/T11, could be justified by a soil moisture increase due to intensive rainfall in that season. Whilst, the strong decrease in the resistivity ratio that is observed in the deeper parts of the investigated section during the 2013 summer season (i.e. for the time phases T2/T1 and T3/T2), and to a much lesser extent during the 2014 summer season (i.e. for the time phases T10/T9, T11/T10 and T12/T11), is likely due to in-depth infiltration of the conductive wastes as previously highlighted by the static ERT data inversion. As expected, no significant changes in the resistivity ratios are observed in the later winter/spring period, i.e. during the filling of the pond.

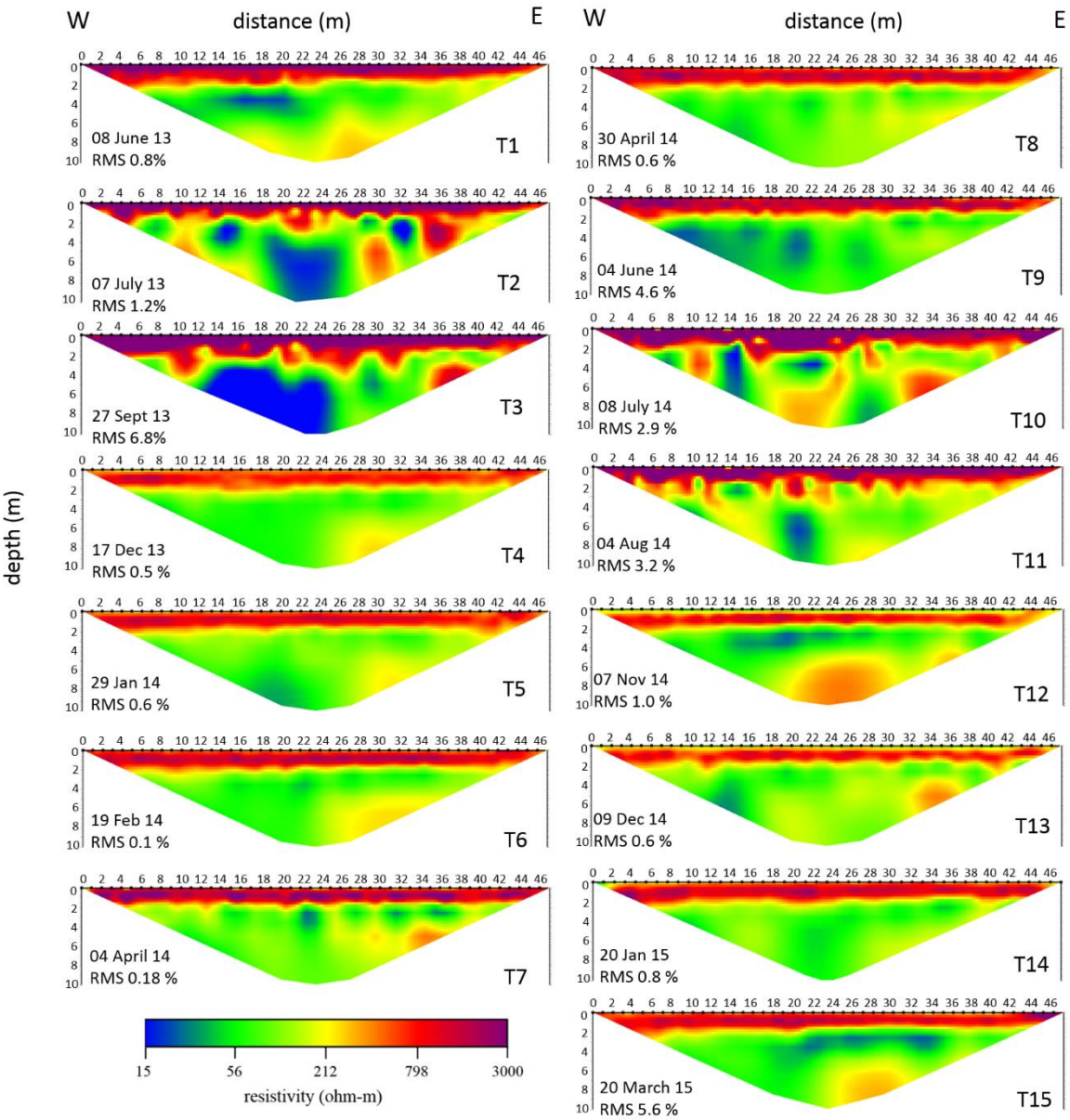

Figure 3.3 Static inversion results of the ERT measurements along the Line 1 of Fig. 3.2a from June 2013 to March 2015.

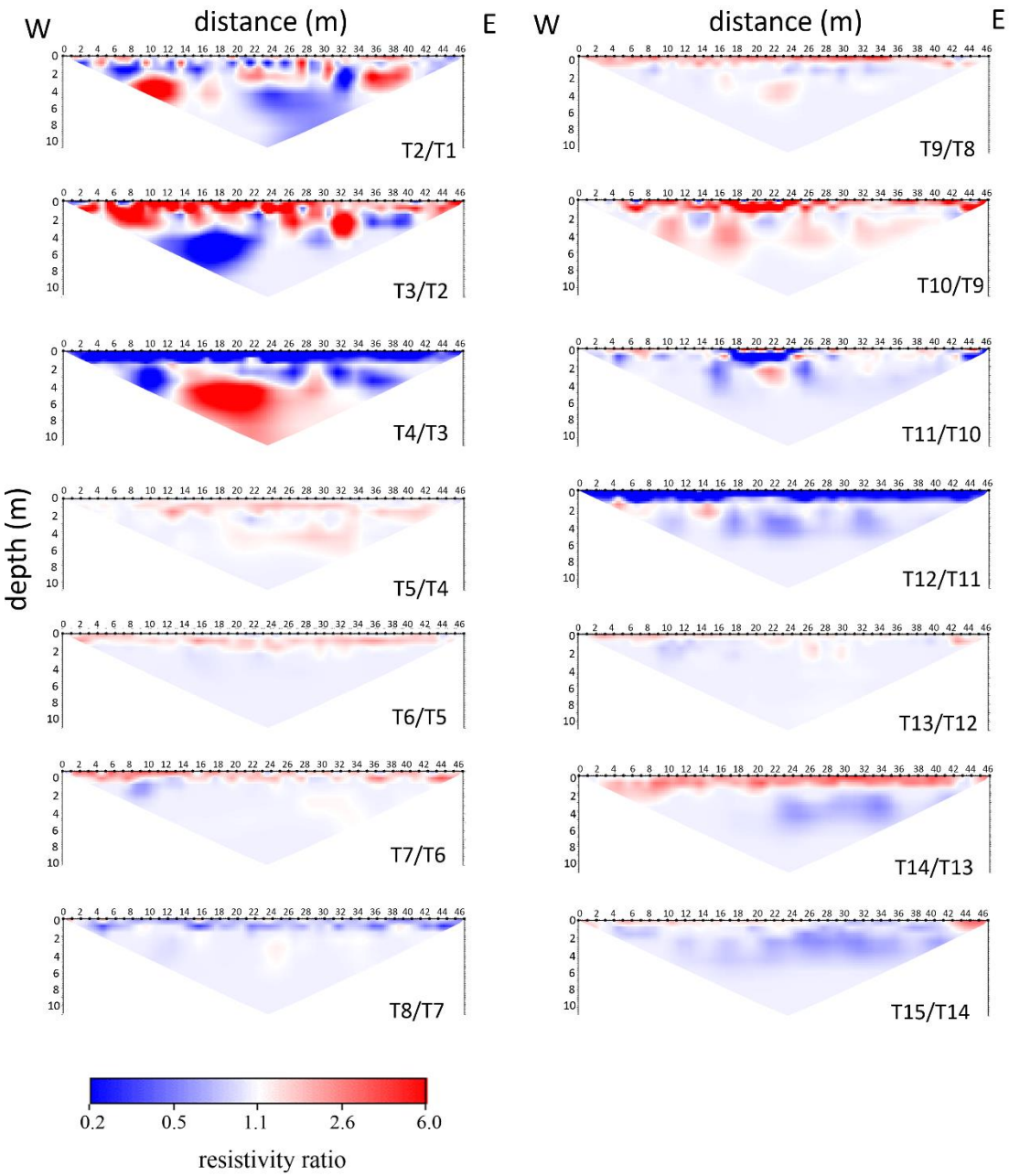

Figure 3.4 Resistivity ratio between sequential time phases resulted by the 4D inversion of the ERT measurements along the Line 1 of Fig. 3.2a from June 2013 to March 2015.

In conclusion, from ERT inversion results it is possible to argue that *i*) the contaminant is following a horizontal pathway towards the measurement profile, i.e. in the direction of Keritis river, *ii*) the top resistive layer (up to 3 m b.g.l.) loses its homogeneity in the summer season suggesting the uprising of the contaminant. These hypotheses have been further validated by the inversion of the SP data acquired over time, as discussed in the following section.

3.3.2 Time evolution of self-potential anomaly sources

The self-potential data were acquired along a profile of length 33 m (Soupios and Karaoulis, 2015) located in the middle part of the ERT Line 1 (Fig. 3.5). The fixed base station data acquisition technique was used with an inter-electrode spacing of 1.5 m between moving electrodes. A total number of five SP datasets was acquired in the time interval from May 2014 to July 2014.

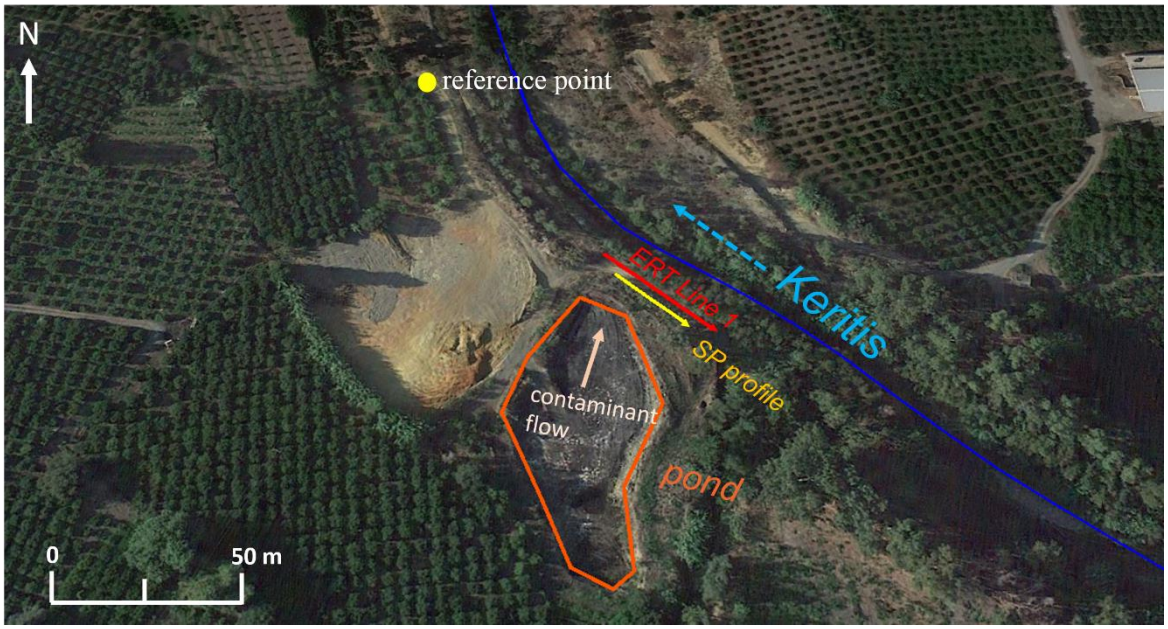

Figure 3.5 Location of the SP profile (yellow line) along the ERT Line 1 (red line). The yellow point indicates the base station used for the acquisition of the SP data along the profile.

A close look on the five obtained SP profiles (Fig. 3.6a) highlights significant variations in the self-potential signal from May 2014 to July 2014. On May 15, a wide SP negative anomaly (centered at about 25 m along the horizontal axis) is observed, even if it is characterized by a relatively small amplitude (about 10 mV). With the exception of a narrow positive anomaly in the western part of the profile, no significant peaks are visible along the entire profile. On the contrary, from the middle of June till the end of July (i.e. the last three profiles of Fig. 3.6a), the SP signal shows a well-defined minimum (about -20 mV in amplitude) approximately in the

same position of the first SP profile, and an intense positive peak (about 53 mV in amplitude) to the right of such a minimum at 25-30 m along the horizontal axis. The central negative SP anomaly could be caused by the contaminant flow trend perpendicularly to the SP measurement profile (see Fig. 3.5), while the positive SP anomaly could be associated with an uprising of the contaminant caused by evaporation phenomena. A comparison between the highlighted SP anomalies and the typical SP anomaly trends attributed by Richards et al. (2010) to different hydrogeological processes (Fig. 3.6b), seems to strengthen the suggested interpretation. Specifically, the shape of the SP negative anomaly, located approximately in the middle of the profile, resembles the type V behavior (see Fig. 3.6b), thus indicating the presence of a horizontal flow pathway most likely due to dynamic conditions of the small stream (see Fig. 3.1) during all the monitoring period, while the shape of the positive SP anomaly, which looks like the type I behavior (see Fig. 3.6b), highlights an upward flow supposedly of contaminant during the summer season.

In order to obtain a quantitative characterization of the SP anomaly sources, in terms of horizontal and vertical position and polarization angle, as well as their possible changes over time, the proposed SP data inversion methods (see Chapter 2) have been applied (Rani et al., 2016a, c).

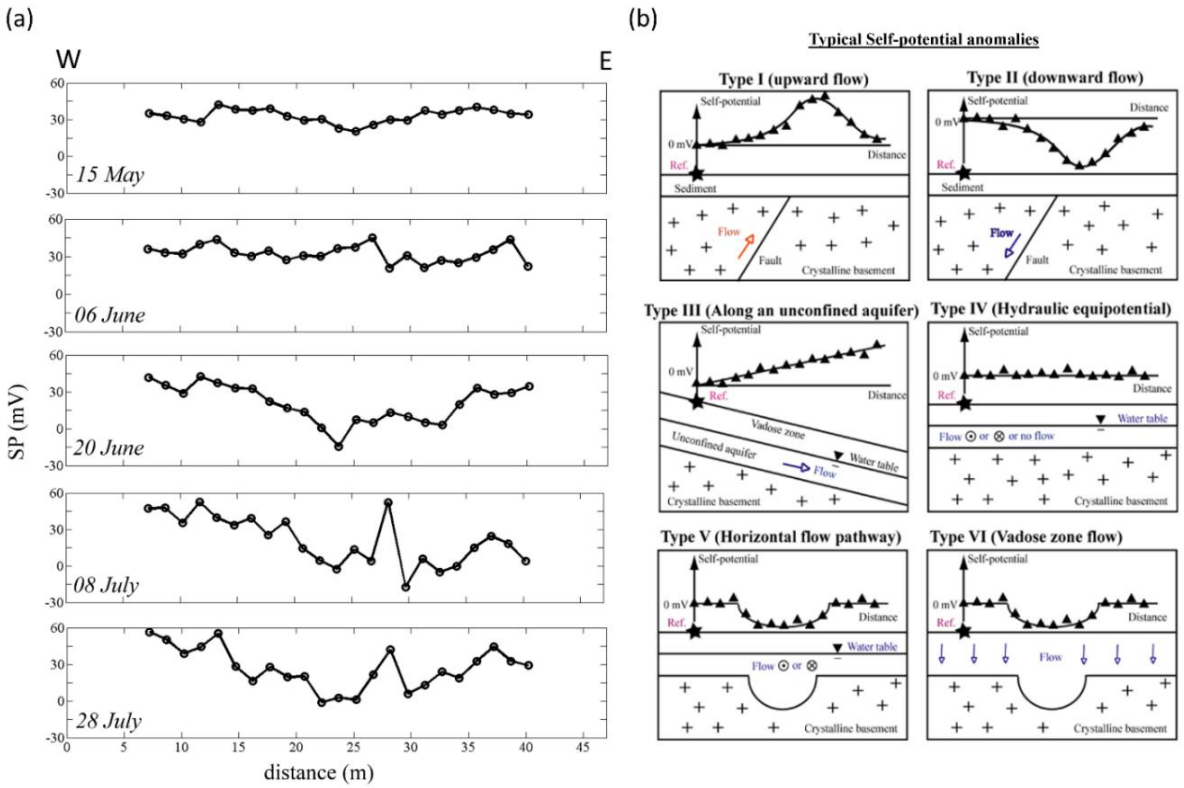

Figure 3.6 (a) Variation of the SP values measured along the profile shown in Fig. 3.5 during five field campaigns (from May 2014 to July 2014). (b) Typical SP anomalies and their potential interpretation (from Richards et al., 2010).

MEM-COP integrated analysis

The MEM approach has been applied to the five measured SP profiles (Fig. 3.6a) to get information about the depth of possible anomaly sources. Even if the profile is only 40 m long, the log power spectrum - wavenumber plot obtained by using the Spector and Grant relation (eq. 2.2 in Chapter 2) shows two straight lines indicating the presence of two anomalous sources (Fig. 3.7). For the successful application of the MEM method, the order of AR process has been calculated by using the Akiake's final prediction error criterion (FPE) (eq. 2.1 in Chapter 2). The order corresponding to the first minimum in the plot FPE vs order has been chosen as the order of the AR process. Fig. 3.7 shows the order selection of the AR process and the power spectrum estimated for the analyzed SP profiles. The depth of both anomalous sources varies between 0.8 and 3.5 m b.g.l. (see Fig. 3.7 and Table 3.1), which are in good agreement with the conductive bodies highlighted by the ERT measurements (see Section 3.3.1).

Profiles	AR order	depth (source I)	depth (source II)
15 May	4	3.1 ± 0.2 m	2.8 ± 0.3 m
06 June	5	2.7 ± 0.3 m	2.0 ± 0.1 m
20 June	7	3.0 ± 0.5 m	1.6 ± 0.3 m
08 July	7	1.5 ± 0.1 m	1.2 ± 0.4 m
28 July	5	2.6 ± 0.3 m	2.4 ± 0.1 m

Table 3.1 Selected AR order and depth values estimated by the MEM spectral method applied to the five SP profiles performed from May to July 2014.

After the depth estimation of the anomaly sources by MEM, the tomographic approach has been applied for the evaluation of their horizontal position and polarization angle. Fig. 3.8 shows the 2D COP tomographic images obtained by using eq. (2.6) for the five measured profiles. Based on the maximum values of positive and negative charge occurrence probability estimates, three potential anomalous zone have been defined. By comparing the obtained tomographic images with those from the synthetic data analysis discussed in Chapter 2 (Section 2.2.2.1), it is possible to identify some similarities with the COP distribution generated by a horizontal cylinder. Thus, a horizontal cylinder source model has been chosen to calculate the SP source parameters (i.e. polarization angle, α, and position along the x-axis, x_0) by using eqs. (2.8) and (2.9), respectively. The obtained parameters for all the investigated SP profiles are reported in Table 3.2.

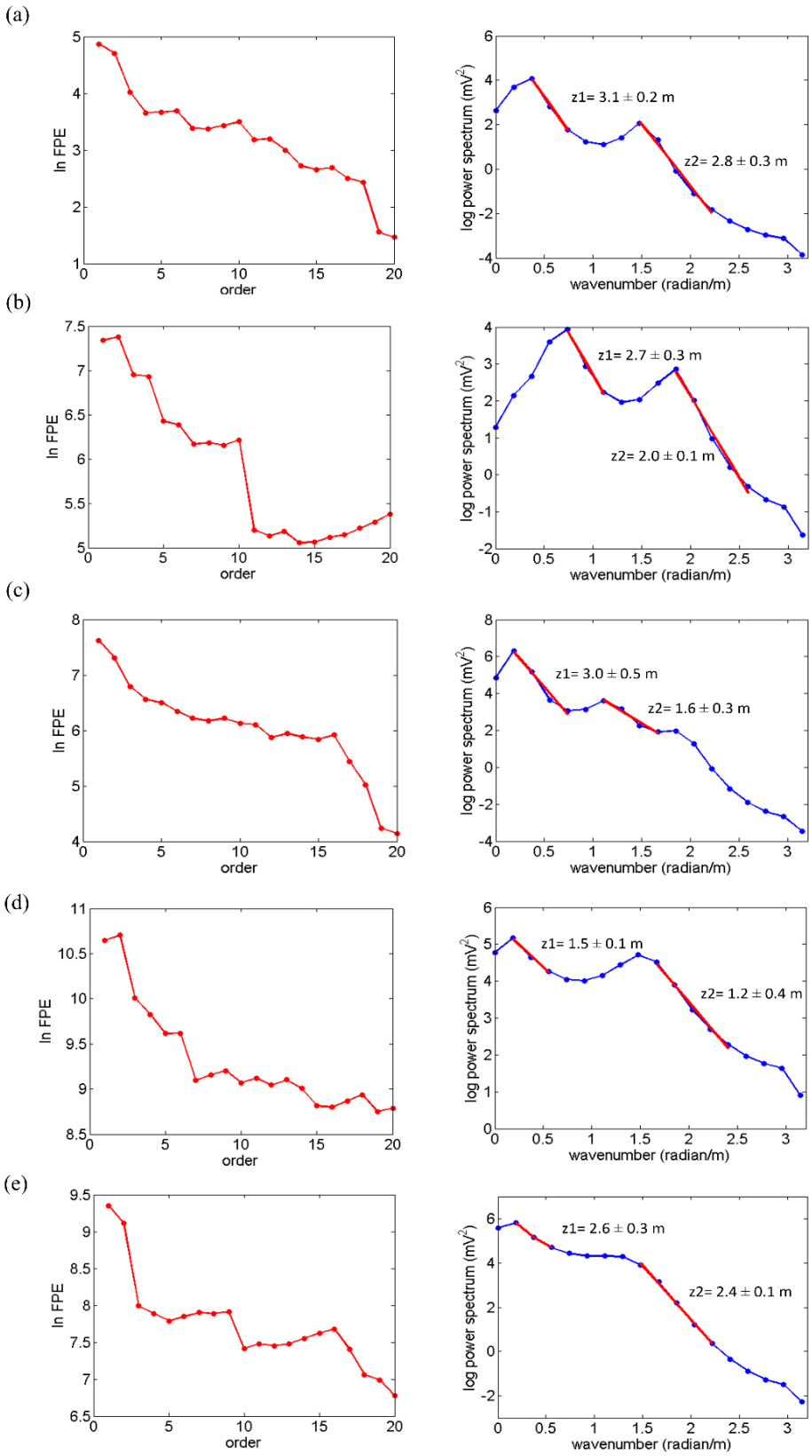

Figure 3.7 Order selection of AR process and power spectrum obtained for the SP measurement profiles of 15 May 2014 (a), 06 June 2014 (b), 20 June 2014 (c), 08 July 2014 (d) and 28 July 2014 (e). In the plots, *z1* and *z2* indicate, respectively, the depth of the two anomaly sources retrieved by applying the MEM inversion method.

Profiles	Region I		Region II		Region III	
	x_0 (m)	α (°)	x_0 (m)	α (°)	x_0 (m)	α (°)
15 May	13.02	22.12	21.50	37.07	-	-
06 June	-	-	23.69	40.62	27.98	20.82
20 June	-	-	20.66	65.83	34.06	67.95
08 July	-	-	21.32	60.84	29.46	13.69
28 July	-	-	21.50	65.43	29.45	19.02

Table 3.2 SP source parameters provided by the COP inversion of the five SP profiles performed from May to July 2014.

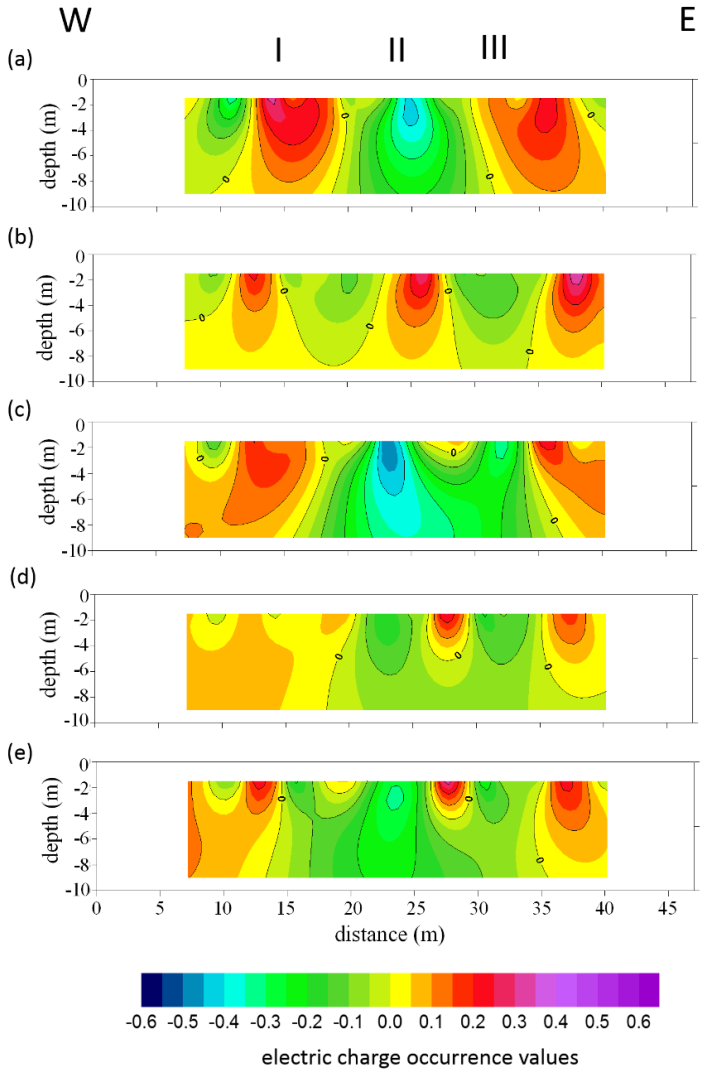

Figure 3.8 2D COP tomographies related to the SP measurements of 15 May (a), 06 June (b), 20 June (c), 08 July (d) and 28 July (e). Three potential anomalous zones (I, II, III) are indicated on the top of the profiles.

Summarizing, it has been found that the 2D COP tomography method is able to identify for all the five dates a possible anomaly in the central part (region II) of the SP profile and a second anomaly located to its eastern part (region III). As it concerns the anomalous region I, it has not been possible to characterize over time its causative source due to less measurement points and not clear distribution of COP zero lines.

Genetic-Price Algorithm (GPA)

As shown in the previous section, the integrated MEM-COP inversion approach is able to provide information about shape, depth, horizontal position and polarization angle of the SP anomaly sources. In order to reconstruct the observed SP signal by using the retrieved source parameters, it is necessary to have an estimate of the electric dipole moment, *k*, which is not provided by the MEM-COP approach. Thus, a trial and error procedure has to be used until the reconstructed curve well approximates the observed one. This approach, besides to be time consuming, may not give good results for very noisy SP data, as for our case.

Therefore, in order to obtain all the SP source parameters for reproducing the observed SP signals and defining the time evolution of the possible anomalous sources, the Genetic-Price algorithm has been applied, it is worth noting that, as the region I is not very well defined by the COP analysis, only two sources belonging, respectively, to region II and III have been considered for the GPA inversion of the SP profiles. First its application, the data collected for the five SP profiles have been carefully up-sampled using spline interpolation in order to increase the data points for the inversion process. Moreover, the source parameters evaluated from MEM and COP have been used as a priori information for the GPA inversion to fix both the number of sources and the bounds of the parameters. Interestingly, the algorithm has provided a shape factor of 1.0, strengthening the hypothesis that the observed SP anomalies are generated by horizontal cylinder-shaped sources, and source parameters estimates consistent with those obtained from MEM-COP approach. Fig. 3.9 shows the SP curves reconstructed by

using the parameters retrieved from the GPA approach (red line). As it can be seen in Fig. 10, they well reproduce the negative anomaly trend observed for the survey of May, associated to the horizontal flow path of the contaminant, and the SP positive peak observed for the two surveys of July, correlated to the uprising of the contaminant due to evaporation processes.

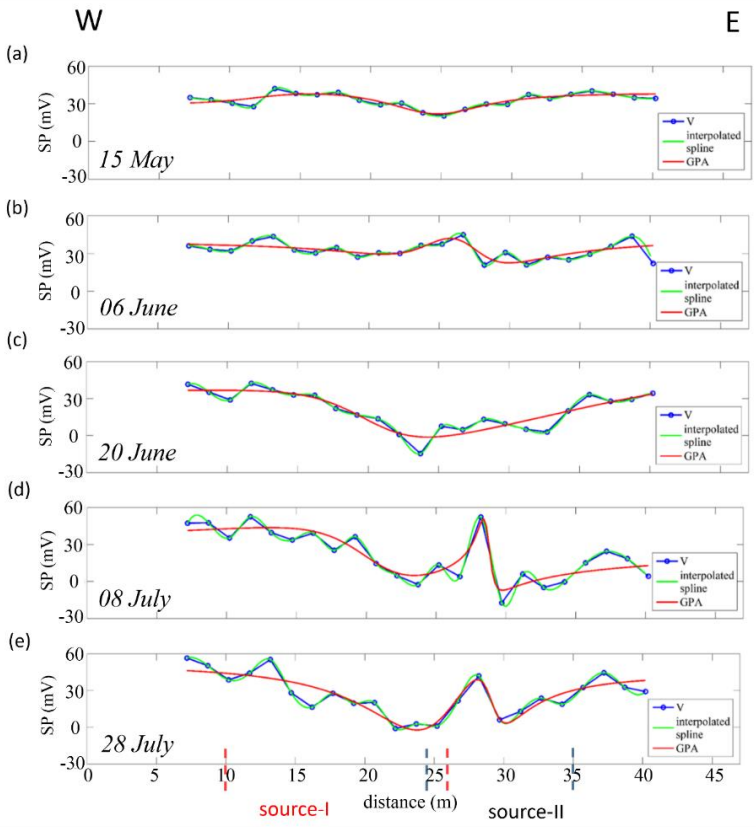

Figure 3.9 Observed SP curve (blue line), interpolated spline (green line) and curves reconstructed by using two horizontal cylinders (red line) as anomalous sources. Bounds for the position x_0 of the two anomaly sources are indicated, respectively, with red and black dashed lines.

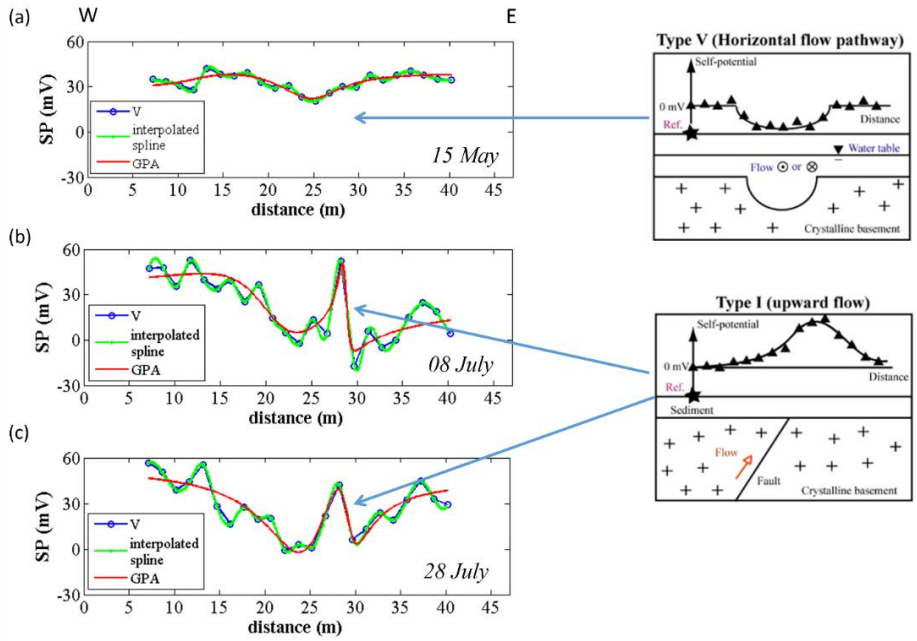

Figure 3.10 Comparison between the curves reconstructed by using two horizontal cylinders as anomalous sources (red lines in the left panels) and the typical self-potential anomalies (right panels, from Richards et al., 2010).

3.4 Numerical simulation models

In this section, the results of two different numerical approaches are presented with the aim to estimate spatial and temporal evolution of the contaminated area located approximately below the waste pond, as revealed by the electrical resistivity tomography survey (see Fig. 3.3). The first approach is based on a simple cellular automaton model that is developed in the attempt to characterize the most dangerous scenario in terms of maximum diffusion distances travelled by the contaminant. The second approach is based on Feflow modeling and aims at simulating possible future scenarios for a larger area and also at reconstructing hydraulic head distribution of values and contaminant mass transport.

3.4.1 Cellular Automata model

As described at the end of Chapter 2, a cellular automaton model has been developed with the aim to simulate diffusion-dispersion phenomena of the pollutant in the unsaturated zone. In this case, the contaminant is supposed to be approximately in the middle of the grid and its

propagation is essentially controlled by the local porosity and the contaminant concentration gradients. In particular, a two-dimensional rectangular grid of M x L cells is used to describe a vertical section of the soil of the investigated area shown in Fig. 3.1. In order to represent the real complex scenario, as a first approximation a three-layer model is assumed with three homogeneous distribution of resistivity values, schematically shown in Fig. 3.11. Such values are chosen on the basis of the inversion results of geoelectrical data discussed in the previous sections. The state of each cell, S, indexed by *i*, with 1 < i < ML, is defined by the values of three parameters: S(i) = ⟨ρ; *c*; n⟩, where ρ is the soil electrical resistivity that provides indication of contaminant for values less than 10 Ωm, *c* is the percentage of local concentration of contaminant and *n* is the local porosity value. In the initial configuration, a rectangular contaminated area (red box in Fig. 3.11) is in the middle of the central layer, with values of the local concentration *c(i)* equal to or larger than the threshold value for diffusion, c_{th} = 1. The shape of such contaminated zone is, again, suggested by the results of the resistivity survey, in particular from ERT carried out along the profile Long 1 shown in Fig. 3.2. The porosity is assumed to be a monotonic decreasing function for the first layer (with values ranging from 0.4 to 0.35) and a monotonic increasing function for the other two layers (with values ranging from 0.35 to 0.50), as shown in Fig. 3.12. Such values are taken from literature for the considered soil types.

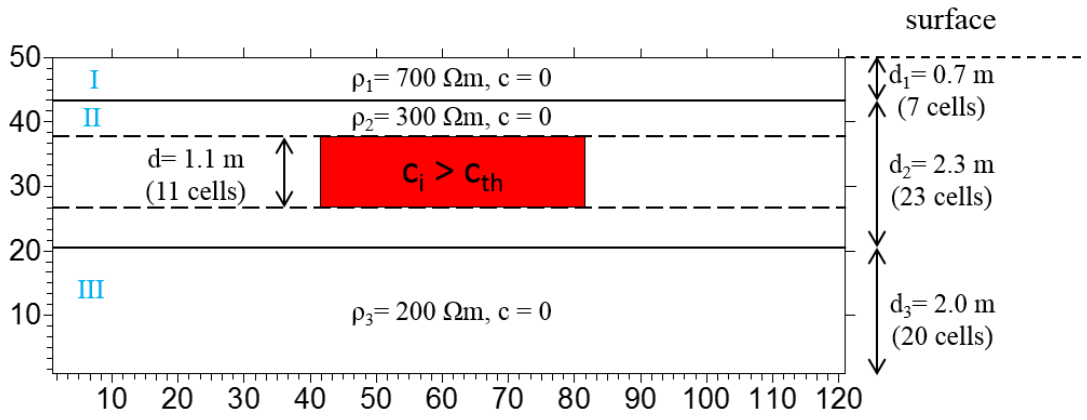

Figure. 3.11 Schematic representation of the three-layer model in the initial configuration.

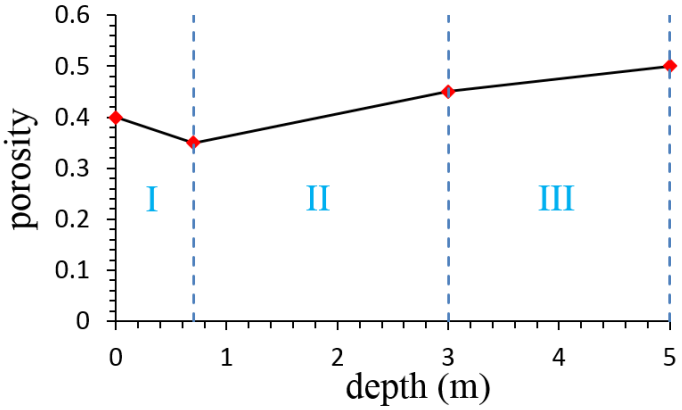

Figure. 3.12 Porosity as a function of the depth below ground level.

As discussed in Chapter 2, the dynamics of the model is governed by a relaxation rule inspired by the SOC theory and described by eq. (2.14). On the basis of such rule, if the cell i is over-contaminated (i.e. $c(i) > c_{th} = 1$, or $c(i) >= c_{th}$), the contaminant propagates into neighbor sites and the value of contaminant concentration at site i is set to a minimum concentration value c_{min}, which is set to 0.1 and kept fixed for the cases discussed in this section. If the contaminant concentration of neighbor sites is larger than c_{th}, the contaminant continues to propagate by eq. (2.14). The relaxation chain process continues up to when the difference in the contaminant concentration between two adjacent cells is larger than the local concentration gradient threshold Δc_{th}. The values for the transfer coefficients f_{nn} (see eq. (2.14)) control the diffusion in the horizontal and vertical directions and the results of a systematic study performed by varying their values is shown below. First, the isotropic case, for which $f_{up} = f_{down} = f_{left} = f_{right} = 0.25$, has been analyzed. Such a case describes the situation where there are no additional driving forces, therefore the contaminant can diffuse in the subsurface with no preferential directions. In this case, it has been found that, if the initial contaminant concentration of the contaminated area is equal to the threshold value for diffusion, i.e. $c(i) = c_{th} = 1$, the contaminant moves a few cells in all directions, and, therefore, it is able to reach neither the top border of the grid, which describes the surface, nor the bottom of the grid, which describes the top of the saturated zone. Thus, an

analysis by varying the initial contaminant concentration has been performed to find the minimum value of $c(i)$ for which contaminant percolates through the soil and reaches the surface (condition that is satisfied for a movement of 13 cells in the upward direction) and the saturated zone (condition that is satisfied for a movement of 26 cells in the downward direction). The results of such an analysis are shown in Fig. 3.13, where the maximum distances travelled by the contaminant, L_{max}, in the upward and downward directions are reported as a function of $c(i)$, respectively. As it can be seen, the relationship between L_{max} and $c(i)$ is not linear. In particular, even if the porosity values increase below the depth of 1 m, the increase of L_{max} with $c(i)$ in the downward direction is slower due to the initial geometry of the contaminated area.

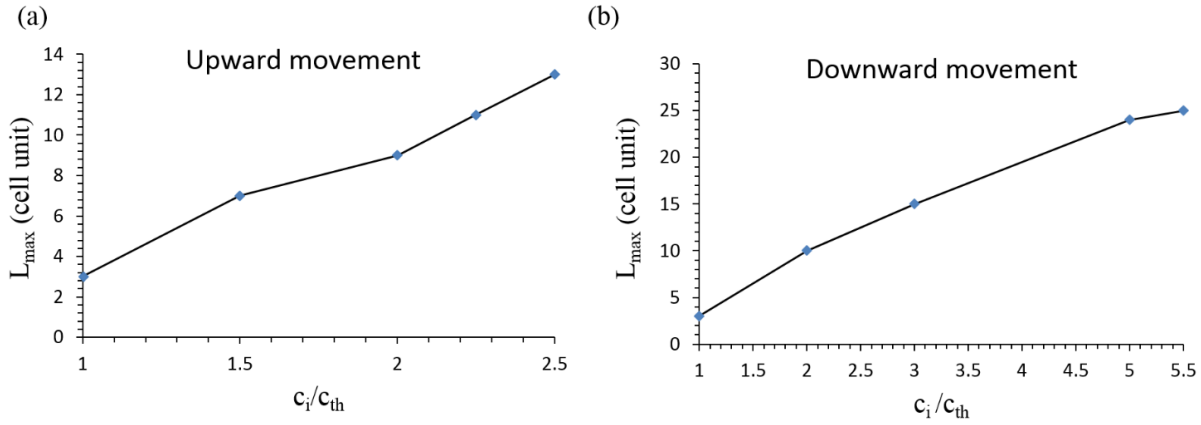

Figure 3.13 Maximum distance travelled by the contaminant in the upward direction (a) and downward direction (b) for isotropic transfer coefficients, as a function of the ratio $c(i)/c_{th}$.

As an example of a simulation output, in Fig. 3.14a and b are reported, respectively, the final configurations related to an isotropic diffusion of the contaminant and the corresponding changes in the resistivity values. Such changes are obtained by considering electrical resistivity as a linear decreasing function of the porosity and the contaminant concentration.

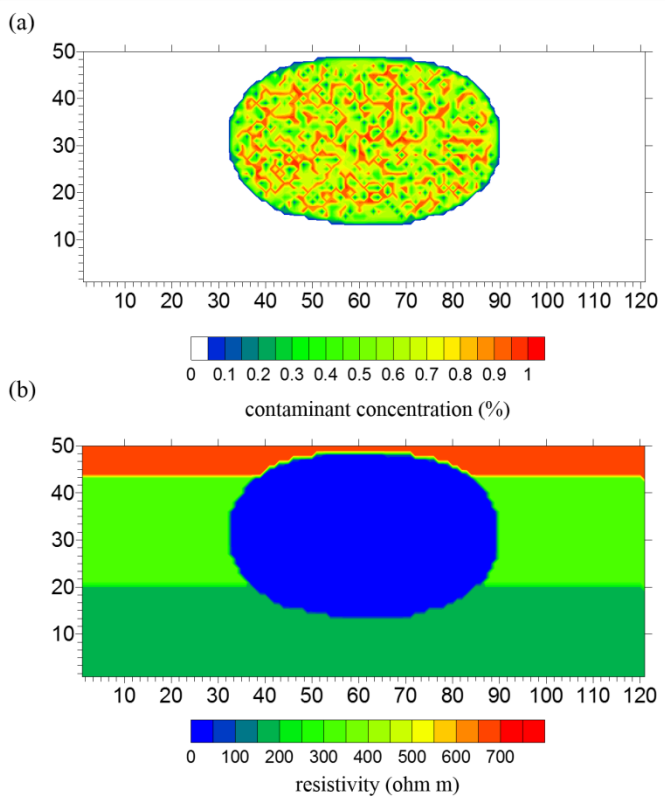

Figure 3.14 (a) Final configuration of contaminant concentration and (b) resistivity variations obtained for isotropic conditions of transfer coefficients, for an initial concentration of contaminant c_i = 2.5.

To better investigate the properties of the model that is able to take into account different conditions in the contaminant propagation, an analysis of the effects of anisotropic variations in transfer coefficients has also been performed. In particular, in the following the results of the numerical analysis by varying the transfer coefficients in down and right directions are shown. This choice is motivated by the geological features of the survey area, and, in particular, it is made to take into account the driving force due to gravity and an additional driving force that moves contaminant in the right direction due to the presence of Keritis river (north-east direction corresponding to the right border of the grid, see Fig. 3.2).

First, the case with the initial contaminant concentration equal to the threshold value for diffusion, i.e. $c(i) = c_{th} = 1$, has been considered. An analysis has been performed to find the maximum distances travelled by the contaminant, L_{max}, by varying the transfer coefficients f_{down} and f_{right}. In all simulations the values for the other two transfer coefficients are kept fixed

(specifically, $f_{up} = f_{left} = 0.1$) and the condition $\Sigma_i f_i = 1$ is satisfied. As it can be seen in Fig. 3.15, in this case, as it is occurs for the isotropic case, the contaminant is not able to reaches the border of the grid, and, thus, it is not able to reach the saturated zone, even if $f_{right} << f_{down}$. However, if larger values for the initial contaminant concentration are considered, the behavior of L_{max} as a function of the ratio between the transfer coefficients f_{right} and f_{down} changes significantly and several features emerge from the analysis. The initial contaminant concentration $c(i)$ shall be at least two times the threshold value for diffusion so that the contaminant reaches the right border of the grid, at least for $f_{right} >> f_{down}$ (see Fig. 3.15a). In particular, contaminant percolation in the right direction is found for all values of the ratio f_{down}/f_{right} only for $c(i)/c_{th} > 2.5$.

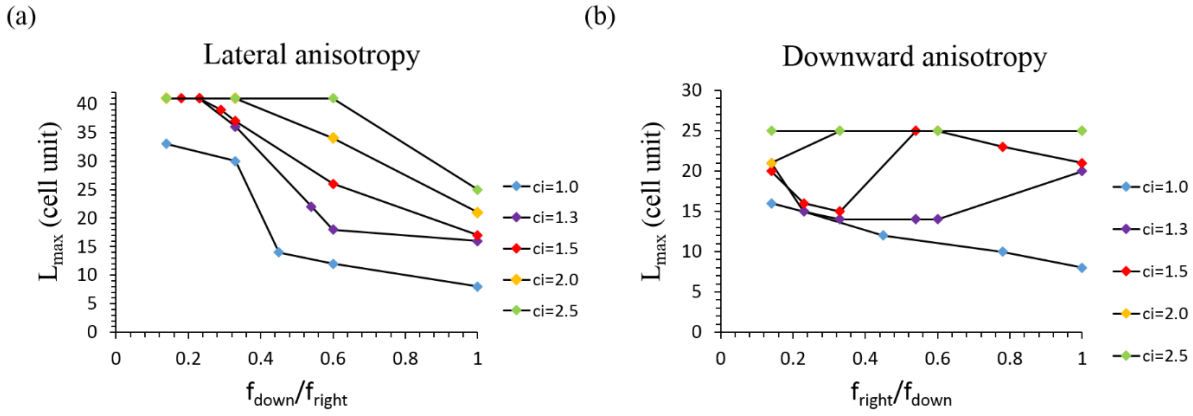

Figure 3.15 (a) Maximum distance travelled by the contaminant in the downward direction and (b) right lateral direction as a function of the transfer coefficients ratios f_{right}/f_{down} and f_{down}/f_{right} , keeping fixed the values $f_{up} = f_{left} = 0.1$. Lines with coloured markers indicate different values of the initial contaminant concentration with respect to the threshold value $c_{th} = 1$.

As it concerns contaminant movement in the downward direction, contaminant percolation is observed for the whole range of the parameter values when $c(i)/c_{th} = 2.5$. In this case, for $1 < c(i)/c_{th} < 2.5$ L_{max} is not a monotonic function of f_{right}/f_{down} and percolation can be reached also for different values of $c(i)/c_{th}$, even if only for a restricted range of values of the transfer coefficients (for instance, see red diamonds in Fig. 3.15b). It is also worth noting that the model predicts the existence of particular values of the ratio f_{right}/f_{down} for which the downward movement of the

contaminant is less favored, i.e. L_{max} decreases. In particular, the region where L_{max} has a minimum value becomes narrower by increasing $c(i)/c_{th}$.

The results of such an analysis could provide some insights on the delineation of dangerous scenarios if they are compared with the results of the geochemical monitoring carried out in the investigated area (Ntarlagiannis et al., 2016). In particular, from the samples collected at 25 cm intervals in two pits (about 2.2 m deep), it has been found that the phenol concentration has the values shown in Fig. 3.16. In this figure, the blue horizontal dashed line represents the background value of the phenol concentration for the area (Doula et al., 2013), while the threshold values for moderate (> 40 mg/kg) and high (> 150 mg/kg) risk zones (Doula et al., 2012) are not shown.

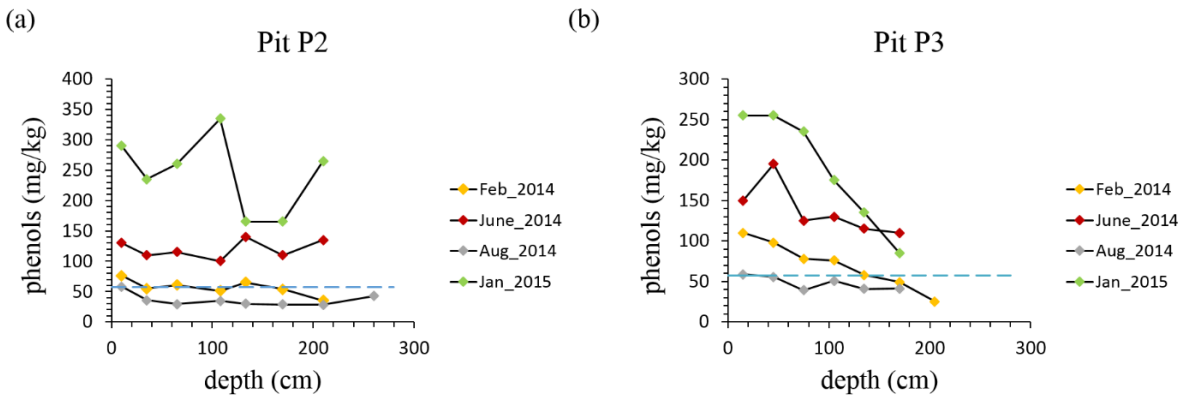

Figure 3.16 Variation in phenol concentration with depth observed in two pits, P2 (a) and P3 (b) located along the ERT Line 1 (see yellow dots in Fig. 3.2). Blue dashed horizontal line indicates the background value for the phenol concentration for the area.

If the background value is assumed to be the value of the threshold c_{th}, from the geochemical data it turns out that the contaminant concentrations in the area between the pond and the river in the periods June 2014 and January 2015 are more than two times the threshold value and, therefore, in such cases the simulations results show that they can reach the saturated zone and also travel large distances in horizontal direction towards the river.

Finally, as an example of simulation outputs, in Fig. 3.17a and b are reported the final configurations corresponding to anisotropic diffusions of the contaminant for different values of the transfer coefficient ratios.

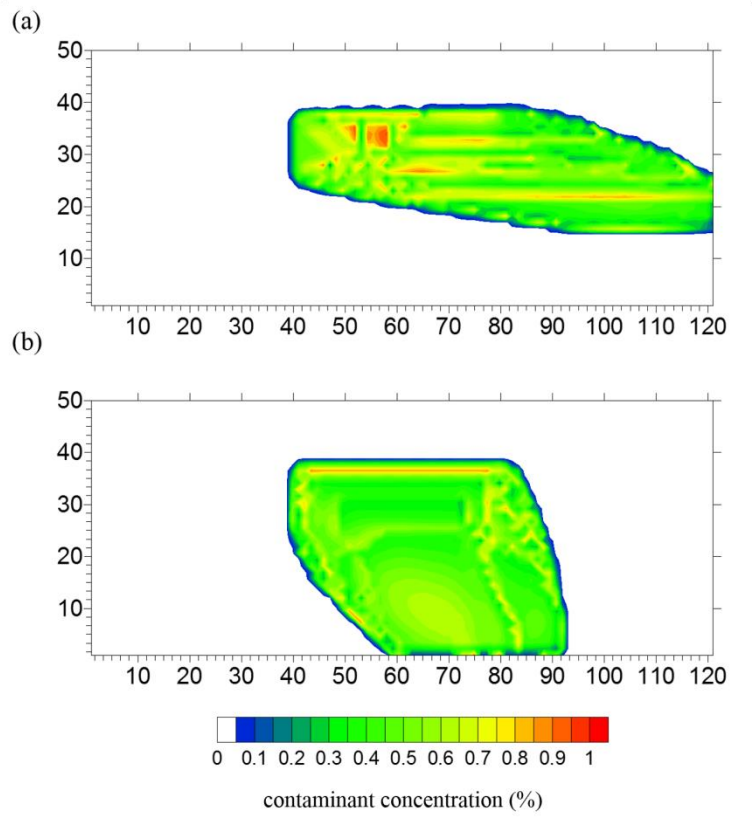

Figure 3.17 Final configuration of contaminant concentration obtained for different values of transfer coefficients ratios, f_{down}/f_{right} = 0.33 (a) and f_{right}/f_{down} = 0.60 (b), for an initial concentration of contaminant c_i = 2.

3.4.2 FEFLOW model

In order to simulate groundwater flow and OOMWs contamination transport under unsaturated and saturated conditions of the survey area, the development of a three dimensional finite-element model by using the FEFLOW simulation software (see section 1.3.1) is ongoing. Until now, simulation of the groundwater flow has been performed and then calibrated through the data from wells present in the survey area, while the study for the mass transport of OOMWs is a

work in progress. In the following, details about the model development, groundwater flow simulation and calibration are presented.

It is worth mentioning that the simulations run in the transient mode for a long period of 58 years (1957-2015), that is, since the pond was used for deposition. It is worth noting that the time series of seasonal variations in rainfall registered for about 20 years have been also taken into account as the input of time-varying boundary condition.

Model development

The conceptual model of the test site (Fig. 3.18) has been developed thanks to the information coming from previous geophysical and geochemical studies performed in the survey area, such as time domain electromagnetic measurements (Kanta et al., 2009), ERT profiles (Simyrdanis et al., 2016), geochemical analysis of soils samples (Kavvadias et al., 2016). The model comprises 8 layers divided as follows: an unsaturated zone (extending from 0 m to 5.0 m b.g.l – below ground level) divided into 5 layers, a saturated zone (from 5.0 to 18.0 m b.g.l), a semi-fractured bedrock and, finally, the bedrock, likely affected by two potential faults.

The horizontal discretization of each layer has been performed using a finite-element mesh consisting of triangular cells, with a total number of 109476 nodes and 192168 elements; such gridding is not uniform because a large number of cells is used to describe the sector comprising the waste pond and the wells.

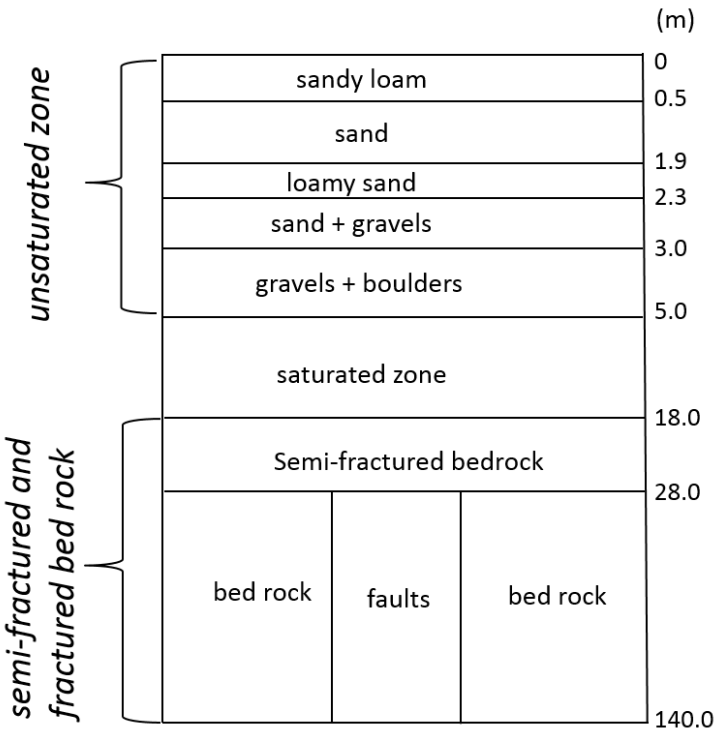

Figure. 3.18 Schematic representation of the conceptual model of the test site for FEFLOW modeling.

For the unsaturated zone, the hydraulic conductivity values for the different types of soil have been taken from the literature and assumed to be isotropic for each layer. Whilst Table 3.3 indicates the values chosen for the parameters of the van Genuchten function (van Genuchten, 1978) (eq. (A.4)), which is used by FEFLOW to model water and solute movement through the unsaturated zone (see Appendix A).

van Genuchten parameters for unsaturated zone		
Layers	A (1/cm)	n
1	0.75	2
2	1.2	3
3	0.9	2
4	2.5	3.24
5	2.5	4

Table 3.3 van Genuchten parameters (see eq. (A.4)) chosen for the five layers of the unsaturated zone. For all the layers the values of residual saturation and maximum saturation have been fixed to 0.05 and 1, respectively.

Regarding the saturated zone, the hydraulic conductivity value has been taken from the study performed by Nikolaidis and Karatzas (2010), which refers to the Chania region that is located close to the survey area.

Flow boundary conditions

Initial conditions for the boundaries of the simulation region have to be defined. The FEFLOW modeling allows to use different boundary conditions for the groundwater flow. In particular, in this study two kinds of boundary conditions have been used. The 1st kind (Dirichlet boundary condition) uses fixed hydraulic head values, which require the knowledge of the groundwater level at boundary. Such kind of boundary condition has been used for taking into account the presence of the river in the simulation region, as shown in Fig. 3.19. The 2nd kind (Neumann boundary condition) uses fixed flux (Darcy flux) across a model boundary. This kind of boundary condition has been used for eastern and southern part of the model domain, where a lateral inflow from nearby Karstic springs is present, as shown in Fig. 3.19.

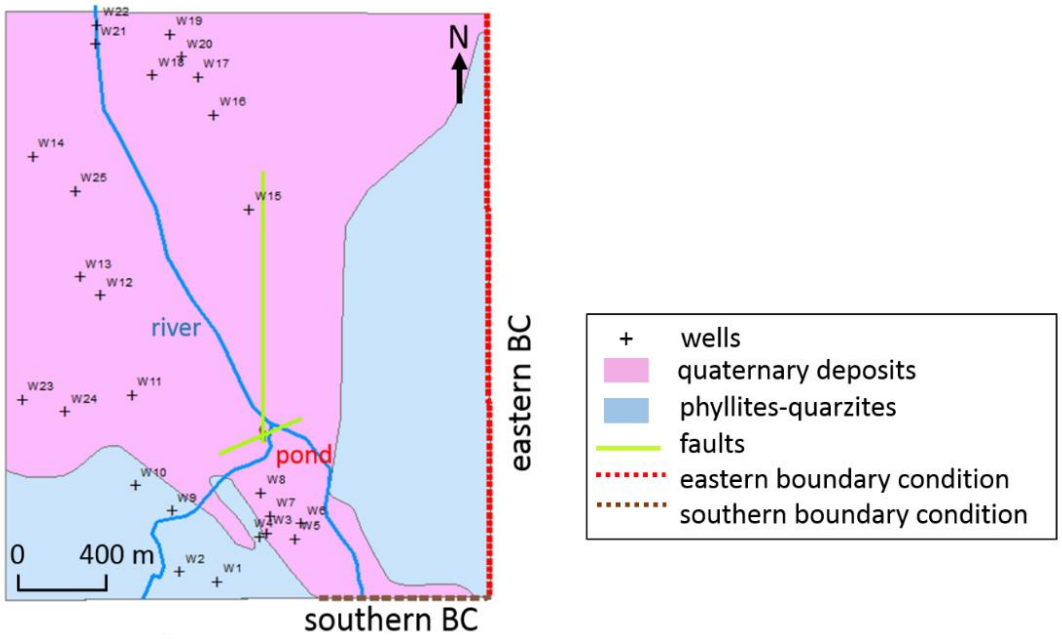

Figure. 3.19 Study area with location of wells, faults and flow boundary conditions (BC).

Discrete features

Discrete features can be added to the model to represent highly conductive one- or two-dimensional features, such as tunnels, pipes, drains, faults or fractures. They are finite-elements of a lower dimension than the basic finite-element mesh. In this study, two-dimensional features are used to describe two faults in the bedrock, as shown in Fig. 3.19. Specifically, triangular 2D discrete elements of 0.5 m thickness and 0.5 m aperture are considered and the Hagen-Poiseuille's law (Sutera and Skalak, 1993) has been used to describe the flow dynamics in the faults.

Groundwater flow calibration

In order to have accurate simulation results and make predictions as close as possible to real scenarios, it is necessary to perform a model calibration. In this section, the results of groundwater flow calibration are presented.

In the simulation region there are more than 25 wells, but continuous hydraulic head data are available only for 18 wells in a time period of two years (1998-99). Thus, the calibration of the flow field was performed on the basis of such data. During the calibration procedure, both the lateral influx rate parameters on the eastern and southern boundaries were changed, while all the other input data were unchanged. The simulated hydraulic heads for the years 1998-99 were compared with the observed hydraulic head data and when the value of the normalized root mean squared error was less than 6% the model was accepted. Despite the hydrogeological complexity of the area and the long simulation period, good results of the calibration process were obtained, as shown in Fig. 3.20. As it can be seen in figure, the simulated data (red diamonds) are closer to measured data (black dashes) for hydraulic head less than 60 m, and only for higher hydraulic heads considerable differences are found.

Finally, Fig. 3.21 shows the distribution of the hydraulic head values in the saturated zone at the end of the whole simulation period (1957-2015). As expected, due to the lateral influx,

higher hydraulic head values are found near the eastern and southern boundaries, which affect the hydraulic head distribution in the central part of the area where the pond is located.

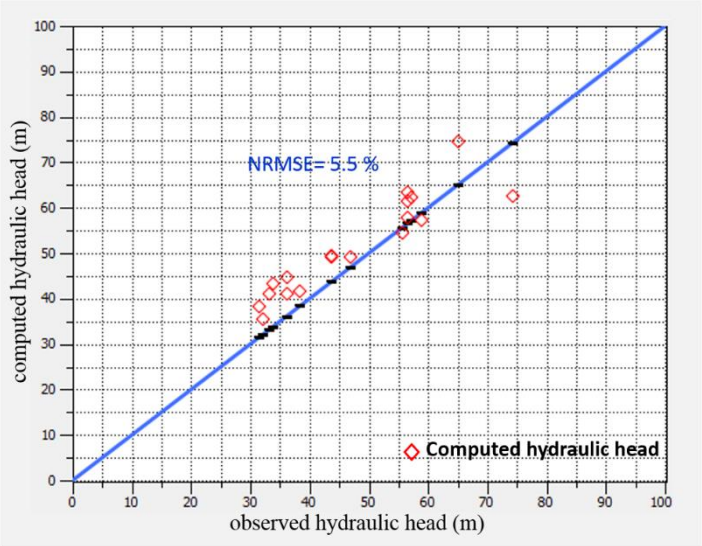

Figure. 3.20 Comparison between observed and computed hydraulic head values.

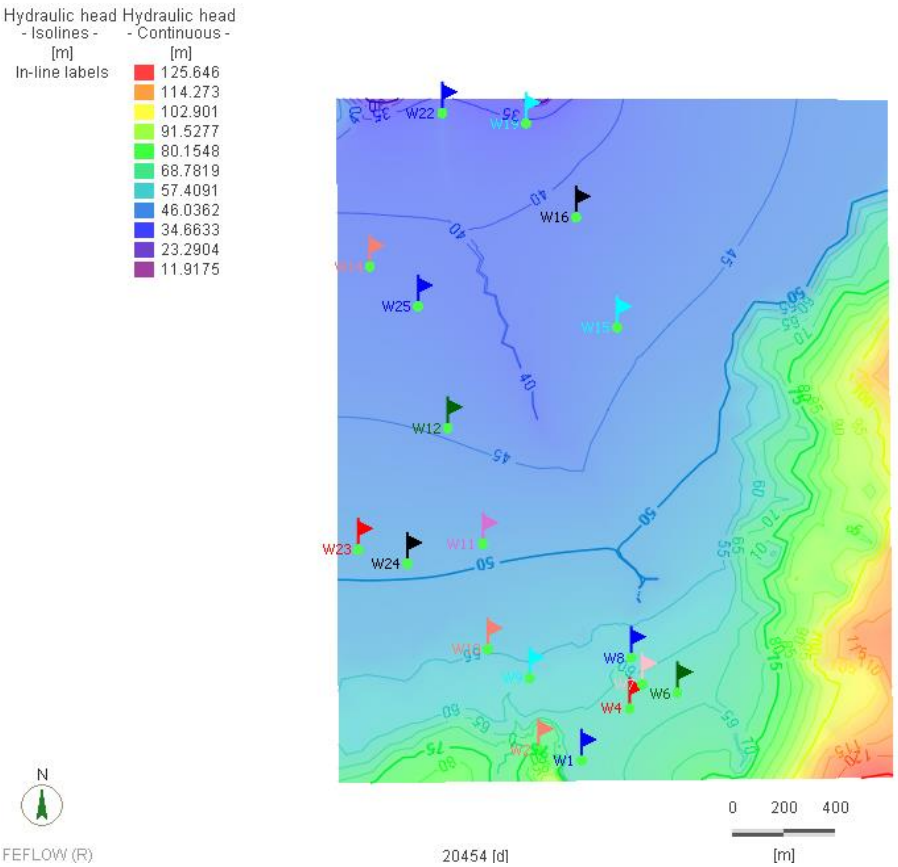

Figure. 3.21 Simulated hydraulic head distribution for the saturated zone at the end of the simulation period (1957-2015).

It is worth noticing that this kind of numerical modeling requires a huge amount of geological, geochemical and hydrogeological data that often are missing. Conversely, the proposed cellular automata approach for simulating the contaminant propagation requires few input data and local rules to describe the system dynamics. However, it is often not easy to identify appropriate rules able to predict the evolution of the system behavior. Thus, information coming from mass transport calculation by FEFLOW can be of great help for selecting the most suitable rules and, consequently, for improving the delineation of the most dangerous scenarios.

Chapter 4

Joint analysis of geoelectrical, hydrogeological and hydrochemical data for contamination estimate of complex aquifer systems

4.1 Introduction

In this Chapter a further application of the geoelectrical prospecting to contamination problems is presented, with the main aim to test its effectiveness not only for identifying and characterizing possible polluted areas, but also for providing information on the nature of the contaminant.

As widely discussed in Chapter 1, the use of geoelectrical methods, such as resistivity, induced polarization and self-potential techniques, are of great help for hydrogeological investigations and estimation of the presence of contamination, because the main hydrogeological properties, such as soil porosity and permeability, can be correlated to electrical parameters, such as the electrical resistivity (Dahlin et al., 1999; Nowroozi et al.,1999; Meju, 2005; Rubin and Hubbard, 2005; Jouniaux et al., 2009; Revil et al., 2012). In particular, much attention has been devoted in recent years to the integrated interpretation of geoelectrical data with geological, hydrogeological and geochemical data (e.g., Hinnell, et al., 2010; Ayolabi et al., 2013; Di Maio et al., 2013) as well as to the modeling of contaminant propagation (e.g., Al-Darby and Abdel-Nasser, 2006; Bear and Cheng, 2009). In this framework, the present Chapter is focused on a multidisciplinary approach that integrates geoelectrical, stratigraphic, hydrogeological and hydrochemical data for charactering possible contamination phenomena in an area of the Solofrana river valley (Castel San Giorgio, Salerno, southern Italy), where frequent flood episodes, triggered by intense or prolonged rainfall, increase the potential

pollution hazard by heavy metals discharged from leather and tanning industries operating in the upper part of the valley.

In the following, after a brief description of the geological and hydrogeological background at river basin scale, the test area is characterized by a multidisciplinary study consisting of geoelectrical measurements (i.e. resistivity, induced polarization and self-potential), stratigraphic and piezometric data analysis and hydrochemical analysis of wells and river water samples. Then, in order to get information about the nature of possible contamination sources, an integrated interpretation of all the analyzed data has been performed. Specifically, a joint interpretation of electrical resistivity data with stratigraphic/hydrogeolgical analyses has been performed to define the hydrostratigraphic model of the test site, while the integration of induced/spontaneous polarization data with geochemical analyses has been made to characterize the nature of the possible contaminants. In particular, a new mechanism related to the zeolite properties has been proposed to explain the results coming from the integration of SP and piezometric data.

Finally, a simple example of contaminant propagation through a cellular automata modeling is presented as a preliminary study to delineate possible risk scenarios for groundwater pollution of the investigated soils.

4.2 Geological and hydrogeological background of the Solofrana river valley

The Solofrana river valley (Fig. 4.1) is located in the inland portion of the Sarno river basin (Campania Region, south-western Italy) and stretches for about 53 km^2 in the south-eastern part of the peri-tyrrhenian Campanian plain of Plio-Pleistocence age (Cinque et al., 1993; Adamo et al., 2003). It is an inter-mountain valley which extends between the volcanic complex of Somma-Vesuvius (NW), the Sarno Mountains (NE), the limestone Lattari Mountains (S) and the Tyrrhenian coast (W). The structural setting of the valley is the result of the mainly compressive

tectonic events attributed to the rollback of the subducting Adria plate and the extensional tectonics related to the opening of the Tyrrhenian basin (Malinverno and Ryan, 1986, Patacca and Scandone, 1989). In the northern and south-western part of valley (San Michele Mt., Sarno Mt., Salto Mt. in Fig. 4.1), the Jurassic and Cretaceous deposits, mainly limestones and dolomites, are widespread, while the south-eastern ridge (Cuculo Mt., Papariello Mt. in Fig. 4.1) outcrops the dolomites of Triassic carbonate series. Along the north-eastern part (Piecentini Mt. in Fig. 4.1) of the Solofrana basin, the siliciclastic deposits of Castevetere formation unconformably overly the Cretaceous carbonates of the Lattari-Picentini mountain units (Critelli and Le Pera, 1995; Patacca and Scandone, 1989, 2007; Bonardi et al., 2009; Paduano, 2013). The soil formations of the Solofrana valley are characterised by the presence of both detrital-alluvial sediments and pyroclastic fall deposits of the Somma-Vesuvius, which are strongly influenced by colluvial and alluvial processes (Cinque et al., 1993; Adamo et al., 2003).

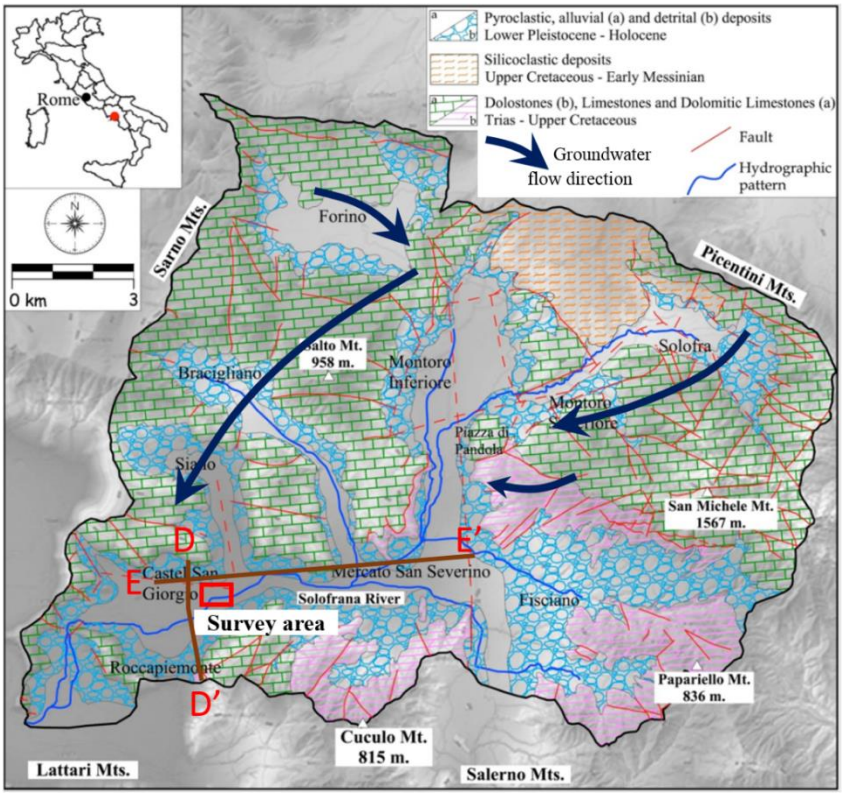

Figure 4.1 Geological and structural sketch of the Solofrana river valley (after Paduano, 2013, modified). The red box delimitates the area investigated with geophysical measurements. The brown lines EE' and DD' indicate the two stratigraphic cross-sections shown in Fig. 4.2.

The geological and geomorphological evolution of the Solofrana river valley has strongly affected its hydrogeological features. According to several studies carried out in early nineties (e.g., Celico et al., 1991; Celico and Piscopo, 1995; De Riso and Ducci, 1992), two aquifers characterize the valley at river basin scale. A shallow aquifer, consisting of pyroclastic alluvial deposits, is separated by a deeper carbonate aquifer by the intercalation of an extensive aquitard of Campanian grey tuff. The deeper aquifer is recharged by precipitations and indirect intake from carbonate bordering hydro-structures (Paduano and Fabbrocino, 2013). In particular, based on stratigraphic and well logs data and geological surveys, Paduano (2013) reconstructed the hydro-stratigraphic model of the Solofrana river valley along different cross-sections. In Fig. 4.2, two cross-sections located in the southern part of the valley, very close to our test site, are shown. As it can be seen in the figure, the presence of a multilayer aquifer at basin scale is clearly evident.

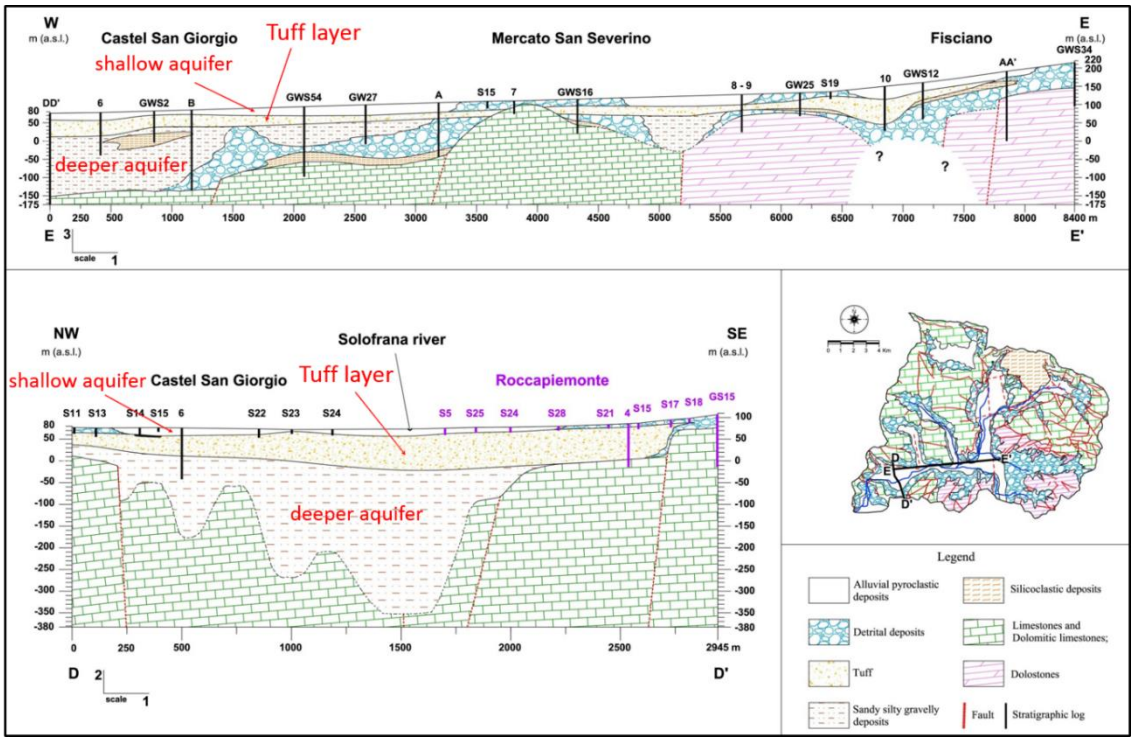

Figure 4.2 Hydro-stratigraphic architecture of the cross-sections along the EE' and DD' profiles indicated in Fig. 4.1 (after Paduano, 2013, modified).

4.3 Multidisciplinary study of the test site

The survey area (Fig. 4.3) is located close to the town of Castel San Giorgio (48 km east from Mt. Somma-Vesuvius, Naples, Italy) in the south-western basin of the Solofrana river valley (Salerno, southern Italy). It has been chosen as test site because its adjacency to the Solofrana river, which often causes floods submerging the surrounding land with polluted water and mud. In fact, since historical times, this river collects the wastewater (mainly effluents containing Cr(VI)) of many tanneries operating in the upper part of the Solofrana valley (Basile et al., 1985). In addition, as this area is continuously used for agricultural purposes, the presence of organic and/or inorganic contaminants would be also expected.

In order to identify and characterize possible contamination in the selected survey area, a multidisciplinary study, consisting of geoelectrical, stratigraphic, hydrogeological and hydrochemical data analysis, has been performed.

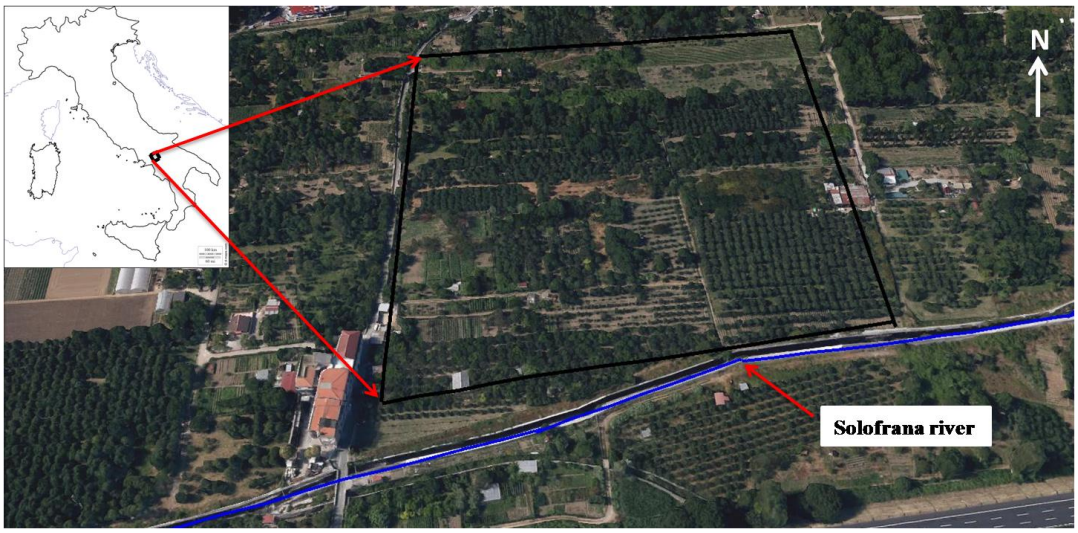

Figure 4.3 Map of the survey area (delimited with a black line) in the Solofrana river valley (Salerno, southern Italy).

4.3.1 Geophysical study

The geophysical survey in the test site (Fig. 4.3) consisted of resistivity, induced polarization (IP) and self-potential (SP) measurements along 15 profiles, each of length 235 m, oriented approximately N-S and E-W and grouped in three sub-areas (Fig. 4.4). The profile distribution was constrained by the presence of obstacles and the denied access to a private property.

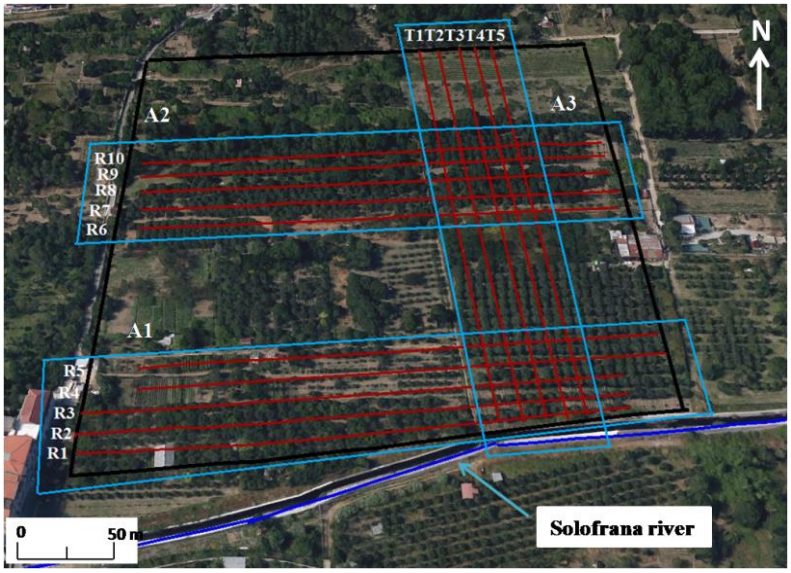

Figure 4.4 Distribution of the geoelectrical measurement profiles in the survey area.

Resistivity and induced polarization measurements

The apparent resistivity and induced polarization (chargeability) data were collected simultaneously along the fifteen profiles distributed in the three sub-areas (A1, A2, A3) of Fig. 4.4. The 2D tomographic technique was applied for the acquisition of both datasets by using a Syscal Pro 48 Switch georesistivity meter (IRIS Instruments) in multi-electrode configuration. As a reasonably good horizontal and vertical resolution was required, a Wenner-Schlumberger array was used (Loke, 2002) with the minimum and the maximum current electrode separation of 15 and 175 m, respectively, and the minimum potential electrode separation of 5 m. For each line, a total number of 514 measurements and an investigation depth of about 35 m below ground

level (b.g.l.) were attained. The inversion of the apparent resistivity (ERT) and chargeability (IPT) pseudosections was performed by using the Res2D algorithm (Loke and Barker, 1996; Loke and Dahlin, 2002), which consists of a least-squares deconvolution method based on a linear process between acquired apparent resistivity (or chargeability) values as a function of real resistivities (or chargeabilities). Thanks to the high spatial resolution planned for the ERT/IPT survey, the data collected by the two-dimensional tomographic technique were analyzed, for each sub-area of Fig. 4.4, by a pseudo-three-dimensional (3D) inversion procedure, according to the Res3Dinv algorithm (Loke and Barker, 1996), thus providing resistivity and chargeability value distributions of the three investigated buried sub-volumes (Di Maio et al., 2015a). For all the 2D and 3D inversion models, a root-mean square (RMS) misfit error less than 2.5% and 10%, respectively, was attained. Figures 4.5, 4.6 and 4.7 show volumetric views of the 3D inversion results obtained for the ERT and IPT profiles related to the areas, respectively, A1, A2 and A3 of Fig. 4.4. For a better visualization of the investigated volumes, the volume data are reported, for each area, with a cut-out transversal to the corresponding profiles direction.

Looking at the 3D resistivity images of Figs 4.5a, 4.6a and 4.7a, a three-layer electro-stratigraphy is clearly evident mostly for the areas A2 (Fig. 4.6a) and A3 (Fig. 4.7a). A shallow conductive layer, which extends to depths of about 10 m b.g.l., overlaps a horizontal more or less homogenous stratum, which enlarges from about 10 m to 25 m b.g.l and is characterized by relatively high resistivity values. The significant decrease in the resistivity values (20 - 40 Ωm), that is observed for all the three investigated sub-areas at depths greater than 25 m from the ground level, clearly identifies the presence of a permeable and porous formation, likely involved by a not negligible water content.

As it concerns the 3D chargeability maps of Figs 4.5b, 4.6b and 4.7b, they generally show low-chargeability value distributions (with values less than 20 mV/V), even if such a trend is locally interrupted by high-chargeability anomalies mostly for the area A1 (Fig. 4.5b). Indeed, in the northernmost part of this area, in correspondence of the progressive 80 m along the *x*-axis, a

sector characterized by high chargeability values (> 80 mV/V) is observed from about 5 m b.g.l. down to the maximum exploration depth (see black lines in Fig. 4.5b). Interestingly, as it can be seen in Fig. 4.5a, this sector is also characterize by relatively low resistivity values (20 - 40 Ω m). As the geological formations of the survey area (see figure 4.2) are not prone to induced polarization phenomena, the simultaneous occurrence of low resistivity and high chargeability values suggests the possible presence of contamination sources.

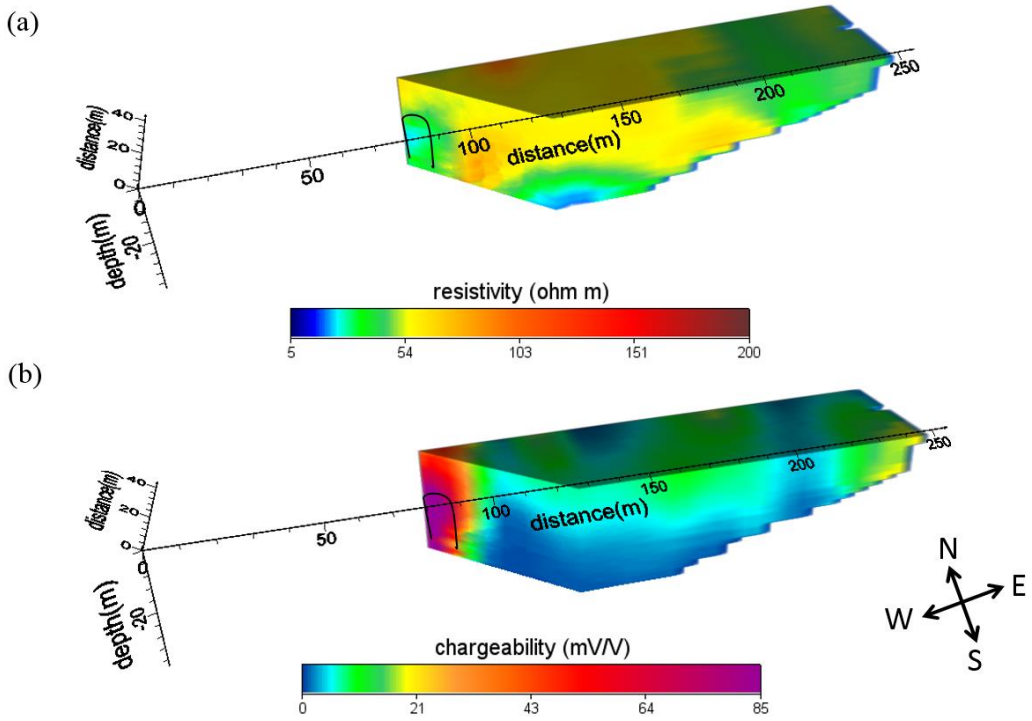

Figure 4.5 Volumetric view of the 3D inversion of the 2D ERT (a) and IPT (b) data obtained from the survey carried out in the sub-area A1 of Fig. 4.4, with a cut-out transversal to the direction of the measurement profiles.

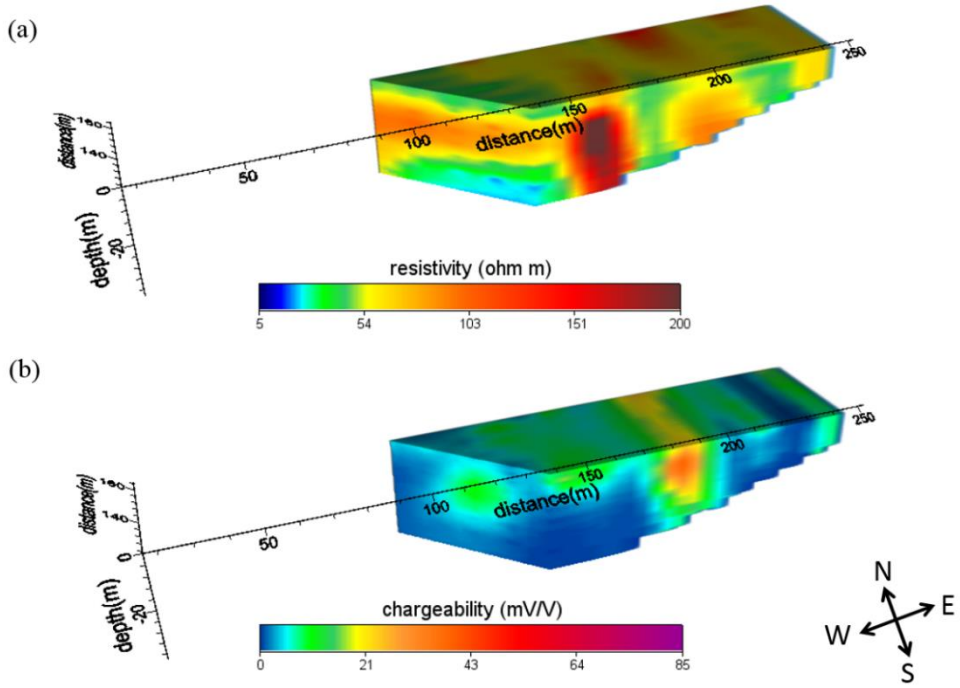

Figure 4.6 Volumetric view of the 3D inversion of the 2D ERT (a) and IPT (b) data obtained from the survey carried out in the sub-area A2 of Fig. 4.4, with a cut-out transversal to the direction of the measurement profiles.

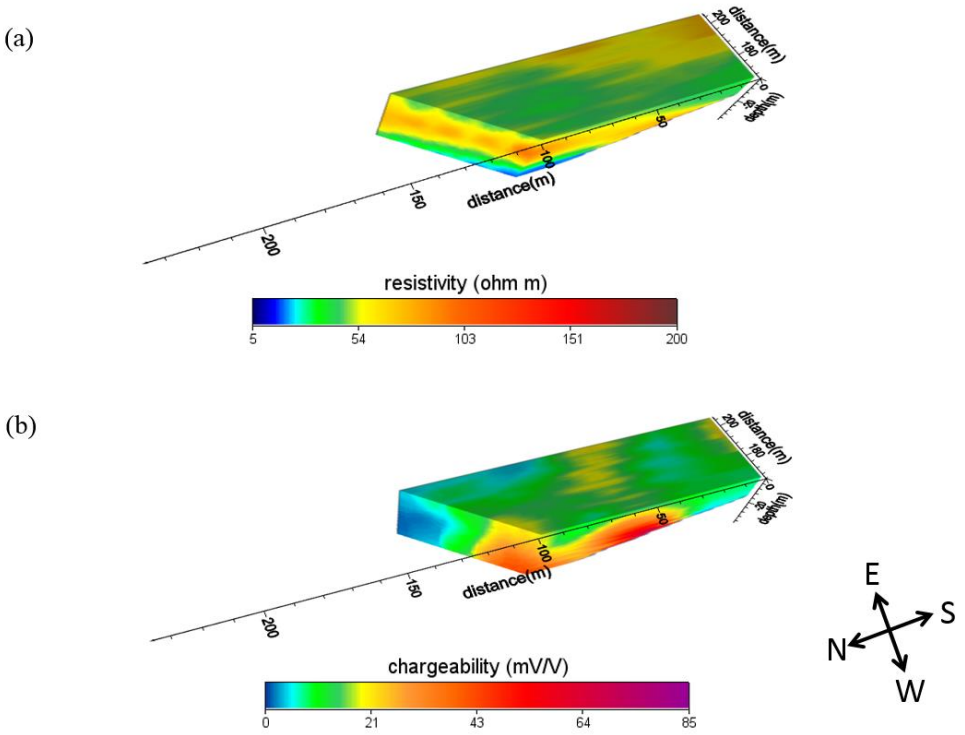

Figure 4.7 Volumetric view of the 3D inversion of the 2D ERT (a) and IPT (b) data obtained from the survey carried out in the sub-area A3 of Fig. 4.4, with a cut-out transversal to the direction of the measurement profiles.

Self-potential measurements

Based on the results of the ERT and IPT prospecting in the sub-area A1, which indicate the presence of electrical anomalies likely related to contamination phenomena, the self-potential (SP) study was mainly focused on this sub-area.

The SP data were acquired along the ERT/IPT profiles by the gradient (leap-frog) technique using non-polarizable electrodes with an inter-electrode spacing of 2.5 m. The survey lines were interconnected at the end of each profile to form a continuous measurement circuit that provided the SP anomaly map of Fig. 4.8. As it can be seen, at large scale, an increasing trend of the SP values from north-west to south-east is clearly visible, whilst localized nuclei, characterized by relatively high negative SP values (-30 mV to -45 mV), are mainly observed in the northernmost part of the map, where resistivity and chargeability values have shown anomalous behaviors (see Fig. 4.5) tentatively associated to a contaminated sector. To confirm this assumption, the modeling of a SP profile crossing the negative anomaly centered at 80 m along the *x*-axis (black line in Fig. 4.8) was performed to determine the depth of its causative source (Di Maio et al., 2015 a). Looking at the shape of the in-depth high-conductivity and -chargeability body (black lines in images of Fig. 4.5) corresponding to the position of the SP anomaly, a vertical cylinder-type source was chosen to model the SP anomaly.

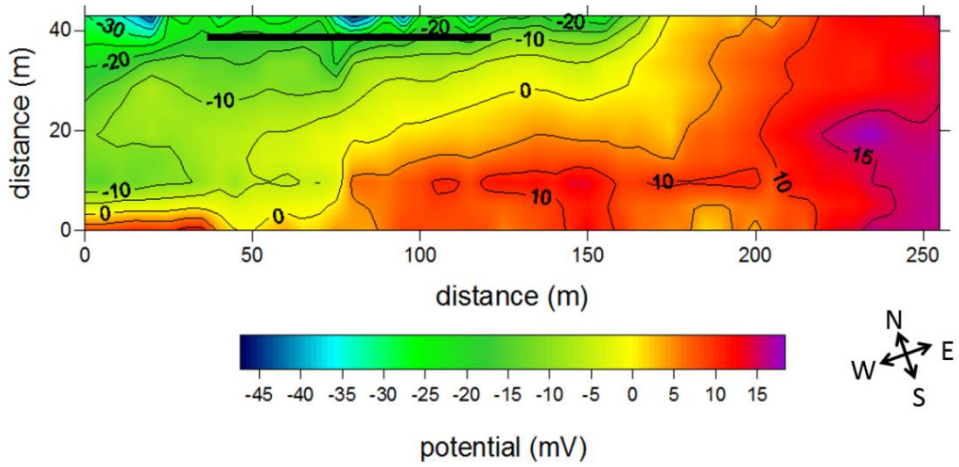

Figure 4.8 SP anomaly map observed for the survey area A1 of Fig. 4.4. The black line indicates the SP profile chosen to model the SP negative anomaly centered at 80 m along the *x*-axis.

As discussed in Chapter 2 (Section 2.2), the SP detected at any surface point $P(x)$ along a profile line perpendicular to the strike of a vertical cylinder can be expressed by eq. (2.3):

$$V(x) = K \frac{(x - x_0)\cos\alpha - z_0 \sin\alpha}{\left[(x - x_0)^2 + z_0^2\right]^p}, \tag{4.1}$$

where K is the electric dipole moment, α is the polarization angle measured from the horizontal positive clockwise, x_0 and z_0 are the coordinates of the body center axis and p is the shape factor related to the form of the buried structure, which is 0.5 in case of semi-infinite vertical cylinder.

A numerical analysis was performed by changing the values of the key parameters: K, α and z_0 in eq. (4.1). Figure 4.9 shows the synthetic curve (red continuous line) that better approximates the experimental data; it has been obtained for a source depth located at 5 m from the surface level, which is the depth of the high conductivity and chargeability structure identified by the resistivity and IP tomographies. Looking at Fig. 4.9, it clearly emerges that the results provided by the simple forward modeling given by eq. (4.1) do not reproduce the experimental curve in the far west of the profile. In such a sector, indeed, the distribution of the field data suggests the presence of more than one anomalous source and a further more detailed modeling is required.

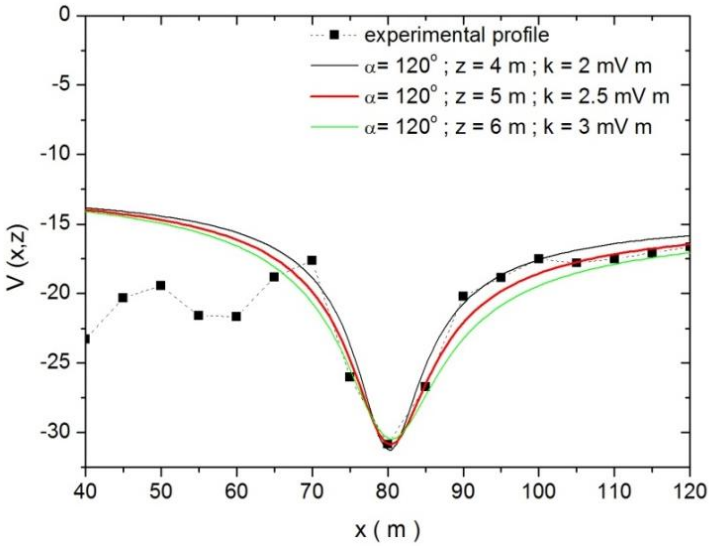

Figure 4.9 Comparison between experimental and modeled SP data. Symbols: SP data observed along the profile indicated with a black line in the map of Fig. 4.8. Continuous lines: SP anomaly curves obtained for a vertical cylinder source model centered at 80 m along the x-axis and located at different depths (z) from the ground surface. α and K indicate the polarization angle and the electric dipole moment, respectively.

4.3.2 Stratigraphic and hydrogeological study

In order to retrieve the stratigraphic setting of the survey area, an analysis of data from shallow and deep wells (de Riso and Ducci, 1992) located in Roccapiemonte and Castel San Giorgio sites (approximately close to the test area, see Fig. 4.1), has been performed. A total of 62 shallow wells and 2 deep wells (black dots and red triangles in Fig. 4.10a, respectively), were analyzed. Fig. 4.10a shows the distribution of the tuff roof indicated by black solid contour lines with a spacing of 5 m. For a better visualization of the tuff morphology in the geophysical survey area, a smaller contour interval of 1 m (black dashed lines) has been used. Considering the elevation (about 80 m above sea level) of the survey area, it was found that the top of the grey tuff layer in the test site is placed at a depth of 11-13 m b.g.l. (Fig. 4.10b). As it can be seen from the stratigraphic sequence of Fig. 4.10b, a sandy-ashes pyroclastic deposit, with presence of pumiceous material, overlay the tuff layer, thus defining the thickness of the shallow aquifer in the investigated area.

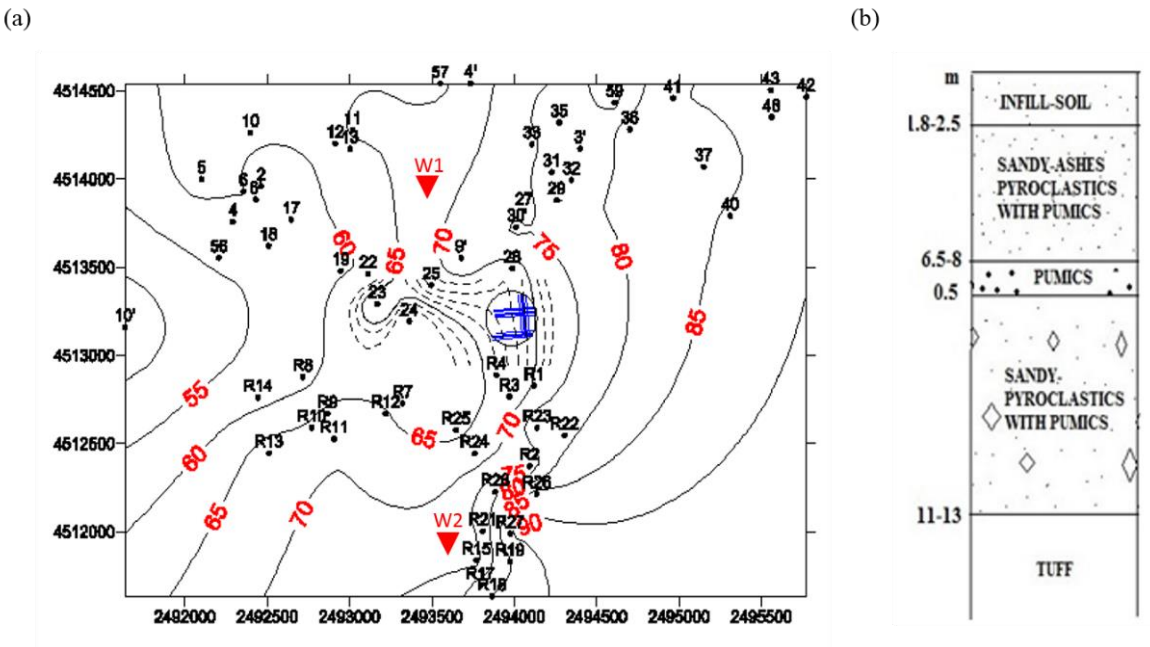

Figure 4.10 (a) Morphology of the roof of the Campanian grey tuff (black solid and dotted contour lines, measured in meters above sea level). Black dots indicate shallow wells in the Roccapiemonte (R_i dots) and Castel San Giorgio (numbers) sites; red triangles identify deep wells; blue lines delineate the geoelectrical profiles. (b) Stratigraphic sequence of the survey area retrieved from the well log analysis.

As it concerns the definition of the groundwater flow direction in the survey area, an analysis of piezometric head measurements, obtained by the wells closest to the test site, was performed. Figure 4.11 shows the piezometric map determined from three wells surrounding the area. Interestingly, an inverse correlation is observed between the groundwater flow direction (arrowed lines in Fig. 4.11) and the increasing trend of the SP values detected in the sub-area A1 (Fig. 4.8).

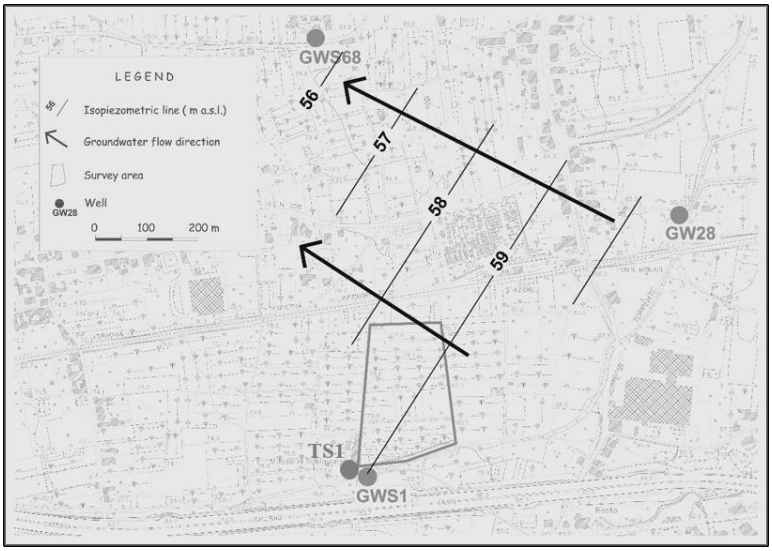

Figure 4.11 Isopiezometric map (continuous black lines) determined from the piezometric head values measured in the three wells: GWS1, GW68, GW28. The arrowed thick lines indicate the groundwater flow direction in the survey area. TS1 is the location of the water sample collected from the Solofrana river.

4.3.3 Hydrochemical study

The hydro-chemical study is mainly consisted of hydrochemical facies characterization of water samples to evaluate groundwater quality in the investigated area. The hydrochemical analyses were performed on groundwater samples collected from the Solofrana river (TS1 in Fig. 4.11) and wells located nearby the test site (GWS1, GW68, GW28 in Fig. 4.11). Table 4.1 shows the results of the performed analyses. Then, the obtained analytical values were plotted on piper (Fig. 4.12a and b) and Schoeller Berkaloff (Fig. 4.12c and d) diagrams to determine the

hydrochemical facies and the ground water quality, respectively, of the analyzed samples (Di Maio et al., 2015b). As the survey area is highly affected by anthropic activities due to nearby tanning factories and agricultural activities, the distribution of cations and anions in the river water sample TS1 (blue line in Fig. 4.12c) shows an amount of chloride and sulphate higher than that observed for the well water samples. Such result is in good agreement with the piper classification diagram (red circle in Fig. 4.14a) that indicates the presence of elements due to anthropic activities, such as Na, K, Cl SO4, in the river water. Moreover, in order to identify possible time variations of the hydrochemical characteristics of the river water near the test site, likely due to anthropogenic processes, piper and Schoeller Berkaloff diagrams (Figs 4.12b and d) have been constructed for water samples collected from the well closest to the river (i.e. GWS1) at different times (Paduano, 2013). Looking at the Figs 4.12b and d, it is clearly evident that no significant variations in hydrochemical facies and water quality are observed over the time.

Concerning the presence of heavy metals in the analyzed water samples, the results of the hydrochemical analyses (Table 4.1) indicate that generally there is not presence of contamination according to Italian regulations, except for nitrate (NO3-), which shows a slightly higher value (see Table 4.1) than the threshold value of 50 mg/L. However, a significant concentration of total chromium (Cr) is observed, even if only the concentration value obtained for the river water sample TS1 is above the Italian threshold value (0.050 mg/L). This is also consistent with the results of previous hydrochemical analyses (Paduano, 2013) performed at basin scale, which found total chromium concentration values greater than the Italian threshold value.

Nom	pH	EC	SiO2	°F	HCO3-	Cl-	SO4--	NO3-
		µS/cm	mg/L	mg/L	mg/L	mg/L	mg/L	mg/L
GWS1	7.35	1104	41.7	36.0	524.5	89.4	67.2	**50.8**
GW28	7.76	951	39.0	45.6	365	75.3	70.9	**57.9**
GW68	7.25	806	41.0	42.0	378	47.4	56.2	**63.2**
TS1	8.03	1952	26.4	32.0	390	322	227.7	29.7

Nom	NO2--	F-	Br-	PO43-	Ca++	Mg++	Na+	K+
	mg/L	mg/L	mg/L	mg/L	mg/L	mg/L	mg/L	mg/L
GWS1	0.03	0.59	<0.15	<0.2	100	26.7	89.2	24.7
GW28	0.02	0.5	<0.15	0.44	120	37.9	49	16.7
GW68	0.04	0.49	<0.15	0.12	104	38.9	24.9	17.0
TS1	0.03	0.52	<0.15	0.72	84.8	26.2	316.3	19.7

Nom	Mn++	NH4+	Li+	Sr++	Al+++	Ba++	H3BO3	Zn++
	mg/L	mg/L	mg/L	mg/L	mg/L	mg/L	mg/L	mg/L
GWS1	-	0.030	0.004	0.40	0.026100	0.019896	0.627000	0.023796
GW28	-	0.025	0.003	0.42	0.018800	0.038051	0.325000	0.005131
GW68	-	0.026	0.003	0.29	-	0.005416	0.325000	0.071900
TS1	0.014	0.028	0.004	0.23	0.009840	0.017031	0.536000	0.070481

Nom	Cd+	As	Cr	Pb ++	Cu++	Se++	Co++	Rb+
	mg/L	mg/L	mg/L	mg/L	mg/L	mg/L	mg/L	mg/L
GWS1	0.000013	0.001257	0.034172	0.000116	0.000430	0.000426	0.000313	0.067091
GW28	-	0.001658	0.009760	0.000025	0.000532	0.000468	0.000095	0.035215
GW68	-	0.001503	0.001420	0.000008	0.000574	0.000682	0.000016	0.036582
TS1	0.000097	0.001079	0.220704	0.000967	0.020362	0.000354	0.002220	0.032664

Table 4.1 Hydrochemical analysis of water samples collected from wells (GWS1, GW68, GW28) and Solofrana river (TS1). Red values indicate nitrate (NO3-) and chromium (Cr) concentrations greater than the Italian threshold values, respectively, 50 mg/L and 0.050 mg/L.

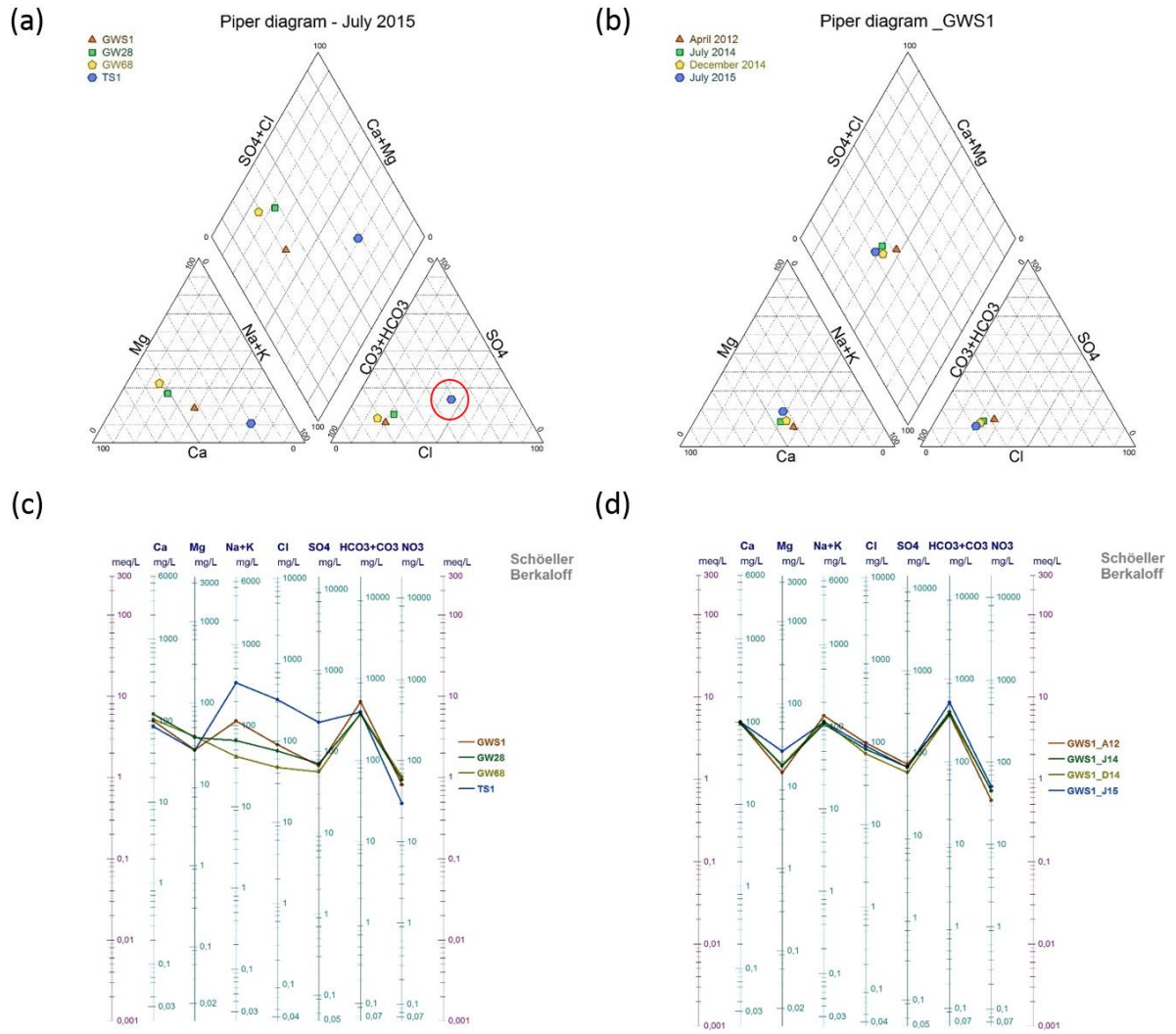

Figure 4.12 Piper (a and b) and Schoeller Berkaloff (c and d) diagrams showing the hydrochemical facies and the groundwater quality, respectively, for the analyzed water samples. (a) Hydrochemical characteristics of the analyzed water samples. (b) Time evolution of the hydrochemical characteristics of the water sample collected from the well GWS1 that is located near the test site (see Fig. 4.11).

On the other hand, presence of ammonium ions (NH4+) is also observed, which could indicate the possible occurrence of ammonium compounds, i.e. organic contaminants, such as Quaternary ammonium compounds (QACs), which are commonly used for agricultural and industrial purposes as surfactant and emulsifiers. The evidence of concentrations of ammonium less than the Italian threshold value (0.050 mg/L) in the survey area does not mean that a low quantity of QACs is present. In fact, as demonstrated by Tezel (2009), high concentration values of QACs can transform in very low amounts of amines and ammonia (Fig. 4.13).

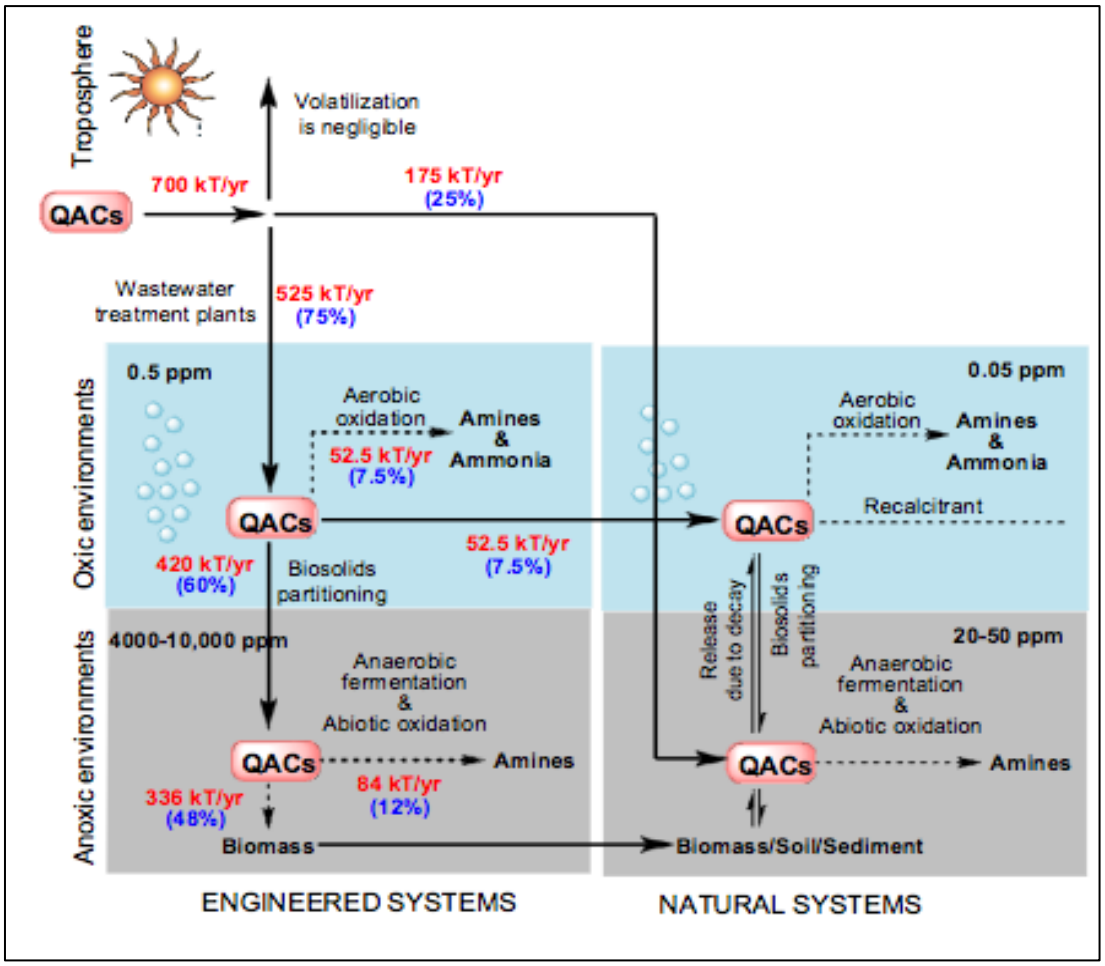

Figure 4.13 Schematic representation of QAC fluxes and expected QAC concentration levels in different compartments of engineered and natural systems calculated on the base of global QAC consumption (after Tazel, 2009)

4.4 Integrated interpretation of geoelectrical, hydrostratigraphical and hydrochemical data

In the following, an integrated interpretation of all the results coming from the multidisciplinary study illustrated in the previous Section is discussed.

The joint interpretation of the stratigraphic data analysis (Fig. 4.10) and the ERT prospecting results (Figs 4.5a, 4.6a, 4.7a), allows to obtain the stratigraphic-geological modelling of the survey area. For a more clear description of the model, Fig. 4.14 compares the stratigraphic sequence of Fig. 4.10b and two resistivity sections extracted from the 3D images of Fig. 4.5a and 4.6a. As it can be seen from the figure:

- the shallow resistive layer, with resistivity values ranging from about 20 Ωm to 50 Ωm, is ascribable to pyroclastic and alluvial deposits, with majority of sandy materials, shown in the upper part of the stratigraphic sequence of Fig. 4.10b;

- the most resistive layer, about 15 m thick and characterized by resistivity values varying in the range 60 - 130 Ωm, can be associated to the Campanian grey tuff layer detected by the stratigraphic analysis (Fig. 4.10b) at depths of 11-13 m from the ground surface. The discontinuous distribution of the resistivity values suggests that the lateral continuity of the layer is locally interrupted by alteration/disintegration phenomena likely induced by an inside water circulation;

- the deep conductive pattern, which is observed down to the maximum exploration depth and is characterized by resistivity values in the range 20 - 40 Ωm, could identify the presence of the deep aquifer recognized by previous hydrogeological studies at regional scale (Celico, 1988; de Riso and Ducci, 1992).

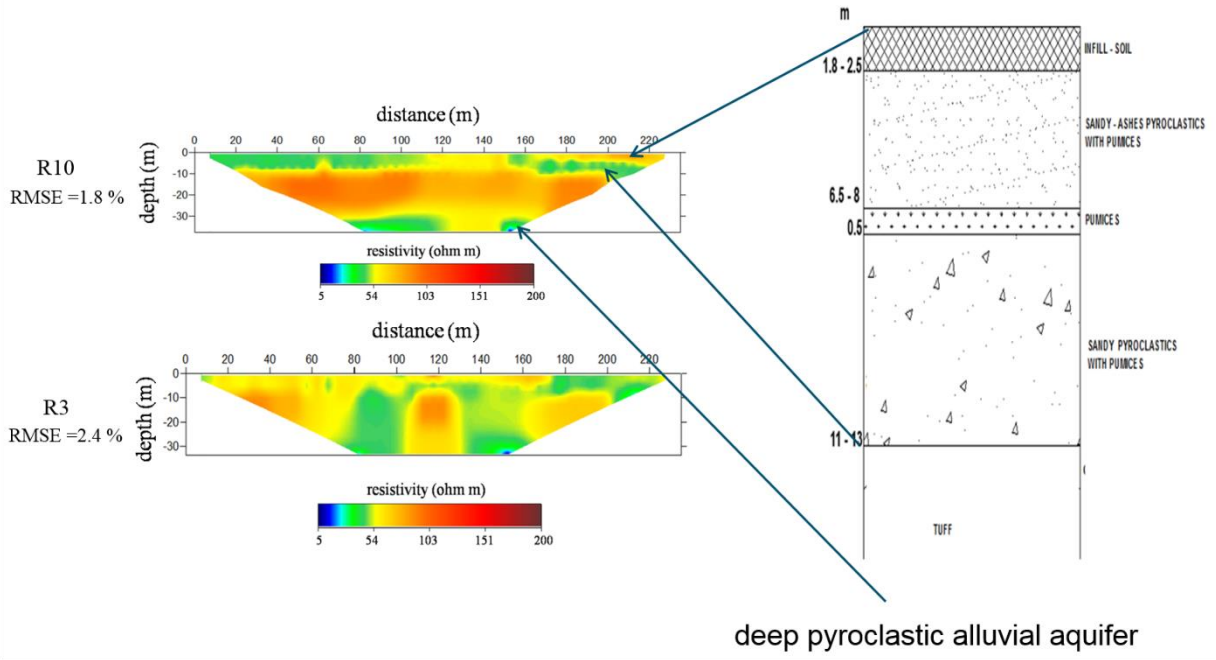

Figure 4.14 Comparison between the stratigraphic sequence of Fig. 4.10b and two resistivity sections extracted from the 3D images of Fig. 4.5a and 4.6a along the profiles R3 and R10 located, respectively, in the sub-areas A1 and A2 (see Fig. 4.4).

As it concerns the definition of possible contamination of the survey area, the IPT results (Figs 4.5b, 4.6b, 4.7b) are compared with the results of the hydrochemical study illustrated in Section 4.3.3. Different sectors characterized by high chargeability values have been found for all the investigated sub-areas, which could be related to underground pollution. However, the integration of ERT and IPT results with the hydrochemical analyses discriminates the sector shown in Fig. 4.15 as possible contaminated site. Indeed, such sector is in the sub-area A1, which is the closest to the Solofrana river, and is characterized by high chargeability and conductivity values that suggest the presence of heavy metals. In particular, the hydrochemical study indicates the Cr as possible contamination source, due to the high concentration value observed for water samples collected from the river (TS1 in Fig. 4.11) and the well closest to the sub-area A1 (GWS1 in Fig. 4.11). In particular, the Cr concentration detected for the river sample is much larger than the threshold value.

	GWS1	GW28	GW68	TS1	*
Zn (µg/L)	23.8	5.1	71.9	70.5	3000
Cr tot (µg/L)	34.2	9.8	1.42	221.0	50
Cu (µg/L)	0.43	0.53	0.57	20.4	1000
Al (µg/L)	26.1	18.8	-	9.8	200

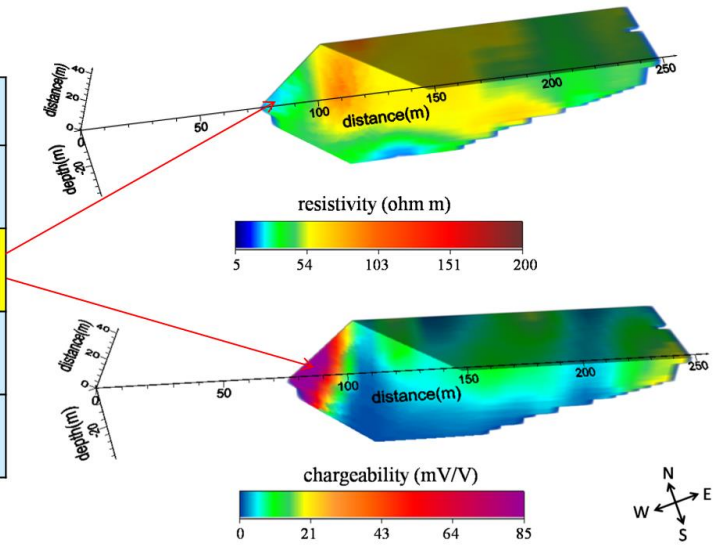

Figure 4.15 Table: concentrations (in µg/L) of heavy metals in the analysed groundwater samples collected from river water (TS1) and different wells (see Fig. 4.11); last column (*) indicates the Italian threshold values for the considered chemical species. Images: two cut-outs of the volumetric distribution of the resistivity and chargeability values observed for the sub-areas A1 (see Fig. 4.4); the cut-out is transversal to the direction of the measurement profiles.

Moreover, in order to study the diagenetic processes that control the hydrogeological behaviour of the widespread pyroclastic lithostratigrafic unit observed for the test site, a new approach that integrates self-potential data with hydrogeological and hydrochemical data has been experienced. In particular, the study focuses on the analysis of the SP electrokinetic component at the aim to test its effectiveness in defining possible groundwater contamination.

In contaminated sites, SP signals originate essentially from two main components: (1) electrokinetic component, associated with the groundwater flow and (2) electrochemical component, associated with oxido-reduction phenomena (Nyquist and Corry, 2002; Naudet et al., 2003; 2004). The electrokinetic component is usually studied to determine the shape of the piezometric surface, which is often not well constrained due to the lack of observation wells. For most earth materials, like silica rocks, the solid surface exhibits a negative charge that generates a negative potential (so-called *zeta potential*) at the solid/fluid interface. Thus, an excess of positive charge in the fluid results. This charge separation is described by the physics of the double layer model at the solid/fluid interface (Revil et al., 2012). Fig. 4.16 shows the double layer model for a silica grain: the fixed negative charge on surface is compensated by mobile charges present in the electrical double layer including the Stern layer of adsorbed counter ions and the diffuse layer. Drag of the excess positive charge under a hydraulic gradient results in a streaming current density.

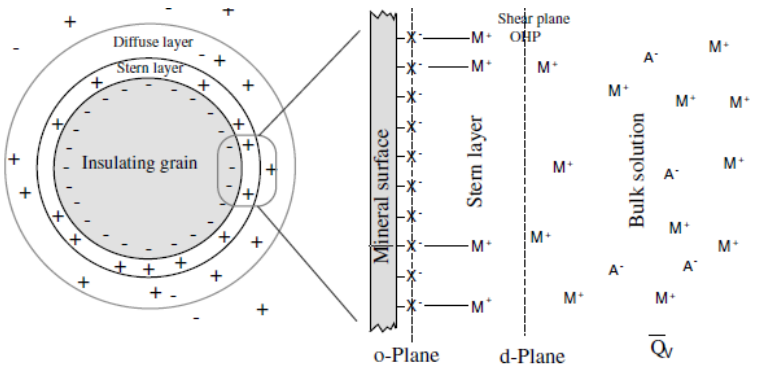

Figure 4.16 Sketch of the electrical double layer at the pore-water/mineral interface coating a spherical grain. The Stern layer is comprised between the o-plane (mineral surface) and the d-plane, which is the inner plane of the electrical diffuse layer (OHP stands for outer Helmholtz plane). The diffuse layer extends from the d-plane into the pores (after Revil and Florsch, 2010; Revil et al., 2012).

For characterizing the hydrodynamic conditions of the studied high flood risk area, the SP electrokinetic component of the SP anomaly map of sub-area A1 shown in Fig. 4.8 has been estimated from the correlation with the piezometric level (Fig. 4.17) by using the expression given by Revil et al. (2003):

$$\varphi - \varphi_0 = C'(h - h_0)\,,$$

where φ represents the self-potential at the measuring station corresponding to the piezometric head h, while φ_0 and h_0 represent, respectively, the self-potential and the piezometric head at the SP base station. Here, $\varphi_0 = 0\ mV$ by definition and C' is the electrokinetic coupling coefficient in mV. Interestingly, unlike most common cases, it has been found that the electrokinetic coefficient is positive, meaning that negative ions are carried in the groundwater flow direction. Indeed, comparing the SP electrokinetic component map (Fig. 4.18), retrieved from the correlation with the piezometric level, with the groundwater flow direction in the survey area, estimated as described in Section 4.3.2 (see Fig. 4.11), a clear inverse correlation is observed between the groundwater flow direction and the increasing trend of the SP electrokinetic component.

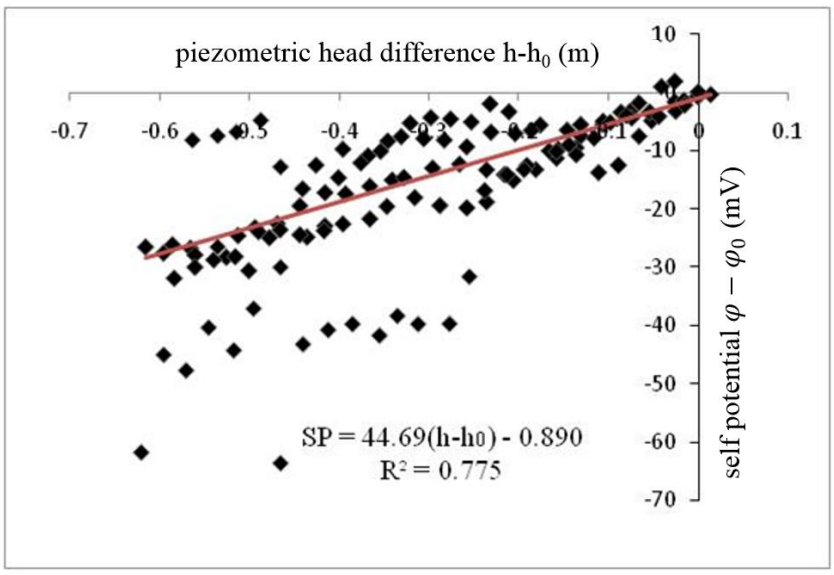

Figure 4.17 Correlation between piezometric head and SP values.

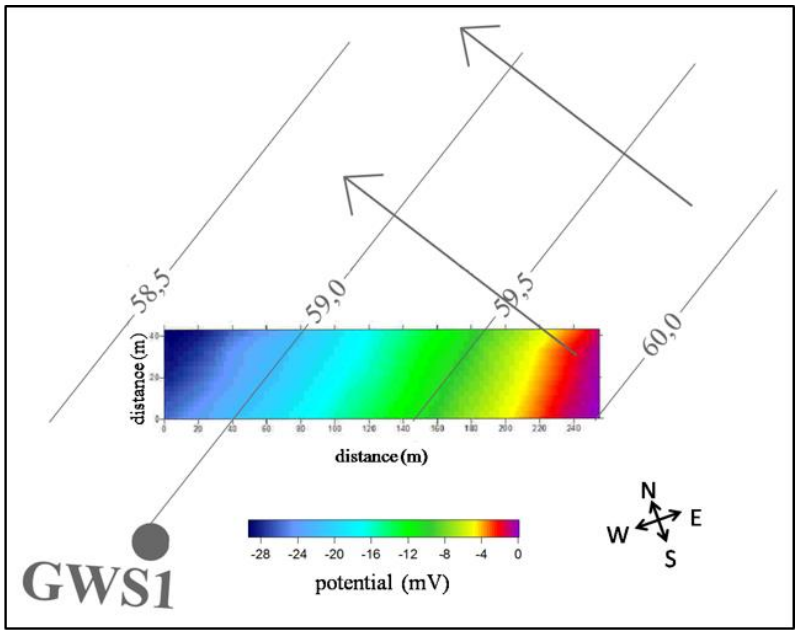

Figure 4.18 SP electrokinetic component map retrieved from the correlation with the piezometric level observed in the survey area (see text). Black continuous lines: isopiezometric contours (m a.s.l. – meters above sea level); arrowed thick lines: groundwater flow direction (see Fig. 4.11).

According to Ishido and Mizutani (1981) and Revil (2002), the Stern model could justify the inversion in sign of the charge carriers only in case of acid environment, but this is not the case of the tested site. Thus, drawing inspiration from the results of the hydrochemical study (see Section 4.3.3), we tentatively attribute to the Quaternary Ammonium Compounds (QACs) present in the study area the cause of the inversion in sign of the charge carriers observed in the SP electrokinetic component map (Di Maio et al., 2015b). Specifically, we suggest that the surfactant effect of the QACs could have modified the surface of the zeolites, giving them a property of anionic exchange. Fig. 4.19 shows a schematic representation of the adsorption of such surfactant on zeolites, which, in turn, should lead to an excess of negative mobile charges in the diffuse layer (see Fig. 4.16).

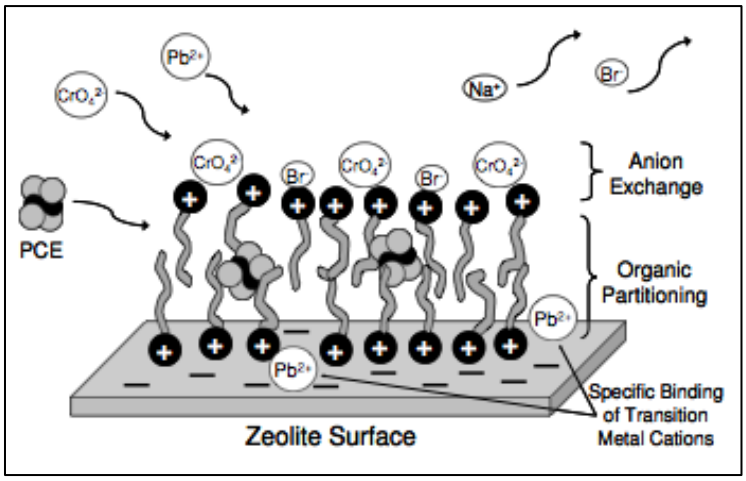

Figure. 4.19 Schematic representation of modification of a zeolite surface by surfactant effect of QACs (Schulze-Makuch et al., 2004, modified).

Summarizing, a multidisciplinary approach that integrates geophysical, hydrogeological and geochemical data has been proposed for the study of soil and groundwater contamination. A test performed on a sample area, often affected by floods with polluted water and mud, has shown that the integration of electric-type geophysical parameters, like resistivity, induced and natural electrical polarization, with hydrogeological data allows to detect and characterize the aquifers, their geometry and heterogeneity, and to identify flow direction and possible contamination of the groundwater. Specifically, the resistivity measurements revealed, in a very good agreement with the hydrogeological data analysis, the presence of a grey tuff layer interposed between two aquifers consisting of pyroclastic-alluvial deposits. The lack of lateral continuity of the tuff layer was attributed to alteration/disintegration phenomena induced by circulation of water likely including pollutant species, as suggested by the high-chargeability values observed in some localized sectors of the investigated volume. The resistivity and chargeability data provided good constraints to model a localized SP anomaly probably linked to presence of contaminants. Moreover, an integrated interpretation of SP data with hydrochemical analysis performed on water samples collected in the sample area allowed to individuate

diagenetic processes, which likely control the hydrogeological behaviour of widespread pyroclastic lithostratigraphic unit in saturated conditions.

4.5 Cellular automata modeling for simulating fluid infiltration

In order to study possible risk scenarios for groundwater pollution of the investigated soils, a simple cellular automaton model (see Section 2.3.1) has been developed for simulating contaminant infiltration induced by flooding phenomena.

Specifically, a two-dimensional square grid of 64x64 cells is used to model a vertical section of the survey area. As it can be seen from the resistivity section along the R10 profile shown in Fig. 4.14, the buried volume can be described, in first approximation, by three homogeneous layers: a shallow conductive layer of thickness 10 m, associated with pyroclastic and alluvial deposits with majority of sandy materials, a more resistive stratum 15 m thick, associated with the Campanian grey tuff, and a deep pyroclastic layer recognized as a deep aquifer. The porosity values, n_i, that characterize the three layers (Fig. 4.20) have been assigned according to estimates given in (Picarelli et al., 2007) for the investigated soils.

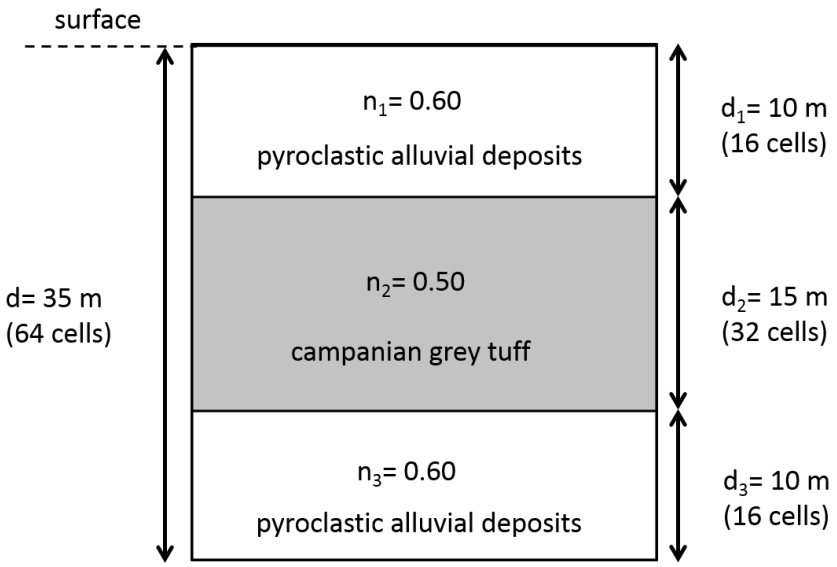

Figure 4.20 Schematic representation of the model grid that shows thickness and porosity values for each layer.

Since the 64 cells of the grid are associated to a vertical depth of 35 m (see Fig. 4.20), the size of the automaton cells is about 1.8x1.8 m^2. The properties of the system have been studied by collecting statistics on $5 \cdot 10^7$ different initial configurations. In Fig. 4.21, the characteristic time, t_{peak}, takes by the contaminant to reach the travelled distance L is plotted as a function of L. As it can be seen, the relationship between the characteristic travel times and the (travelled) distances is linear with a good approximation. As expected, the infiltration rate is constant within the first layer and it is slightly affected by the tuff layer. However, although the porosity difference between the layers is quite small, the effect of the soil discontinuity is visible in the slight change of the curve slope. The error bars in the plot are estimated by considering the width at half the peak height. As expected, the length of such vertical bars increases as the peak of the conditional probability of observing the contaminant at the time t and at distance L from the top of the grid is less well-defined by increasing the contaminant infiltration depth.

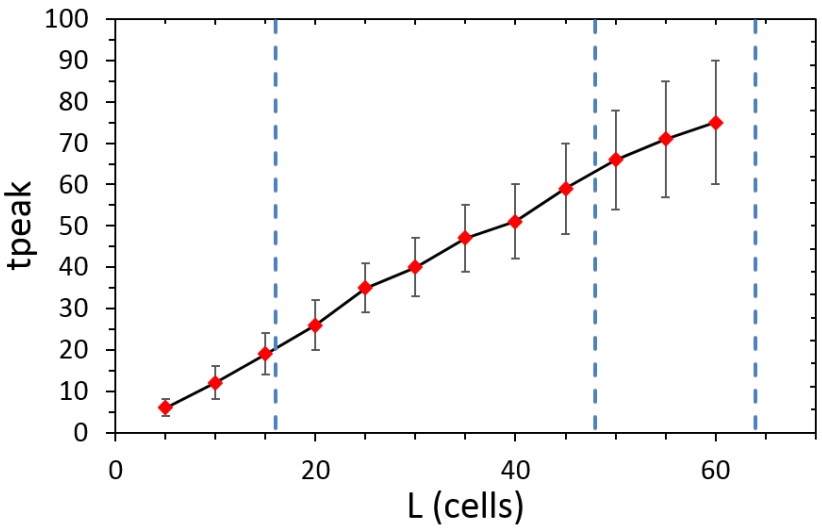

Figure 4.21 Times related to the peaks of the probability distributions according to the distance L travelled by the contaminant.

4.6 Further work

The present case study has outlined the significance of joint analysis of geoelectrical, hydrogeological and hydrochemical data to monitor soil and groundwater contamination. In particular, the integrated interpretation of self-potential and hydrogeological data has shown a negative correlation between SP and groundwater flow direction, which could be explained by the surfactant effect due to the presence of quaternary ammonium compounds related to the agricultural activities. In this regard, further work will be focused on the analysis of SP and groundwater flow correlations in other flood risk areas with similar land use. Moreover, the study of the relationships between the SP residual map, related to the electrochemical component of the observed SP data, and the redox potential will be performed in order to characterize the contaminated areas and to strengthen the results of the ERT and IPT prospecting.

Finally, as it concerns the modeling of contaminant infiltration, further research work will be devoted to a more accurate study of the proposed cellular automata model. In particular, numerical simulations will be performed to analyze how infiltration rate changes with depth at the aim to define the most dangerous scenario, that is, when the contaminant reaches the deepest aquifer.

Conclusions and perspectives

The research activity developed for my PhD was focused on development, testing and application of data inversion methods and numerical models for solving environmental problems linked to contaminant detection and transport in soil and groundwater.

First, three different approaches for self-potential data inversion, respectively based on spectral, tomographical and global optimization methods, have been proposed and tested on synthetic and field data.

As regards the spectral approach, three methods, i.e. classical periodogram method (PM), high-resolution multi taper method (MTM) and maximum entropy method (MEM) have been first applied on SP data, in particular for estimating the depth of the anomaly causative sources. An extended comparative study among the three proposed methods has been performed by applying the spectral methods to SP synthetic data generated by simple geometrical bodies, such as sphere, horizontal and vertical cylinder and inclined sheet. The main results of this numerical analysis is that generally MEM is able to give depth values closer to actual values than those provided by PM and MTM. The effectiveness of the proposed spectral approach has also emerged from the analysis of SP experimental signals. Indeed, a very good correlation of the obtained depth values with those provided by other numerical methods has been found (Rani et al., 2015; Di Maio et al., 2017).

Although the spectral approach has proved to be able to provide an accurate depth estimation of the SP anomaly sources, for their full characterization a combination of spectral methods with other inversion methods is required. Hence, an approach based on integration of spectral analysis and 2D tomographic technique has been proposed. In such an approach, MEM has been used to find the source depth and, then, COP distribution has been computed to get information about the polarization angle and the position of the anomaly source. Specifically, from the numerical study performed on synthetic examples of horizontal cylinders and inclined

sheets, mathematical equations that link the lines of zeros of COP function with polarization angles and horizontal position of the causative sources along the profile have been found. By using such equations for the analysis of field examples, a good agreement has been retrieved between the estimated source parameters and the results obtained from different numerical methods, which has demonstrated the potentiality of integrating high resolution spectral analysis and tomographic approach (Di Maio et al., 2016a).

Finally, in order to fully characterize anomalous bodies responsible of the observed SP signals without any a priori information on their shape, a global optimization approach based on a hybrid genetic-price algorithm (GPA) has been proposed. An extensive numerical analysis on SP signals affected by different percentage of white Gaussian random noise have shown that the GPA is able to provide fast and accurate estimations of the true parameters for all tested examples. In particular, the calculation of the root-mean squared error between the true and inverted SP parameters is found to be crucial for the identification of the source anomaly shape. Finally, applications of the GPA to self-potential field data have demonstrated the effectiveness of such an approach for SP data inversion (Di Maio et al., 2016b).

In future research, the proposed SP data inversion methods will be extended to apply them on multiple SP anomaly sources. In particular, the application of the Genetic-Price algorithm on complex field examples is in progress.

As concerns the development of numerical methods for modeling contaminant propagation in soil and groundwater, two cellular automata have been proposed to simulate diffusion-dispersion processes in saturated and unsaturated conditions. Then, the developed models have been applied to two field cases.

The first test area is located in the western part of the island of Crete (Greece) close to the Keritis river and close to an olive oils mills waste (OOMW) deposition pond. In this case, contamination is mainly due to phenol concentrations from OOMW, which can propagate

through the soil in vertical direction reaching the saturated zone at a depth of about 5 m or in horizontal direction towards the river. The area has been characterized by previous geological, geochemical and geophysical studies. In particular, by applying a combination of the three proposed SP data inversion methods, it has been possible to characterize the SP anomaly source and follow its evolution over time.

On the basis of the geological and geophysical characterization of the area, a cellular automaton model has been developed for simulating contaminant diffusion in the unsaturated zone. The CA grid represents the vertical section of a three layers model, where each cell describes a small portion of soil characterized by the values of three physical parameters: electrical resistivity, porosity and contaminant concentration. By using a relation rule typical of critically self-organized systems and performing an analysis by varying the diffusion transfer coefficients, the simulation results suggest very likely contaminant percolation in the saturated zone in two specific periods of the year.

Finally, a finite element model based on FEFLOW simulation software has been developed for simulating the groundwater flow and contamination transport under unsaturated and saturated conditions of the survey area. The flow calibration has shown a good agreement between observed and computed hydraulic heads, while the study for mass transport and calibration with resistivity and geochemical data is in progress.

The second selected test area is located in southern Italy close to the Solofrana river and it is often affected by floods with polluted water and mud. The area has been first characterized by a multidisciplinary study, which has integrated the results of a geoelectrical survey, consisting of resistivity and induced polarization tomographies and SP profiles, with hydrogeological and geochemical data. In particular, resistivity and hydrogeological data have identified the presence and the thickness of a tuff layer interposed between two pyroclastic aquifers. The geochemical analysis performed on water samples collected from river and wells located near the survey area

has allowed to define the groundwater quality and the nature of the possible contaminant. Finally, a negative correlation found between groundwater flow and SP electrokinetic component revealed the unusual sign of charge carriers along the groundwater flow direction, which has been explained in terms of surfactant effect on the zeolites surface.

On the basis of such a characterization, a cellular automaton (CA) model has been developed for simulating contaminant infiltration induced by flooding phenomena. The CA grid represents the vertical section of a three layers model, where each cell describes a small portion of dry or wet soil. By performing an analysis on millions of initial different configurations, the conditional probability distributions of observing the contaminant at the time t and at distance L from the top of the grid have been calculated, and, as a preliminary result, a plot L-t for estimating mean infiltration rates of the contaminant in the three soil layers has been obtained.

Further research work will be devoted to a more accurate study of the proposed cellular automata model. In particular, numerical simulations will be performed to analyze how infiltration rate changes with depth at the aim to define the most dangerous scenario.

Appendix A

Basic equations of FEFLOW

The mass conservation equation of a fluid in variably saturated media is given as:

$$\left[S_o s^f(\psi) + \varepsilon \cdot C(\psi)\right]\frac{\partial h}{\partial t} + \nabla \cdot q = Q_h, \tag{A.1}$$

The basic formulation involves both the fluid pressure head, ψ, and the saturation $s^f(\psi)$ as unknown variables. The basic Richards equation is used as only one balance equation for these two unknowns (Hillel, 1980):

$$s^f(\psi)\varepsilon R_d(C)\frac{\partial C}{\partial t} + q \cdot \nabla C - \nabla \cdot \left[\left(\varepsilon s^f(\psi) D_d I + D\right) \cdot \nabla C\right] + \left[s^f(\psi)\varepsilon R(C)\vartheta + Q_h\right]C = s^f(\psi) Q_c. \tag{A.2}$$

The preceding equations are coupled with Darcy's law, written in the form:

$$q = -K_r\left(s^f\right)K\nabla h, \tag{A.3}$$

where

S_0 = *specific storage coefficient (compressibility)*
Ψ = *pressure head*
s^f = *water saturation*
ε = *porosity*
C = *contaminant concentration*
h = *hydraulic head*
q = *Darcy's velocity*
Q_h = *lumped balance flux of fluid*
R_d = *derivative term of retardation*
D_d = *molecular diffusion*
I = *unit identity tensor*
D = *tensor of hydrodynamic dispersion*
R = *retardation factor*
Q_c = *contaminant mass source/sink*
K_r = *relative conductivity*
K = *hydraulic conductivity tensor*.

In order to solve the preceding system of non-linear equations (1.5 and 1.6) for *h*, *q* and *C* under unsaturated-saturated conditions, it is necessary to determine the constitutive relationships for retrieving the following parameters: moisture capacity, $C(\psi)$, and hydraulic conductivity, $K_r(s^f)$. For this purpose, the van Genuchten parametric model (van Genuchten, 1978), described by the following equations, is used by FEFLOW to model water and solute movement through the unsaturated zone:

$$s_e^f = \begin{cases} \dfrac{1}{\left[1+\left(A|\psi|\right)^n\right]^m} & for\ \psi < 0 \\ 1 & for\ \psi \geq 0 \end{cases}, \tag{A.4}$$

$$K_r = \left(s_e^f\right)^{\frac{1}{2}} \left\{1-\left[1-\left(s_e^f\right)^{\frac{1}{m}}\right]^m\right\}^2, \tag{A.5}$$

$$s_e^f = \frac{s^f - s_r^f}{s_s^f - s_r^f}, \tag{A.6}$$

where s_e^f, s_r^f and s_s^f are, respectively, the effective, residual and maximum saturation of the fluid, *A* is a scale parameter inversely proportional to mean pore diameter (cm^{-1}), *n* and *m* are the shape parameters of soil water characteristic, m = 1 − 1/n, 0 < m < 1.

Under saturated conditions (s^f = 1), the above mentioned non-linear equation systems reduce to linear systems (Diersch, 2002).

Appendix B

COP function for the SP anomaly generated by a horizontal cylinder

For the case of a horizontal cylinder whose center axis is placed at (0, z_{0c}) in the vertical section through the SP profile, the COP function is written as (eq. (2.6)):

$$\eta(\xi,\delta) = -D\delta^{3/2} \sum_{\chi=\chi_{min}}^{\chi=\chi_{max}} \Delta V(\chi) \frac{(\chi-\xi)}{\left[(\chi-\xi)^2+\delta^2\right]^{3/2}}, \qquad \text{for } \delta > 0$$

where $\Delta V(\chi)$ is the potential drop calculated by considering eq. (2.7) with x_{0c} = 0. Due to the complexity of the COP function, the properties of $\eta(\xi,\delta)$ as a function of the polarization angle α_c and the source depth z_{0c} were investigated numerically by using the software Mathematica. First, keeping fixed the depth of the source (z_{0c} = 30 m), $\eta(\xi,\delta)$ was calculated by varying χ_{min} and χ_{max} and it was found that if their absolute values are sufficiently large, the properties of $\eta(\xi,\delta)$ do not depend on the limits of the sum. In this working condition, the following analysis is valid if the length of the profile is symmetric with respect to the SP source position.

As it can be seen in Fig. 2.6, the 2D tomography maps have three zero lines, but only the central zero line can be well approximated by a straight line. In the following, it is shown how good is this approximation and that the slope of such a straight line, i.e. the inclination angle β_c, is a linear function of the polarization angle α_c. For each fixed value of α_c and z_{0c}, ten points of the central line of zeros of the COP function are obtained by solving the equation $\eta(\xi,\delta) = 0$ and the best fitting straight line through this set of points is found. The procedure is, then, repeated for ten different values of α_c, by keeping z_{0c} fixed, and the inclinations of the best fitting straight lines, i.e. the β_c values, are reported as black points in Fig. B1, while the corresponding values for the adjusted R^2 are reported in the inset. The relationship between β_c and α_c is, thus,

obtained by the linear fit shown as a red line in Fig. A1. The entire procedure was repeated by using different values of the source depth z_{0c} and no significant changes were found for the slope coefficient m_c. Therefore, with a good level of approximation, it has been found that the value of the polarization angle of the cylinder can be retrieved from the slope of the straight line of zeros of the COP function $\eta(\xi, \delta)$. Furthermore, the effect of Gaussian noise on original data was investigated. In particular, within 10% of noise only slight changes of the slope coefficient m_c were found. As an example, the right panel of Fig. B1 shows the results obtained for data affected by 5% of Gaussian random noise.

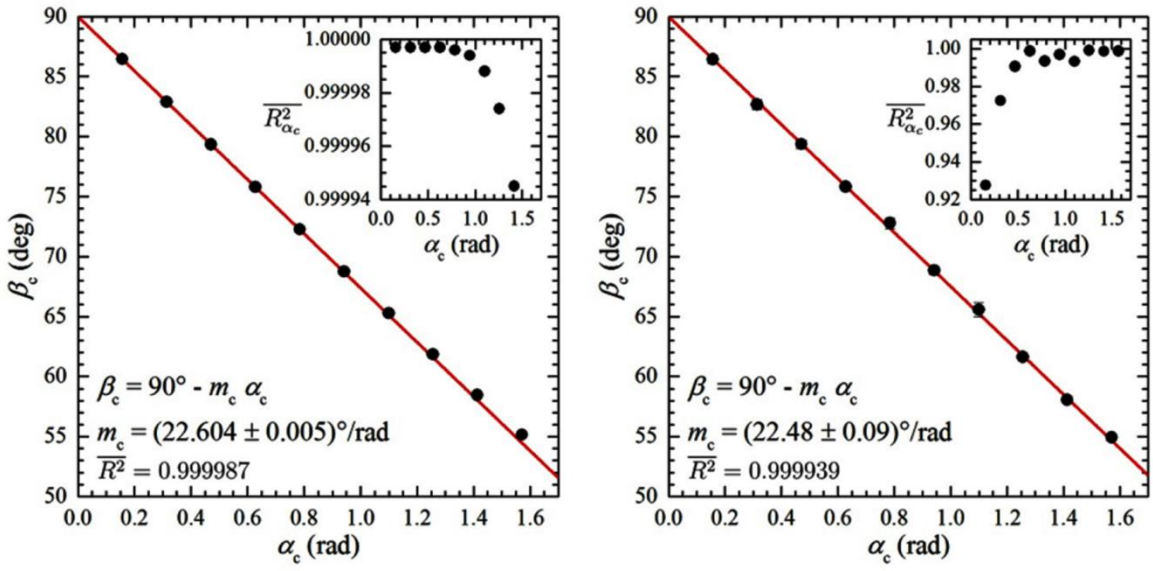

Figure B1 (Left) Relationship between the inclination angle of the COP central zero line β_c (degrees) and the polarization angle α_c (radians) for the case z_{0c} = 30 m. Each black point is determined from a linear fit whose adjusted R^2 is shown in the inset. (Right) Relationship between β_c (degrees) and α_c (radians) for the case z_{0c} = 30 m with 5% of Gaussian random noise added to original data.

As concerns the determination of the x_{0c} coordinate of the center axis of the body, it has been found that x_{0c} is related to the intercept of the central zero line of the COP function by a shift Δx_{0c} that is a linear function of the source depth z_{0c} and the polarization angle α_c. This result has been obtained from the following analysis. For each fixed value of α_c and z_{0c}, ten points of the central line of zeros of the COP function are obtained by solving the equation $\eta(\xi, \delta) = 0$ and

the best fitting straight line through this set of points is found. The procedure is, then, repeated for ten different values of α_c at each fixed value of z_{0c} and the intercepts of the best fitting straight lines, i.e. the Δx_{0c} values, are reported as points in Fig. B2. As it can be seen, the relationship between Δx_{0c} and α_c is linear, $\Delta x_{0c} = q_c(z_{0c})\alpha_c$, for $\alpha_c \leq \pi/3$ with a good degree of accuracy. The values of q_c for different z_{0c} are obtained by the linear fits shown as lines in Fig. A2, with the adjusted R^2 reported in the inset. Then, the q_c values are reported in Fig. B3 by varying z_{0c} and, again, a linear relationship is found, which leads to the following overall relationship between Δx_{0c}, α_c and z_{0c}: $\Delta x_{0c} = r_c \alpha_c |z_{0c}|$.

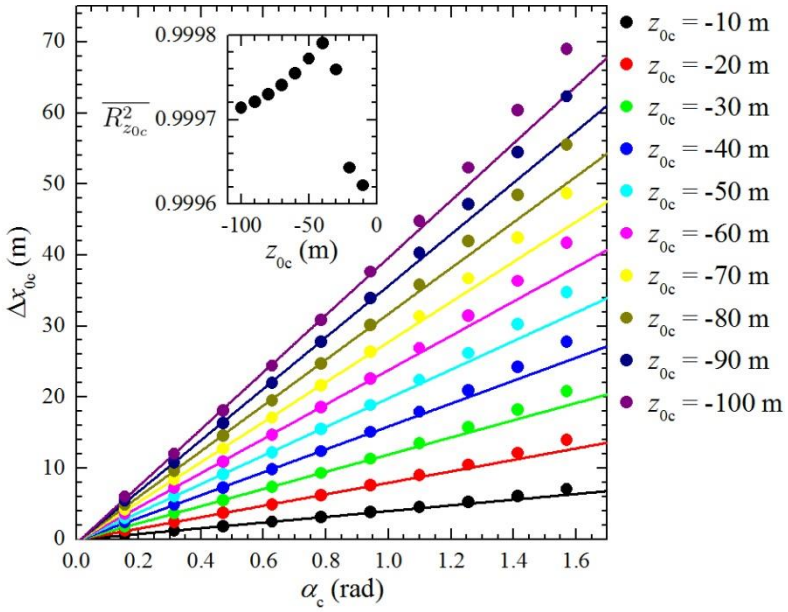

Figure B2 Relationship between the shift of the COP central zero line Δx_{0c} (m) with respect to x_{0c} and the polarization angle α_c (radians) for different values of z_{0c}. The adjusted R^2 of the linear fits shown as lines are reported in the inset.

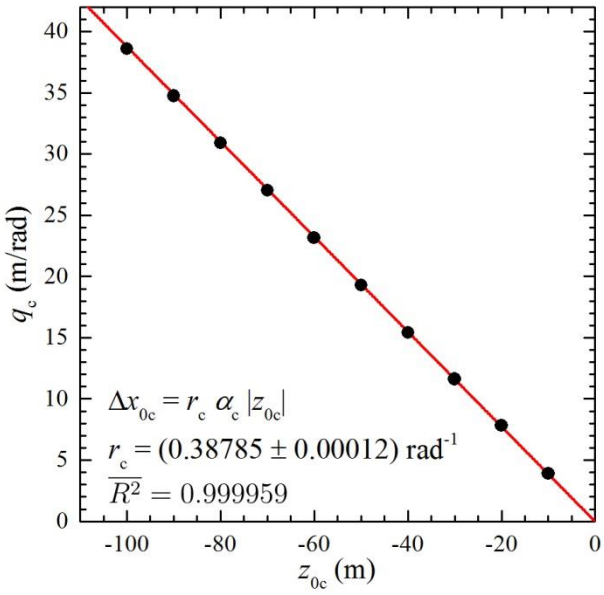

Figure B3 Relationship between the inclination angle of the best fitting straight lines of Fig. B2 and the source depth z_{0c}.

Appendix C

COP function for the SP anomaly generated by an inclined sheet

For the case of an inclined sheet whose center axis is placed at (0, z_{0s}) in the vertical section through the SP profile, the COP function is written as (eq. (2.6)):

$$\eta(\xi,\delta) = -D\delta^{3/2} \sum_{\chi=\chi_{min}}^{\chi_{max}} \Delta V(\chi) \frac{(\chi-\xi)}{[(\chi-\xi)^2+\delta^2]^{3/2}}, \quad for \delta > 0$$

where $\Delta V(\chi)$ is the potential drop calculated by considering eq. (2.4) with x_{0s} = 0. Due to the complexity of the COP function, the properties of $\eta(\xi,\delta)$ as a function of the polarization angle α_s and the source depth z_{0s} were investigated numerically by using the software Mathematica.

A numerical analysis similar to the previous case was performed. As shown in Fig. 2.8, the 2D tomography maps also have one central line of zeros of the COP function that can be well approximated by a straight line. To demonstrated how good is this approximation and that the slope of such a straight line, i.e. the inclination angle β_s, is a linear function of the polarization angle α_s, these steps are followed. For each fixed value of α_s and z_{0s}, ten points of the central line of zeros of the COP function are obtained by solving the equation $\eta(\xi,\delta) = 0$ and the best fitting straight line through this set of points is found. The procedure is, then, repeated for ten different values of α_s, by keeping z_{0s} fixed, and the inclinations of the best fitting straight lines, i.e. the β_s values, are reported as black points in Fig. C1, while the corresponding values for the adjusted R^2 are reported in the inset. The relationship between β_s and α_s is, thus, obtained by the linear fit shown as a red line in Fig. C1. The entire procedure was repeated by using different values of the source depth z_{0s} and no significant changes were found for the slope coefficient m_s. Therefore, with a good level of approximation, it has been found that the value of the polarization angle of the cylinder can be retrieved from the slope of the straight line of zeros of the COP function

$\eta(\xi, \delta)$. Furthermore, the effect of Gaussian noise on original data was investigated. In particular, within 10% of noise only slight changes of the slope coefficient m_s were found. As an example, the right panel of Fig. C1 shows the results obtained for data affected by 5% of Gaussian random noise.

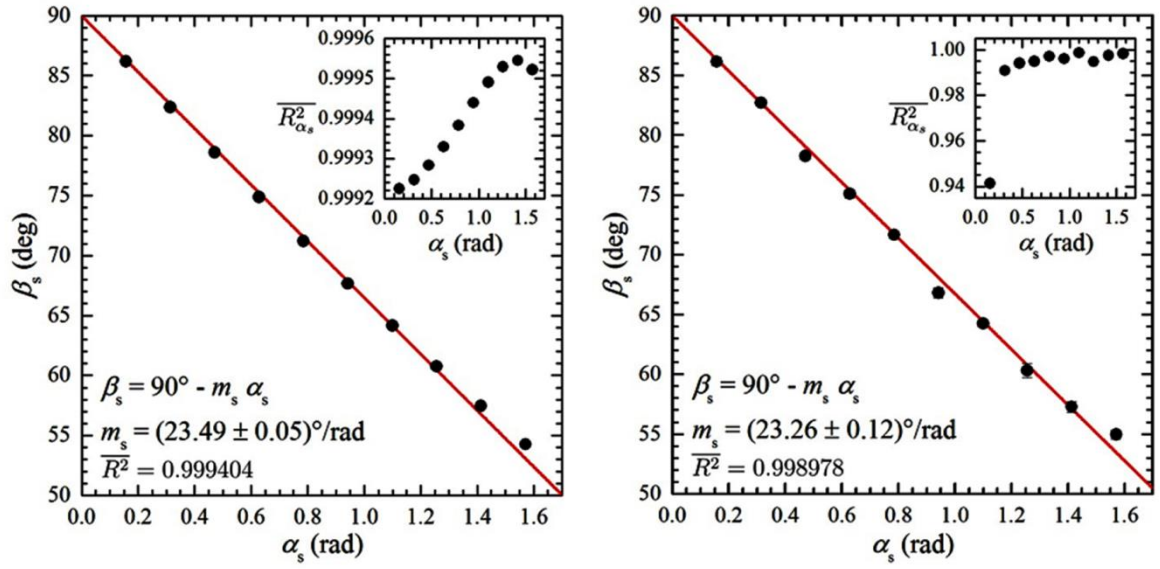

Figure C1 (Left) Relationship between the inclination angle of the COP central zero line β_s (degrees) and the polarization angle α_s (radians) for the case z_{0s} = 30 m and a = 15 m. Each black point is determined from a linear fit whose adjusted R^2 is shown in the inset. (Right) Relationship between β_s (degrees) and α_s (radians) for the case z_{0s} = 30 m with 5% of Gaussian random noise added to original data.

As concerns the determination of the x_{0s} coordinate of the center axis of the body, it has been found that x_{0s} is related to the intercept of the central zero line of the COP function by a shift Δx_{0s} that is a linear function of the source depth z_{0s} and the polarization angle α_s. This result has been obtained from the following analysis. For each fixed value of α_s and z_{0s}, and keeping fixed the value of a, ten points of the central line of zeros of the COP function are obtained by solving the equation $\eta(\xi, \delta) = 0$ and the best fitting straight line through this set of points is found. The procedure is, then, repeated for ten different values of α_s at each fixed value of z_{0s} and the intercepts of the best fitting straight lines, i.e. the Δx_{0s} values, are reported as points in Fig. B2.

As it can be seen, the relationship between Δx_{0s} and α_s is linear, $\Delta x_{0s} = q_s(z_{0s})\alpha_s$, for $\alpha_s \leq \pi/3$ and $z_{0s} \geq 20$ m with a good degree of accuracy. The values of q_s for different z_{0s} are obtained by the linear fits shown as lines in Fig. C2, with the adjusted R^2 reported in the inset. Then, the q_s values are reported in Fig. C3 by varying z_{0s} and, again, a linear relationship is found, which leads to the following overall relationship between Δx_{0s}, α_s and z_{0s}: $\Delta x_{0s} = \alpha_s(t_s + r_s z_{0s})$.

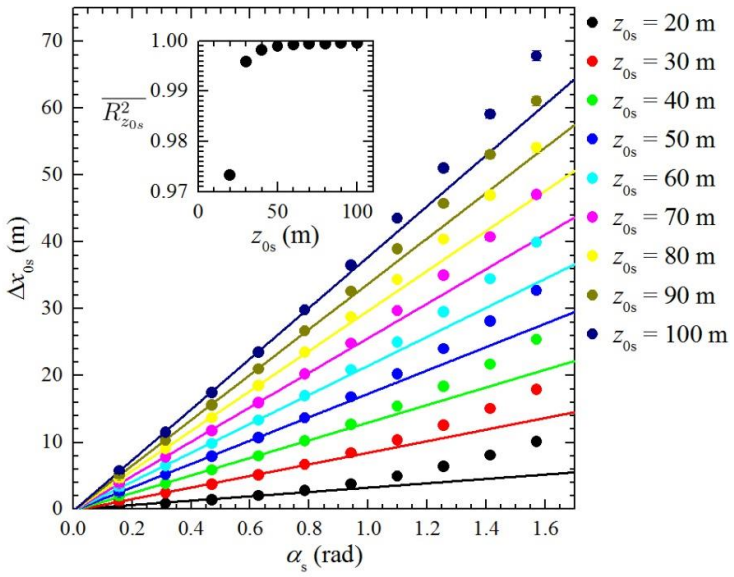

Figure C2 Relationship between the shift of the COP central zero line Δx_{0s} (m) with respect to x_{0s} and the polarization angle α_s (radians) for different values of z_{0s}. The adjusted R^2 of the linear fits shown as lines are reported in the inset.

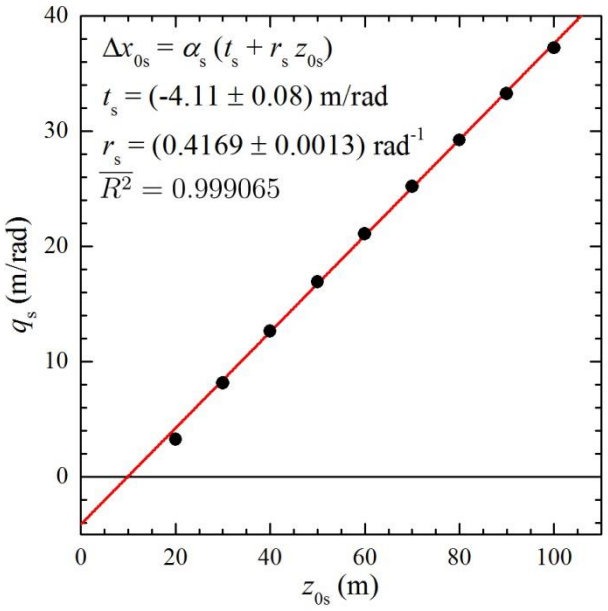

Figure C3 Relationship between the inclination angle of the best fitting straight lines of Fig. C2 and the source depth z_{0s}.

References

Abdelrahman, E.M., Essa, K. S., Abo-Ezz, E.R., Soliman, K.S., 2006a. Self-potential data interpretation using standard deviation of depths computed from moving-average residual anomalies. Geophysical Prospecting 54, 409-423.

Abdelrahman, E.M., Essa, K.S., Abo-Ezz, E.R., Soliman, K.S., 2006b. A least-squares depth-horizontal position curves method to interpret residual SP anomaly profiles. Journal of Geophysics and Engineering 3, 252-259.

Abdelazeem, M., Gobashy, M., 2006. Self-potential inversion using genetic algorithm. JKAU: Earth Science 17, 83-101.

Abdelrahman, E.M., Essa, K. S., Abo-Ezz, E. R., Sultan, M., Sauck, W.A., Gharieb, A.G., 2008. New least-squares algorithm for model parameters estimation using self-potential anomalies. Computers & Geosciences 34, 1569-1576.

Abu-Zeid, N., Bianchini, G., Santarato, G., Vaccaro, C., 2004. Geochemical characterization and geophysical mapping of landfill leachates: the Marozzo Canal case study (NE Italy). Environmental Geology 45, 439–447.

Adamo, P., Denaix, L., Terribile, F., Zampella, M., 2003. Characterization of heavy metals in contaminated volcanic soils of the Solofrana river valley (southern Italy). Geoderma 117, 1-25.

Agarwal, B.N.P., 1984. Quantitative interpretation of self-potential anomalies. In: Expanded Abstract Volume of the 54th SEG Annual Meeting and Exposition. Atlanta, pp. 154–157.

Agarwal, B.N.P., Srivastava, S., 2009. Analyses of self-potential anomalies by conventional and extended Euler deconvolution techniques. Computer & Geosciences 35, 2231-2238.

Al-Darby, A., Abdel-Nasser, G., 2006. Nitrate leaching through unsaturated soil columns: Comparison between numerical and analytical solutions. Journal of Applied Sciences 6(4), 735–743. doi:10.3923/jas.2006.735.743.

Alexakis, D.D., Sarris, A., Kalaitzidis, C., Papadopoulos, N., Soupios, P., 2016. Integrated use of satellite remote sensing, GIS and ground spectroscopy techniques for monitoring olive oil mill waste disposal areas in Crete Island-Greece. International Journal of Remote Sensing 37 (3), 669–693.

Anderson, M.P., Woessner, W.W., 1992. Applied Groundwater Modeling. Academic Press, Inc. San Diego, California. 381pp.

Anderson, M.P., Woessner, W.W., Hunt, R.J., 2002. Applied Groundwater Modeling: Simulation of flow and advective transport. Elsevier, 2nd edition.

Asfahani, J., Tlas, M.J., Hammadi, M., 2001. Fourier analysis for quantitative interpretation of Self-potential anomalies caused by horizontal cylinder and sphere. Journal of King Abdulaziz University, Earth Sciences 13, 41-54.

Atchuta Rao, D., Ram Babu, H.V., Sivakumar Sinha, G.D.J., 1982. A Fourier transform method for the interpretation of self-potential anomalies due to two-dimensional inclined sheets of finite depth exent, Pure and Applied Geophysics 120, 365-374.

Atchuta Rao, D., Ram Babu, H.V., 1983. Quantitative interpretation of self-potential anomalies due to two-dimensional sheet-like bodies. Geophysics 48(12), 1659-1664.

Atekwana, E., Werkema, D.D., Atekwana, E., 2006. Biogeophysics: the effects of microbial processes on geophysical properties of the shallow subsurface. In: Vereecken, H. (Ed.), NATO Science Series: IV: Earth and Environmental Sciences #71: Applied Hydrogeophysics. Springer Netherlands, p. 395.

Atekwana, E.A., Slater, L.D., 2009. Biogeophysics: A new frontier in earth science research. Reviews of Geophysics 47, 1–30. http://dx.doi.org/10.1029/2009RG000285.

Auken, E., Gazoty, A., Fiandaca, G., Pedersen, J., Christiansen, A.V., 2011. Mapping of Landfills using Time-domain Spectral Induced Polarization Data – The Eskelund Case Study, 17th European Meeting of Environmental and Engineering Geophysics (Near Surface), Leicester, UK, Expanded abstracts, 12-14 September 2011.

Avolio, M.V., Lupiano, V., Mazzanti, P., Di Gregorio, S., 2008. Modelling combined subaerial-subaqueous flow-like landslides by Macroscopic Cellular Automata. In: H. Umeo et al. (Eds): ACRI LNCS 5191: 329–336.

Ayolabi, E.A., Folorunso, A.F., Kayode, O.T., 2013. Integrated Geophysical and Geochemical Methods for Environmental Assessment of Municipal Dumpsite System. International Journal of Geosciences 4, 850-862.

Bak, P., Tang, C., Wiesenfeld, K., 1987. Self-organized criticality: An explanation of 1/f noise, Physical Review Letters, 59, 381.

Bak, P., Chen, K., Creutz, M., 1989. Self-Organized Criticality in the Game of Life. Nature 342, 780.

Bandini, S., Mauri, G., Serra, R., 2001. Cellular automata: from a theoretical parallel computational model to its application to complex systems. Parallel Computing 27 (5), 539–553.

Bandini, S., Simone, C., 1996. Reaction diffusion computational models. In Proceedings of the 3rd Systems Science European Congress, Rome.

Bansal, A.R., Dimri, V.P., Vidya Sagar, G., 2006. Depth estimation from gravity data using the maximum entropy method (MEM) and multi taper method (MTM). Pure and Applied Geophysics 163, 1417-1434.

Bansal, A.R., Dimri, V.P., 2010. Scaling spectral analysis: A new tool for interpretation of gravity and magnetic data. Earth Science India e-Journal 3(I), 54-68.

Basile, G., Palmieri, F., Violante, P., 1985. Il fiume Sarno: valutazione delle variazioni dell'inquinamento. Universita` degli studi di Napoli Federico II. Istituto di Chimica Agraria. Convegno Nazionale. Inquinamento Idrico e conservazione dell'Ecosistema. Vico Equense 22 – 23 February, pp. 258 – 293.

Bear, J., 1972. Dynamics of Fluids in Porous Media. American Elsevier, New York. 764 pp.

Bear, J., Verruijt, A., 1987. Modeling Groundwater Flow and Pollution. Reidel Publishing Co., Dordrecht, Holland: 414 pp.

Bear, J., Bachmat, Y., 1991. Introduction to Modeling of Transport Phenomena in Porous Media, Kluwer Acad., Norwell, Mass.

Bear, J., Cheng, A.H.D., 2009. Modeling Groundwater Flow and Contaminant Transport: Theory and applications of transport in porous media. Springer, Vol. 23, 850 pp.

Beaufoy, G., 2001. The environmental impact of olive oil production in the European union: practical options for improving the environmental impact.

Bhagavantam, D., 1975. An experimental study of seepage through partially lined earthen channels. Civil Eng. Trans., Inst. Eng. (Australia) 77–9.

Bhattacharya, B.B., Roy, N., 1981. A note on the use of nomograms for self-potential anomalies. Geophysical Prospecting 29(1), 102-107.

Bhattacharya, B.B., Shalivahan, Jardani, A., Bera, A., 2007. Three-dimensional probability tomography of self-potential anomalies of graphite and sulphide mineralization in Orissa and Rajasthan, India. Near Surface Geophysics, 5, 223-230.

Binley, A., Henry-Poulter, S., Shaw, B., 1996. Examination of solute transport in an undisturbed soil column using electrical resistance tomography. Water Resources Research, 32, 763-769.

Binley, A., Shaw, B., Henry-Poulter, S., 1996. Flow pathways in porous media: electrical resistance tomography and dye staining image verification. Measurement Science and Technology: IOPscience, 384–390.

Binley, A.M., Cassiani, G., Middleton, R., Winship, P., 2002. Vadose zone flow model parameterisation using cross-borehole radar and resistivity imaging. Journal of Hydrology 267, 147 – 159.

Binley, A., Kemna, A., 2005. DC Resistivity and Induced Polarization Methods. In book: Hydrogeophysics, pp.129-156.

Biswas, A., Sharma, S.P., 2014. Resolution of multiple sheet-type structures in self-potential measurements. Earth System Science 123, 809-825.

Bloem, E., French, H.K., Binley, A., Schotanus, D., Eggen, G., 2010. Time-lapse resistivity measurements combined with soil water sampling to characterize solute movement in the unsaturated zone at Oslo airport, Gardermoen. Fall Meeting 2010, Abstract no. H13G-04, American Geophysical Union, Washington, DC.

Bonardi, G., Ciarcia, S., Di Nocera, S., Matano, F., Sgrosso, I., Torre, M., 2009. Carta delle principali unità cinematiche dell'Appennino meridionale. Italian Journal of Geosciences (Bollettino della Società geologica italiana) 128, 1, 47-60.

Brachetti, P., De Felice Ciccoli, M., Di Pillo, G., Lucidi, S., 1997. A new version of the Price's Algorithm for Global Optimization. Journal of Global Optimization 10, 165-184.

Breede, K., Kemna, A., Esser, O., Zimmermann, E., Vereecken, H., Huisman, J.A., 2011. Joint measurement setup for determining spectral induced polarization and soil hydraulic properties. Vadose Zone Journal 10, 716–726.

Bresco, M., Raiconi, G., Barone, F., De Rosa, R., Milano, L., 2005. Genetic approach helps to speed classical Price algorithm for global optimization. Soft Computing 9, 525-535.

Burg, J.P., 1975. Maximum entropy spectral analysis, Ph.D. Thesis, Stanford University, California.

Burks, A.W., 1970 Essays on Cellular Automata, Univ. of Illinois Press.

Canter L.W., Knox, R.C., Fairchild, D.M., 1987. Ground Water Quality Protection, Lewis Publishers, Inc., Chelsea, Michigan, 562 pp.

Cassiani G, Binley A., 2005. Modeling unsaturated flow in a layered formation under quasi-steady state conditions using geophysical data constraints. Advances in Water Resources 28, 467–477.

Cassiani, G., Bruno, V., Villa, A., Fusi, N., Binley, A.M., 2006. A saline trace test monitored via time-lapse surface electrical resistivity tomography. Journal of Applied Geophysics 59, 244-259.

Celico P., 1988. Prospezioni idrogeologiche. Vol. II, Liguori ed., Naples, Italy.

Celico, P., Mennella, A., Piro, M., Stanzione, D., 1991. Interscambi idrici sotterranei nella Valle del Solofrana (AV-SA). Atti del I Convegno Nazionale dei Giovani Ricercatori in Geologia Applicata, 22-23 ottobre, Gargnano (BS). Ricerca Scientifica ed Educazione Permanente 93, 307-316.

Celico, F., Piscopo, V., 1995. Idrodinamica sotterranea e vulnerabilità intrinseca all'inquinamento delle piane del Sarno e del Solofrana (Campania). Quad. Geologia Applicata 2, 407 – 415.

Chambers, J.C., Kuras, O., Meldrum, P.I., Ogilvy, R.D., Hollands, J., 2006. Electrical resistivity tomography applied to geologic, hydrogeologic, and engineering investigations at a former waste-disposal site. Geophysics 71 (6), B231–B239.

Chambers, J.C., Wilkinson, P.B., Wardrop, D., Hameed, A., Hill, I., Jeffrey, C., Loke, M.H., Meldrum, P.I., Kuras, O., Cave, M., Gunn, D.M., 2012. Bedrock detection beneath river terrace deposits using three-dimensional electrical resistivity tomography. Geomorphology 177-178, 17-25.

Chen, H., Chen, S., Matthaeus, W.H., 1992. Recovery of the Navier-Stokes equations using a lattice-gas Boltzmann method. Physical Reviews 45 (8), R5339-R5342.

Chopard, B., Masselot, A., 1999. Cellular automata and lattice Boltzmann methods: a new approach to computational fluid dynamics and particle transport. Future Generation Computer Systems 16, 249–257.

Cinque, A., Patacca, E., Scandone, P., Tozzi, M., 1993. Quaternary kinematic evolution of the Southern Apennines. Relationship between surface geological features and deep lithospheric structures. Annali di Geofisica 36 (2), 249- 260.

Cooley, J.W., Tukey, J.W., 1965. An algorithm for the machine calculation of complex Fourier series, Mathematics of Computation 19, 297-301.

Critelli, S., Le Pera, E., 1995. La formazione di Castelvetere nell'evoluzione petrostratigrafica dell'avanfossa del Tortoniano - Messiniano dell'Appennino meridionale. Bollettino della Società geologica italiana 114, 615-634.

Dagan, G., 1988. Time-dependent macro dispersion for solute transport in anisotropic heterogeneous aquifers. Water Resources Research 24 (9) 1491-1500.

Dahlin, T., Jens, E., Dowen, R., Mangeya, P., Auken, E., 1999. Geophysical and hydrogeologic investigation of groundwater in the Karoo stratigraphic sequence at Sawmills in northern Matabeleland, Zimbabwe: a case history. Hydrogeology Journal 15 (5), 945–960.

Dahlin, T., 2001. The development of DC resistivity imaging techniques. Computers & Geosciences 27, 1019–1029.

Daily, W., Ramirez, A., LaBrecque, D., Nitao, J., 1992. Electrical resistivity tomography of vadose water movement. Water Resources Research 28 (5), 1429 – 1442.

Daily, W.D., Ramirez, A.L., LaBrecque, D.J., Barber, W., 1995. Electrical resistance tomography experiments at the Oregon Graduate Institute. Journal of Applied Geophysics 33, 227 – 237.

Das, B., Agarwal, B.N.P., 2012. Depth determination of 2-D SP anomaly source using Energy Spectrum method and its advantages. 9th Biennial International Conference & Exposition on Petroleum Geophysics, Hyderabad 2012, Expanded Abstract P-187.

de Riso, R., Ducci, D., 1992. Schema idrogeologico dell'Alto Sarno (T. Solofrana - Campania). Geologia Tecnica e Ambientale 3, 29-38.

Di Gregorio, S., Serra, R., Villani, M., 1999. Applying cellular automata to complex environmental problems: The simulation of the bioremediation of contaminated soils. Theoretical Computer Science 217 (1), 131-156.

Diersch, H. J. G., Perrochet, P., 1999. On the primary variable switching technique for simulating unsaturated-saturated flows. Advances in Water Resources 23(3), 271-301.

Diersch, H. J. G., 2002. FEFLOW: physical basis of modeling. Reference manual, WASY, Berlin.

Di Maio, R., Patella, D., 1991. Basic theory of electrokinetic effects associated with earthquakes. Bollettino di Geofisica Teorica e Applicata 33 (130/131), 145-154.

Di Maio, R., Patella, D., 1994. Self-potential anomaly generation in volcanic areas. The Mt. Etna case history, Acta Vulcanologica, 4, 119-124.

Di Maio, R., Mauriello, P., Patella, D., Petrillo, Z., Piscitelli, S., Siniscalchi, A., 1998. Electric and electromagnetic outline of the Mount Somma-Vesuvius structural setting, Journal of Volcanology and Geothermal Research 82, 219-238.

Di Maio, R., Patella, D., Petrillo, Z., Siniscalchi, A., Cecere, G., De Martino, P., 2000. Application of electric and electromagnetic methods to the definition of the Campi flegrei caldera (Italy), Annals of Geophysics 43(2), 375-390.

Di Maio, R., Piegari, E., "3D imaging of geoelectrical data for characterizing a municipal solid waste landfill", unpublished work.

Di Maio, R., Cecere, G., De Martino, P., Piegari, E., 2013. Electric effects induced by artificial seismic sources at Somma-Vesuvius volcano, Annals of Geophysics 56, S0445.

Di Maio, R., Fabbrocino, S., Forte, G., Piegari, E., 2013a. A three-dimensional hydrogeological-geophysical model of a multi-layered aquifer in the coastal alluvial plain of Sarno River (southern Italy). Hydrogeology Journal 22, 691-703, doi: 10.1007/s10040-013-1087-8.

Di Maio, R., Piegari, E., Rani, P. Giovanni, F., 2015a. Multi-methodological geophysical approach for contamination detection in a high flood risk area (Southern Italy). 21st European Meeting of Environmental and Engineering Geophysics, Near Surface Geoscience 2015, Turin (Italy), 6-10 September, 2015, EarthDoc, 5 pp., doi: 10.3997/2214-4609.201413787.

Di Maio, R., Fabbrocino, S., Piegari, E., Rani, P., 2015b. Electrokinetic component of the self-potential for complex aquifer system characterization. 42nd IAH International Congress, Rome (Italy), 13-18 September, 2015.

Di Maio, R., La Manna, M., Piegari, E., 2015c. 3D Reconstruction of Buried Structures from Magnetic, Electromagnetic and ERT Data: Example from the Archaeological Site of Phaistos (Crete, Greece). Archaeological Prospection 23(1), 3-13.

Di Maio, R., Piegari, E., Rani, P., Avella, A., 2016a. Self-potential data inversion through the integration of spectral analysis and tomographic approaches. Geophysical Journal International, 206, 1204-1220

Di Maio, R., Rani, P., Piegari, E., Milano, M., 2016b. Self-Potential data inversion through a Genetic-Price algorithm. Computer & Geosciences, 94, 86-95. doi: 10.1016/j.cageo.2016.06.005.

Di Maio, R., Piegari, E., Rani, P., 2016c. A comparative analysis of SP data inversion by spectral, tomographic and global optimization approaches, 78th EAGE Conference and Exhibition 2016, DOI: 10.3997/2214-4609.201600560.

Di Maio, R., Piegari, E., Rani, P., 2017, Source depth estimation of Self-Potential anomalies by spectral methods, Journal of Applied Geophysics, 136, 315–325.

Dimri, V.P., 1992. Deconvolution and inverse theory: Application to geophysical problems, 1st edition, Elsevier.

Dokou, Z., Karatzas, G. 2012. Saltwater intrusion estimation in a karstified coastal system using density-dependent modelling and comparison with the Ghyben-Herzberg approach. Hydrological Sciences Journal 57(5), 985–999.

Doula, M.K., Elaiopoulos, K., Kavvadias, V.A., Mavraganis, V., 2012. Use of Clinoptilolite to improve and protect soil quality from the disposal of Olive Oil Mills Wastes. Journal of Hazardous Materials 207-208, 103-110.

Doula, M.K., Kavvadias, V., Elaiopoulos, K., 2013. Proposed soil indicators for olive mill waste (OMW) disposal areas. Water Air Soil Pollution 224, 769–784. http://dx.doi.org/10.1007/s11270-013-1621-2.

ERTLab, 2014. Multi-Phase Technologies and Geostudi Astier.

Essa, K., Mahanee, S., Smith, P.D., 2008. A new inversion algorithm for estimating the best fitting parameters of some geometrically simple body to measured self-potential anomalies. Exploration Geophysics 39, 155-63.

Essa, K.S., 2011. A new algorithm for gravity or self-potential data interpretation. Journal of Geophysics and Engineering 8, 434-446.

Falgas, E., Ledo, J., Benjumea, B., Queralt, P., Marcuello, A., Teixidó, T., Martí, A., 2011. Integrating hydrogeological and geophysical methods for the characterization of a deltaic aquifer system. Surveys in Geophysics 32, 857–873.

Faillettaz, J., Louchet, F., Grasso, J.R., 2004. Two-threshold model for scaling laws of noninteracting snow avalanches. Physical Review Letters 93, 208001.

Forsyth, P.A., Wu, Y.S., Pruess, K., 1995. Robust numerical methods for saturated-unsaturated flow with dry initial conditions in heterogeneous media. Advances in Water Resources 18(1), 25-38.

Frisch, U., Hasslacher, B., Pomeau, Y., 1986. Lattice-gas automata for the Navier–Stokes equation. Physical Reviews Letters 58, 1505–1508.

Fujinawa, K., Iba, T., Fujihara, Y., Watanabe, T., 2009. Modeling interaction of fluid and salt in an aquifer/lagoon system. Groundwater 47 (1), 35-48. http://dx.doi.org/10.1111/j.1745-6584.2008.00482.x.

Garambois, S., Dietrich, M., 2001. Seismoelectric wave conversions in porous media: Field measurements and transfer function analysis. Geophysics, 66, 1417–1430.

Garambois, S., Dietrich, M., 2002. Full waveform numerical simulations of seismoelectromagnetic wave conversions in fluid-saturated stratified porous media. Journal of Geophysical Research 107(B7), ESE 5–1.

Garambois, S., Seneshal, P., Perrod, H., 2002. On the use of combined geophysical methods to assess water content and water conductivity of near-surface. Journal of Hydrology, 259, 32-48.

Garcia-Abdeslem, J., Ness, G.E., 1994. Inversion of the power spectrum from magnetic anomalies. Geophysics 59, 391-401.

Gasperikova, E., Hubbard, S.S., Watson, D.B., Baker, G.S., Peterson, J.E., Kowalsky, M.B., Smith, M., Brooks, S., 2012. Long-term electrical resistivity monitoring of recharge-induced contaminant plume behavior. Journal of Contaminant Hydrology 142–143, 33–49.

Gazoty, A., Auken, E., Pedersen, J., Fiandaca, G., Christiansen, A.V., 2011. Reliability of Time domain Induced Polarization data, Symposium on the Application of Geophysics to Engineering and Environmental Problems (SAGEEP), Charleston, South Carolina, USA, 10–14 April 2011, SAGEEP 24, doi:10.4133/1.3614088.

Gelhar, L. W., 1986. Stochastic subsurface hydrology from theory to applications. Water Resources Research 22(9S), 135S–145S, doi:10.1029/WR022i09Sp0135S.

Ghil, M., Allen, M.R., Dettinger, M.D., Ide, K., Kondrashov, D., Mann, M.E., Robertson, A.W., Saunders, A., Tian, Y., Varadi, F., Yiou, P., 2002. Advanced spectral methods for climatic time series. Reviews of Geophysics 40, 3.1-3.41.

Goldberg, D. E., 1989. Genetic Algorithms in search, optimization and machine learning. Addison Welsey Publishing Company, INC., New York, 432 pp.

Göktürkler, G., Balkaya, Ç., 2012. Inversion of self-potential anomalies caused by simple-geometry bodies using global optimization algorithms. Journal of Geophysics and Engineering 9, 498-507.

Green, R.T., Painter, S.L., Sun, A., Worthington, S.R.H., 2006. Groundwater contamination in karst terranes. Water, Air, and Soil Pollution 6, 157–170.

Gupta, D. K., Arora, Y., Singh, U.K., Gupta, J.P., 2012. Recursive Ant Colony Optimization for estimation of parameters of a function. 1st International Conference on Recent Advances in Information Technology (RAIT), Dhanbad, pp. 448-454.

Hahn, A., Kind, E.G., Mishra, D.C., 1976. Depth estimation of magnetic sources by means of Fourier amplitude spectra. Geophysical Prospecting 24, 287-308.

Halihan, T., Paxton, S., Graham, I., Fenstemakerb, T., Rileya, M., 2005. Postremediation evaluation of a LNAPL site using electrical resistivity imaging. Journal of Environmental Monitoring 7, 283-287.

Heenan, J., Slater, L.D., Ntarlagiannis, D., Atekwana, E.A., Fathepure, B.Z., Dalvi, S., Ross, C., Werkema, D.D., Atekwana, E.A., 2015. Electrical resistivity imaging for long-term autonomous monitoring of hydrocarbon degradation: lessons from the Deepwater Horizon oil spill. Geophysics 80 (1), B1–B11. http://dx.doi.org/10.1190/geo2013-0468.1.

Helmstetter, A., Hergarten, S., Sornette, D., 2004. Properties of foreshocks and aftershocks of the nonconservative SOC Olami–Feder–Christensen model. Physical Reviews E 70, 046120.

Hergarten, S., Neugebauer, J., 1998. Self-organized criticality in a landslide model. Geophysical Research Letters 25, 801–804.

Hillel, D., 1980. Fundamentals of Soil Physics, Academic Press, San Diego.

Hinnell, A. C., Ferré, T.P.A., Vrugt, J.A., Huisman, J.A., Moysey, S., Rings, J., Kowalsky, M.B., 2010. Improved extraction of hydrologic information from geophysical data through coupled hydrogeophysical inversion. Water Resources Research 46(4), W00D40, doi:10.1029/2008WR007060.

Illman, W.A., Berg, S.J., Yeh, T., C.J., 2012. Comparison of approaches for predicting solute transport: Sandbox experiments. Groundwater 50 (3), 421-431. http://dx.doi.org/10.1111/j.1745-6584.2011.00859.x.

Indraratna, B., Ranjith, P., 2001. Hydromechanical Aspects and Unsaturated Flow in Jointed Rock. August Aimé Balkema Publications, Tokyo.

Ishido, T., Mizutani, H., 1981. Experimental and theoretical basis of electrokinetic phenomena in rock-water systems and its applications to geophysics. Journal of Geophysical Research 86, 1763-1775.

Iuliano, T., Mauriello, P., Patella, D., 2001. A probability tomography approach to the analysis of potential field data in the Campi Flegrei Caldera (Italy). Annals of Geophysics 44, 403-420.

Iuliano, T., Mauriello, P., Patella, D., 2002. Looking inside Mount Vesuvius by potential fields integrated probability tomographies. Journal of Volcanology and Geothermal Research 113, 363-378.

Jakovovic, D., Werner, A.D., Simmons, C.T., 2011. Numerical modelling of saltwater up-coning: comparison with experimental laboratory observations. Journal of Hydrology 402(3–4), 261–273.

Jardani, A., Dupont, J.P., Revil, A., 2006. Self-potential signals associated with preferential ground water flow pathways in sinkholes. Journal of Geophysical Research 111, B09204.

Jegathambal, P., Sundarambal, P., 2014. Cellular Automata for Simulation of PCE Degradation in Subsurface Media. Open Journal of Water Pollution and Treatment 1 (1), 10-20.

Jennings A.A., Manocha A., 1994. Modeling soil bioremediation, in: D.L. Wise, D.J. Trantolo (Eds.), Remediation of Hazardous Waste Contaminated Soils, Marcel Dekker, New York.

Jouniaux, L., Maineult, A., Naudet, V., Pessel, M., Sailhac, P., 2009. Review of self-potential methods in hydrogeophysics. Comptes Rendus Geoscience, doi:10.1016/j.crte.2009.08.008.

Juanico, D.E., Longjas, A., Batac, R., Monterola, C., 2008. Avalanche statistics of driven granular slides in a miniature mound. Geophysical Research Letters 35, L19403. doi:10.1029/ 2008GL035567.

Kanta A., Soupios P., Vallianatos F., Rust D., 2009. Geophysical characterization and delineation of the Keritis Basin, Crete island, Greece using time domain electromagnetic method. AMIREG 2009.

Kanta A., Soupios P., Barsukov P., Kouli M., Vallianatos F., 2013. Aquifer characterization using shallow geophysics in the Keritis Basin of Western Crete, Greece. Environmental Earth Sciences (Springer), doi:10.1007/s12665-013-2503-z.

Kavvadias, V., Elaiopoulos,K., Theocharopoulos, S., Soupios, M., 2016. Fate of Potential Contaminants Due to Disposal of Olive Mill Wastewaters in Unprotected Evaporation Ponds. Bulletin of Environmental Contamination and Toxicology, pp 1-8. doi: 10.1007/s00128-016-1922-4.

Kay, S.M., Marple, S.L., 1981. Spectrum analysis - a modern perspective. Proceedings of the IEEE 69, 1381-1419.

Kearey, P., Brooks, M., Hill, I., 2002. An Introduction to Geophysical Exploration, 3rd Edition, Wiley-Blackwell.

Keller, G. V., Frischknecht, F. C., 1966. Electrical Methods in Geophysical Prospecting, Pergamon Press, New York.

Kim, J.H., Yi, M. J., Park, S.G., Kim, J.G., 2009. 4-D inversion of DC resistivity monitoring data acquired over a dynamically changing earth model. Journal of Applied Geophysics 68, 522–532.

Kirmizakis, P., Ntarlagiannis, D., Kalderis, D., Soupios, P., 2016. Monitoring of organic load reduction in olive-mill wastewater by biochar using the spectral induced polarization (SIP) method, poster presentation at 88th Congress of Geological Society of Italy.

Koestel, J., Vanderborght, J., Javaux, M., Kemna, A., Binley, A., Vereecken, H., 2009. Noninvasive 3-D transport characterization in a sandy soil using ERT: 1. Investigating the validity of ERT-derived transport parameters. Vadose Zone Journal 8(3), 711-722.

Kumar, D., 2012. Efficacy of Electrical Resistivity Tomography Technique in Mapping Shallow Subsurface Anomaly. Journal Geological Society of India 80, 304-307.

Kyriacou, A., Lasaridi, K.E., Kotsou, M., Balis, C., Pilidis, G., 2005. Combined Bioremediation and Advanced Oxidation of Green Table Olive Processing Wastewater. Process biochemistry 40, 1401.

LaBrecque, D. J., Ramirez, A.L., Daily, W.D., Binley, A.M., Schima, S., 1996. ERT monitoring of environmental remediation processes. Measurement Science and Technology, 7, 375-383.

Ladd, A. J. C., 1994. Numerical simulations of particulate suspensions via a discretized Boltzmann equation. Part 1. Theoretical foundation. Journal of fluid Mechanics 271, 285-309.

Lahaie, F., Grasso, J.R., 1998. A fluid–rock interaction cellular automaton of volcano mechanics: application to the Piton de la Fournaise. Journal of Geophysical Research 103, 9637–9649.

Lawrence, A.R., Stuart, M., Cheney, C., Jones, N., Moss, R., 2006. Investigating the scale of structural controls on chlorinated hydrocarbon distributions in the fractured-porous unsaturated zone of a sandstone aquifer in the UK. Hydrogeology Journal 14 (8), 1470- 1482.

Lee, K.Y., Mohamed, P.S., 2002. A real-coded genetic algorithm involving a hybrid crossover method for power plant control system design. Proceedings of the 2002 Congress on Evolutionary Computation, Honolulu, HI, USA, 1069-1074.

Lemarchand, N., Grasso, J.R., 2007. Interactions between earthquakes and volcano activity. Geophysical Research Letters 34, L24303. doi:10.1029/2007GL031438.

Leroux, V., Dahlin, T., Rosqvist, H., 2010. Time-domain IP and resistivity sections measured at four landfills with different contents, 16th European Meeting of Environmental and Engineering Geophysics (Near Surface), Zurich (Switzerland), 6 - 8 September 2010.

Li, X., Yin, M., 2012. Application of differential evolution algorithm on self-potential data. PLoS One 7(12), 1-11.

Lloyd, J. W., 1999. Water resources of hard rock aquifers in arid and semi-arid zones. Studies and Reports in Hydrology 58, UNESCO, Paris.

Loke, M.H., Barker, R.D., 1996. Rapid least-squares inversion of apparent resistivity pseudosections using a quasi-Newton method. Geophysical Prospecting 44, 131-152.

Loke, M.H., 2002. Tutorial: 2-D and 3-D electrical imaging surveys. Geotomo Software, Malaysia.

Loke, M.H., Dahlin, T., 2002. A comparison of the Gauss-Newton and quasi- Newton methods in resistivity imaging inversion: Journal of Applied Geophysics 49, 149–162.

Loke, M.H., Acworth, I., Dahlin T., 2003. A comparison of smooth and blocky inversion methods in 2D electrical imaging surveys. Exploration Geophysics, 34, 182–187.

Loke M.H., Chambers J.E., Rucker D.F., Kuras, O., Wilkinson, P.B., 2013. Recent developments in the direct-current geoelectrical imaging method. Journal of Applied Geophysics 95, 135–156.

Loke, M. H., Dahlin, T., Rucker, D.F., 2014. Smoothness-constrained time-lapse inversion of data from 3D resistivity surveys. Near Surface Geophysics 12, 5–24.

Luke, S., 2009. Essentials of Metaheuristics, Lulu. Available at http://cs. gmu.edu/ ~sean/book/metaheuristics/.

Malinverno, A., Ryan, W.B.F, 1986. Extension in the Tyrrhenian Sea and shortening in the Apennines as result of arc migration driven by sinking of the lithosphere. Tectonics 5, 227-245.

Mamer, E.A., Lowry, C.S., 2013. Locating and quantifying spatially distributed groundwater/surface water interactions using temperature signals with paired fiber-optic cables. Water Resources Research 49,1-11. http://dx.doi.org/10.1002/2013WR014235.

Maus, S., Dimri, V.P., 1995. Potential field power spectrum inversion for scaling geology. Journal of Geophysical Research 100, 12605–12616.

McDonald, M. G., Harbaugh, A. W., 1988. A modular three dimensional finite difference groundwater flow model. Techniques of Water Resources Investigations, Chapter A1, US Geological Survey, p. 586.

Meijerink, A. M. J., Bannert, D., Batelaan, O., Lubcyznski, M.W., Pointet, T., 2007. Remote Sensing Applications to Groundwater. IHP-VI, Series on Groundwater No. 16, UNESCO, Paris, 312 pp.

Meiser, P., 1962. A method for quantitative interpretation of self-potential measurement. Geophysical Prospecting 10, 203-218.

Meju, M., 2005. Simple relative space–time scaling of electrical and electromagnetic depth sounding arrays: implications for electrical static shift removal and joint DC TEM data inversion with the most-squares criterion. Geophysical Prospecting 53, 1–17.

Milano, M., Koumoutsakos, P., 2002. A clustering genetic algorithm for cylinder drag optimization. Journal of Computational Physics175, 79-107.

Mizutani, H., Ishido, T., Yokokura, T., Ohnishi, S., 1976. Electrokinetic phenomena associated with earthquakes. Geophysical Research Letters 3, 365-368.

Mondal, N. C., Rao, A. V., Singh, V. P., 2010. Efficacy of electrical resistivity and induced polarization methods for revealing fluoride contaminated groundwater in granite terrain. Environmental Monitoring and Assessment, 168, 103–114.

Monteiro Santos, F.A., 2010. Inversion of self-potential of idealized bodies' anomalies using particle swarm optimization. Computer & Geosciences 36, 1185-1190.

Müller, K.J., Vanderborght, A., Englert, A., Kemna, J., Huisman, A., Rings, J., Vereecken, H., 2010. Imaging and characterization of solute transport during two tracer tests in a shallow aquifer using electrical resistivity tomography and multilevel groundwater samplers. Water Resources Research 46, W03502. doi:10.1029/2008WR007595.

Murty, B.V.S., Haricharan, P., 1985. Nomograms for the complete interpretation of spontaneous potential profiles over sheet-like and cylindrical two-dimensional sources. Geophysics 50, 1127-1135.

Naidu, P.S., 1972. Maximum likelihood (ML) estimation of depth from the spectrum of aeromagnetic fields. Pure and Applied Geophysics 95, 141-149.

Narasimhan, T.N., 1982. Numerical Modeling in Hydrogeology. In Recent Trends in Hydrogeology, pp. 273-296, Special Paper 189 Geological Society of America, Boulder, Colorado.

Naudet, V., Revil, A., Rizzo, E., Bottero, J.Y., Bégassat, P., 2003. Relationship between self-potential (SP) signals and redox conditions in contaminated groundwater. Geophysical Research Letters 30, 2091, doi: 10.1029/2003 GL018096.

Naudet, V., Revil, A., Rizzo E., Bottero, J-Y., Bégassat, P. 2004. Groundwater redox conditions and conductivity in a contaminant plume from geoelectrical investigations. Hydrology and Earth System Sciences 8(1), 8-22.

Negi, J.G., Dimri, V.P., Agarwal, P.K., Pandey, O.P., 1986. A spectral analysis of the profiles for thickness estimation of flood basalt of India, Exploration Geophysics. 17, 105–111.

Neuman, S. P., Winter, C. L., Newman, C. M., 1987. Stochastic Theory of Field-Scale Fickian Dispersion in Anisotropic Porous Media. Water Resources Research 23(3), 453-466.

Neuman, S. P., Zhang, Y.K., 1990. A quasi-linear theory of non-Fickian and Fickian subsurface dispersion, 1. Theoretical analysis with application to isotropic media. Water Resources Research, 26, (5), 887-902.

Nikolaidis, N., Karatzas, G., 2006. Detailed Study for the OptimumWater Resources Management of Agia Water Boreholes (Public Water Service of Chania Municipality).

Nikolaidis, N., Karatzas, G.P., 2010, Technical report on the water management of the Keritis and Koiliaris watersheds, Chania, Crete, Crete Region (in greek).

Ntarlagiannis, D., Robinson, J., Soupios, P., Slater, L., 2016. Field-scale electrical geophysics over an olive oil mill waste deposition site: Evaluating the information content of resistivity versus induced polarization (IP) images for delineating the spatial extent of organic contamination, Journal of Applied Geophysics 135, 418-426.

Noever, D.A., 1993. Himalayan sandpiles. Physical Reviews E 47, 724–725.

Nourbehecht, B., 1963. Irreversible thermodynamic effects in inhomogeneous media and their applications in certain geoelectrical problems. PhD Thesis, MIT, Cambridge, USA.

Nowroozi, A.A., Horrocks, S.B., Henderson, P., 1999. Saltwater intrusion into the freshwater aquifer in the eastern shore of Virginia: a reconnaissance electrical resistivity survey. Journal of Applied Geophysics 42, 1–22.

Nwankwoala, H.O., Udom, G.J., 2008. Hydrogeophysics: an overview of general concepts, applications and future perspectives. Scientia Africana 7, 54–63. doi: 10.4314/sa.v7i2.46018.

Nyquist, J.E., Cory, C.E., 2002. Self-potential: the ugly duckling of environmental geophysics. The Leading Edge 21, 446-451.

Ogata, A., Banks, R. B., 1961. A solution of differential equation of longitudinal dispersion in porous media. U. S. Geological Survey, Prof. Paper no. 411-A.

Ogata, A., 1970. Theory of dispersion in granular media. U S Geological Survey Prof. Paper, 411-I, 34.

Olami, Z., Feder, H.J.S., Christensen, K., 1992. Self-organized criticality in a continuous, nonconservative cellular automaton modeling earthquakes, Physical Review Letters 68, 1244–1247, 1992.

Onsager, L., 1931. Reciprocal relations in irreversible processes. I. Physical Reviews 37, 405-426.

Paduano, P., 2013. Groundwater planning and protection: assessment of environmental indexes in complex aquifer systems. the Solofrana river valley case study (south Italy), PhD thesis.

Paduano, P., Fabbrocino, S., 2013. Environmental state of groundwater resources in complex aquifer systems. Rendiconti online della Società Geologica Italiana 24, 216-218.

Paniconi, C., Aldama, A.A., Wood, E.F., 1991. Numerical evaluation of iterative and noniterative methods for the solution of the nonlinear Richards equation. Water Resources Research 27(6), 1147-1163.

Pankow, J.F., Feenstra, S., Cherry, J.A., Ryan, M.C., 1996. Dense chlorinated solvents in groundwater: Background and history of the problem. In: Pankow, J.F., and J.A. Cherry (Eds.), Dense Chlorinated Solvents and other DNAPLs in Groundwater, History, Behavior, and Remediation. Waterloo Press, Portland, Oregon, United States, pp. 1-52.

Papadopoulos, N. and Chatziathanasiou, S., 2011. ERT pollution monitoring in areas of olive oil mills' wastes (OOMW): Preliminary results from a disposal site in Crete (Greece). Berichte Geol. B.-A., 93, ISSN 1017-8880, Book of extended abstracts, 193-197.

Papadopoulos, N., Soupios, P., Kim, J., Simirdanis, K., Kirkou, S., Tsourlos, P., 2014. Mapping of olive oil mills' wastes (OOMW) through electrical resistivity tomography: a case study from Alikianos site in eastern Crete (Greece). European Meeting of Environmental and Engineering Geophysics, Athens.

Patacca, E., Scandone P., 1989. Post-Tortonian mountain building in the Apennines. The role of the passive sinking of a relic lithospheric slab. In Boriani, A., Bonafede, M., Piccardo, G.B., Vai, G.B., (Eds.), The lithosphere in Italy. Advances in Earth Science Research. It. Nat. Comm. Int. Lith. Progr., Mid-term Conf. (Rome, 5-6 May 1987), Proceedings Conv. Lincei 80, pp. 157-176.

Patacca, E., Scandone, P., 2007. Geology of the Southern Apennines. Italian Journal of Geosciences, Special Issue 7, 75-119.

Patella, D., 1997a. Introduction to ground surface self-potential tomography. Geophysical Prospecting 45, 653-681.

Patella, D., 1997b. Self-potential global tomography including topographic effects. Geophysical Prospecting 45, 843-863.

Parasnis, D. S. 1986, Principles of Applied Geophysics. 2nd edition, Chapman and Hall. 275pp.

Park, J., Lindberg, C.R., Vernon III, F.L., 1987. Multitaper spectral analysis of high-frequency seismograms, Journal of Geophysical Research 92, 12,675-12,684.

Paul, M. K., 1965. Direct interpretation of self-potential anomalies caused by inclined sheets of infinite extensions. Geophysics 30, 418-423.

Pawlowski, R.S., 1994. Green's equivalent-layer concept in gravity band-pass filter design. Geophysics 59, 69-76.

Pedersen, L.B., 1991. Relations between potential fields and some equivalent sources. Geophysics 56, 961-971.

Pekşen, E., Yas T., Kayman, A.Y., Özkan, C., 2011. Application of particle swarm optimization on self-potential data. Journal of Applied Geophysics 75, 305-318.

Peleg, N., Gvirtzman, H., 2010. Groundwater flow modeling of two levels perched karstic leaking aquifers as a tool for estimating recharge and hydraulic parameters. Journal of Hydrology 388, 13–27.

Percival, D.B., Walden, T.A., 1993. Spectral Analysis for Physical Applications: Multitaper and Conventional Univariate Techniques. Cambridge University Press, Cambridge.

Perrone, A., Lappena, V., Piscitelli, S., 2014. Electrical resistivity tomography technique for landslide investigation: A review. Earth-Science Reviews 135, 65–82.

Petiau, G., 2000. Second generation of lead-lead chloride electrodes for geophysical applications. Pure and Applied Geophysics 157(3), 357–382. doi:10.1007/s000240050004.

Picarelli, L., Evangelista, A., Rolandi, G., Paone, A., Nicotera, M.V., Olivares, L., Scotto di Santolo, A., Lampitiello, S., Rolandi, M., 2006. Mechanical properties of pyroclastic soils in Campania Region. Proc. 2nd Int. Work. on Characterization and Engineering Properties of Natural Soils, Singapore, 3, pp. 2331–2383.

Piegari, E., Cataudella, V., Di Maio, R., Milano, L., Nicodemi, M., 2006. A cellular automaton for the factor of safety field in landslides modeling. Geophysical Research Letters 33, L01403. doi:10.1029/2005GL024759.

Piegari, E., Di Maio, R., Milano, L., 2009. Characteristic scales in landslide modeling. Nonlinear Processes in Geophysics 16: 515–523. DOI: 10.5194/npg-16-515-2009.

Piegari, E., Di Maio, R., Scandone, R., Milano, L., 2011. A cellular automaton model for magma ascent: degassing and styles of volcanic eruptions. Journal of Volcanology and Geothermal Research 202, 22-28, doi:10.1016/ j.jvolgeores.2011.01.007.

Pierwola, J., 2013. Investigation of soil contamination using resistivity and induced polarization methods. Polish Journal of Environmental Studies 22(6), 1781– 1788.

Pinder, G. F., 2002. Groundwater Modeling using Geographical Information System. John Wiley and Sons, Inc., New York, 233 pp.

Price, W.L., 1976. A controlled random search procedure for global optimization. The Computer Journal, 20, 357-370.

Pride, S., 1994. Governing equations for the coupled electromagnetics and acoustics of porous media. Physical Review B 50 (21), 15678–15696.

Ramalho, E.C., Carvalho, J.P., Goncalves, R., Monteiro Santos, F.A., 2012. Understanding the 3D structure of a thermal water fissured granite aquifer by use of geophysical studies. Pure and Applied Geophysics 16911, 2031–2046.

Ramirez, A.L., Daily, W.D., LaBrecque, D.J., Owen, E., Chesnut, D., 1993. Monitoring an underground steam injection process using electrical resistance tomography. Water Resources Research 29, 73-87.

Rani, P., Di Maio, R., Piegari, E., 2015. High-resolution spectral analysis methods for self-potential data inversion. In: Expanded Abstract Volume of the 85th SEG Annual Meeting and Exposition. New Orleans, pp. 1596–1601.

Rani, P., Di Maio, R., Piegari, E., Simyrdanis, K., Papadopoulos, N., Dokou, Z., Kourgialas, N., Karatzas, Z., Soupios, P., 2016a. Application of time-lapse electrical resistivity tomography and groundwater simulation models to monitor the transport of organic contaminants under unsaturated and saturated conditions, oral presentation, 60th IAH 2016, Montpellier France.

Rani, P., Di Maio, R., Piegari, E., Simyrdanis, K., Papadopoulos, N., Soupios, P., 2016b. Application of self-potential method for monitoring the contamination from Olive oil mills' waste (OOMW), poster presentation, 60th IAH 2016, Montpellier France.

Rani, P., Di Maio, R., Piegari, E., Soupios, P., 2016c. Time evolution of self potential anomaly sources due to organic contaminant transport by different data inversion approaches, oral presentation at 88th Congress of Geological Society of Italy.

Rao, B.S.R., Murthy, I.V.R., Reddy, S.J., 1970. Interpretation of self-potential anomalies of some simple geometrical bodies. Pure and Applied Geophysics 78, 60-77.

Rao, S.V.S., Mohan, N.L., 1984. Spectral interpretation of self-potential anomaly due to an inclined sheet. Current Science 53, 474-477.

Revil, A., Pezard, P.A., Glover, P.W. J., 1999a. Streaming potential in porous media. 1. Theory of the zeta potential, Journal of Geophysical Research 104 (B9), 20021-20031.

Revil, A., Schwaeger, H., Cathles, L. M., Manhardt, P., 1999b. Streaming potential in porous media. 2. Theory and application to geothermal systems, Journal of Geophysical Research 104 (B9), 20033-20048.

Revil, A., Ehourane, L. & Thyreault, E., 2001. Tomography of self-potential anomalies of electrochemical nature, Geophysical Research Letters, 28, 4363-4366.

Revil, A., 2002. Comment on ‘‘Rapid fluid disruption: A source for self-potential anomalies on volcanoes’’ by M. J. S. Johnston, J. D. Byerlee, and D. Lockner. Journal of Geophysical Research, 107 (B8), 2155.

Revil, A., Naudet, V., Nouzaret, J., Pessel, M., 2003. Principles of electrography applied to self-potential electrokinetics sources and hydrogeological applications. Water Resources Research 39, 1114, doi: 10.109/2001WR000916.

Revil, A., Florsch, N., 2010. Determination of permeability from spectral induced polarization data in granular media. Geophysical Journal International 181, 1480–1498. doi:10.1111/j.1365-246X.2010.04573.x.

Revil, A., Karaoulis, M., Johnson, T., Kemna, A., 2012. Review: Some low-frequency electrical methods for subsurface characterization and monitoring in hydrogeology. Hydrogeology Journal 20, 617-658.

Revil, A., Jardani, A., 2013. The self-potential method: Theory and applications in Environmental Geosciences, 1st Edition. Cambridge University Press, New York, 369 pp.

Reynolds, J. M., 2011. An Introduction to Applied and Environmental Geophysics, 2nd edition, John Willey & Sons.

Richards, K., Revil, A., Jardani, A., Henderson, F., Batzle, M., Haas, A., 2010. Pattern of shallow ground water flow at Mount Princeton Hot Springs, Colorado, using geoelectrical methods. Journal of Volcanology and Geothermal Research, 198, 217-232.

Rivett, M.O., Clark, L., 2007. A quest to locate sites described in the world’s first publication on trichloroethene contamination of groundwater. Quarterly Journal of Engineering Geology & Hydrogeology 40(3), 241-249. doi: 10.1144/1470-9236/06-047.

Rubin, Y., Hubbard, S., 2005. Water and Science Technology Library. Hydrogeophysics 50, Springer, Houten, The Netherlands.

Rucker, D.F., Loke, M.H., Levitt, M.T., Noonan, G.E., 2010. Electrical-resistivity characterization of an industrial site using long electrodes. Geophysics 75, WA95.

Rushton, K. R., 2003. Groundwater Hydrology: Conceptual and Computational Models. John Wiley and Sons, Chichester, U.K.

Sahimi, M., 1993. Flow phenomena in rocks: from continuum models to fractals, percolation, cellular automata and simulated annealing. Reviews of Modern Physics 65, 1393-1534.

Schulze-Makuch, D., Bowman, R., Pillai, S., 2004. Removal of biological pathogens using surfactant-modified zeolite. US 20040108274 A1.

Seferou, P., Soupios, P., Kourgialas, N. N., Dokou, Z., Karatzas, G. P., Candasayar, E., Papadopoulos N., Dimitriou V., Sarris A., Sauter, M., 2013. Olive-oil mill wastewater transport under unsaturated and saturated laboratory conditions using the geoelectrical resistivity tomography method and the FEFLOW model. Hydrogeology Journal 21(6), 1219–1234.

Sharma, P.V., 1997. Environmental and Engineering Geophysics. Cambridge University Press, UK.

Sill, W. R., 1983. Self-potential modeling from primary flows. Geophysics 48, 76–86.

Simyrdanis, K., Papadopoulos, N., Soupios, P., Kirkou, S., Tsoulos, P., 2016. Characterization and Monitoring of Subsurface Contamination from Olive Oil Mills' Wastes through Electrical Resistivity Tomography, Near Surface Geophysics (Under review).

Slater, L.D., Brown, D., Binley, A., 1996. Determination of hydraulically conductive pathways in fractured limestone using cross-borehole electrical resistivity tomography, European Journal of Environmental and Engineering Geophysics 1, 35- 52.

Slater, L., Binley, A., Brown, D., 1997. Electrical imaging of fractures using ground-water salinity change. Groundwater 35, 436 - 442.

Slater, L., Lesmes, D., 2002. The Induced polarization method. New Jersey Geological Survey Open-File Report FOR 90-1, 160pp.

Slater, L., Binley, A., 2003. Evaluation of permeable reactive barrier (PRB) integrity using electrical imaging methods. Geophysics 68, 911-921.

Slater, L.D., and Glaser, D.R., 2003. Controls on induced polarization in sandy unconsolidated sediments and application to aquifer characterization. Geophysics 68, 1547- 1558.

Slater, L., Binley, A., 2006. Synthetic and field-based electrical imaging of a zerovalent iron barrier: Implications for monitoring long-term barrier performance. Geophysics 71(5), B129–B137, doi:10.1190/ 1.2235931.

Slepian, D., 1978. Prolate spheroidal wave functions, Fourier analysis, and uncertainty - V: The discrete case, Bell System Technical Journal 57, 1371-1430.

Soupios, P., Papadopoulos, N., Papadopoulos, I., Kouli, M., Vallianatos, F., Sarris, A., Manios, T., 2007a. Application of integrated methods in mapping waste disposal areas. Environmental Geology 53(3), 661– 675. doi:10.1007/s00254-007-0681-2.

Soupios, P., Papadopoulos, I., Kouli, M., Georgaki, I., Vallianatos, F., Kokinou, E., 2007b. Investigation of waste disposal areas using electrical methods: a case study from Chania, Crete, Greece. Environmental Geology 51(7), 1249–1261. doi:10.1007/s00254-006-0418-7.

Soupios, P., Kouli, M., Vallianatos, F., Vafidis, A., Stavroulakis, G., 2007c. Estimation of aquifer hydraulic parameters from surficial geophysical methods: A case study of Keritis basin in Chania (Crete, Greece). Hydrology 338, 122–131.

Soupios, P., Piscitelli, S., Vallianatos, F., Lapenna, V., 2008. Contamination delineation and characterization of waste disposal sites performing integrated and innovative geophysical methods. In: Waste management research trends, vol 11, pp 221–259.

Soupios, P., Karaoulis, M., 2015. Application of Self-Potential (SP) Method for Monitoring Contaminants Movement. 8th Congress of the Balkan Geophysical Society, Chania (Greece).

Spector, A., Grant, F.S., 1970. Statistical models for interpreting aeromagnetic data, Geophysics 35, 293-302.

Srivastava, S., Agarwal, B.N.P., 2009. Interpretation of self-potential anomalies by enhanced local wavenumber technique, Journal of Applied Geophysics 68, 259-268.

Srivastava, S., Datta, D., Agarwal, B.N.P., Mehta, S., 2014. Applications of Ant Colony Optimization in determination of source parameters from total gradient of potential fields, Near Surface Geophysics, 12, 373-389.

Stoica, P., Moses, R.L., 2005. Spectral Analysis of Signals. Prentice Hall, New Jersey.

Strack, O.D.L., 1989. Groundwater Mechanics. Prentice Hall, Englewood Cliffs, NJ.

Sumner, J. S., 1976, Principles of induced polarization for geophysical exploration. Elsevier.

Sundararajan, N., Srinivas, Y., 1996. A modified Hilbert transform and its application to self-potential interpretation. Journal of Applied Geophysics 36, 137-143.

Sundararajan, N., Srinivasa Rao, P., Sunitha, V., 1998. An analytical method to interpret self-potential anomalies caused by 2D inclined sheets. Geophysics 63, 1551-1555.

Supper, R., Romer, A., Kreuzer, G., Jochum, B., Ottowitz, D., Ita, A., Kauer, S., 2012. The GEOMON 4D electrical monitoring system: current state and future developments. Instrumentation and Data Acquisition Technology. Proceedings of GELMON 2011, Berichte Geol. B.-A., 93, pp. 23–26. ISSN 1017 – 8880.

Sutera, S.P., Skalak, R., 1993. The history of poiseuille's law. Annual Review of Fluid Mechanics 25, 1-19.

Tait, N.G., Davison, R.M., Whittaker, J.J., Leharne, S.A., Lerner, D.N., 2004. Borehole Optimisation System (BOS)- A GIS based risk analysis tool for optimising the use of urban groundwater 19, 1111-1124.

Telford, W.M., Geldart, L.P., Sheriff, R.E., Keys, D.A., 1990. Applied Geophysics. 2nd edition, Cambridge University Press.

Tezel, U., 2009. Fate and effect of Quaternary Ammonium Compounds in biological systems. PhD Thesis, Georgia Institute of Technology.

Thangarajan, M., 2004. Regional Groundwater Modeling. Capital Book Publishing Company, New Delhi.

Thomson, D.J., 1982. Spectrum estimation and harmonic analysis. Proceedings of IEEE 70, 1055-1096.

Tlas, M., Asfahani, J. 2008. Using of the Adaptive Simulated Annealing (ASA) for quantitative interpretation of self-potential anomalies due to simple geometrical structures, JKAU: Earth Science 19, 99-118.

Toffoli, T., Margolus, N., 1987. Cellular Automata Machines, MIT Press, Cambridge, MA.

Tyler, S. W., Wheatcraft, S. W., 1988. Application of fractals mathematics to soil water retention estimation. Soil Science Society of America Journal 53, 987-96.

Ulrych, T.J., Bishop, T.N., 1975. Maximum entropy spectral analysis and autoregressive decomposition. Reviews of Geophysics and Space Physics 13, 183-200.

van Genuchten, M. Th, 1978. Mass transport in saturated-unsaturated media: one-dimensional solutions. Research Rep. no. 87- WR-11, Water Resources Program, Princeton University, Princeton, NJ.

Wilkinson, P.B., Chambers, J.E., Lelliot, M., Wealthall, G.P., Ogilvy, R.D., 2008. Extreme sensitivity of crosshole electrical resistivity tomography measurements to geometric errors. Geophysical Journal International 173, 49-62.

Wolfram, S., 1986. Random sequence generation by cellular automata. Advances in Applied Mathematics 7, 123-169.

Xu, M. and Eckstein, Y., 1995. Use of weighted least-Squares method in evaluation of the relationship between dispersivity and field scale. Ground Water, 33, 905–908, doi:10.1111/j.1745-6584.1995.tb00035.x.

Yang, X., 1999. Stochastic inversion of 3D ERT data, Ph.D. thesis, the University of Arizona, Tucson, Arizona, USA.

Yi, M.J., Kim, J.H., Chung, S.H., 2003. Enhancing the Resolving Power of Least-Squares Inversion with Active Constraint Balancing. Geophysics 68, 931-941.

Yüngül, S., 1950. Interpretation of spontaneous-polarization anomalies caused by spherical ore bodies. Geophysics 15, 237-246.

Zhang, X.H., 2009. Remediation Techniques for Soil and Groundwater: point sources of pollution: Local effects and it's control, vol. II. Encyclopedia of Life Support Systems (EOLSS).

Zhao, L., Zhou, M., Zhang, T., Sun, H., 2013. Polyfluorinated and perfluorinated chemicals in precipitation and runoff from cities across eastern and central china. Archives of Environmental Contamination and Toxicology 64, 198–207.

Zogola, B., Mendecki, M.J., Zuberek, W.M., Robak, M., 2012. Application of self potential method in the area contaminated with oil derivatives. Acta Geodynamica et Geomaterialia 9 (2), 179-189.